Numerical relativity, compact objects, and fundamental fields

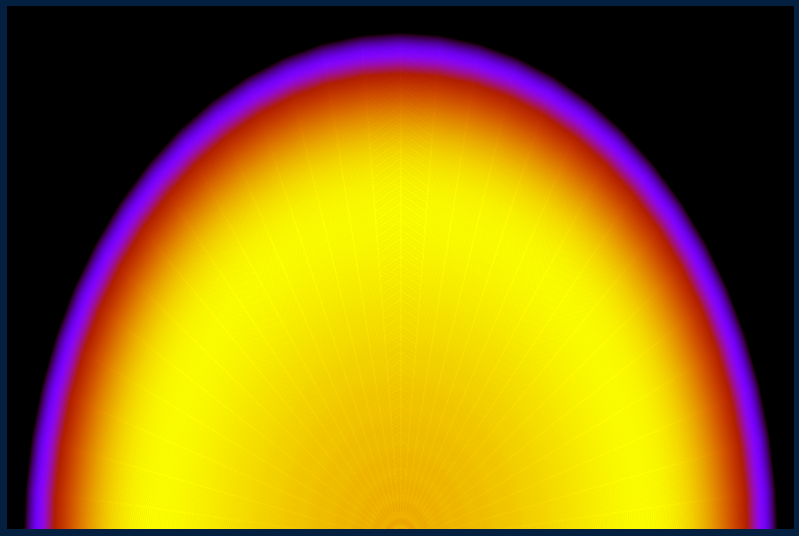

Nicolás Sanchis Gual

Director:

José Antonio Font Roda

Doctorat en Física

Departament d'Astronomia i Astrofísica

Universitat de València

TESIS DOCTORAL

Abril 2018

VNIVERSITAT DE VALÈNCIA

Numerical relativity, compact objects, and fundamental fields

Nicolás Sanchis Gual

Doctorat en Física
Departament d'Astronomia i Astrofísica
Universitat de València

TESIS DOCTORAL

Director:
José Antonio Font Roda

Abril 2018

A mis padres, Miguel Ángel y María Antonia, y a mis hermanos, Roger y Migue.
A Paulita.

Agradecimientos

Esta tesis doctoral no podría haberse llevado a cabo sin el apoyo y consejo de muchas personas.

En primer lugar, quiero agradecer a mi director Prof. Toni Font todo su inestimable apoyo y la confianza que ha depositado en mí. Me ha guiado y ayudado durante todo el desarrollo de la tesis, proponiendo los temas interesantes en los que hemos trabajado conjuntamente y aportando ideas y consejos esenciales para su buen término. Quiero agradecer también sus sugerencias sobre grupos musicales (Steven Wilson) y libros (Haruki Murakami), y su compresión con mis viajes a Tenerife.

De igual modo, quiero darle las gracias al Dr. Pedro Montero por codirigir y ayudarme con la primera parte de mi tesis doctoral y, en especial, por los códigos numéricos NADA que desarrolló, y que he usado ampliamente durante toda la tesis. Agradecerle su amabilidad y hospitalidad en mis visitas a Munich.

Dar las gracias a mis colaboradores Prof. Juan Carlos Degollado, Prof. Carlos Herdeiro y Prof. Eugen Radu, que han formado parte de la mayoría de los trabajos que conforman esta tesis. Sus interesantes discusiones e ideas han sido de gran valor para el desarrollo del presente trabajo. Quiero agradecer a Carlos, a Eugen, a António Morais, a Pedro Cunha y a todo el grupo de Aveiro su calurosa hospitalidad en mis múltiples visitas.

Agradecer a Borja Reina y al Prof. Raül Vera, la muy interesante colaboración y las entretenidas charlas por Skype.

Así mismo, a todos los miembros del Departamento de Astronomía y Astrofísica, en especial a José María Ibáñez por sus experimentados consejos y su contagioso entusiasmo en los temas que le apasionan, a Vicent Quilis, a Antonio Marquina, a Miguel Ángel Aloy y a Martin Obergaulinger por las provechosas discusiones científicas. También, a Feli, Manel y Lupe por sus atentos correos y llamadas, siempre pendientes de los plazos, de los documentos y de ayudarnos con la interminable burocracia. Mención especial a los buñuelos, la xocolatada y los dulces navideños.

Quiero recordar con mucho cariño al Prof. Diego Sáez, fallecido este año, que fue siempre muy amable y con el que tuve la suerte de dar una asignatura.

A mis compañeros y amigos, Alex, Vass, Jesús, Jose, Nicolas, Isa, Adri, Tomek, Rebecca, Jens, Sergio, Alejandro Cruz, y a mis "estudiantes", Alejandro Escorihuela y Fabrizio, porque es difícil encontrar gente tan fantástica y con ellos estos años de doctorado se han pasado volando. Por todas las risas, las "vacasaos", Baza, las noches bohemias, Juego de tronos, el kictipp y la porra amañada de Vass, que cualquier excusa es buena para ir al Wok, Juan Antonio Chistoso y muchas cosas más.

A mis amigos, en especial y sin que sirva que demérito a los demás, a Carlos, a Pablo, a Quilis, a Gabriel, a Hèctor y a Héctor, a Marc, a Lorena, a Natalia, a Miquel, a Bárbara, a Laura, a Alba, a Marta, a Monleón, a Omar y a Mario, por su amistad, su apoyo, su cariño y sus preguntas curiosas sobre mi investigación (y para que sirve) a lo largo del doctorado.

Muy especialmente, a mi familia; mis padres, Miguel Ángel y María Antonia, que son mi ejemplo a seguir y mi apoyo, por hacerme mejor persona, siempre recordándome que haga deporte y me cuide; a mis hermanos, Migue y Roger, porque les quiero; a mis tíos, Ximo y Fina, por ser siempre tan cariñosos; a mi prima, Anna, que para mí siempre será la pequeña; y a mis primos[4], Carlos y Pablo, porque ellos también son familia.

Finalmente, a mi chica, Paulita, gracias de corazón, por animarme cuando no me salían las cosas, por alegrarse más que yo con mis logros, por ser la mejor, estar siempre ahí y hacerme feliz. También quiero dar las gracias a su familia (Trini, Juli, Carlos, Carlitos, Elena, ...) por su sincero afecto y cariño.

Acknowledgements

This doctoral thesis could not have been carried out without the support and advice of many people.

First of all, I would like to thank my director Prof. Toni Font for all his invaluable support and the trust he placed in me. He has guided and helped me throughout the development of the thesis, proposing the interesting topics on which we have worked together and providing ideas and essential tips for its good term. I would also like to thank him for his suggestions about musical groups (Steven Wilson) and books (Haruki Murakami), and his understanding with my trips to Tenerife.

Likewise, I would like to thank Dr. Pedro Montero for co-directing and helping me with the first part of my thesis and, especially, for the numerical codes NADA that he developed, which I have widely used throughout the thesis. Thank you for your kindness and hospitality during my visits to Munich.

I would like to thank my collaborators Prof. Juan Carlos Degollado, Prof. Carlos Herdeiro and Prof. Eugen Radu, who have been part of most of the works of this thesis. Their interesting discussions and ideas have been of great value for the development of this work. I would also like to thank Carlos, Eugen, António Morais, Pedro Cunha and the whole group of Aveiro for their warm hospitality on my multiple visits.

I would like to thank Borja Reina and Prof. Raül Vera, the very interesting collaboration and the entertaining talks on Skype.

To all the members of the Department of Astronomy and Astrophysics, especially to José María Ibáñez for his expert advice and his contagious enthusiasm in the topics that he is passionate about, to Vicent Quilis, to Antonio Marquina, to Miguel Ángel Aloy and to Martin Obergaulinger for the fruitful scientific discussions. Also, to Feli, Manel and Lupe for their attentive and thoughtful emails and calls, always pending of the deadlines, of the documents and of helping us with the endless bureaucracy. Special mention to buñuelos, xocolatada and Christmas sweets.

I would like to remember with great affection Prof. Diego Sáez, who passed away this year and who was always very kind and I was fortunate to teach with.

To my colleagues and friends, Alex, Vass, Jesus, Jose, Nicolas, Isa, Adri, Tomek, Rebecca, Jens, Sergio, Alejandro Cruz, and my " students ", Alejandro Escorihuela and Fabrizio, because it is difficult to find such fantastic people and with them these years have flown by. For all the laughter, the " vacasaos ", Baza, the bohemian nights, Game of thrones, kictipp and Vassili's rigged draw, that any excuse is good enough to go to the Wok, Juan Antonio Chistoso and many other things.

To my friends, especially and without detriment to others, Carlos, Pablo, Quilis, Gabriel, Hector and Hector, Marc, Lorena, Natalia, Miquel, Barbara, Laura, Alba, Marta, Monleón, Omar and Mario, for their friendship, their support, their affection and their curious questions about my research (and what it is point of it) throughout my PhD.

Very especially, to my family; my parents, Miguel Ángel and María Antonia, who are my model to follow and my support, for making me a better person, always reminding me to exercise and take care of myself; to my brothers, Migue and Roger, because I love them; to my uncles, Ximo and Fina, for always being so affectionate; my cousin, Anna, who will always be the little one for me; and my cousins[4], Carlos and Pablo, because they are also family.

Finally, to my girlfriend, Paulita, thanks from the bottom of my heart, for encouraging me when things did not come out, for being more happy than me with my achievements, for being the best, always being there and making me happy. I also would like to thank her family (Trini, Juli, Carlos, Carlitos, Elena, ...) for their sincere affection and kindness.

Abstract

The recent detections of gravitational waves are opening a new window to the Universe. The nature of black holes and neutron stars may now be unveiled, but gravitational radiation may also lead to exciting discoveries of new exotic compact objects, oblivious to electromagnetic waves. In this thesis, I have investigated three main topics involving fundamental scalar and vector bosonic fields coupled to gravity within General Relativity and under the assumption of spherical symmetry: *(i)* quasistationary configurations of real scalar fields around Schwarzschild black holes as scalar field dark matter models, *(ii)* the superradiant instability and the formation of charged hairy black holes, and *(iii)* bosonic stars. These systems could have important astrophysical relevance, if ultralight bosonic fields exist in Nature. In 2012, the first non-gauge boson particle, the Higgs boson, was discovered in the Large Hadron Collider (LHC).

The main work in this thesis deals with numerical-relativity evolutions of bosonic fields in the strong-field regime of gravity. Recently, scalar field configurations around black holes have been studied in the linearized regime, taking the spacetime as a background. It was found that very long-lived scalar field quasibound states may form around the black hole. To investigate time evolutions in highly dynamical scenarios, it is required to perform numerical simulations of the fully non-linear Einstein-Klein-Gordon or Einstein-Proca coupled systems. To this aim I have extended numerical-relativity codes in 1D and 3D using spherical coordinates that solve the relativistic hydrodynamics equations coupled to the Einstein equations, implementing the fundamental equations describing the bosonic fields. Firstly, I have carried out numerical evolutions of scalar fields around black holes, taking into account the back-reaction of the field onto the gravitational field dynamics. Therefore, the spacetime could dynamically change: mass growth due to the absorption of part of a self-gravitating scalar field or from the adiabatic accretion of some other form of matter, or black hole formation from the gravitational collapse of a polytropic star described with an equation of state (EOS) similar to that

of a supermassive star. In all cases, my non-linear simulations have revealed a well-determined oscillating frequency that pointed out to the presence of the quasibound states described in the linearized literature. Another interesting phenomena involving bosonic fields and black holes is the superradiant instability, that can be triggered by the scattering of the field off the black hole. A bosonic field may then extract energy from the black hole and, if a trapping mechanism is introduced, it can grow exponentially. Building on previous numerical works in the linearized regime, I have studied the instability for a charged scalar field around a Reissner-Nordström (charged) black hole in a cavity, showing that the endpoint is a solution in which the black hole and the bosonic field are in equilibrium, i.e. a hairy black hole. Moreover, I found that the collapse of charged scalar field solitons in a cavity may also form these solutions. Finally, I have considered equilibrium models of bosonic stars as self-gravitating, everywhere non-singular, horizonless Bose-Einstein condensates of massive fields, namely boson stars with and without self interaction and Proca stars. These compact objects are regarded as black hole mimickers as they only interact through gravity. By performing accurate numerical simulations, I have observed that Proca stars resemble in many ways its scalar cousins, even with a self-interaction term. A separation between stable and unstable configurations occuring at the solution with maximal ADM mass has been indicated by previous results from linear perturbation theory. My simulations not only confirm this result but furthermore they show that the different outcomes of unstable models, namely migration to the stable branch, total dispersion of the scalar field, or collapse to a Schwarzschild black hole, are present for both fields. In the latter case, a field remnant lingers outside the horizon, forming a quasibound state. A further parallelism can be established with neutron stars, for which the collapse and the migration, but not the dispersion, has also been found numerically.

Regarding the numerical-relativity framework, in this thesis I have modified the CCZ4 formulation, which is a conformal and traceless decomposition of the Einstein equations, to make its evolution equations suitable for curvilinear coordinates. I have found that the Hamiltonian constraint violations could be reduced by one to three orders of magnitude for non-vacuum spacetimes with respect to the standard BSSN formulation. For Schwarzschild black holes, however, the results were not significantly better.

This thesis also contains some miscellaneous research work on two topics, namely slowly-rotating (fermionic) stars and my contribution to the Virgo Collaboration. The latter has consisted in producing gravitational waveforms from numerical simulations of collapsing stars described by a non-convex equation

of state (EOS). For the former I have studied numerically the recently amended Hartle's model of slowly-rotating stars within perturbation theory, which correctly takes into account density discontinuities in the surface of the star for the correction of the mass, δM, for different EOS. I have helped to develop a numerical code providing initial models of rotating stars for a number of EOS, beyond polytropes and the constant-density idealization. We were able to determine and include the universality of δM in the so-called I-Love-Q relations.

Resumen

Introducción

Las detecciones directas de ondas gravitatorias, la primera el 14 de Septiembre de 2015, provenientes de la fusión de binarias de objetos compactos (agujeros negros y estrellas de neutrones) abren una ventana a descubrir nuevos sistemas que permanecían vetados a las observaciones en el espectro electromagnético. Se espera ahora poder estudiar mediante las ondas gravitatorias otros sistemas como explosiones supernova, púlsares, el fondo estocástico de ondas gravitatorias de origen astrofísico y cosmológico, pero también objectos inesperados, como estrellas de bosones o estrellas de Proca. Este tipo de estrellas está compuesto por materia bosónica y no emiten radiación electromagnética, al contrario que las estrellas fermiónicas, por ejemplo las estrellas de neutrones, que son las únicas que se han observado hasta ahora.

Para estudiar objectos compactos en el régimen de gravedad intensa, es necesario recurrir a la Relatividad General de Albert Einstein, siendo la confirmación de la existencia de las ondas gravitatorias la última de sus predicciones. Es también necesario recurrir a ordenadores para estudiar sistemas dinámicos y sin altos grados de simetría: este campo de investigación se conoce como Relatividad Numérica. El uso de ordenadores permite llevar a cabo experimentos en laboratorios virtuales mediante simulaciones numéricas. El incremento continuado de la potencia de cálculo de los ordenadores ha contribuido decisivamente a los recientes espectaculares descubrimientos de las ondas gravitacionales.

En esta tesis doctoral, he trabajado principalmente en el campo de la Relatividad Numérica investigando la dinámica de campos bosónicos autogravitantes y alrededor de agujeros negros, en concreto: (i) campos escalares reales alrededor de agujeros negros de Schwarzschild, (ii) campos escalares complejos cargados en una cavidad interaccionando con un agujero negro de Reissner-Nordström, y (iii) estrellas de Proca y estrellas de bosones con autointeracción. Además, también he participado en el desarrollo de un código numérico para la construcción

de modelos de equilibrio de estrellas en rotación lenta a partir del formalismo modificado de Hartle.

Objetivos

El objetivo principal del trabajo de la presente tesis ha sido realizar evoluciones temporales utilizando la Relatividad Numérica para estudiar diferentes sistemas que involucran campos bosónicos fundamentales en escenarios de gravedad intensa, potencialmente relevantes astrofísicamente, si estos campos fundamentales existiesen en la naturaleza con masas extremadamente pequeñas, del orden de 10^{-20} eV. En 2012, fue descubierto el bosón de Higgs, con una masa de aproximadamente 125 GeV [Collaboration 2012, Chatrchyan et al. 2012, Collaboration et al. 2012].

En el marco de las simulaciones numéricas, he estudiado el funcionamiento de una nueva formulación de las ecuaciones de Einstein. Esta es la recientemente propuesta formulación Z4 de las ecuaciones de Einstein, que permite una reducción de uno a tres órdenes de magnitud en la violación de la restricción Hamiltoniana con respecto a la formulación BSSN (Baumgarte-Shapiro-Shibata-Nakamura). Esto permitiría realizar simulaciones numéricas más precisas, puesto que en estos formalismos, llamados de evolución libre, no se resuelven estas restricciones sino que se calculan para monitorizar la exactitud de la solución. Sin embargo, las ecuaciones del formalismo CCZ4 (*Conformal and covariant formulation of the Z4 system*) no son totalmente covariantes y adecuadas para las coordenadas curvilíneas, sistema de coordenadas que emplean los códigos numéricos que he utilizado en este trabajo.

En cuanto a las evoluciones numéricas, numerosos estudios en el régimen lineal han investigado si los agujeros negros supermasivos que existen en el centro de las galaxias pueden suponer una amenaza para los modelos de materia oscura basados en campos escalares. Tomando un campo escalar real prueba en un espacio-tiempo de Schwarzschild de fondo, tales estudios han demostrado que se forman estados cuasiligados que oscilan con una frecuencia definida alrededor del agujero negro a partir de distribuciones iniciales arbitrarias. Estos estados pueden existir por tiempos muy largos (mayores que la edad del Universo) dependiendo del valor de la masa de la partícula del campo escalar μ. No obstante, la aproximación de campo prueba del régimen lineal es inadecuada cuando el campo es autogravitante y afecta a la dinámica del propio espacio-tiempo (por ejemplo, cambiando la masa del agujero negro). Para suplir esta

deficiencia, es necesario realizar simulaciones numéricas no lineales, resolviendo el sistema acoplado Einstein-Klein-Gordon.

De igual modo, resulta interesante estudiar la formación y supervivencia de los estados cuasiligados en otros escenarios altamente dinámicos relacionados con la formación del agujero negro supermasivo central en las galaxias, como en el colapso de una estrella supermasiva o en procesos de acreción de materia a ritmos elevados. En el primer caso, también se han de resolver las ecuaciones de la hidrodinámica acopladas a la gravedad.

Además, a diferencia de los fermiones, un campo bosónico dispersado por un agujero negro con carga eléctrica Q (en este caso el campo debe estar cargado) o momento angular J puede extraer energía del agujero negro y aumentar su amplitud. Este fenómeno se conoce como *superradiancia*. En el caso cargado, si se introduce una cavidad reflectante, o debido al pozo de potencial creado por el término de masa de un campo masivo, el crecimiento de la amplitud del campo se vuelve exponencial, provocando una inestabilidad cuyo desenlace era desconocido hasta el estudio realizado en esta tesis. Estudios previos perturbativos en el régimen lineal muestran la etapa de crecimiento exponencial, pero, al no tener en cuenta la acción del campo sobre el espacio-tiempo, no pueden alcanzar el régimen no lineal. El estado final podría ser un agujero negro con pelo, es decir, una configuración estática del espacio-tiempo dónde el agujero negro y el campo escalar están en equilibrio. Para investigar el régimen no lineal son necesarias simulaciones de relatividad numérica de estos sistemas. El estudio de un campo escalar cargado alrededor de un agujero negro de Reissner-Nordström con carga Q en una cavidad puede realizarse en simetría esférica resolviendo las ecuaciones de Einstein-Maxwell acopladas a las ecuaciones de Klein-Gordon. Además, las escalas temporales del crecimiento de la inestabilidad superradiante son órdenes de magnitud más pequeñas que en el caso de un agujero negro en rotación, por lo que el estudio es algo más sencillo. Si los agujeros negros astrofísicos tuvieran pelo, estos servirían como detectores de partículas bosónicas ultraligeras.

Por otra parte, un campo escalar cargado también puede formar solitones en una cavidad. El colapso de solitones cargados puede ser un mecanismo para la formación de agujeros negros con pelo.

Los campos bosónicos pueden formar configuraciones macroscópicas análogas a las estrellas de neutrones. Se denominan estrellas de bosones o estrellas de Proca a las distribuciones estacionarias de campo escalar o vectorial, respectivamente, que oscilan con una determinada frecuencia y cuyo espacio-tiempo no depende del tiempo, es estático. Se han encontrado secuencias de modelos de equilibrio en simetría esférica de estos dos tipos de estrellas que se asemejan a las de las

estrellas de neutrones y las enanas blancas: una rama de modelos estables frente a perturbaciones radiales, una masa máxima y otra rama con modelos inestables. Para estudiar la estabilidad no lineal bajo perturbaciones de estos modelos de estrellas bosónicas, se deben realizar de nuevo simulaciones numéricas. Si se introduce un término de autointeracción en el potencial, se puede aumentar arbitrariamente las masas máximas. Al no interaccionar electromagnéticamente, a estas estrellas se les ha llamado imitadores de agujeros negros, aunque algunas de sus propiedades definitorias serían diferentes, como las sombras de dichos objetos compactos o el *quasinormal mode ringdown* de las ondas gravitatorias emitidas debido a una perturbación.

Por último, recientemente se extendió el modelo clásico de Hartle que describe estrellas relativistas en rotación lenta, introduciendo una corrección a la masa. Dicha corrección no resulta menospreciable cuando la densidad en la superficie de la estrella no es nula. Se ha comprobado que su efecto en la masa total puede ser muy importante para estrellas idealizas con densidad constante. Por lo tanto, es necesario estudiar numéricamente con el formalismo extendido ecuaciones de estado realistas con discontinuidades en la densidad en la superficie de la estrella.

Metodología

La versión original del código de relatividad numérica NADA en 2D [Montero, Font, and Shibata 2008] impone la condición de axisimetría en coordenadas cartesianas mediante el uso del método Cartoon [Alcubierre et al. 2001]. El código ha sido utilizado con éxito en simulaciones de la evolución de agujeros negros, colapso gravitatorio, y en sistemas formados por agujeros negros rodeados por toros de acreción autogravitantes. Recientemente, ha sido extendido a 3D en coordenadas esféricas y ha sido testeado exhaustivamente en evoluciones de estrellas compactas (Tolman-Oppenheimer-Volkoff, TOV), tanto en simetría esférica como en rotación rápida, estables o colapsando a agujero negro, y en el test del colapso de Oppenheimer-Snyder [Baumgarte et al. 2013]. Durante la realización de mi Trabajo de Fin de Máster, extendí el código implementando la extracción de la radiación gravitatoria. También existe una versión del código en 1D y en simetría esférica llamada NADA1D [Montero and Cordero-Carrión 2012].

Ambos códigos, en su forma original, permiten resolver las ecuaciones de evolución del campo gravitatorio, escritas en el formalismo BSSN, y de las

ecuaciones de la hidrodinámica. Estas son un conjunto de ecuaciones diferenciales en derivadas parciales de primer orden que se integran para obtener la evolución temporal de un sistema utilizando los métodos PIRK (Partially-Implicit Runge-Kutta) con una precisión de segundo orden, especialmente diseñados para realizar simulaciones numéricas en coordenadas curvilíneas [Montero and Cordero-Carrión 2012]. Los códigos de Relatividad Numérica NADA1D y NADA3D, desarrollados por Thomas Baumgarte, Pedro Montero e Isabel Cordero-Carrión, usan coordenadas esféricas. Muchos fenómenos astrofísicos son simétricos con respecto al eje de rotación (por ejemplo, discos de acreción) o las coordenadas esféricas se adaptan mejor a su geometría (por ejemplo, el colapso gravitacional de las estrellas de neutrones). Sin embargo, estas coordenadas son una fuente de inestabilidades numéricas debido a la presencia de términos que van como $1/r$ o $1/\sin\theta$, pero estos métodos evitan esos problemas al introducir operadores implícitos que específicamente tratan esos términos. Gracias a esto, se obtuvieron con NADA1D simulaciones numéricas estables de vacío y con materia sin la necesidad de utilizar un algoritmo de regularización como en el trabajo de Ruiz, Alcubierre, and Nunez [2008]. Este enfoque también se ha implementado con éxito en 3D sin ninguna suposición de simetría en Baumgarte et al. [2013] y en Montero, Baumgarte, and Müller [2014] se consiguió la primera implementación exitosa de la evolución de la hidrodinámica relativista acoplada a espacio-tiempos dinámicos en coordenadas esféricas sin supuestos de simetría.

En esta tesis el código NADA en 1D ha sido desarrollado para incluir la formulación fCCZ4 de las ecuaciones de Einstein, más precisa que la formulación BSSN. Esta formulación es una ampliación de CCZ4, reescribiendo sus ecuaciones de forma adecuada para coordenadas curvilíneas. Para evaluar su correcta implementación, realizé un estudio comparativo con BSSN en una batería de tests: estrellas esféricas estables (TOV), test de migración, y colapso de modelos TOV inestables a agujero negro.

Asimismo, he implementado en esta versión del código las ecuaciones de Klein-Gordon para un campo real y un campo complejo cargado. Se han llevado a cabo evoluciones de un campo escalar autogravitante como modelo de materia oscura en el caso de un agujero negro de Schwarzschild y en el caso de una estrella descrita con la ecuación de estado de una estrella supermasiva que colapsa a agujero negro, para comprobar si el campo escalar puede sobrevivir a este evento. Además, he investigado la evolución de un agujero negro cuya masa aumenta por acreción de materia para estudiar la influencia de este proceso en la evolución del campo escalar.

Para investigar el régimen no lineal del fenómeno de superradiancia para el campo escalar cargado, es necesario implementar las ecuaciones de evolución para un campo escalar complejo con carga eléctrica. En este caso, tanto el campo como el espacio-tiempo (un agujero negro de Reissner-Nordström) están acoplados mediante la interacción eléctrica, por lo que el código debe resolver también las ecuaciones de Maxwell para el campo eléctrico. Los términos fuente en el lado derecho de las ecuaciones de Einstein deben tener en cuenta ambos campos, escalar y eléctrico. Las simulaciones realizadas han abarcado un amplio rango de parámetros (masa de la partícula del campo escalar, carga, energía inicial, término de autointeracción). Del mismo modo, se ha estudiado la estabilidad y el colapso de solitones cargados en una cavidad.

En el caso de configuraciones de equilibrio de campos bosónicos autogravitantes, en esta tesis estudié estrellas de bosones con autointeracción, incluyendo un término de cuarto orden en el potencial del campo escalar. Se utilizó un código adicional para calcular los datos iniciales de los modelos de estas estrellas, obteniendo las secuencias de las configuraciones de equilibrio. Al incluir el término de autointeracción, la masa máxima de los modelos de equilibrio es mayor que en ausencia de dicho término. Se modificó NADA1D para tener en cuenta el nuevo potencial en las evoluciones numéricas.

Para los campos vectoriales, se implementó las ecuaciones del campo de Proca masivo en el código NADA en 3D para estudiar la estabilidad y el colapso de estrellas de Proca en simetría esférica. Reduciendo el número de celdas en las direcciones angulares en este código, podemos recuperar el código de simetría esférica. En el futuro se estudiará la evolución de estrellas de Proca con momento angular.

Para el modelo extendido de estrellas relativistas de rotación lenta de Hartle, se modificó un código que genera modelos iniciales de estrellas tipo TOV, incluyendo las perturbaciones de segundo orden y la posibilidad de utilizar ecuaciones de estado analíticas o tabuladas. Además, comparamos algunos modelos con el código RNS [Stergioulas and Friedman 1994, Stergioulas 1996], que permite construir numericamente modelos exactos de estrellas relativistas en rotación.

Conclusiones

Formulación fCCZ4

Además de la formulación BSSN, otras descomposiciones conformes y sin traza de las ecuaciones de Einstein basadas en el sistema Z4 [Bona et al. 2003]

han sido propuestas por Bernuzzi y Hilditch [Bernuzzi and Hilditch 2010, Ruiz, Hilditch, and Bernuzzi 2011, Weyhausen, Bernuzzi, and Hilditch 2012, Hilditch et al. 2013], la llamada formulación Z4c, y también por Alic et al. [Alic et al. 2012, Alic, Kastaun, and Rezzolla 2013], la formulación CCZ4. Estas formulaciones incorporan un esquema de amortiguamiento de las restricciones desarrollado por Gundlach et al. [Gundlach et al. 2005] que introduce un conjunto de parámetros para controlar dinámicamente las violaciones de las restricciones. Este procedimiento ha sido testeado extensivamente y los resultados muestran una reducción de las violaciones de la restricción Hamiltoniana de entre 1 y 3 órdenes de magnitud con respecto a BSSN.

Sin embargo, ambas formulaciones rompen la 4-covarianza, descartando los términos no principales que no son de amortiguamiento o modificando el parámetro de amortiguación que elimina las inestabilidades cuando se usa la versión totalmente covariante del sistema CCZ4 en la evolución de agujeros negros. Además, en su forma original, las formulaciones BSSN y CCZ4 o Z4c están particularmente desarrolladas para coordenadas cartesianas: involucran campos que no son verdaderos tensores (es decir, las funciones conformes de la conexión) y asumen que el determinante de la métrica conforme es la unidad. Brown [Brown 2009] introdujo una formulación covariante de las ecuaciones BSSN que es adecuada para sistemas de coordenadas curvilíneas, mediante la introducción de una referencia métrica [Bonazzola 2004].

En Sanchis-Gual et al. [2014] reescribí las ecuaciones de evolución de CCZ4 manteniendo la 4-covarianza completa, incluso para agujeros negros, y, siguiendo el trabajo de Brown, introduje una métrica de referencia para hacerlas adecuadas para coordenadas esféricas, bajo el supuesto de simetría esférica. A continuación, realicé evoluciones numéricas de vacío (agujero negro de Schwarzschild) y con materia (modelos politrópicos relativistas de estrellas de neutrones, tanto estables como inestables) para evaluar la precisión de la formulación fCCZ4 con respecto a BSSN. Estudié estos sistemas para varios valores de los parámetros de amortiguación κ_1 y κ_2, y, dependiendo de esta elección, encontré que las violaciones de la restricción Hamiltoniana se redujeron entre 1 y 3 órdenes de magnitud con respecto a BSSN. Sin embargo, efectos nocivos de sobreamortiguamiento podían tener lugar para valores demasiado altos de κ_1. Para el test con un agujero negro, pude obtener evoluciones estables para parámetros particularmente ajustados, pero la masa del horizonte aparente (que debe conservarse durante la fase estacionaria) sufría una disminución lenta para fCCZ4 en tiempos tardíos ($t = 1875$) de menos de 0.005%. Debido a estos resultados para simulaciones que involucran agujeros negros y al inconveniente de tener que elegir valores

correctos par los parámetros de amortiguación, utilicé la formulación BSSN en las simulaciones numéricas posteriores presentadas en esta tesis.

Simulaciones de Relatividad Numérica de campos escalares alrededor de agujeros negros

Existe gran evidencia observacional que apunta a la existencia de agujeros negros supermasivos en el centro de la mayoría de las galaxias. La evolución de estos agujeros negros está directamente conectada a la evolución de su galaxia anfitriona [Kormendy and Gebhardt 2001]. En este contexto, los campos escalares han sido propuestos como candidatos a materia oscura [Sahni and Wang 2000, Hu, Barkana, and Gruzinov 2000, Matos and Urena-Lopez 2000, Matos and Urena-Lopez 2001]. En estos modelos, la materia oscura se compone de partículas bosónicas que pueden condensarse en objetos macroscópicos que forman estrellas de bosones o halos alrededor de los agujeros negros centrales. Para ser considerados como alternativas plausibles, deben sobrevivir durante escalas de tiempo cosmológicas en presencia de los agujeros negros [Barranco et al. 2011] y en escenarios altamente dinámicos.

Varios estudios han investigado en el régimen linealizado la dinámica de los campos escalares alrededor de agujeros negros. En estos estudios, el espacio-tiempo de un agujero negro se toma como fondo independiente del tiempo donde el campo escalar evoluciona [Witek et al. 2013, Barranco et al. 2012, Barranco et al. 2014, Dolan 2012, Cruz-Osorio, Guzman, and Lora-Clavijo 2011]. Estos trabajos han demostrado que los campos escalares masivos que rodean a agujeros negros estacionarios pueden formar estados cuasiligados como resultado de la presencia del pozo de potencial debido al término de masa. Estos estados decaen en el infinito y, por lo tanto, se localizan alrededor del agujero negro. Veremos en el siguiente apartado que si el agujero negro tiene carga eléctrica o momento angular, la amplitud del campo escalar puede crecer de forma exponencial.

Estos estados cuasiligados son configuraciones de campo escalar que pueden permanecer mucho tiempo alrededor de los agujeros negros [Barranco et al. 2014]. Están caracterizados por tener una frecuencia compleja: la parte real representa la frecuencia de oscilación y la parte imaginaria proporciona, dependiendo de la cadencia, su tasa de decaimiento o de crecimiento, si un modo es superradiantemente inestable. La aproximación de campo de prueba es válida siempre que la energía del campo sea pequeña y dejará de serlo, eventualmente, a medida que la energía aumenta. Además, el efecto de la autogravedad del campo escalar en la dinámica del espacio-tiempo se vuelve no despreciable cuando la masa inicial del campo es lo suficientemente grande en comparación con la masa agujero

negro. Por tanto, simulaciones no lineales de configuraciones de campos escalares autogravitantes son necesarias para estudiar correctamente el sistema. En este estudio, me centré en los casos en los que la masa de la nube de campo escalar puede ser mayor que la masa del agujero negro y por lo tanto, constituye una fuerte desviación del régimen linealizado, una distribución significativa de campo escalar en un espacio-tiempo altamente dinámico.

Para llevar a cabo estos estudios numéricos, implementé la ecuación real de Klein-Gordon acoplada a las ecuaciones de Einstein en NADA1D [Sanchis-Gual et al. 2015]. Las ecuaciones de evolución temporal se realizaron usando el mismo método PIRK de segundo orden mencionado anteriormente aplicado a la formulación BSSN. Se consideró una distribución gaussiana inicial del campo escalar alrededor de un agujero negro de Schwarzschild y se resolvió la restricción Hamiltoniana. Primero, recuperé los resultados del régimen linealizado cuando la energía del campo es pequeña en comparación con la masa agujero negro. Las simulaciones de larga duración para grandes energías iniciales de campo escalar mostraron que los estados cuasiligados se pueden identificar por una frecuencia de oscilación real incluso después de que la masa del agujero negro aumente súbitamente debido a la absorción de parte del campo. Encontramos que para un agujero negro ya formado, aparecían soluciones cuasiestacionarias autogravitantes con menos energía total que la distribución inicial.

Por otra parte, la formación de agujeros negros supermasivos es un problema fundamental en el estudio de la formación de galaxias. Aún se desconoce cómo los agujeros negros supermasivos pueden formarse y crecer para alcanzar los valores actuales cuando el Universo tenía menos de 10^9 años. Una posibilidad [Begelman, Volonteri, and Rees 2006b, Begelman 2010, Mayer et al. 2010] supone que los agujeros negros centrales se forman a través del colapso directo de estrellas supermasivas con masas $\geq 5 \times 10^4 \mathrm{M}_\odot$, que evolucionarían como configuraciones de equilibrio dominadas por la presión de radiación antes de colapsar para formar las semillas de los agujeros negros supermasivos [Shibata and Shapiro 2002, Montero, Janka, and Müller 2012].

Los halos de campo escalar también deberían sobrevivir al colapso de estrellas supermasivas. En consecuencia, el principal objetivo de mi segundo trabajo en este tema fue evaluar el papel de la formación del agujero negro en presencia de configuraciones de campo escalar que se asemejan a los estados cuasiligados encontrados en investigaciones previas, donde el agujero negro existe desde el comienzo. Para analizar la viabilidad de este escenario, hice simulaciones numéricas del colapso gravitacional de una estrella politrópica con índice adiabático $\gamma = 4/3$, para simular estrellas supermasivas radiativas, en un ambiente rico

en campo escalar [Sanchis-Gual et al. 2015]. La evolución de las ecuaciones de la hidrodinámica relativista también se tuvo en cuenta en este estudio. El campo escalar y la materia de la estrella están acoplados únicamente a través de la gravedad. Los resultados mostraron que el campo escalar no es absorbido por completo o no se dispersa después del colapso, de manera que puede formar estados cuasiligados con una frecuencia (o frecuencias) de oscilación bien determinada.

Otra posible hipótesis para la existencia de agujeros negros supermasivos es que éstos se formaron y crecieron a través de procesos de acreción y fusión de los primeros restos estelares [Bromm and Loeb 2003a, Haiman and Loeb 2001a]. Se cree que los agujeros negros supermasivos podrían ser el resultado final del crecimiento de semillas de agujeros negros en galaxias con alto corrimiento al rojo a través de episodios de acreción y fusiones de binarias de agujeros negros masivos [Kauffmann and Haehnelt 2000, Volonteri, Haardt, and Madau 2003]. Estos agujeros negros supermasivos deben crecer rápidamente para adquirir sus masas totales en un corto período de ~ 1 Gyr, haciendo que éste sea un evento altamente dinámico.

Si bien se puede argumentar que los agujeros negros supermasivos han crecido en gran medida a través de procesos de acreción, el crecimiento exponencial necesario para hacer crecer las semillas de agujeros negros de masa estelar y obtener los cuásares luminosos supermasivos que se observan a $z \sim 7$, es demasiado lento cuando el ritmo de acreción está limitado por el ritmo de Eddington [Mortlock et al. 2011]. Para eludir este problema, algunos estudios invocan varias alternativas como, procesos de acreción súper-Eddington durante breves períodos de tiempo [Begelman 1979, Alexander and Natarajan 2014, McKinney et al. 2014], formación a través de acreción y fusión de los primeros remanentes estelares [Bromm and Loeb 2003b, Haiman and Loeb 2001b], o considerando más semillas masivas del colapso de discos pre-galácticos a alto redshift [Begelman, Volonteri, and Rees 2006a, Begelman 2010, Mayer et al. 2010].

Es interesante preguntarse si la acreción rápida de materia por un agujero negro puede tener algún efecto en la distribución del campo escalar como halo de materia oscura. En ausencia de acreción, la existencia de configuraciones longevas de nubes de campo escalar alrededor de agujeros negros sin momento angular ha sido confirmada por un buen número de trabajos. Por lo tanto, se ha demostrado que los agujeros negros supermasivos en núcleos galácticos no representarían una seria amenaza para estos modelos de materia oscura basados en campos escalares (ultraligeros), suponiendo, por tanto, una alternativa viable

a la descripción habitual de la materia oscura mediante partículas masivas que interactúan débilmente (WIMPs). Utilizando la hipótesis de un crecimiento rápido de los agujeros negros supermasivos por acreción, investigué el efecto sobre el campo escalar en esa situación dinámica mediante el estudio de las propiedades de los estados cuasiligados cuando el espacio-tiempo es el de un agujero negro en simetría esférica capturando materia [Sanchis-Gual et al. 2016c]. Suponiendo que la masa del agujero negro crece adiabáticamente debido a la materia que captura, mostramos que estados cuasiligados duraderos para el campo escalar aún pueden formarse y sobrevivir en tal escenario. Sin embargo, las escalas de tiempo se reducen, pero sólo de manera significativa para tasas de acreción extremadamente altas y poco realistas.

La inestabilidad superradiante y agujeros negros cargados con pelo

Hasta ahora, he descrito los resultados de nuestras simulaciones numéricas de un campo escalar masivo alrededor de un agujero negro de Schwarzschild. Esta puntualización es importante pues, en este caso, los estados cuasiligados sólo pueden conducir a modos que decaen exponencialmente, con una frecuencia imaginaria negativa. Por lo tanto, el agujero negro terminará absorbiendo todo el campo escalar después de una escala de tiempo determinada por la masa de partícula de campo escalar μ y el espacio-tiempo tenderá asintóticamente a la métrica de Schwarzschild.

Para agujeros negros en rotación, descrito por la métrica de Kerr dentro de la Relatividad General, las ondas bosónicas dispersadas por un agujero negro extraen parte de la energía y el momento angular del agujero negro y aumentan su propia energía y momento angular a través del proceso clásico de superradiancia [Bardeen, Press, and Teukolsky 1972, Starobinsky 1973, Press and Teukolsky 1972, Damour, Deruelle, and Ruffini 1976, Zouros and Eardley 1979b, Detweiler 1980b, Cardoso et al. 2004, Dolan 2007, Rosa 2010, Brito, Cardoso, and Pani 2015b]. Este fenómeno ocurre para los campos bosónicos escalares, vectoriales y tensoriales. En East, Ramazanoğlu, and Pretorius [2014], se demostró numéricamente por primera vez en el régimen no lineal que las ondas gravitatorias se amplifican cuando son reflejadas por un agujero negro de Kerr, disminuyendo el espín. La superradiancia se activa si el campo tiene un número cuántico azimutal, m, distinto de cero, oscila con frecuencia ω y cumple la condición de sincronización

$$\omega < m\Omega_{\mathrm{H}}, \tag{1}$$

donde $\Omega_{\rm H}$ es la velocidad angular del horizonte. La parte imaginaria de la frecuencia es entonces positiva y el campo crece exponencialmente. En el caso de las ondas gravitatorias, la masa del gravitón es cero (dentro de la Relatividad General), por lo que las ondas se dispersan después de la reflexión. Pero, si se introduce un término masivo o una condición de contorno similar a un espejo, los modos superradiantes quedan atrapados, extrayendo energía continuamente del agujero negro y creciendo en el tiempo, desencadenando así una inestabilidad del sistema formado por el agujero negro y el campo escalar. En consecuencia, en esta configuración, el agujero negro de Kerr (sin pelo) es inestable y el campo escalar crece con el tiempo en el exterior del agujero negro.

Para alcanzar el régimen no lineal de la inestabilidad y entender su desenlace, son necesarias simulaciones numéricas. Esto representa un desafío notable con la tecnología actual de los códigos de Relatividad Numérica [Okawa, Witek, and Cardoso 2014, East, Ramazanoğlu, and Pretorius 2014], pues la tasa de crecimiento máxima de la inestabilidad es tan pequeña para campos escalares que la inestabilidad puede permanecer indistinguible de los errores numéricos de las simulaciones numéricas [Okawa, Witek, and Cardoso 2014]. Se han realizado estudios [Zouros and Eardley 1979a, Detweiler 1980a, Furuhashi and Nambu 2004, Cardoso and Yoshida 2005, Hod 2012a] en los que se ha encontrado que el crecimiento máximo de la inestabilidad se corresponde a un tiempo de aproximadamente $\tau^{-1} \sim 1.11 \times 10^{-7}\,(GM/c^3)$, para una masa $\mu \sim 0.39$ y un espín del agujero negro de $a = 0.98$.

Una situación análoga y numéricamente más favorable se produce al considerar agujeros negros cargados, de tipo Reissner-Nordström. En este caso, la energía y la carga eléctrica se extraen del agujero negro por un campo bosónico *cargado* [Bekenstein 1973, Hod 2012b]. Las tasas de crecimiento de la inestabilidad superradiante cargada pueden ser de hasta un orden de magnitud mayor que para los agujeros negros en rotación [Herdeiro, Degollado, and Rúnarsson 2013, Hod 2013, Degollado and Herdeiro 2014]. La correspondiente condición para tener modos superradiantes es, para el caso cargado, la siguiente

$$w < w_{\rm c} \equiv q\phi_H, \tag{2}$$

donde q es la carga de la partícula del campo escalar y ϕ_H es el potencial eléctrico en el horizonte ($w_{\rm c}$ indica la frecuencia crítica). Además, para formar una *bomba de agujero negro cargado* debe introducirse un mecanismo de captura, por ejemplo, un espejo,. Considerar un campo escalar con masa no es suficiente

ya que la repulsión eléctrica impide el desarrollo de estados cuasiligados para el rango de parámetros de $\{\mu, q\}$ necesario para desencadenar la inestabilidad.

La inestabilidad cargada puede ocurrir en simetría esférica, por lo tanto extendí la implementación numérica en el código NADA1D para tener en cuenta un campo escalar cargado complejo y las ecuaciones de Maxwell para el campo eléctrico. El sistema completo de Einstein-Maxwell-Klein-Gordon-(cargado) (EMKG) fue resuelto numéricamente. La configuración inicial considerada fue una perturbación de un campo escalar cargado en una cavidad, con un agujero negro de Reissner-Nordström. Mis simulaciones [Sanchis-Gual et al. 2016b] establecieron que el estado final genérico es un agujero negro *con pelo*: un horizonte cargado, rodeado por un condensado de campo escalar que almacena parte de la carga y la energía iniciales del agujero negro, y con una fase que oscila con la frecuencia umbral de la inestabilidad superradiante. La fase de crecimiento exponencial del campo se satura y el equilibrio se alcanza cuando la condición $\omega = \omega_{\rm c}$ se cumple. La parte imaginaria de la frecuencia del campo es cero y se forma un agujero negro con pelo. Resultados similares se encontraron en Bosch, Green, and Lehner [2016], considerando un espacio-tiempo anti-De Sitter (AdS) con condiciones de contorno reflectantes en $\mathscr{I}$.

En un trabajo posterior [Sanchis-Gual et al. 2016a], me dispuse a variar los diferentes valores de los parámetros de la configuración, es decir, la carga inicial agujero negro, la perturbación inicial del campo escalar, la carga de campo escalar y la masa, así como el radio del espejo, para estudiar la variación del proceso de crecimiento del pelo. Además, también consideré el efecto de agregar un término de autointeracción (no lineal) al campo escalar. En todos los casos, se forman agujeros negros con pelo.

Muy recientemente, se han realizado simulaciones numéricas de la inestabilidad superradiante del sistema Kerr-Proca [East and Pretorius 2017, East 2017]. Para los campos de Proca, las escalas de tiempo de la inestabilidad son más cortas que en el caso escalar. Estas simulaciones capturaron tanto la fase de crecimiento exponencial, como se espera debido a la inestabilidad superradiante, como la saturación que conduce a la formación de un agujero negro de Kerr con pelo Proca.

Por otra parte Ponglertsakul, Winstanley, and Dolan [2016] and Ponglertsakul and Winstanley [2017] han obtenido soluciones similares al solitón del sistema EMKG, que son regulares y sin horizonte. Los agujeros negros con pelo se pueden considerar como un estado ligado de estos solitones con un horizonte. Siguiendo esos trabajos, en los que se discute la estabilidad de los solitones EMKG en una cavidad, estudié la estabilidad de estas soluciones con simulaciones numéricas,

evolucionando varios modelos de solitones cargados usando los métodos numéricos descritos anteriormente [Sanchis-Gual et al. 2017a].

Concretamente, consideré dos diferentes esquemas para imponer la "cavidad", que es algo virtual para las soluciones estacionarias de estos solitones pero necesario para la evolución dinámica del sistema. Con ambas posibilidades, observé algunas diferencias cuantitativas y cualitativas, pero obtuve evidencia numérica de que, de hecho, un agujero negro con pelo puede formarse tras el colapso de un solitón inestable. Por lo tanto, el decaimiento de estos solitones inestables podría ser un canal diferente para la formación de agujeros negros con pelo cargados. Sin embargo, también observé, para ambos esquemas, que algunos solitones inestables colapsaban a un agujero negro de Reissner-Nordström, en lugar de a uno con pelo.

Estrellas de bosones y de Proca

Las soluciones de campo escalar de tipo solitón, es decir, soluciones estáticas con simetría esférica del sistema Einstein-Klein-Gordon (EKG) para un campo masivo y complejo, se conocen como estrellas de bosones. El destino dinámico de estos objetos compactos se ha investigado utilizando teoría de perturbaciones [Gleiser and Watkins 1989, Lee and Pang 1989] y en el régimen no lineal mediante simulaciones numéricas [Seidel and Suen 1990, Balakrishna, Seidel, and Suen 1998, Hawley and Choptuik 2000, Guzman 2004a]. En particular Seidel and Suen [1990] fueron los que primero mostraron que el destino de las soluciones inestables de estrellas de bosones es la formación de un agujero negro o la migración de la estrella a la rama estable, independientemente del signo de la energía de ligadura. Un tercer resultado para estrellas de bosones inestables es su total dispersión [Balakrishna, Seidel, and Suen 1998, Guzman 2004a, Guzmán 2009] una situación que solo ocurre para estrellas bosónicas con energía de ligadura negativa.

Por otra parte, estrellas de bosones vectoriales, o *estrellas de Proca*, se han obtenido recientemente como soluciones numéricas completamente no lineales del sistema Einstein-Proca-(complejo) (EP) [Brito et al. 2016]. Al igual que las estrellas bosónicas escalares, son autogravitantes, condensados de Bose-Einstein no singulares y sin horizonte de un campo vectorial con masa, por lo que se asemejan en muchos aspectos, pero no completamente, a sus "primos" escalares, las estrellas de bosones. En mi primer estudio de este tipo de objetos compactos [Sanchis-Gual et al. 2017b], presenté evoluciones numéricas completamente no lineales de estrellas de Proca, en simetría esférica, para analizar su estabilidad y el punto final de la evolución de las estrellas inestables. Las

simulaciones confirmaron que la separación entre configuraciones estables e inestables se produce en la solución con una masa máxima ADM [Brito et al. 2016]

$$M_{\max} \sim 1.058\ M^2_{\rm Planck}/\mu, \tag{3}$$

que es ligeramente más grande que la masa máxima para las mini-estrellas de bosones, que hacen referencia a campos escalares sin autointeracción. El signo de la energía de ligadura de la solución y la perturbación determinan los tres resultados posibles para los modelos inestables: *(i)* migración a la rama estable, *(ii)* dispersión total del campo, o *(iii)* colapso a un agujero negro de Schwarzschild. En este último caso, un remanente longevo de campo de Proca compuesto por estados cuasi ligados, puede formarse fuera del horizonte después del colapso, con una vida que escala inversamente a la masa de Proca, como mis simulaciones previas habían demostrado para el caso de un campo escalar.

Estos destinos finales de los modelos inestables son muy similares a los observados para estrellas de bosones y estrellas de neutrones en simetría esférica. Para las últimas, se pueden construir modelos de equilibrio inestable para cualquier ecuación de estado. Cualquier perturbación hará que la estrella colapse a un agujero negro o migre a la rama estable, a densidades centrales más pequeñas. El signo de la perturbación determina el camino que seguirá la estrella [Font et al. 2002]. Por lo tanto, estas observaciones son análogas a lo que hemos descrito para estrellas bosónicas (escalares y vectoriales).

Las estrellas bosónicas han sido llamadas "imitadores de agujeros negros", pero si no incorporan un potencial de auto-interacción, su masa máxima no es lo suficientemente grande como para mostrar los mismos efectos gravitacionales que los agujeros negros o las estrellas de neutrones. La auto-interacción proporciona un apoyo adicional contra el colapso gravitacional aumentando las posibles masas máximas, lo que permite alcanzar modelos con significancia astrofísica.

En un trabajo posterior [Escorihuela-Tomàs et al. 2017], mi aportación consistió en supervisar a un estudiante de Máster a realizar simulaciones numéricas. Siguiendo la idea anteriormente mencionada y utilizando las mismas técnicas numéricas que en el caso de Proca, construimos y desarrollamos una muestra de modelos iniciales de estrellas de bosones, incorporando un potencial de autointeracción con un término de cuarto orden. Seguimos la dinámica del sistema durante un período de tiempo muy largo, más allá de la formación de agujeros negros, y revisitamos la estabilidad de las soluciones para diferentes valores de la constante de acoplamiento de autointeracción λ, que incorpora valores tan grandes como $\Lambda \equiv \lambda/4\pi G\mu^2 = 100$, no analizados previamente. Nuestros

hallazgos fueron consistentes con los tres desenlaces posibles de los modelos inestables obtenidos previamente tanto para el caso $\lambda = 0$ de las (mini-)estrellas de bosones como para el caso con autointeracción [Guzman 2004b]. Además, demostramos que también pueden formarse estados cuasi ligados de vida larga después del colapso de una estrella del bosones con autointeracción. Como se indicó anteriormente, estos resultados también se obtuvieron recientemente en simulaciones esféricas de estrellas Proca inestables que colapsan a agujeros negros [Sanchis-Gual et al. 2017b].

La formación dinámica de estrellas de bosones fue discutida por primera vez por Seidel and Suen [1994a], quienes demostraron que, en simetría esférica, una configuración de campo escalar complejo genérico colapsa para formar una estrella de bosones. En simetría esférica, no se emite radiación gravitacional, y el mecanismo disipativo que extrae el exceso de energía para que se forme un objeto compacto se llamó *enfriamiento gravitacional* y toma la forma de eyección de partículas escalares. En un trabajo reciente [Di Giovanni et al. 2018] ayudé a realizar simulaciones numéricas completamente no lineales del sistema Proca-Einstein en simetría esférica. En este trabajo mostramos que la autogravedad del sistema también induce la formación de objetos compactos que, para condiciones iniciales apropiadas, alcanzan asintóticamente las soluciones estacionarias tipo solitón conocidas como estrellas de Proca, mediante el mecanismo de enfriamiento gravitatorio.

Y es que la verdadera naturaleza de los candidatos astrofísicos a agujero negro ha sido una cuestión central de la astrofísica relativista durante décadas. La dificultad de observar la existencia de un horizonte de sucesos permite la posibilidad de que, en realidad, se trate de otros objetos compactos exóticos *sin horizonte*, cuya fenomenología fuera lo suficientemente similar a la de los agujeros negros, de modo que las observaciones fueran incapaces de distinguir estos dos tipos de objetos.

La correspondencia entre las frecuencias de oscilación natural de un agujero negro (llamadas modos cuasinormales [Berti, Cardoso, and Starinets 2009]) y las vibraciones del anillo de luz [Goebel 1972, Cardoso et al. 2009, Khanna and Price 2017], implica que los objetos compactos con un anillo de luz, *objetos ultracompactos* (UCO), pero sin horizonte de sucesos pueden imitar la parte inicial de la señal de la onda gravitatoria correspondiente al ringdown de agujeros negros perturbados. Las partes posteriores de esta señal pueden contener signaturas de la verdadera naturaleza del objeto (a través de los llamados *ecos* [Cardoso et al. 2016, Cardoso and Pani 2017, Westerweck et al. 2017, Conklin, Holdom, and Ren 2017]) pero la pequeña relación señal-ruido desafía la posibilidad de obtener

detecciones lo suficientemente limpias de esta parte de la señal, al menos en el futuro cercano.

En Cunha et al. [2017] consideramos estrellas de bosones con simetría esférica, así como estrellas de Proca, como ejemplos de referencia de UCOs sin horizonte, y simultáneamente como una prueba de concepto de que los imitadores de agujero negro son dinámicamente posibles a través de la física conocida. Mi aportación a esta investigación consistió en evolucionar numéricamente los modelos ultracompactos de estrellas de Proca. Nuestro estudio numérico reveló que las estrellas bosónicas, tanto escalares como vectoriales, al poseer anillos de luz que les permite, en principio, vibrar como lo hacen los agujeros negros, tienen, no obstante, patrones de efecto lente distintos en comparación a las sombras estándar de un agujero negro. Sin embargo, las estrellas bosónicas solo se convierten en UCO en un régimen en el que también son inestables bajo perturbaciones. Nuestras simulaciones revelaron que las mismas perturbaciones que podrían hacerlas vibrar como un agujero negro en realidad inducirán su colapso gravitacional. Al realizar simulaciones totalmente no lineales mostramos que éste es un proceso rápido, y un horizonte se forma en un tiempo breve respecto al que tarda la luz en cruzar el dominio computacional (*light-crossing time*). En conjunto, nuestros resultados enfatizan la dificultad, al menos en simetría esférica, para construir un modelo dinámico razonable de UCO sin horizonte cuya fenomenología puede imitar a la de un agujero negro.

Modelo modificado de Hartle

La construcción de modelos analíticos de objetos astrofísicos compactos en Relatividad General se basa en la teoría de empalmes de espacio-tiempos. La idea es considerar dos diferentes regiones bien delimitadas, un fluido interior y un vacío en el exterior, e imponer condiciones de empalme adecuadas en una hipersuperficie temporal Σ que los separa. Por lo tanto, se construye un modelo global uniendo los datos de los límites comunes en Σ. Si bien la búsqueda de un modelo global *exacto* para un objeto compacto en rotación es un desafío importante, la situación se vuelve manejable cuando se recurre a métodos aproximados como la teoría de perturbaciones. En este contexto, se han desarrollado modelos que describen estrellas en rotación [Hartle 1967], efectos de marea [Damour and Nagar 2009] o estrellas colapsadas [Brizuela et al. 2010].

En su trabajo pionero, Hartle y Thorne presentaron el tratamiento general relativista de estrellas compactas en rotación aisladas en equilibrio [Hartle 1967, Hartle and Thorne 1968], conocido como "modelo de Hartle". Este sirve como base para construir modelos analíticos en simetría axial (ver [Stergioulas 2003] y

referencias en el mismo). Un esquema perturbativo se basa en una configuración esférica (sin rotación), sobre la cual se toman perturbaciones de segundo orden estacionarias (giratorias) y axiales. Los modelos se construyen suponiendo un fluido perfecto interior con ecuación de estado barotrópica que gira rígidamente y sin movimientos convectivos. Bajo estas suposiciones, las perturbaciones son descritas por cuatro funciones, cuyos valores en la superficie de la estrella determinan el arrastre de los sistemas de referencia inerciales, la deformación y la masa total de la estrella en términos de la densidad central. A cada orden de la perturbación, esos valores se calculan *(i)* integrando desde el centro regular dada un ecuación de estado, *(ii)* resolviendo el vacío exterior asintóticamente plano, y *(iii)* asumiendo la continuidad de las funciones en la superficie eligiendo un sistema de coordenadas explícito.

Como se muestra en Reina and Vera [2015] usando el marco teórico desarrollado por Mars [2005], una función perturbativa relevante del modelo, que entra en el cálculo de la masa de la estrella, presenta una discontinuidad proporcional a la densidad de energía (de fondo) en la superficie estelar. Por lo tanto, la expresión original para la masa total de una estrella en rotación lenta dada en Hartle [1967] tiene que ser modificada. Estrellas con densidad constante se analizaron en Reina [2016], quien demostró que las desviaciones en los diagramas masa-radio están lejos de ser insignificantes. En un trabajo posterior [Reina et al. 2017] estudiamos estrellas de neutrones con ecuaciones de estado más realistas y también estrellas de quarks, para ver los efectos de la existencia de una discontinuidad en la superficie en las configuraciones de equilibrio obtenidas con el formalismo de Hartle modificado. Encontramos que las diferencias son también importantes.

Además, también estudiamos las llamadas relaciones I-Love-Q [Yagi and Yunes 2013], donde "I" y "Q" se refieren al momento de inercia y al momento cuadrupolar de la estrella, respectivamente, y los números *Love* "k_l" están asociados a la distribución del campo de mareas en un sistema binario debido a la presencia de una estrella compañera. Sorprendentemente, estos parámetros están relacionados de manera universal e independientemente de la ecuación de estado. En [Yagi and Yunes 2014] se obtuvo una expresión modificada para los números de Love que lleva a relaciones universales I-Love-Q. El primer resultado obtenido por estos autores fue incorrecto al suponer (erroneamente) la continuidad de las perturbaciones en Σ_0. Una función conectada a los números Love muestra una discontinuidad proporcional a la densidad de energía en la superficie estelar, que no es nula en estrellas de quarks.

Para realizar estos análisis, ayudé a desarrollar un código numérico, modificando otro anterior que generaba soluciones de las ecuaciones TOV, y a incluir las condiciones de empalme perturbadas de Reina and Vera [2015], para entonces: *(i)* aplicar las correcciones en el contexto del modelo de Hartle para estrellas de quarks con ecuación de estado lineal, revisitando el trabajo de Colpi and Miller [1992]; *(ii)* establecer las discontinuidades involucradas en el sector $l \geq 2$ del problema del campo de marea de primer orden y mostrar cómo esas condiciones, que de hecho coinciden con las presentadas por Price and Thorne [1969], conducen a las correcciones reconocidas en Damour and Nagar [2009] y usadas en Hinderer et al. [2010] y Yagi and Yunes [2014]; *(iii)* completar las relaciones I-Love-Q incorporando la modificación de la masa, δM, ahora correctamente calculada, que indica relaciones universales para todas las cantidades perturbativas.

Mi aportación a la Colaboración Virgo

En julio de 2016, el Valencia Virgo Group [*Valencia Virgo Group*], del cual soy miembro, se convirtió en el primer grupo español que forma parte de la Colaboración Virgo. Un año después, el grupo obtuvo los derechos de autoría completa, después de tener éxito en la evaluación interna. Mi trabajo en la colaboración consiste en el modelado de ondas gravitacionales y en la estimación de parámetros a partir de estas señales.

Las propiedades termodinámicas de la ecuación de estado de la materia a altas densidades (por encima de la densidad de saturación nuclear) y la posible existencia de estados exóticos tales como transiciones de fase de la materia nuclear/hadrónica al plasma de quark-gluón [Schertler et al. 2000, Glendenning and Kettner 2000] pueden influir críticamente en la estabilidad y dinámica de las estrellas compactas relativistas. Desde un punto de vista teórico, establecer la existencia de esos estados requiere el análisis de la "convexidad" de la ecuación de estado. Hay indicios de la existencia de posibles regiones en la ecuación de estado de materia densa donde la termodinámica puede ser realmente no convexa. Los flujos sujetos a dinámicas no convexas, denominados flujos de Bethe-Zel'dovich-Thompson (o BZT) [Bethe 1942, Zel'dovich 1946, Thompson 1971] se caracterizan por la aparición de ondas compuestas (choques más rarefacción) durante la evolución [Argrow 1996, Guardone and Vigevano 2002, Voss 2005, Cinnella and Corre 2006, Ibáñez et al. 2013, Serna and Marquina 2014]. En un proyecto en curso [Ibañez et al. 2018], investigamos los efectos de una ecuación de estado fenomenológica no convexa [Ibáñez et al. 2017] sobre la estructura de equilibrio de estrellas compactas estables. En particular realicé evoluciones numéricas con el código NADA3D para estudiar la dinámica de estrellas de

neutrones inestables en rotación uniforme que colapsan gravitacionalmente a agujeros negros. Mostré cómo la dinámica del colapso con una ecuación de estado no convexa se aparta en gran medida de la zona convexa, dejando huellas distintivas en las formas de onda gravitacionales.

Además, he estado trabajando en la extracción de ondas gravitatorias de la fusión de sistemas binarios de estrellas de Proca (colisión frontal y orbital). El objetivo a medio plazo de estas simulaciones es crear un amplio catálogo de ondas gravitatorias de la fusión de estrellas de bosones y de Proca, para poder compararlas con los resultados de las colisiones de binarias de agujeros negros y con las observaciones de los detectores avanzados LIGO y Virgo.

Publications

- Cunha, P. V., Font, J. A., Herdeiro, C., Radu, E., **Sanchis-Gual, N.**, & Zilhão, M. (2017).
  Lensing and dynamics of ultracompact bosonic stars.
  Physical Review D, 96(10), 104040.

- Escorihuela-Tomàs, A., **Sanchis-Gual, N.**, Degollado, J. C., & Font, J. A. (2017).
  Quasistationary solutions of scalar fields around collapsing self-interacting boson stars.
  Physical Review D, 96(2), 024015.

- Reina, B., **Sanchis-Gual, N.**, Vera, R., & Font, J. A. (2017).
  Completion of the universal I–Love–Q relations in compact stars including the mass.
  Monthly Notices of the Royal Astronomical Society: Letters, 470(1), L54-L58.

- **Sanchis-Gual, N.**, Degollado, J. C., Font, J. A., Herdeiro, C., & Radu, E. (2017).
  Dynamical formation of a hairy black hole in a cavity from the decay of unstable solitons.
  Classical and Quantum Gravity, 34(16), 165001.

- **Sanchis-Gual, N.**, Herdeiro, C., Radu, E., Degollado, J. C., & Font, J. A. (2017).
  Numerical evolutions of spherical Proca stars.
  Physical Review D, 95(10), 104028.

- **Sanchis-Gual, N.**, Degollado, J. C., Herdeiro, C., Font, J. A., & Montero, P. J. (2016).
  Dynamical formation of a Reissner-Nordström black hole with scalar hair

in a cavity.
Physical Review D, 94(4), 044061.

- **Sanchis-Gual, N.**, Degollado, J. C., Montero, P. J., Font, J. A., & Herdeiro, C. (2016).
Explosion and final state of an unstable Reissner-Nordström black hole.
Physical Review Letters, 116(14), 141101.

- **Sanchis-Gual, N.**, Degollado, J. C., Izquierdo, P., Font, J. A., & Montero, P. J. (2016).
Quasistationary solutions of scalar fields around accreting black holes.
Physical Review D, 94(4), 043004.

- **Sanchis-Gual, N.**, Degollado, J. C., Montero, P. J., Font, J. A., & Mewes, V. (2015).
Quasistationary solutions of self-gravitating scalar fields around collapsing stars.
Physical Review D, 92(8), 083001.

- **Sanchis-Gual, N.**, Degollado, J. C., Montero, P. J., & Font, J. A. (2015).
Quasistationary solutions of self-gravitating scalar fields around black holes.
Physical Review D, 91(4), 043005.

- **Sanchis-Gual, N.**, Montero, P. J., Font, J. A., Müller, E., & Baumgarte, T. W. (2014).
Fully covariant and conformal formulation of the Z4 system in a reference-metric approach: comparison with the BSSN formulation in spherical symmetry.
Physical Review D, 89(10), 104033.

Contents

Part I

Summary

Chapter 1

Introduction

1.1 Motivation

On September 14, 2015, the gravitational-wave signal (GW150914) from the merger of a black hole binary (BBH) was detected by the two advanced Laser Interferometer Gravitational-Wave Observatories (LIGO) [Abbott et al. 2016]. As of today, four additional signals from the merger of BBHs have been detected [Abbott et al. 2016, Abbott et al. 2017c, Abbott et al. 2017b, Abbott et al. 2017a], the latter, GW170814, in coincidence with the advanced Virgo detector. Moreover, on August 17, 2017, the advanced LIGO and Virgo detectors observed the gravitational waves from the merger of a binary neutron star system [Abbott et al. 2017d]. This landmark detection has initiated the field of Multi-Messenger Astronomy in which, through the unprecedented coordinated action of LIGO, Virgo and some 70 astronomical facilities, both ground-based and in space, key evidence to address open issues in relativistic astrophysics has been collected. Without any doubt, the continuous increase in computational power has contributed to the recent discoveries in the newborn field of Gravitational-Wave Astronomy. The use of computers has allowed to carry out in virtual laboratories numerical experiments of the strong-field regime of gravity in order to solve theoretical problems not accessible to analytical studies and to explain the observational data. Indeed, the gravitational waveform from BBH mergers like GW150914 was predicted a decade ago by breakthrough numerical studies that performed time evolutions of BBHs using fully non-linear numerical relativity (NR) codes to accurately solve Einstein's equations [Pretorius 2005, Campanelli et al. 2006, Baker et al. 2006].

The main purpose of the field of NR is to investigate and comprehend the system under study and provide falsifiable observational predictions, particularly gravitational-wave templates. A simulation is an approximation to reality as it hardly contains all the physics at play. Nonetheless, there is an important work of simplification and modelisation of the true physical properties of the system. Therefore, the level of complexity can be adjusted in the simulations, allowing to test the implications of the physics considered in each model. In the end, the observations validate the correct model.

A large number of areas in modern astronomy, such as high-energy astrophysics or the new-born field of Gravitational-Wave Astronomy, require General Relativity (GR) to correctly describe the systems under study. In scenarios where compact objects are involved, such as BHs, neutron stars or other exotic theoretical objects (e.g. scalar and vector boson stars), the Einstein equations play a fundamental role in the description and analysis of the dynamics of the gravitational field. Moreover, objects like neutron stars are characterized, besides strong gravity, by the presence of high-velocity fluids and shock waves (discontinuous solutions of the thermodynamic quantities). The general equations governing the dynamics of relativistic astrophysical systems are an intricate set of time-dependent, partial differential equations, coupling the general relativistic magneto-hydrodynamics (GRMHD) equations and the Einstein equations of the gravitational field. Regarding boson stars, for which matter is described by a scalar/vector field, the Klein-Gordon and the Proca equations, respectively, are another set of evolution equations to consider, as those govern the coupling of the bosonic fields to gravity. In this thesis, I have studied a number of astrophysically-motivated scenarios in which this type of fields could play a relevant role.

Scalar boson stars (henceforth, boson stars) and its vector “cousins", known as Proca stars, are made of particles with integer spin (zero for boson stars and one for Proca) following the Bose-Einstein statistics. Fermions, on the other hand, obey the Fermi-Dirac statistics and have half-integer spin. At zero temperature, the former condense into the lowest energy level state and can be classically described as a wavefunction, characterized by the mass of the particle, μ. On the contrary, it is not possible for fermions to occupy the same quantum state due to the Pauli exclusion principle. Applying this principle [Chandrasekhar 1931, Chandrasekhar 1935], Subrahmanyan Chandrasekhar obtained the maximum mass a relativistic gas of electrons, a white dwarf, could support against the gravitational force by the Fermi degeneracy pressure. The same principle holds for neutron stars.

In the mid-1950s, John Wheeler thought of a particle-like compact object composed only of classical fundamental fields, in particular the electromagnetic field, coupled to gravity that he called *geons*. The solutions he found were nonetheless unstable. It was David J. Kaup that, in the 1960s, introduced the concept of Klein-Gordon geons, what we call nowadays boson stars, by considering a complex scalar field, instead of a real field, with an harmonic dependence

$$\phi(\mathbf{r},t) \equiv \phi_{\mathrm{Re}}(\mathbf{r},t) + i\,\phi_{\mathrm{Im}}(\mathbf{r},t) = \phi_0\, e^{i\,\omega t}. \tag{1.1}$$

The idea behind this requirement is that in this way the amplitude of the field remains constant with time. Hence, the field is time dependent and oscillates with a determined frequency, while the spacetime is kept static. The $\frac{\pi}{2}$ phase difference between the real and the imaginary parts evades the so-called Derrick's theorem, stating that no regular, static, nontopological localized scalar field is stable in three (or higher) dimensional flat space. The star forms a stationary, soliton-like solution.

Furthermore, a real field can also form massive solitonic solutions coupled to gravity, known as *oscillatons*. In the real case, the field oscillates with time and so does the spacetime, which is no longer static. These solutions are very similar to boson stars, but are not stable in the sense that they disperse away in a finite time. However, the decay is extremely slow [Page 2004], within timescales that could be longer than the Hubble time, and, if they exist, they might be considered astrophysical objects.

As for white dwarfs and neutron stars, a quantum-mechanical principle, the Heisenberg uncertainty principle, can be identified as the mechanism that supports boson stars against gravity, assuming that the field is in a macroscopic quantum state

$$\Delta x \Delta p \geq \hbar. \tag{1.2}$$

The scalar field is described as a wavefunction, which will propagate at the speed of light. The tendency of the field to disperse away will balance its self-gravitating attraction. In Liebling and Palenzuela [2012], the authors give the following expression for the maximum mass of a boson star using (1.2)

$$M_{\mathrm{max}} = \frac{1}{2}\frac{\hbar c}{G\mu} = 0.5\, M^2_{\mathrm{Planck}}/\mu, \tag{1.3}$$

where M_{Planck} is the Planck mass. This results in a good, simple estimate of the correct mass, which is

$$M_{\mathrm{max}} \sim 0.633\ M^2_{\mathrm{Planck}}/\mu, \tag{1.4}$$

showing that it is inversely proportional to the scalar field particle mass μ. Fermion and boson stars are both supported against gravity by quantum-mechanical principles. Boson stars and Proca stars are theoretical exotic objects, but are described within GR and a clear parallelism can be drawn with observed compact objects. In addition, with the discovery of the Higgs boson [Collaboration 2012, Chatrchyan et al. 2012, Collaboration et al. 2012] we now know that (non-gauge) boson particles exist in Nature.

Numerical evolutions of stable and unstable neutron, boson and Proca stars, some of them performed for the first time in this thesis, have shown that the same different fates against linear perturbations can be obtained: a branch of stable models, collapse to BH, migration to the stable branch (i. e. expanding to smaller central values) and dispersion. The migration to the stable branch is only a mathematically posible outcome for neutron stars, not a physical one. If boson and Proca stars form in Nature, one can wonder if there is any actual natural mechanism to obtain this type of dynamics. Moreover, neutron stars can not disperse away. This outcome is precisely related to the principles counteracting the gravitational attraction mentioned above for each type of particle.

Boson stars are considered *black hole mimickers* because they do not interact with the electromagnetic field and produce the same gravitational effects up to their surface. The path of photons traversing the object and lensed by the strong gravitational field around these two types of compact objects, or *shadow*, would thus be different, due to the lack of an horizon in the scalar case. Besides, the maximum value reported in Eq. (1.4) is only valid for mini-boson stars, which refer to models without self-interaction. Including a self-interacting term, λ, in the scalar-field potential introduces a new parameter that allows to increase the mass to arbitrarily large values, for increasing λ.

In an astrophysical context, recent models for the evolution of the universe, dark energy, and string theory require the existence of ultra-light scalar degrees of freedom [Arvanitaki et al. 2010, Arvanitaki and Dubovsky 2011, Kamionkowski, Pradler, and Walker 2014]. In cosmology, classical, minimally coupled, scalar fields have also been proposed as the constituents of dark matter halos in galaxies [Hwang 1997, Matos, Guzman, and Urena-Lopez 2000, Matos and Urena-Lopez 2001, Matos and Urena-Lopez 2000, Marsh and Ferreira 2010, Hu, Barkana, and Gruzinov 2000]. The Compton wavelength, $\lambda_C = h/(m\,c)$, for an ultralight scalar field of mass $\hbar\mu \sim 10^{-22} - 10^{-24}$ eV is of the order of the radius of the dark matter halos (i.e. kpc). Schwarzschild BHs can develop quasi-bound configurations that may be very long lived. Besides, astrophysical Kerr BHs (and Reissner-Nordström) suffer from superradiant instabilities due to massive

scalar, vector and tensor perturbations. Trapped by the potential well due to the mass term, the bosonic field grows exponentially extracting rotational energy from the BH, spinning it down. This system was called the *BH bomb* [Press and Teukolsky 1972]. The endpoint of the superradiant instability has been an open issue since the 1960s. Hairy BH solutions have also be recently found: the bosonic field is in equilibrium with the BH, the spacetime being static [Herdeiro and Radu 2014, Herdeiro and Radu 2015]. BHs may then be used as particle detectors if scalar or vector hair could be observed around them [Brito, Cardoso, and Pani 2015a].

It is becoming increasingly clear that scalar or even vector fields could have a tremendous impact in many areas of astrophysics and theoretical physics, being a link between these fields. The opening of a new window to the Universe with the dawn of gravitational-wave astronomy means that it could be now possible to validate or discard the existence of such objects. Numerical studies, such as those presented in this thesis, can be undertaken to understand and make important predictions related to the properties and dynamics of bosonic matter.

1.2 Numerical relativity

As stated before, one of the main objectives of NR is to provide accurate gravitational-wave templates from relevant astrophysical systems to facilitate the detection by gravitational-wave observatories. Performing numerical evolutions of BBH mergers and extracting the corresponding waveform allowed to infer the physical system parameters from the detections by the LIGO-Virgo collaborations. In August 17, 2017, a gravitational wave from a binary neutron-star merger was detected. However, the part of the signal corresponding to the plunge and post-merger fell beyond the sensibility of the current detectors. Thus, no signal could be matched to the ones obtained from numerical simulation and no conclusive information could be derived about the dense matter equation of state (EOS).

GR is the best description we have of the dynamics of the gravitational field in the strong-field regime. It has passed all tests done so far. The Einstein equations relate the geometry of spacetime and the mass-energy distribution. They are a system of ten, non-linear, coupled, partial differential equations in four dimensions. Exact solutions with astrophysical relevance are only known under the assumption of a high degree of symmetries (e.g. the Schwarzschild metric in spherical symmetry, the Kerr metric in axisymmetry, and cosmological solutions). Nevertheless, for complex and highly dynamical systems, such as

gravitational collapse, supernovae, head-on collisions or mergers of compact objects, it is not possible to obtain analytical solutions. Hence, the equations have to be numerically solved using computers.

It is important to point out that the Einstein equations are written in a covariant way, there is no clear distinction between its space and time terms. To study the time evolution of a system, an initial value or Cauchy problem has to be solved: given some initial and boundary conditions and knowing the fundamental equations, we can study the time evolution of the gravitational field. Therefore, it is required to split explicitly space and time. Proceeding in this way is known as the 3+1 formalism of GR.

In this formalism, spacetime is foliated into three-dimensional spatial hypersurfaces defined by a coordinate time. The four-dimensional tensors are decomposed in their time and spatial parts, using the normal vector n^μ and the three-dimensional spatial metric γ_{ij}. The Einstein equations are then rewritten and two sets of equations are obtained: the evolution equations for γ_{ij} and for the extrinsic curvature K_{ij}, and the constraint equations, namely the Hamiltonian and Momentum constraints (see e.g. Baumgarte and Shapiro [2003] and references therein for details). It has been shown that the Arnowitt-Deser-Misner (ADM) equations of the 3+1 original formalism are unstable for long-term numerical simulations, especially when BHs are involved, due to their weak hyperbolic form.

1.2.1 The BSSN formulation

New formulations were presented to make the evolution equations better suited for numerical purposes. In particular, the Baumgarte-Shapiro-Shibata-Nakamura (BSSN) formalism, originally proposed by Nakamura, Oohara, and Kojima [1987] and subsequently modified by Shibata-Nakamura [Shibata and Nakamura 1995] and Baumgarte-Shapiro [Baumgarte and Shapiro 1999], is a conformal and traceless reformulation of the ADM equations. It is the standard formulation of the 3+1 equations used in most 3+1 NR codes due to its stability properties, which depend on the use of the momentum constraint equations for the evolution equation of the "conformal connection functions", and to the developments associated with gauge conditions, essential to perform accurate and long-term stable evolutions.

1.2.2 The fCCZ4 formulation

Other conformal and traceless decompositions of the Einstein equations based on the Z4 system [Bona et al. 2003] have been presented by Bernuzzi and Hilditch [Bernuzzi and Hilditch 2010, Ruiz, Hilditch, and Bernuzzi 2011, Weyhausen, Bernuzzi, and Hilditch 2012, Hilditch et al. 2013], the so-called Z4c formulation, and also by Alic et al. [Alic et al. 2012, Alic, Kastaun, and Rezzolla 2013], the CCZ4 formulation. They incorporate the constraint damping scheme developed by Gundlach et al. [2005] that introduces a set of parameters to dynamically control the constraint violations by means of constraint-damping terms. These formulations have been extensively tested and the numerical results show a reduction for the Hamiltonian constraint violations by 1 to 3 order of magnitude with respect to the BSSN formulation.

However, both formulations break the 4-covariance, by discarding non-damping, non-principal terms or by modifying the damping parameter that removes the instabilities when using the fully covariant version of the CCZ4 system in the evolution of black holes. Besides, in their original form the BSSN and the CCZ4 or Z4c formulations are particularly tuned for Cartesian coordinates: they involve fields which are not true tensors (i.e. the conformal connection functions) and assume that the determinant of the conformal metric is equal to one. Brown [2009] introduced a covariant formulation of the BSSN equations that is well-suited for curvilinear coordinate systems, by adopting a reference-metric approach [Bonazzola 2004]. Our NR codes, NADA1D and NADA3D, developed by Thomas Baumgarte, Pedro Montero and Isabel Cordero-Carrión, use spherical coordinates. Many astrophysical phenomena are symmetric with respect to the rotation axis (e.g. accretion disks) or spherical coordinates adapt better to their geometry (e.g. the gravitational collapse of neutron stars).

It must be pointed out that there are singularities associated with curvilinear coordinate systems which are a known source of numerical problems (because of the presence of terms in the evolution equations that behave like $1/r$ near the origin ($r = 0$) or like $1/\sin\theta$ near the axis). In particular, Cordero-Carrión, Cerdá-Durán, and Ibáñez [2012] recently adopted a partially implicit Runge-Kutta (PIRK) method to evolve hyperbolic, wave-like equations in the Fully Constrained formulation of the Einstein equations. Assuming spherical symmetry, a second-order PIRK scheme was used by Montero and Cordero-Carrión [2012] with the BSSN Einstein equations. The latter, in particular, obtained stable numerical simulations of both vacuum and non-vacuum spacetimes without the need for a regularization algorithm at the origin in the NADA1D code.

This approach has been successfully implemented in 3D without any symmetry assumption by Baumgarte et al. [2013] and by Montero, Baumgarte, and Müller [2014] were the first successful implementation of relativistic hydrodynamics coupled to dynamical spacetimes in spherical polar coordinates with no symmetry assumptions was reported.

In this thesis I rewrote the CCZ4 evolution equations [Sanchis-Gual et al. 2014] keeping the full 4-covariance, even for BHs, and, following Brown [2009], I introduced the reference-metric approach, to make them suited for spherical coordinates, under the assumption of spherical symmetry. I then performed numerical evolutions of both vacuum spacetimes (Schwarzschild BH) and non-vacuum spacetimes (stable and unstable relativistic polytropic models of neutron stars) to compare the accuracy of the fCCZ4 formulation with respect to BSSN. These systems were studied for serveral choices of the damping parameters κ_1 and κ_2, and, depending on those choices, it was found that the Hamiltonian constraint violations were reduced about 1 to 3 orders of magnitude with respect to BSSN. However, overdamping effects could take place for too high values of κ_1. For the single puncture test I was able to obtain stable evolutions for particularly tuned parameters, but the mass of the apparent horizon (which has to be conserved during the stationary phase) suffered a slow decrease for fCCZ4 at late times ($t = 1875$) of less than 0.005%. Because of these results for BH spacetimes and the drawback of having to fine-tune the damping parameters, the rest of the numerical simulations presented in this thesis were performed using the BSSN formulation.

1.3 Numerical-relativity simulations of scalar fields and black holes

1.3.1 Quasistationary solutions around black holes

Large observational evidence points to the existence of supermassive black holes (SMBHs) in the centers of most galaxies. The evolution of these BHs is directly connected to their host galaxy evolution [Kormendy and Gebhardt 2001]. In this context, scalar fields have been proposed as strong candidates for dark matter [Sahni and Wang 2000, Hu, Barkana, and Gruzinov 2000, Matos and Urena-Lopez 2000, Matos and Urena-Lopez 2001]. In these models, dark matter is composed of bosonic particles that may condensate into macroscopic objects forming boson stars or halos around black holes. In order to consider them plausible alternatives, these configurations must survive for cosmological time

scales in the presence of BHs [Barranco et al. 2011] and in a highly dynamical scenario.

Several studies have investigated in the linearized regime the dynamics of scalar fields around BHs. The BH spacetime is taken as the background where the scalar field evolves [Witek et al. 2013, Barranco et al. 2012, Barranco et al. 2014, Dolan 2012, Cruz-Osorio, Guzman, and Lora-Clavijo 2011]. These works showed that massive scalar fields surrounding stationary BHs could form quasibound states as a result of the presence of a potential well due to the mass term. These states decay at infinity and, thus, they are localized around the BH. We will see in the next subsection that if the BH has electric charge or angular momentum, it can yield exponentially growing modes.

Those quasibound states are scalar field configurations that may be very long lived [Barranco et al. 2014]. They are characterized by a complex frequency: the real part represents the oscillation frequency and the imaginary part gives, depending on the sign, either their decay rate or the growth rate, if a mode is superradiantly unstable. The test-field approximation is valid as long as the energy content of the field is small and it will break down eventually as the energy increases. The backreaction of the scalar field onto the spacetime dynamics becomes non-negligible when the initial mass of the field is large enough compared to the BH mass. In such a situation, non-linear simulations of self-gravitating scalar field configurations are mandatory. In this thesis, I focused on the cases in which the mass of the scalar-field cloud may be larger than the mass of the black hole and therefore constitutes a strong deviation from the linearized regime, representing a large scalar field environment in a highly dynamical spacetime.

To carry out this numerical study, I implemented the real Klein-Gordon equation coupled to the Einstein equations in NADA1D [Sanchis-Gual et al. 2015]. The time-evolution equations were performed using the same second-order PIRK method mentioned above applied to the BSSN formulation. An initial Gaussian distribution of a scalar field was set around a Schwarzschild BH and the Hamiltonian constraint was solved. First, I recovered the results of the linearized regime when the energy of field is small compared to the BH mass. The long-term simulations for large scalar field initial energies showed that quasibound states could be identified by a real oscillation frequency even after the BH mass suddenly increased due to the absorption of part of the field. We found that for a BH already formed, self-gravitating quasistationary solutions appeared with less total energy than that of the initial distribution.

On the other hand, the formation of SMBH is a fundamental issue in the study of galaxy formation. It is still unknown how such SMBH can form and grow to reach the current values when the Universe was less than 10^9 years old. One possibility assumes that central BHs formed via direct collapse of supermasive stars (SMS) (see Begelman, Volonteri, and Rees [2006b], Begelman [2010], and Mayer et al. [2010]), with masses $\geq 5 \times 10^4 M_\odot$, which then would evolve as equilibrium configurations dominated by radiation pressure before collapsing to form a SMBH seed [Shibata and Shapiro 2002, Montero, Janka, and Müller 2012].

The quasistationary scalar field halos found in my first investigation [Sanchis-Gual et al. 2015] should also survive the collapse of SMS. In consequence, the main objective of my second work in this topic was to assess the role of BH formation in the presence of scalar field configurations which resemble the quasibound states found in previous investigations where the BH is assumed to exist from the start [Sanchis-Gual et al. 2015]. To test this scenario, I performed NR simulations which track the gravitational collapse of a polytropic star, with adiabatic index $\gamma = 4/3$ to simulate radiation-supported SMS, in the presence of a scalar-field environment. The evolution of the relativistic hydrodynamics equations was also taken into account and the scalar field and the matter of the star were coupled only through gravity. The results of the simulations showed that the scalar field was not completely absorbed or dispersed after the collapse and it formed quasibound states with a well determined oscillation frequency (or frequencies).

Another possible hypothesis is that SMBH were formed through accretion and merging of the first stellar remnants [Bromm and Loeb 2003a, Haiman and Loeb 2001a]. SMBHs are expected to be the final result of the growth of seed BHs in high redshift galaxies through accretion episodes and mergers of massive BH (MBH) binaries [Kauffmann and Haehnelt 2000, Volonteri, Haardt, and Madau 2003]. These SMBHs must grow rapidly in order to acquire its mass within a short period of ~ 1 Gyr, making the formation of SMBHs a highly dynamical event.

While one can argue that SMBHs have grown largely through accretion, to circumvent the problem of an exponential growth at the Eddington-limited e-folding time being too slow to grow stellar-mass BH seeds into the supermassive luminous quasars that are observed at $z \sim 7$ [Mortlock et al. 2011] some studies invoke various possibilities, namely super-Eddington accretion for brief periods of time [Begelman 1979, Alexander and Natarajan 2014, McKinney et al. 2014], formation through accretion and merging of the first stellar remnants [Bromm

and Loeb 2003b, Haiman and Loeb 2001b], or considering more massive seeds from the collapse of pre-galactic disks at high redshifts [Begelman, Volonteri, and Rees 2006a, Begelman 2010, Mayer et al. 2010].

It is thus worth wondering if rapid BH accretion may have any effect on the distribution of the associated scalar-field dark matter halo. In the absence of accretion the existence of long-lasting scalar-field configurations surrounding a (non-rotating) BH have been found. Therefore, it has been shown that SMBHs at galactic centers would not represent a serious threat to dark-matter models based on (ultra-light) scalar fields as a viable alternative to the usual description of dark matter as weakly interacting massive particles (WIMPs). Because of the rapid growth of accretion-powered SMBHs, I investigated in Sanchis-Gual et al. [2016c] the outcome of the scalar field within such a dynamical situation by studying the properties of scalar field quasibound states in the background of a spherically symmetric accreting BH. Assuming that the BH mass grows adiabatically due to the presence of infalling matter we show that indeed, long-lasting, quasibound states can still form and survive in such scenario. The timescales are nevertheless reduced, but only for extremely high, unrealistic, accretion rates.

1.3.2 The superradiant instability and charged hairy black holes

In the previous section, I have described the results of our NR simulations of massive scalar fields around *Schwarzschild* BHs. Indeed, this distinction is needed: in this case, quasibound states can only lead to exponentially decaying modes, with negative imaginary frequency. Hence, the BH will end up absorbing all the scalar field after some timescale determined by the scalar field particle mass μ and the spacetime will tend asymptotically to the Schwarzschild metric.

For rotating BHs, however, described by the Kerr metric within GR, bosonic waves scattered off the BH extract energy and angular momentum and increase the energy of the field through the classical process of *superradiance* [Bardeen, Press, and Teukolsky 1972, Starobinsky 1973, Press and Teukolsky 1972, Damour, Deruelle, and Ruffini 1976, Zouros and Eardley 1979b, Detweiler 1980b, Cardoso et al. 2004, Dolan 2007, Rosa 2010, Brito, Cardoso, and Pani 2015b]. This phenomenon happens for scalar, vector and tensor bosonic fields. In East, Ramazanoğlu, and Pretorius [2014] it was numerically shown for the first time in the nonlinear regime that gravitational waves are amplified when reflected by a Kerr BH, decreasing the hole's spin. The superradiant instability is triggered

if the field has non-zero azimuthal quantum number m, oscillates with frequency ω and fulfills the synchronization condition

$$\omega < m\Omega_{\rm H}, \tag{1.5}$$

where $\Omega_{\rm H}$ is the horizon angular velocity. The imaginary part of the frequency is then positive and the field grows exponentially. In the case of gravitational waves, the graviton mass is zero (within GR), so the waves are scattered away after reflection. But, if a mass term is introduced or a mirror-like boundary condition, superradiant modes are trapped, continuously extracting energy from the BH to the field and growing in time, thus triggering an instability of the BH-scalar field system. Consequently, in this setup, the *bald* Kerr BH is unstable and the scalar field grows in time outside the BH. Several studies have shown that the timescale of the instability is maximal, $\tau^{-1} \sim 1.11 \times 10^{-7}\,(GM/c^3)$, for $\mu \sim 0.39$ and a BH spin of $a = 0.98$ [Zouros and Eardley 1979a, Detweiler 1980a, Furuhashi and Nambu 2004, Cardoso and Yoshida 2005, Hod 2012a].

Fully nonlinear simulations are required in order to reach the nonlinear regime of the instability and its endpoint. This represents a remarkable challenge with current NR technology [Okawa, Witek, and Cardoso 2014, East, Ramazanoğlu, and Pretorius 2014]. The maximum growth rate of the instability is so small that it may remain indistinguishable from numerical errors when performing nonlinear numerical simulations [Okawa, Witek, and Cardoso 2014].

A more favorable situation occurs for charged (Reissner-Nordström) BHs. In this case Coulomb energy and charge are extracted from the BH by a *charged* bosonic field [Bekenstein 1973, Hod 2012b]. The growth rates of the charged superradiant instability can be orders of magnitude larger than for their rotating counterparts [Herdeiro, Degollado, and Rúnarsson 2013, Hod 2013, Degollado and Herdeiro 2014]. The condition for the growth of the superradiant modes is for the charged case

$$\omega < \omega_{\rm c} \equiv q\phi_H, \tag{1.6}$$

where q is the scalar field particle charge, ϕ_H is the electric potential at the horizon, and $\omega_{\rm c}$ is the critical frequency. A trapping mechanism, e.g. a mirror, has to be introduced to form a *charged BH bomb*. Considering a massive field is not enough, since the electric repulsion prevents the development of quasibound states due to the potential well for the parameter range of $\{\mu, q\}$ triggering the instability.

The charged BH version of the instability can occur within spherical symmetry. Therefore, I extended the NADA1D code to take into account a complex charged scalar field and the Maxwell equations for the electric field, and solved numerically

the full Einstein-Maxwell-(charged)Klein-Gordon system (EMKG) [Sanchis-Gual et al. 2016b]. The initial setup considered was a charged scalar-field perturbation in a cavity, as a trapping mechanism, with the Reissner-Nordström BH. The NR simulations established that the generic final state is a *hairy* BH: a charged horizon, surrounded by a scalar-field condensate storing part of the charge and energy of the initial BH, and with a phase oscillating at the threshold frequency of the superradiant instability. The exponential growth phase of the field saturates and the equilibrium is reached when the condition from (1.6), $\omega = \omega_c$, is satisfied. The imaginary part of the frequency of the field becomes zero and a hairy BH forms. Similar results for the unstable Reissner-Nordström BH were found in Bosch, Green, and Lehner [2016], considering an anti-de Sitter (AdS) spacetime with reflecting boundary conditions at $\mathscr{I}$.

In a subsequent investigation [Sanchis-Gual et al. 2016a] I varied the different parameters in the setup, namely the BH initial charge, the initial scalar perturbation, the scalar field charge and mass, as well as the radius of the mirror, to study the variation of the hair-growth process. Moreover, we considered the effect of adding a (non-linear) self-interaction term to the scalar field. The outcome was hairy BH formation.

Very recently, numerical simulations of the Kerr-Proca superradiant instability have been performed [East and Pretorius 2017, East 2017]. For Proca fields, the timescales are shorter than in the scalar case. These authors obtained an exponential growth phase, as expected due to the superradiant instability, followed by its saturation leading to the formation of Kerr BHs with Proca hair.

1.3.2.1 Solitons

Soliton-like solutions of the EMKG system, which are everywhere regular and horizonless, have been presented by Ponglertsakul, Winstanley, and Dolan [2016] and Ponglertsakul and Winstanley [2017]. Hairy BHs may be regarded as a bound state of these solitons with a horizon. Following those works, in which the linear stability of the EMKG solitons in a cavity was addressed, I studied the stability of these solutions numerically, evolving several charged soliton models by using the numerical methods described above [Sanchis-Gual et al. 2017a].

Specifically, I considered two different schemes to impose the "cavity", which is something virtual for the stationary soliton solutions, as something necessary for the dynamical evolution of the system. For these two possibilities, I observed some quantitative and qualitative differences, but convincing numerical evidence that indeed a hairy BH may form from the decay of an unstable soliton was collected. The decay of these unstable solitons could hence be a different channel

for the formation of charged hairy BHs. But I also observed, for both schemes, that some unstable solitons decay into a (bald) RN BH, rather than a hairy one.

1.4 Boson and Proca stars

In Section 1.1, scalar-field soliton-like solutions, i.e. static, spherically -symmetric solutions of the EKG system for a massive and complex field, were presented as boson stars. The dynamical fate of these compact objects has been investigated using both perturbation theory [Gleiser and Watkins 1989, Lee and Pang 1989] and fully nonlinear numerical simulations [Seidel and Suen 1990, Balakrishna, Seidel, and Suen 1998, Hawley and Choptuik 2000, Guzman 2004a]. In particular, Seidel and Suen [1990] first showed that the fate of unstable boson-star solutions was either the formation of a black hole or the migration of the star to the stable branch, regardless of the sign of the binding energy. A third outcome for unstable boson stars is their total dispersion [Balakrishna, Seidel, and Suen 1998, Guzman 2004a, Guzmán 2009] a situation which only happens for boson stars with negative binding energy.

On the other hand, vector boson stars, or *Proca stars*, have been only recently obtained as fully nonlinear numerical solutions of the Einstein-(complex)-Proca (EP) system [Brito et al. 2016]. Like boson stars, they are self-gravitating, everywhere non-singular, horizonless Bose-Einstein condensates of a massive vector field, which resemble in many ways, but not completely, their scalar cousins, the boson stars. In Sanchis-Gual et al. [2017b] I presented fully nonlinear numerical evolutions of Proca stars, in spherical symmetry, to study their stability and the endpoint of the evolution of the unstable stars. The simulations confirmed that the separation between stable and unstable configurations occurs at the solution with maximal ADM mass [Brito et al. 2016]

$$M_{\rm max} \sim 1.058\ M^2_{\rm Planck}/\mu, \tag{1.7}$$

which is slightly larger than the maximum mass for mini-boson stars. The sign of the binding energy of the solution and the perturbation determine the three different possible outcomes for the unstable models: *(i)* migration to the stable branch, *(ii)* total dispersion of the field, or *(iii)* collapse to a Schwarzschild black hole. In the latter case, a long-lived Proca field remnant composed by quasi-bound states can form outside the horizon after BH formation, with a lifetime that scales inversely with the Proca mass, as in the scalar field case [Barranco et al. 2012].

The fates for the unstable model are very similar to those observed for boson stars and neutron stars in spherical symmetry. High density unstable equilibrium models of neutron stars can be built for any EOS. Any perturbation will cause them to either collapse to a black hole or to migrate to the stable branch of equilibrium models, at smaller central densities. The sign of the perturbation determines the path the unstable star will follow [Font et al. 2002]. These observations parallel closely what we have found in this work for bosonic stars (both scalar and vector).

Boson stars are regarded as “black hole mimickers" but if they do not incorporate a self-interaction potential, their maximum mass is not large enough for boson stars to show the same gravitational effects as black holes or neutron stars. Self-interaction provides extra support against gravitational collapse increasing the possible maximum masses, allowing to reach models with astrophysical significance.

Following this idea and using the same numerical techniques than in the Proca case, we built and evolved a sample of initial models of boson stars, incorporating a self-interaction potential with a quartic term [Escorihuela-Tomàs et al. 2017]. We followed the dynamics of the system for a very long amount of time, beyond black hole formation. We revisited the stability of the solutions for different values of the self-interaction coupling constant λ, incorporating values as large as $\Lambda \equiv \lambda/4\pi G\mu^2 = 100$, not previously accounted for. Our findings were consistent with the three different outcomes for unstable models, reported previously for both the $\lambda = 0$ (mini-)boson star case and for self-interacting boson stars [Guzman 2004b]. Moreover, we showed that long-lived, quasi-bound states can also form after the collapse of a self-interacting boson star. As stated before, these results have also recently been obtained in spherical simulations of unstable Proca stars collapsing to black holes [Sanchis-Gual et al. 2017b].

The dynamical formation of boson stars was first discussed by Seidel and Suen [1994a] who found that, in spherical symmetry, a generic complex scalar field configuration collapses to form a boson star. In spherical symmetry, no gravitational radiation is emitted, and the dissipative mechanism that extracts the excess energy to form a compact object was called *gravitational cooling* and takes the form of ejection of scalar particles. In a recent paper [Di Giovanni et al. 2018], I helped to perform fully nonlinear numerical simulations of the Proca-Einstein system in spherical symmetry. We showed that the self-gravitation of the system also induces the formation of compact objects that, for appropriate initial conditions, asymptotically approach the soliton-type stationary solutions known as Proca stars, through the mechanism of gravitational cooling.

Indeed, the true nature of astrophysical BH candidates has been a central question in relativistic astrophysics for decades. The difficulty of observing the presence of an event horizon allows for the possibility that they may, in reality, be some sort of exotic *horizonless* compact objects, whose phenomenology is sufficiently similar to that of BHs, so that current observations are unable to distinguish between these two types of objects.

The correspondence between a BH's natural oscillation frequencies (the so-called quasinormal modes [Berti, Cardoso, and Starinets 2009]) and a light ring (LR) vibrations [Goebel 1972, Cardoso et al. 2009, Khanna and Price 2017], implies that compact objects with a LR, i.e. *ultra-compact objects* (UCOs), but with no event horizon can mimic the initial part of the ringdown gravitational-wave signal of perturbed BHs. Later parts of the ringdown signal may have signatures of the true nature of the object (through the so called *echoes* [Cardoso et al. 2016, Cardoso and Pani 2017, Westerweck et al. 2017, Conklin, Holdom, and Ren 2017]) but the low signal to noise ratio challenges clean detections of this part of the signal, at least in the near future.

In Cunha et al. [2017] we considered spherically symmetric boson stars, as well as Proca stars, as a reference example of horizonless UCOs, and simultaneously as a proof of concept that BH mimickers are dynamically possible through known physics. Our numerical study revealed that for bosonic stars, both the scalar and the vector ones, the presence of the LR that allows them to, in principle, vibrate as BHs do, gives rise to a quite distinct pattern of light lensing from that of standard BH shadows. However, bosonic stars only become UCOs in a regime wherein they are also perturbatively unstable. Therefore, we found that the same perturbations that could make them vibrate as a BH would actually induce their gravitational collapse into one. By performing fully non-linear simulations we showed that this is a fast process, and a horizon forms within a few light-crossing times. Altogether, these results emphasise the difficulty, at least in spherical symmetry, in constructing a reasonable dynamical model of horizonless UCOs whose phenomenology can mimic that of a BH.

1.5 Miscellany

1.5.1 Amended Hartle's model

The construction of analytic models of astrophysical compact bodies in GR relies on the matching of spacetimes theory. The idea is to consider two different bounded regions, namely an interior fluid and a vacuum exterior, and to impose

appropriate matching conditions on a timelike hypersurface Σ separating them. Therefore, a global model is constructed by joining the common boundary data on Σ. While the search for an exact global model for a rotating compact body is a major challenge, the situation becomes tractable when one resorts to approximate methods such as perturbation theory. In this context, models that describe rotating stars [Hartle 1967], tidal effects [Damour and Nagar 2009], or collapsing stars [Brizuela et al. 2010] have been developed.

In their pioneering work, Hartle and Thorne presented the general relativistic treatment of isolated rotating compact stars in equilibrium [Hartle 1967, Hartle and Thorne 1968], known as "Hartle's model" in short. This stands as the basis to construct analytical models in axial symmetry (see Stergioulas [2003] and references therein). A perturbative scheme is built upon a spherical non-rotating configuration, on top of which stationary (rotating) and axial perturbations are taken to second order. Models are built assuming a perfect fluid interior with barotropic EOS that rotates rigidly and with no convective motions. Under these assumptions the perturbations are described by four functions, whose values at the surface of the star determine the dragging of inertial frames, the deformation, and the total mass of the star in terms of the central density. At each order those values are computed *(i)* integrating from the regular centre given an EOS, *(ii)* solving the asymptotically flat vacuum exterior, and *(iii)* assuming the continuity of the functions across the surface choosing an explicit coordinate system.

As shown by Reina and Vera [2015] using the framework of Mars [2005], a relevant perturbative function of the model presents a discontinuity proportional to the (background) energy density in the stellar surface, that enters the computation of the mass of the star. Therefore, the original expression for the total mass of the rotating star given in [Hartle 1967] has to be amended. Constant-density stars were analyzed in Reina [2016], showing that the deviations in the mass-radius diagrams are far from negligible. In Reina et al. [2017] we studied more realistic EOS and quark stars to see if a discontinuity exists at the surface. We found that the deviations in the amended equilibrium models are also non-negligible.

Yagi and Yunes found that the so-called I-Love-Q relations in compact stars, where "I" and "Q" refer to the moment of inertia and the quadrupole moment of the star, respectively, and the Love numbers "k_l" are associated with the tidal field due to the presence of a companion star in a binary system, are related in an EOS-independent way [Yagi and Yunes 2013]. Their original finding was corrected in Yagi and Yunes [2014] where an amended expression for the

Love numbers that leads to universal I-Love-Q relations was provided. Their first result was incorrect precisely due to the assumption of continuity of the perturbations across Σ_0. A function connected to the Love numbers exhibits a discontinuity proportional to the energy density at the stellar surface, which does not vanish for quark stars.

In Reina et al. [2017] we also addressed the issue of the I-Love-Q relations in compact stars taking into account the amended mass term in Hartle's model. To perform this analysis, we developed a numerical code, modifying a TOV solver and including the perturbed matching conditions from Reina and Vera [2015] to then: *(i)* apply the corrections in the context of Hartle's model to quark stars with linear EOS, revisiting the work of Colpi and Miller [1992]; *(ii)* set forth the discontinuities involved in the $l \geq 2$ sector of the first-order tidal-field problem and show how those conditions, which indeed coincide with those in Price and Thorne [1969], lead to the corrections recognised in Damour and Nagar [2009] and used in Hinderer et al. [2010] and Yagi and Yunes [2014]; *(iii)* complete the I-Love-Q relations incorporating δM, now correctly computed, that indicate universal relations for all perturbative quantites.

1.5.2 The Virgo Collaboration

In July 2016, the Valencia Virgo Group [*Valencia Virgo Group*], of which I am member, became the first Spanish group to be part of the Virgo Collaboration. One year later, the group obtained full-authorship rights, after succeeding in the internal evaluation. My work within this collaboration involves gravitational-wave modelling through NR simulations and parameter estimation.

The thermodynamical properties of the EOS of high-density matter (above nuclear saturation density) and the possible existence of exotic states such as phase transitions from nuclear/hadronic matter into quark-gluon plasma, [Schertler et al. 2000, Glendenning and Kettner 2000] may critically influence the stability and dynamics of compact relativistic stars. From a theoretical point of view, establishing the existence of those states requires the analysis of the "convexity" of the EOS. There are indications of the existence of possible regions in the dense-matter EOS where the thermodynamics may actually be non-convex. Flows subject to non-convex dynamics, dubbed Bethe-Zel'dovich-Thompson (or BZT) flows [Bethe 1942, Zel'dovich 1946, Thompson 1971] are characterized by the appearance of compound waves (rarefaction shocks) during the evolution [Argrow 1996, Guardone and Vigevano 2002, Voss 2005, Cinnella and Corre 2006, Ibáñez et al. 2013, Serna and Marquina 2014]. In an ongoing project, we investigated

the effects of a phenomenological, non-convex EOS on the equilibrium structure of stable compact stars [Ibáñez et al. 2017]. I performed numerical evolutions to study the dynamics of unstable and uniformly-rotating neutron stars that collapse gravitationally to black holes. My simulations showed how the dynamics of the collapse with a non-convex EOS greatly departs from the convex case, leaving distinctive imprints on the gravitational waveforms. A publication summarising these results is currently in preparation [Ibañez et al. 2018].

Moreover, I have been working on the extraction of gravitational waves from NR simulations of the merger of Proca star binaries (head-on collision and orbital merger). The mid-term goal of this project is to create a comprehensive catalog of gravitational waves from boson and Proca star mergers that could be compared with the results of BBH mergers and with the actual observations of the advanced LIGO and Virgo detectors.

Chapter 2

Discussion

2.1 Scalar fields, Proca fields, and black holes

Most of the research work presented in this thesis has had to do with the investigation, through fully non-linear numerical-relativity simulations, of the dynamics of bosonic fields coupled to gravity in a series of strong-field spherically symmetric scenarios. First, I have conducted studies of self-gravitating and linear real scalar fields in Schwarzschild BH spacetimes in three different situations: *(i)* with the BH already formed, *(ii)* with the BH dynamically forming during the evolution from the gravitational collapse of polytropic stars and of the field itself, and *(iii)* in an accreting BH spacetime.

I have performed a large number of (second-order) accurate and long-term stable simulations of dynamical non-rotating BHs surrounded by self-gravitating scalar fields. The models of our sample covered a broad range of cases from the test-field regime to the fully non-linear regime. I was able to determine well-defined real oscillation frequencies for the field. The time evolution of the field produces in most models a characteristic beating pattern due to the non-linear combination of two close oscillation frequencies, evidencing the presence of a quasibound state around the BH. We thus confirmed earlier findings from perturbation theory also in the case of highly dynamical spacetimes (i.e. those consisting of a black hole and a rich scalar field environment). Our simulations revealed that there are states which closely resemble the quasi-bound states in the test-field approximation.

The formation of a BH or the sudden growth of its mass due, for instance, to the absorption of part of a self-gravitating scalar field, may have repercussions for the field itself. However, we found that the scalar field survives and lingers

for long periods of time. By comparing the evolutions of the scalar field in collapsing, black-hole-forming spacetimes with spacetimes that already contain a non-rotating black hole, it is possible to determine the influence of the collapse of the star on the scalar-field dynamics. The differences are mainly due to the initial (or lack of) accretion phase onto the black hole that contributes to the growth of its mass and to the different dynamics, in the case of self-gravitating scalar fields. For certain values of the mass of the scalar field μ (see Sanchis-Gual et al. [2015]) the formation of the BH during the collapse of the star enhances the chances of the scalar field to remain in a quasi-bound state. This result may have implications for models of BH formation surrounded with dark matter halos in the early epochs of the Universe.

If the BH mass grows continuously, it affects the decay rate of the field. The imaginary part of the frequency becomes non-linear and accretion speeds up. The growth must however be maintained for long periods of time to be a threat to the scalar field. My series of works on this subject [Sanchis-Gual et al. 2015, Sanchis-Gual et al. 2015, Sanchis-Gual et al. 2016c] complement and extend previous studies performed in the linear regime: quasibound states ("wigs") around BHs exist and may be very long lived even when non-linearities, the self-gravitation of the field, and the dynamics of the BH spacetime are taking into account. I compared the BH mass growth rates obtained in my simulations with estimates from observational surveys, extrapolating our results to realistic values of the scalar field mass μ. It was found that even for the high mass accretion rates considered in Sanchis-Gual et al. [2016c], e.g. $\dot{M}_{\rm BH} = 5 \times 10^{-7}$, in units of $c = G = M_{\odot} = 1$, quasibound states around accreting BHs can survive for cosmological timescales. Therefore, my results provide further support to the intriguing possibility of the existence of dark matter halos based on (ultra-light) scalar fields surrounding SMBHs at galactic centers.

Secondly, I perturbed a Reissner-Nordström BH by introducing a complex charged scalar field trapped inside a cavity with a reflecting boundary, i.e., a mirror [Sanchis-Gual et al. 2016b]. This configuration can trigger a superradiant instability. This system has the advantage with respect to the rotating case that it can be done in spherical symmetry and the timescales are orders of magnitude smaller. Linear studies of this system have also been performed [Degollado and Herdeiro 2014, Herdeiro, Degollado, and Rúnarsson 2013] but to reach the non-linear regime in which the backreaction of the field is non-negligible and it can extract energy from the BH, numerical-relativity simulations are required. I found that the endpoint of the instability is a charged hairy BH. The field extracts Coulomb energy and charge of the BH until the superradiant

condition (1.6) is fulfilled and an equilibrium state is reached. The energy extraction is more efficient the lower the scalar.field charge, the larger the BH charge and the smaller the mirror radius. The trend with the charge extraction is opposite: it is less efficient the lower the charge coupling, the larger the BH charge and the smaller the mirror radius. In addition, when introducing a scalar field quartic self-coupling, the final scalar field magnitude profile acquires larger spatial gradients, which justifies the larger energy transferred from the BH to the scalar field, despite the lower amplitude of the final scalar field profile, as compared to the non-self-interacting case. The final hairy BH is essentially insensitive to varying the initial perturbation, even though the details of the evolution depend on it. A mode analysis reveals that various modes contribute to the superradiant growth in the early states of the process. However, a single mode remains at the end, in equilibrium with the BH; thus the other modes became non-superradiant and decay back into the BH before equilibrium is attained.

It should be pointed out that the scenario discussed in Sanchis-Gual et al. [2016b] is a toy model, since Reissner-Nordström BHs are not thought to have astrophysical significance. However, the model allows to numerically study the charged BH bomb, which is a convenient surrogate to the superradiant instability in Kerr BH spacetimes, with astrophysical relevance. Indeed, it was recently found that a similar result was obtained for a Proca perturbation of the Kerr metric satisfying the superradiant condition [East and Pretorius 2017]. A hairy BH was again at the endpoint of the superradiant instability, having more entropy than the bald Kerr BH. A bosonic hair could be observed from the BH shadows or numerical simulations of merging hairy BHs could provide different gravitational waveforms.

Finally, let me remark that the hairy BHs I dynamically showed to form in [Sanchis-Gual et al. 2016b, Sanchis-Gual et al. 2016a] can be interpreted as the bound state of a Reissner-Nordström BH and a charged scalar soliton in a cavity. The latter class of solutions was recently studied in detail by Ponglertsakul, Winstanley, and Dolan [2016]. It was shown in this work that, amongst these solitonic solutions, some are unstable. An interesting question is, thus, what is the development of the instability for such unstable solitons, and in particular, if they evolve into a hairy BH. The technology described herein can be used to tackle this question. We hope to report on it in the near future.

Solitonic solutions can also be constructed for a massive complex charged scalar field. Due to the Coulomb repulsion, a mirror has to be added. Numerical simulations can be performed to study the instability of these solutions.

In [Sanchis-Gual et al. 2017a] I explored stable and unstable models, showing that the unstable cases could collapse to form a bald Reissner-Nordström BH or a charged hairy BH, thus being another dynamical formation channel of these compact objects.

Other solitonic solutions involving massive bosonic fields are boson stars and Proca stars. The corresponding sequences of equilibrium models are distributed in the same way than for neutron stars and white dwarfs. They are characterized by a maximum mass, which indicates the critical point separating the stable and unstable branches against linear perturbations. Time evolutions of spherically symmetric mini-boson stars, self-interacting boson stars and Proca stars were carried out in [Escorihuela-Tomàs et al. 2017, Sanchis-Gual et al. 2017b, Cunha et al. 2017] to assess their stability. The different outcomes of the unstable models were similar, depending on the perturbation, and we were able to identify a quasibound state remnant forming after the formation of a BH from the gravitational collapse of boson stars and Proca stars.

2.2 Amended Hartle's model

The assumptions in Hartle's original paper [Hartle 1967] are well established and there is no mention to the supposed continuity of the energy density at the surface of the star. The model is constructed for any EOS, and thus for any value of the energy density at the surface. That is, in part, the beauty of the model, and it has been widely used as such. Moreover, the right use of the perturbed matching yields the corrections used in [Yagi and Yunes 2014] to find universal I-Love-Q relations. Our results [Reina et al. 2017] show that the second order $l = 0$ parameter $\overline{\delta M}$ completes the universal relations that involve the first order parameter I, the second order $l = 2$ parameter $\overline{Q}$, and the tidal number k_2. This can be used to fix the problems inherent to the relations involving only the latter three parameters, due to the assumption of continuity of the perturbations across Σ_0.

Using a modified TOV solver, we computed the corrected mass vs radius configurations of rotating quark stars, comparing them to the work of Colpi and Miller [1992]. Besides, owing to these corrections we found a universal relation involving the second-order contribution to the mass δM. Thus, the set of universal relations for the tidal problem in binary systems, namely I, Love, Q, is completed with δM.

Chapter 3

Outlook

There are a number of research projects that I plan to pursue in the near future. Some of those have already been initiated and results have been obtained and submitted for publication [Di Giovanni et al. 2018, Sanchis-Gual, Quilis, and Font 2018]. Some other projects are natural extensions of topics of research discussed in this thesis.

The first of these projects deals with the study of the gravitational-wave background from a realistic cosmological quasar distribution produced by supermassive black holes (SMBH). Using the DR9Q quasar catalogue from the ninth data release of the Sloan Digital Sky Survey, I have created a complete sample of quasars from $z = 0.3$ to 5.4 statistically consistent with the DR9Q catalogue. Using the spectroscopic information, I estimated the masses of the SMBH hosted by the quasars in the sample. The background gravitational-wave emission is obtained by the addition of the individual signals from each quasars modeled as plane waves whose interference can be constructive or destructive depending of their evolutionary state. The resulting signal is a gravitational radiation background that falls within the sensitivity of the LISA interferometer.

In a second project I performed a numerical study of the structure and dynamics of compact stellar configurations described by a BZT fluid. This was motivated by the indications of the existence of possible regions in the dense-matter EOS where the thermodynamics can be non-convex. We chose a particularly simple form of the EOS, namely an ideal gas EOS with an adiabatic index which depends on the density [Ibáñez et al. 2018]. While this phenomenological EOS can only be regarded as a toy model, it serves nonetheless to exemplify the particularities that appear in the dynamics when the EOS is nonconvex. Our study considers two different situations, firstly, the equilibrium

structure of stable compact stars and, secondly, the dynamics of unstable and uniformly-rotating neutron stars that collapse gravitationally to BHs and their gravitational-wave emission.

With the dawn of gravitational-wave astronomy, obtaining gravitational waveforms from systems involving exotic compact objects, such as boson stars and Proca stars, may help discover their existence. In particular, in order to construct waveform templates from mergers of such type of binaries, it is necessary to perform numerical-relativity simulations. In the near future, I plan to perform such simulations and build a waveform catalog that could be used by the LIGO-Virgo collaborations. In addition to NR simulations, I will also apply machine learning techniques to produce synthetic gravitational waveforms from existing numerical catalogs to try and fill in the blanks of the catalogs.

I also plan to investigate the *dynamical* formation of the rotating Proca star and boson star solutions obtained recently by numerical means by Brito et al. [2016]. The recent NR simulations of Bezares, Palenzuela, and Bona [2017] and Palenzuela et al. [2017] showed, somewhat surprisingly, that the outcome of the merger of two spherically-symmetric boson stars with the same mass is the formation of either a BH or a spherically-symmetric boson star. More simulations exploring a much broader parameter space are certainly necessary to rule out boson star mergers as a mechanism for forming boson stars with angular momentum. The same type of analysis will be also carried out for Proca stars.

Finding the mechanism leading to the dynamical formation of a rotating boson star or a rotating Proca star will be a short-term goal for my future research, extending our recent investigation in the spherically-symmetric case [Di Giovanni et al. 2018]. The formation of compact bosonic objects through a dissipationless cooling mechanism from an initial Gaussian distribution of scalar field was first investigated by Seidel and Suen [1994b]. In [Di Giovanni et al. 2018] we performed fully non-linear numerical simulations within the spherically symmetric Einstein-(complex)Proca system. Starting with Proca field distributions that obey the Hamiltonian, momentum and Gaussian constraints, we showed that the self-gravity of the system induces the formation of compact objects, which, for appropriate initial conditions, asymptotically approach stationary soliton-like solutions known as Proca stars. The excess energy of the system is dissipated by the mechanism of gravitational cooling in analogy to what occurs in the dynamical formation of scalar boson stars [Seidel and Suen 1994b]. For rotating stars, I will consider a similar initial setup but adding angular momentum by choosing a nonzero azimuthal number m, in particular $m = 1$. The goal is to

find out if the gravitational cooling mechanism can also lead to the formation of rotating boson stars or Proca stars.

Part II

Appendices

Appendix A

Publications

The format of the present doctoral thesis as a compendium of publications requires the permission from the corresponding publishers. Permission to re-use published material was obtained from all journals.

- Copyright credit to Physical Review D y Physical Review Letters, whose publisher is the American Physical Society.
- Copyright credit to Classical and Quantum Gravity, whose publisher is IOP Publishing.
- Copyright credit to Monthly Notices of the Royal Astronomical Society: Letters, whose publisher is Oxford University Press.

PHYSICAL REVIEW D **89,** 104033 (2014)

Fully covariant and conformal formulation of the Z4 system in a reference-metric approach: Comparison with the BSSN formulation in spherical symmetry

Nicolas Sanchis-Gual,[1] Pedro J. Montero,[2] José A. Font,[1] Ewald Müller,[2] and Thomas W. Baumgarte[3]
[1]*Departamento de Astronomía y Astrofísica, Universitat de València, Doctor Moliner 50, 46100 Burjassot (València), Spain*
[2]*Max-Planck-Institute für Astrophysik, Karl-Schwarzschild-Strasse 1, 85748 Garching bei München, Germany*
[3]*Department of Physics and Astronomy, Bowdoin College, Brunswick, Maine 04011, USA*
(Received 14 March 2014; published 21 May 2014)

We adopt a reference-metric approach to generalize a covariant and conformal version of the Z4 system of the Einstein equations. We refer to the resulting system as "fully covariant and conformal," or fCCZ4 for short, since it is well suited for curvilinear as well as Cartesian coordinates. We implement this fCCZ4 formalism in spherical polar coordinates under the assumption of spherical symmetry using a partially implicit Runge-Kutta method and show that our code can evolve both vacuum and nonvacuum spacetimes without encountering instabilities. Our method does not require regularization of the equations to handle coordinate singularities, nor does it depend on constraint-preserving outer boundary conditions. It also does not need any modifications of the equations for evolutions of black holes. We perform several tests and compare the performance of the fCCZ4 system, for different choices of certain free parameters, with that of BSSN. Confirming earlier results we find that, for an optimal choice of these parameters and for neutron-star spacetimes, the violations of the Hamiltonian constraint can be between 1 and 3 orders of magnitude smaller in the fCCZ4 system than in the BSSN formulation. For black hole spacetimes, on the other hand, any advantages of fCCZ4 over BSSN are less evident.

DOI: 10.1103/PhysRevD.89.104033 PACS numbers: 04.25.D-, 95.30.Lz, 95.30.Sf, 97.60.Lf

I. INTRODUCTION

Numerical relativity has become a field of intense activity, and considerable progress has been made during the last decade. The possible detection of gravitational waves by the second-generation enhanced detectors (Advanced LIGO [1], Advanced VIRGO [2], and KAGRA [3]) represents a major incentive for the development of numerical simulations able to provide accurate gravitational waveforms from astrophysical sources.

Many current numerical relativity codes use the so-called BSSN formulation of Einstein equations, originally proposed by Nakamura *et al.* [4] and subsequently modified by Shibata and Nakamura [5] and Baumgarte and Shapiro [6]. The stability properties of the BSSN formulation are a result of the "conformal connection functions," which are introduced as new independent variables. In combination with certain gauge conditions—in particular the "1 + log" slicing condition [7] and the "Gamma-driver condition" [8]—the BSSN formulation has allowed for accurate and stable simulations of strong-field spacetimes, including black holes and neutron stars.

Recently, other conformal and traceless decompositions of the Einstein equations, based on the Z4 system [9], have been proposed by Bernuzzi and Hilditch [10], the so-called Z4c formulation, and also by Alic *et al.* [11,12], the CCZ4 formulation. Unlike the BSSN formulation, both the Z4c and CCZ4 systems incorporate the constraint damping scheme developed by Gundlach *et al.* [13] that allows for the dynamical control of the constraint violations by means of constraint damping terms. The Z4c system discards nondamping nonprincipal terms, breaking the four covariance, but allowing the evolution equations to take a form that is very similar to BSSN. The CCZ4 system, on the other hand, retains all damping terms and maintains the four covariance. Nevertheless, the CCZ4 system as presented initially in [11] suffers from numerical instabilities that develop in black hole spacetimes unless the four covariance is broken. This issue was addressed by Alic *et al.* [12], who prescribed a modification for the damping parameter that removes the instabilities when using the fully covariant version of the CCZ4 system in the evolution of black holes. Both conformal decompositions of the Z4 system have been tested extensively [10–12,14–17]. Numerical results show that in nonvacuum simulations violations of the Hamiltonian constraint can be as much as 1 to 3 orders of magnitude smaller than those in the BSSN formulation.

Both the BSSN and the CCZ4 or Z4c formulations in their original form are developed under the assumption of Cartesian coordinates; in particular, they assume that the determinant of the conformal metric is equal to one. In the case of the BSSN formulation, this issue was resolved by [18–20], who introduced a covariant formulation of the

BSSN equations that is well suited for curvilinear coordinate systems by adopting a reference-metric framework [21]. This approach allows, for example, for implementations in spherical polar coordinates, which is of great interest since many astrophysical phenomena are symmetric with respect to the rotation axis (e.g., accretion disks) or are such that spherical coordinates adapt better to their geometry (e.g., gravitational collapse).

The singularities associated with curvilinear coordinate systems, however, are a known source of numerical problems. For instance, one problem arises because of the presence of terms in the evolution equations that diverge like $1/r$ near the origin $r = 0$. Several methods have been proposed to deal with the singular terms that appear in curvilinear coordinates. Cordero-Carrión *et al.* [22] recently adopted a partially implicit Runge-Kutta (PIRK) method to evolve hyperbolic, wavelike equations in the fully constrained formulation of the Einstein equations (see [21]). Montero and Cordero-Carrión [23], assuming spherical symmetry, applied a second-order PIRK method to the BSSN equations and obtained stable numerical simulations of vacuum and nonvacuum spacetimes without the need for a regularization algorithm at the origin. This approach has been successfully implemented in three dimensions without any symmetry assumption by [24] and more recently by [25] who reported the first successful implementation of relativistic hydrodynamics coupled to dynamical spacetimes in spherical polar coordinates with no symmetry assumptions.

The purpose of this paper is threefold. We first generalize the covariant and conformal Z4 system using a reference-metric approach. We refer to this new system as "fully covariant and conformal Z4" or fCCZ4 for short. This approach allows us to write the evolution equations in a fully covariant form suitable for spherical polar and other curvilinear coordinates. Second, we implement the fCCZ4 system in spherical polar coordinates under the assumption of spherical symmetry and show that by using the PIRK scheme we obtain robust and stable numerical evolutions of both vacuum and nonvacuum spacetimes. Third, we show that the fCCZ4 formulation with the PIRK scheme can handle spacetimes containing black holes without the appearance of any instability and without the need for the modification prescribed by Alic *et al.* [12]. Finally, we compare results obtained with the BSSN and the fCCZ4 formulations. Confirming earlier results, we find that, for certain choices of free parameters, fCCZ4 can significantly reduce constraint violations, in particular for neutron-star spacetimes. For black hole simulations, however, the advantages of fCCZ4 over BSSN are less evident. We also discuss implications of the presence of free and dimensional damping parameters in the fCCZ4 formalism.

The paper is organized as follows. Section II describes the fCCZ4 evolution equations. In Sec. III A we write the fCCZ4 equations in spherical coordinates under the assumption of spherical symmetry. Section IV describes the numerical implementation, and Sec. V shows results from a number of numerical experiments, namely a pure gauge wave, the evolution of a single black hole, the evolution of a spherical relativistic star in equilibrium, the so-called migration test, and the gravitational collapse of a spherical relativistic star leading to the formation of a black hole. We summarize and discuss the respective advantages and disadvantages of fCCZ4 and BSSN in Sec. VI. Throughout this article we use gravitational units $c = G = 1$. Greek indices denote spacetime indices (0 to 3), while Latin indices denote space indices only (1 to 3).

II. THE FULLY COVARIANT AND CONFORMAL Z4 FORMULATION

The Z4 constraint damped system [9,13] in its four-dimensional covariant form replaces the Einstein equations by

$$ {}^{(4)}R_{\mu\nu} + \nabla_\mu {}^{(4)}Z_\nu + \nabla_\nu {}^{(4)}Z_\mu - \kappa_1[n_\mu {}^{(4)}Z_\nu + n_\nu {}^{(4)}Z_\mu - (1+\kappa_2) g_{\mu\nu} n_\sigma {}^{(4)}Z^\sigma] = 8\pi\left(T_{\mu\nu} - \frac{1}{2} g_{\mu\nu} T\right), \quad (2.1) $$

where ${}^{(4)}R_{\mu\nu}$ is the Ricci tensor of the four-dimensional spacetime $\mathcal{M}$ with metric $g_{\mu\nu}$, ∇_μ the covariant derivative associated with metric $g_{\mu\nu}$, $T_{\mu\nu}$ the stress-energy tensor, and $T \equiv g_{\mu\nu} T^{\mu\nu}$ its trace. The above equation reduces to Einstein's equations when the additional four vector ${}^{(4)}Z_\mu$ vanishes. The two arbitrary constants κ_1 and κ_2 serve as constraint damping coefficients. While κ_2 is dimensionless, κ_1 has units of inverse length.

In the $3+1$ decomposition, we assume that the spacetime $\mathcal{M}$ can be foliated by a family of spatial slices Σ that coincide with level surfaces of a coordinate time t. We denote the future-pointing unit normal on Σ with n^μ and write the line element as

$$ ds^2 = -\alpha^2 dt^2 + \gamma_{ij}(dx^i + \beta^i dt)(dx^j + \beta^j dt), \quad (2.2) $$

where α is the lapse function, β^i the shift vector, and γ_{ij} the spatial metric induced on Σ. In terms of the lapse and shift, the normal vector n^μ can be expressed as

$$ n_\mu = (-\alpha, 0, 0, 0) \quad \text{or} \quad n^\mu = (1/\alpha, -\beta^i/\alpha). \quad (2.3) $$

As in the BSSN formulation, we adopt a conformal decomposition of the spatial metric

$$ \gamma_{ij} = e^{4\phi} \bar{\gamma}_{ij}, \quad (2.4) $$

where $e^{4\phi}$ is the conformal factor and $\bar{\gamma}_{ij}$ the conformally related metric. We refer to the connection coefficients associated with $\bar{\gamma}_{ij}$ as $\bar{\Gamma}^i_{jk}$. Instead of determining the conformal factor by fixing the determinant of the conformal

metric, $\bar{\gamma}$ to unity, as is suitable for Cartesian coordinates, we adopt

$$e^{4\phi} = (\gamma/\bar{\gamma})^{1/3}, \tag{2.5}$$

where γ is the determinant of γ_{ij}. In order to determine the conformal factor, we then impose Brown's Lagrangian condition [19]

$$\partial_t \bar{\gamma} = 0. \tag{2.6}$$

We denote the conformally rescaled extrinsic curvature as

$$\bar{A}_{ij} = e^{-4\phi}\left(K_{ij} - \frac{1}{3}\gamma_{ij}K\right), \tag{2.7}$$

where K_{ij} is the physical extrinsic curvature and $K = \gamma^{ij}K_{ij}$ its trace.

We next introduce a reference metric $\hat{\gamma}_{ij}$ with corresponding reference connection $\hat{\Gamma}^i_{jk}$. We then define the difference between the connections associated with the conformally related and the reference metric as

$$\Delta\Gamma^i_{jk} \equiv \bar{\Gamma}^i_{jk} - \hat{\Gamma}^i_{jk} \tag{2.8}$$

and note that, unlike the individual connections, these objects transform as a tensor field.

In the Z4 system, the Hamiltonian and momentum constraints result in equations for the four-vector ${}^{(4)}Z_\mu$. In a $3+1$ decomposition, these equations can be written as evolution equations for the projection of the ${}^{(4)}Z_\mu$ along the normal n^μ, which, following convention, we define as

$$\Theta \equiv -n_\mu {}^{(4)}Z^\mu = \alpha {}^{(4)}Z^0, \tag{2.9}$$

and the spatial projection of ${}^{(4)}Z_\mu$,

$$Z_i \equiv \gamma_i{}^{\mu} {}^{(4)}Z_\mu. \tag{2.10}$$

Here Z_i now denotes a spatial vector whose index can be raised with the (inverse) spatial metric, $Z^i = \gamma^{ij}Z_j$.

Defining

$$\partial_\perp \equiv \partial_t - \mathcal{L}_\beta, \tag{2.11}$$

where $\mathcal{L}_\beta$ denotes the Lie derivative along the shift vector β^i, the fully covariant and conformal Z4 system in a reference-metric approach (fCCZ4) is then given by the following set of evolution equations:

$$\partial_\perp \bar{\gamma}_{ij} = -\frac{2}{3}\bar{\gamma}_{ij}\bar{D}_k\beta^k - 2\alpha\bar{A}_{ij}, \tag{2.12}$$

$$\begin{aligned}\partial_\perp \bar{A}_{ij} = &-\frac{2}{3}\bar{A}_{ij}\bar{D}_k\beta^k - 2\alpha\bar{A}_{ik}\bar{A}^k_j + \alpha\bar{A}_{ij}(K - 2\Theta) \\ &+ e^{-4\phi}[-2\alpha\bar{D}_i\bar{D}_j\phi + 4\alpha\bar{D}_i\phi\bar{D}_j\phi \\ &+ 4\bar{D}_{(i}\alpha\bar{D}_{j)}\phi - \bar{D}_i\bar{D}_j\alpha \\ &+ \alpha(\bar{R}_{ij} + \mathcal{D}_i Z_j + \mathcal{D}_j Z_i - 8\pi S_{ij})]^{\mathrm{TF}},\end{aligned} \tag{2.13}$$

$$\partial_\perp \phi = \frac{1}{6}\bar{D}_i\beta^i - \frac{1}{6}\alpha K, \tag{2.14}$$

$$\begin{aligned}\partial_\perp K = &e^{-4\phi}[\alpha(\bar{R} - 8\bar{D}^i\phi\bar{D}_i\phi - 8\bar{D}^2\phi) \\ &- (2\bar{D}^i\alpha\bar{D}_i\phi + \bar{D}^2\alpha)] + \alpha(K^2 - 2\Theta K) \\ &+ 2\alpha\mathcal{D}_i Z^i - 3\alpha\kappa_1(1+\kappa_2)\Theta + 4\pi\alpha(S - 3E),\end{aligned} \tag{2.15}$$

$$\begin{aligned}\partial_\perp \Theta = &\frac{1}{2}\alpha[e^{-4\phi}(\bar{R} - 8\bar{D}^i\phi\bar{D}_i\phi - 8\bar{D}^2\phi) \\ &- \bar{A}^{ij}\bar{A}_{ij} + \frac{2}{3}K^2 - 2\Theta K + 2\mathcal{D}_i Z^i] \\ &- Z^i\partial_i\alpha - \alpha\kappa_1(2+\kappa_2)\Theta - 8\pi\alpha E,\end{aligned} \tag{2.16}$$

$$\begin{aligned}\partial_\perp \tilde{\Lambda}^i = &\bar{\gamma}^{jk}\hat{D}_j\hat{D}_k\beta^i + \frac{2}{3}\Delta\Gamma^i\bar{D}_j\beta^j + \frac{1}{3}\bar{D}^i\bar{D}_j\beta^j \\ &- 2\bar{A}^{jk}(\delta^i{}_j\partial_k\alpha - 6\alpha\delta^i{}_j\partial_k\phi - \alpha\Delta\Gamma^i{}_{jk}) \\ &- \frac{4}{3}\alpha\bar{\gamma}^{ij}\partial_j K + 2\bar{\gamma}^{ki}\left(\alpha\partial_k\Theta - \Theta\partial_k\alpha - \frac{2}{3}\alpha K Z_k\right) \\ &- 2\alpha\kappa_1\bar{\gamma}^{ij}Z_j - 16\pi\alpha\bar{\gamma}^{ij}S_j.\end{aligned} \tag{2.17}$$

Here the superscript TF denotes the trace-free part of a tensor; κ_1 and κ_2 are the damping coefficients introduced by [13], and $\hat{D}_i$, $\mathcal{D}_i$, and $\bar{D}_i$ denote the covariant derivatives built from the connection associated with the reference metric $\hat{\gamma}_{ij}$, the physical metric γ_{ij}, and the conformal metric $\bar{\gamma}_{ij}$, respectively. We have also defined

$$\tilde{\Lambda}^i \equiv \bar{\Lambda}^i + 2\bar{\gamma}^{ij}Z_j, \tag{2.18}$$

where

$$\bar{\Lambda}^i \equiv \Delta\Gamma^i = \bar{\gamma}^{jk}\Delta\Gamma^i_{jk}. \tag{2.19}$$

The vector $\tilde{\Lambda}^i$ plays the role of the "conformal connection functions" in the original CCZ4 system; its evolution equation (2.17) is a reformulation of the evolution equation for the variables Z_i.

The matter sources E, S_i, S_{ij}, and S denote the density, momentum density, stress, and the trace of the stress as observed by a normal observer, respectively:

$$E \equiv n_\mu n_\nu T^{\mu\nu}, \tag{2.20}$$

$$S_i \equiv -\gamma_{i\mu}n_\nu T^{\mu\nu}, \tag{2.21}$$

$$S_{ij} \equiv \gamma_{i\mu}\gamma_{j\nu}T^{\mu\nu}, \tag{2.22}$$

$$S \equiv \gamma^{ij}S_{ij}. \tag{2.23}$$

In Eq. (2.13), we compute the Ricci tensor $\bar{R}_{ij}$ associated with $\bar{\gamma}_{ij}$ from

$$\bar{R}_{ij} = -\frac{1}{2}\bar{\gamma}^{kl}\hat{\mathcal{D}}_k\hat{\mathcal{D}}_l\bar{\gamma}_{ij} + \bar{\gamma}_{(i}\hat{\mathcal{D}}_{j)}\Delta\Gamma^k + \Delta\Gamma^k\Delta\Gamma_{(ij)k} + \bar{\gamma}^{kl}(2\Delta\Gamma^m_{k(i)}\Delta\Gamma_{j)ml} + \Delta\Gamma^m_{ik}\Delta\Gamma_{mjl}). \tag{2.24}$$

Here we compute the $\Delta\Gamma^i$ from their definition (2.19). Given $\Delta\Gamma^i$, and values for $\tilde{\Lambda}^i$, the vectors Z_i, which are not evolved independently, can be determined from (2.18).

Unless stated otherwise, we fix the gauge freedom by imposing the so-called nonadvective $1+\log$ condition for the lapse [26]

$$\partial_t\alpha = -2\alpha(K - 2\Theta) \tag{2.25}$$

and a variation of the "Gamma-driver" condition for the shift vector [8]

$$\partial_t\beta = B^i, \tag{2.26}$$

$$\partial_t B^i = \frac{3}{4}\partial_t\tilde{\Lambda}^i. \tag{2.27}$$

Finally, when $\Theta = Z_i = 0$, the evolution equations (2.12)–(2.17) imply that the Hamiltonian and momentum constraints hold in the form

$$\mathcal{H} \equiv \frac{2}{3}K^2 - \bar{A}_{ij}\bar{A}^{ij} + e^{-4\phi}(\bar{R} - 8\bar{\mathcal{D}}^i\phi\bar{\mathcal{D}}_i\phi - 8\bar{\mathcal{D}}^2\phi) - 16\pi E = 0, \tag{2.28}$$

$$\mathcal{M}^i \equiv e^{-4\phi}\left(\frac{1}{\sqrt{\bar{\gamma}}}\hat{\mathcal{D}}_j(\sqrt{\bar{\gamma}}\bar{A}^{ij}) + 6\bar{A}^{ij}\partial_j\phi - \frac{2}{3}\bar{\gamma}^{ij}\partial_j K + \bar{A}^{jk}\Delta\Gamma^i_{jk}\right) - 8\pi S^i = 0, \tag{2.29}$$

where $\bar{R}$ is the trace of $\bar{R}_{ij}$.

In Cartesian coordinates, when $\bar{\gamma} = 1$ and $\hat{\Gamma}^i_{jk} = 0$, the above equations reduce to the CCZ4 equations of [11], except that we have set their coefficients κ_3 to unity.

III. SPHERICAL SYMMETRY

A. The fCCZ4 equations

Under the assumption of spherical symmetry, the space-line element can be written in spherical coordinates (r, θ, φ) as

$$dl^2 = e^{4\phi}[a(r,t)dr^2 + r^2 b(r,t)d\Omega^2], \tag{3.1}$$

where $d\Omega^2 = d\theta^2 + \sin^2\theta d\varphi^2$ is the solid angle element and $a(r,t)$ and $b(r,t)$ are the metric functions. Since the evolution equations for the conformally related metric and the conformal factor, Eqs. (2.12) and (2.14), take the exact form as their counterparts in the BSSN formulation, their spherically symmetric versions also remain unchanged

$$\partial_t X = \beta^r\partial_r X - \frac{1}{3}X\sigma\bar{\mathcal{D}}_m\beta^m + \frac{1}{3}X\alpha K, \tag{3.2}$$

$$\partial_t a = \beta^r\partial_r a + 2a\partial_r\beta^r - \frac{2}{3}\sigma a\bar{\mathcal{D}}_m\beta^m - 2\alpha a A_a, \tag{3.3}$$

$$\partial_t b = \beta^r\partial_r b + 2b\frac{\beta^r}{r} - \frac{2}{3}\sigma b\bar{\mathcal{D}}_m\beta^m - 2\alpha b A_b, \tag{3.4}$$

(see [27] for the BSSN system in spherical symmetry). Here $X \equiv e^{-2\phi}$ and $\sigma = 1$ to impose the Lagrangian condition (2.6) on the time evolution of the determinant of the conformal metric. The covariant derivative of the shift vector can be written as

$$\bar{\mathcal{D}}_m\beta^m = \partial_r\beta^r + \beta^r\left(\frac{\partial_r(ab^2)}{2ab^2} + \frac{2}{r}\right), \tag{3.5}$$

and we have defined

$$A_a \equiv \bar{A}^r_r, \qquad A_b \equiv \bar{A}^\theta_\theta. \tag{3.6}$$

Note that the quantity X is evolved in Eq. (3.2) instead of the conformal factor ϕ itself.

The evolution equation for the trace of the extrinsic curvature K is

$$\partial_t K = -\mathcal{D}^2\alpha + \alpha(R + 2\mathcal{D}_m Z^m + K^2 - 2\Theta K) + \beta^r\partial_r K - 3\alpha\kappa_1(1+\kappa_2)\Theta + 4\pi\alpha(S_a + 2S_b - 3E), \tag{3.7}$$

while for Θ we have

$$\partial_t\Theta = \frac{1}{2}\alpha\left(R + 2\mathcal{D}_m Z^m - (A_a^2 + 2A_b^2) + \frac{2}{3}K^2 - 2\Theta K\right) + \beta^r\partial_r\Theta - Z^r\partial_r\alpha - \alpha\kappa_1(2+\kappa_2)\Theta - 8\pi\alpha E. \tag{3.8}$$

Here we defined $S_a \equiv S^r_r$ and $S_b \equiv S^\theta_\theta$. The divergence of the Z_i vector with respect to the physical metric is

$$\mathcal{D}_m Z^m = \partial_r Z^r + Z^r\left(\frac{\partial_r(ab^2)}{2ab^2} + \frac{2}{r} + 6\partial_r\phi\right). \tag{3.9}$$

In spherical symmetry, the evolution equation (2.13) for the independent component of the traceless part of the conformal extrinsic curvature, A_a, reduces to

$$\partial_t A_a = \beta^r \partial_r A_a - \left(\mathcal{D}^r \mathcal{D}_r \alpha - \frac{1}{3}\mathcal{D}^2\alpha\right) + \alpha\left(R^r_r - \frac{1}{3}R\right) + \alpha\left(2\mathcal{D}_r Z^r - \frac{2}{3}\mathcal{D}_m Z^m\right) + \alpha A_a(K - 2\Theta) - 16\pi\alpha(S_a - S_b), \tag{3.10}$$

where R^r_r is the mixed radial component of the physical, spatial Ricci tensor. The covariant derivative of the Z_r is

$$\mathcal{D}_r Z^r = \left[\partial_r Z^r + Z^r\left(\frac{\partial_r a}{2a} + 2\partial_r\phi\right)\right]. \tag{3.11}$$

From the definition (2.18) we have

$$\tilde{\Lambda}^r \equiv \bar{\Lambda}^r + \frac{2}{a}Z_r, \tag{3.12}$$

where

$$\bar{\Lambda}^r = \frac{1}{a}\left[\frac{\partial_r a}{2a} - \frac{\partial_r b}{b} - \frac{2}{r}\left(1 - \frac{a}{b}\right)\right]. \tag{3.13}$$

The evolution equation for $\tilde{\Delta}^r$ in spherical symmetry can then be derived from Eq. (2.17),

$$\begin{aligned}\partial_t \tilde{\Lambda}^r = {}& \beta^r \partial_r \tilde{\Lambda}^r - \bar{\Lambda}^r \partial_r \beta^r + \frac{1}{a}\partial_r^2 \beta^r + \frac{2}{b}\partial_r\left(\frac{\beta^r}{r}\right) \\ & + \frac{\sigma}{3}\left(\frac{1}{a}\partial_r(\bar{\mathcal{D}}_m \beta^m) + 2\bar{\Lambda}^r \bar{\mathcal{D}}_m \beta^m\right) - \frac{2}{a}(A_a \partial_r \alpha + \alpha \partial A_a) \\ & + 2\alpha\left(A_a \bar{\Lambda}^r - \frac{2}{rb}(A_a - A_b)\right) + \frac{2\alpha}{a}\left[\partial_r A_a \frac{2}{3}\partial_r K \right. \\ & \left. + 6A_a \partial_r \phi + (A_a - A_b)\left(\frac{2}{r} + \frac{\partial_r b}{b}\right) - 8\pi S_r\right] \\ & + \frac{2}{a}\left(\alpha \partial_r \Theta - \Theta \partial_r \alpha - \frac{2}{3}\alpha K Z_r\right) \\ & + \frac{2}{a}\left(\frac{2}{3}Z_r \bar{\mathcal{D}}_m \beta^m - Z_r \partial_r \beta^r\right) - \frac{2}{a}\kappa_1 Z_r. \end{aligned} \tag{3.14}$$

The Hamiltonian and momentum constraints are given by the following two equations that we compute to monitor the accuracy of the numerical evolutions:

$$\mathcal{H} \equiv R - (A_a^2 + 2A_b^2) + \frac{2}{3}K^2 - 16\pi E = 0, \tag{3.15}$$

$$\mathcal{M}^r \equiv \partial_r A_a - \frac{2}{3}\partial_r K + 6A_a \partial_r \phi + (A_a - A_b)\left(\frac{2}{r} + \frac{\partial_r b}{b}\right) - 8\pi S_r = 0. \tag{3.16}$$

The gauge condition for the lapse and the shift are the same as in Eqs. (2.25)–(2.27), but taking only the radial component for the shift and the vector B^i and replacing $\tilde{\Lambda}^i$ by $\tilde{\Lambda}^r$ as in the evolution equation (3.14).

B. Hydrodynamics

The general relativistic hydrodynamics equations, expressed through the conservation equation for the stress-energy tensor $T^{\mu\nu}$ and the continuity equation, are

$$\nabla_\mu T^{\mu\nu} = 0, \qquad \nabla_\mu(\rho u^\mu) = 0, \tag{3.17}$$

where ρ is the rest-mass density and u^μ the four velocity of the fluid. Following [28], we write the equations of general relativistic hydrodynamics in a conservative form in spherical symmetry. We define the fluid three velocity as seen by a normal observer as

$$v^r \equiv \frac{u^r}{\alpha u^t} + \frac{\beta^r}{\alpha} \tag{3.18}$$

and the Lorentz factor between the fluid and the normal observer as

$$W \equiv \alpha u^t. \tag{3.19}$$

We also define the fluid density, momentum density, and energy density, all as observed by a normal observer, as

$$D = \rho W, \tag{3.20}$$

$$S_r = \rho h W^2 v_r, \tag{3.21}$$

$$\tau = \rho h W^2 - P - D, \tag{3.22}$$

where h is the specific enthalpy and P the pressure. We then assemble these variables into a vector $\mathbf{U}$ of conserved fluid variables

$$\mathbf{U} = \sqrt{\gamma}(D, S_r, \tau). \tag{3.23}$$

Defining corresponding fluxes, $\mathbf{F}^r$, as

$$\begin{aligned}\mathbf{F}^r = \sqrt{-g}[&D(v^r - \beta^r/\alpha), \\ &S_r(v^r - \beta^r/\alpha) + P, \\ &\tau(v^r - \beta^r/\alpha) + P v^r],\end{aligned} \tag{3.24}$$

we can cast the equations of hydrodynamics (3.17) in conservative form

$$\partial_t \mathbf{U} + \partial_r \mathbf{F}^r = \mathbf{S}. \tag{3.25}$$

Here $\mathbf{S}$ is a vector of source terms given by

$$\mathbf{S} = \sqrt{-g}\Big[0, T^{00}\Big(\frac{1}{2}(\beta^r)^2\partial_r\gamma_{rr} - \alpha\partial_r\alpha\Big) + T^{0r}\beta^r\partial_r\gamma_{rr} + T^0_r\partial_r\beta^r\frac{1}{2}T^{rr}\partial_r\gamma_{rr}, (T^{00}\beta^r + T^{0r})(\beta^r K_{rr} - \partial_r\alpha) + T^{rr}K_{rr}\Big]. \quad (3.26)$$

To close the system of equations, we choose a Gamma-law equation of state

$$P = (\Gamma - 1)\rho\epsilon, \quad (3.27)$$

where Γ is the adiabatic index and ϵ is the specific internal energy.

IV. NUMERICAL IMPLEMENTATION

A. PIRK method

We have implemented the fCCZ4 system under the assumption of spherical symmetry in the one-dimensional code described in Montero and Cordero-Carrión [23]. This code solves the Einstein equations coupled to the general relativistic hydrodynamics equations. The Einstein equations are solved using either the BSSN or the fCCZ4 formalisms. We employ a second-order PIRK method to integrate the evolution equations in time. Writing a system of PDEs as follows

$$\begin{cases} u_t = \mathcal{L}_1(u, v), \\ v_t = \mathcal{L}_2(u) + \mathcal{L}_3(u, v), \end{cases} \quad (4.1)$$

where $\mathcal{L}_1$, $\mathcal{L}_2$, and $\mathcal{L}_3$ represent general nonlinear differential operators, the second-order PIRK method takes the following form:

$$\begin{cases} u^{(1)} = u^n + \Delta t L_1(u^n, v^n), \\ v^{(1)} = v^n + \Delta t\Big[\frac{1}{2}L_2(u^n) + \frac{1}{2}L_2(u^{(1)}) + L_3(u^n, v^n)\Big], \end{cases} \quad (4.2)$$

$$\begin{cases} u^{n+1} = \frac{1}{2}[u^n + u^{(1)} + \Delta t L_1(u^{(1)}, v^{(1)})], \\ v^{n+1} = v^n + \frac{\Delta t}{2}[L_2(u^n) + L_2(u^{n+1}) + L_3(u^n, v^n) \\ \qquad + L_3(u^{(1)}, v^{(1)})], \end{cases} \quad (4.3)$$

where we denote L_1, L_2, and L_3 as the corresponding discrete operators. In particular, we note that L_1 and L_3 are treated in an explicit way, whereas the L_2 operator contains the singular terms appearing in the sources of the equations and, therefore, is treated partially implicitly.

In the first stage, u is evolved explicitly; the updated value $u^{(1)}$ is used in the evaluation of the L_2 operator for the computation of $v^{(1)}$. Once all of the values of the first stage are obtained, u is evolved explicitly (using the values of the variables of the previous time step and previous stage), and the updated value u^{n+1} is used in the evaluation of the L_2 operator for the computation of v^{n+1}.

The precise evolution algorithm we use in the code is as follows:

(i) First, the hydrodynamic conserved quantities, the conformal metric components a and b, the conformal factor ϕ or the quantity X, the lapse function α, and the radial component of the shift vector β^r are evolved explicitly (as u is evolved in the previous PIRK scheme).

(ii) Second, the traceless part of the extrinsic curvature, A_a, the trace of the extrinsic curvature, K, and the projection of the four-vector Z^μ along the normal direction, Θ, are evolved partially implicitly, using updated values of α, a, b, and X.

(iii) Next, the quantity $\tilde{\Lambda}^r$ is evolved partially implicitly using the updated values of α, a, b, β^r, X, A_a, K, and Θ.

(iv) Finally, B^r is evolved partially implicitly using the updated values of $\tilde{\Lambda}^r$.

We note that the matter source terms are always included in the explicitly treated parts. In the Appendix, we give the exact form of the source terms included in each operator. We also note that the PIRK method has similarities with the implicit-explicit (IMEX) schemes (see, e.g., [29]), namely in treating some of the (stiff) unstable source terms as implicit. However, unlike IMEX schemes, the PIRK method does not require any analytical or numerical inversion of any operator to treat numerically unstable terms in the sources of the equations (see [30] for further details).

B. Numerics

The spatial domain for our computations is defined as $0 \le r \le L$, where L refers to the location of the outer boundary. We use a cell-centered grid to avoid the origin from coinciding with a grid point. At the origin, we impose boundary conditions derived from the assumption of spherical symmetry, while at the outer boundary, we impose Sommerfeld boundary conditions for the spacetime variables [8,23].

We compute derivatives in the spacetime evolution using a fourth-order centered finite difference approximation on a uniform grid except for the advection terms (i.e., terms of the form $\beta^r\partial_r u$), for which we adopt a fourth-order upwind scheme. We also use fourth-order Kreiss-Oliger dissipation [31] to avoid high-frequency noise appearing near the outer boundary.

For the equations of hydrodynamics, we implement a high-resolution shock-capturing scheme that consists of a second-order slope limiter reconstruction scheme [monotonized central (MC) limiter] to obtain the left and right states of the primitive variables at each cell interface and the Harten-Lax-van Leer-Einfeldt (HLLE) approximate

Riemann solver [32,33]. We add a low-density atmosphere to handle vacuum regions; more specifically, we treat the atmosphere as a perfect fluid with rest-mass density several orders of magnitude smaller than that of the bulk matter. Further details of our implementation can be found in [23].

V. NUMERICAL EXPERIMENTS

We now describe several numerical experiments with the fCCZ4 formalism. For each one we describe the initial data for the gravitational field and hydrodynamics quantities in the corresponding section; in addition, we always impose $\Theta = 0$ and $Z_r = 0$ at the initial time $t = 0$.

A. Pure gauge dynamics

We first consider the propagation of a pure gauge pulse. Following [23,27] we choose as initial data

$$\phi = A_a = A_b = K = \tilde{\Lambda}^r = 0, \tag{5.1}$$

$$a = b = 1, \tag{5.2}$$

$$\alpha = 1 + \frac{\alpha_0 r^2}{\lambda^2 + r^2}\left[e^{-(r-r_0)^2/\lambda^2} + e^{-(r+r_0)^2/\lambda^2}\right], \tag{5.3}$$

with $\alpha_0 = 0.01$ and $r_0 = 5\lambda$. The quantity λ is the length scale of the test. In this test, we employ zero shift and harmonic slicing. The slicing condition is suitably written for the fCCZ4 formulation by introducing the Θ variable in the evolution equation for the lapse function,

$$\partial_t \alpha = -\alpha^2 (K - 2\Theta). \tag{5.4}$$

We choose a grid resolution of $\Delta r = 0.1\lambda$ (except for the convergence test described at the end of this section) and a time step of $\Delta t = C\Delta r$, where C is the Courant factor. Among our first observations is that the fCCZ4 formalism requires a smaller Courant factor than the BSSN formalism, confirming similar findings by [12]; we found stable evolution for $C = 0.3$ for fCCZ4 and $C = 0.5$ for BSSN.

In Fig. 1 we show the Hamiltonian constraint at four different times ($t/\lambda = 0, 5.1, 10.5, 15$) for evolutions performed with the BSSN and the fCCZ4 formulations. Following [10] and [12], we also compare different choices for the damping parameters $\kappa_1\lambda = \{0, 0.02, 0.07, 0.2\}$ and $\kappa_2 = \{-0.5, 0.5\}$ for the fCCZ4 system, although the results for κ_2 are not shown in the figure for clarity. For the BSSN system, the violations of the Hamiltonian constraint settle down to approximately 10^{-3} close to the origin at $r = 0$ and do not decrease with time after that (recall that we do not employ any regularization scheme at the origin). As shown in Fig. 1, the behavior for the fCCZ4 system is different. Here, the constraint violations propagate toward the outer boundary; close to the origin, the constraint violations end up being approximately 3 order of magnitude smaller than for the BSSN system. We also note that the constraint violations decrease with increasing values of the damping parameter κ_1. However, one should handle this parameter with precaution, as we observed that

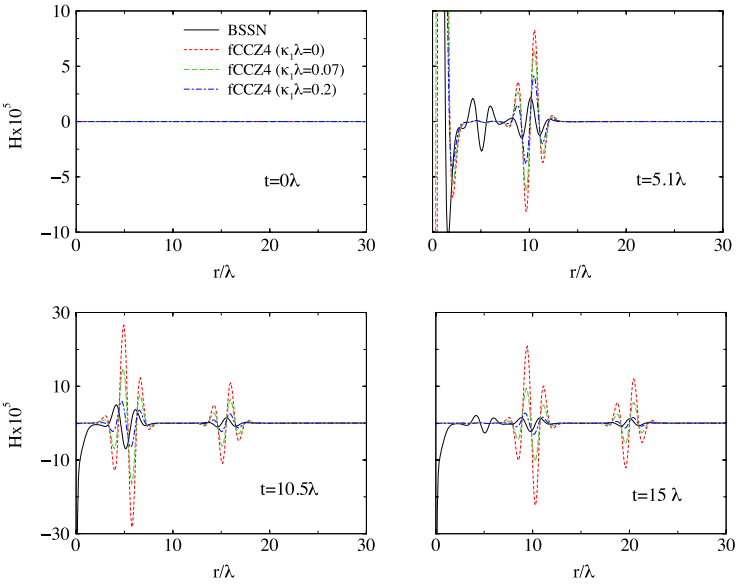

FIG. 1 (color online). Hamiltonian constraint violation for a pure gauge pulse test as a function of radius at four different times for both BSSN (solid line) and fCCZ4 (dashed lines).

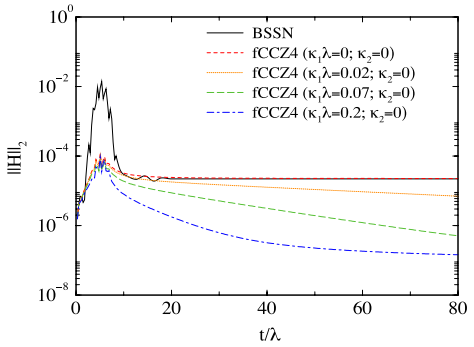

FIG. 2 (color online). L2 norm of the Hamiltonian constraint for a pure gauge pulse test for BSSN (solid line) and fCCZ4 (dashed and dotted lines) as a function of time and for different choices of the damping parameters.

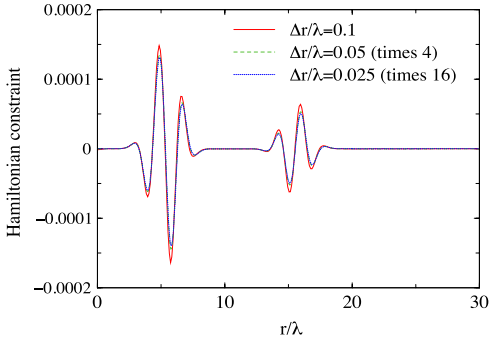

FIG. 3 (color online). Pure gauge pulse: Hamiltonian constraint violations at $t = 10.5\lambda$ for three different resolutions $\Delta r/\lambda = \{0.1, 0.05, 0.025\}$, rescaled by the factors corresponding to second-order convergence.

taking larger values for κ_1 (e.g., $\kappa_1/\lambda = 5$) reduces the propagation of the Hamiltonian constraint violation considerably and leads to overdamping effects: a "pulse" remains near the origin.

In Fig. 2 we plot the L2 norm, which is normalized by the total number of grid points of the Hamiltonian constraint for BSSN and fCCZ4 as a function of time for different values of the parameter κ_1. The largest violations occur at $t \sim 5\lambda$ when the ingoing pulse reaches the origin and reflects (see Fig. 1). For any value of the damping parameters the L2 norm of the Hamiltonian constraint is 2 orders of magnitude smaller for fCCZ4 than for BSSN at the same time.

At times $t > 5\lambda$, different choices of the damping parameters lead to a different evolution of the L2 norm. The undamped fCCZ4 system ($\kappa_1 = \kappa_2 = 0$) does not show any improvement in the constraint violation with respect to BSSN. Increasing κ_1 while keeping $\kappa_2 = 0$, we obtain constraint violations which are 1 to 3 orders of magnitude smaller than with BSSN. Choosing $\kappa_2 = 0.5$ and $\kappa_1\lambda = 0.07$ further improves the results. With $\kappa_2 = -0.5$ and $\kappa_1\lambda = 0.07$, we find a larger violation of the constraint than with $\kappa_2 = \{0.5, 0\}$ (not shown for clarity). Overall, we find that these results for the κ_2 parameter are similar to those reported by [12] for simulations of binary neutron stars.

We also performed three simulations with different resolutions $\Delta r/\lambda = \{0.1, 0.05, 0.025\}$ to test the convergence of the code. We show in Fig. 3 the rescaled Hamiltonian constraint at $t = 10.5\lambda$ for the particular choice of damping parameters $\kappa_1\lambda = 0.07$ and $\kappa_2 = 0$, demonstrating that the expected second-order convergence of our PIRK time-evolution scheme is achieved.

B. Schwarzschild black hole

We next evolve a single Schwarzschild black hole given by wormhole initial data and follow the coordinate evolution to the trumpet geometry. We show that we are able to evolve spacetimes containing singularities without breaking the original covariance of the Z4 formulation. We use the gauge conditions given by Eqs. (2.25)–(2.27), for which the evolution settles down to a maximally sliced trumpet [26,34]. The computational domain has a resolution of $\Delta r = 0.025M$, $\Delta t = 0.5\Delta r$, and we use $N_r = 60,000$ grid points to place the outer boundary sufficiently far away from the "puncture" at $r = 0$.

In Fig. 4, we plot the time evolution of the apparent horizon (AH) mass (defined as $M_{\rm AH} = \sqrt{\mathcal{A}/16\pi}$, where $\mathcal{A}$ is the proper area of the horizon) for BSSN and fCCZ4. The upper panel shows this quantity from the onset of the numerical simulation, while the lower panel shows the AH mass only during the stationary phase when the wormhole topology has settled to the trumpet topology. We neither display the AH mass for the fCCZ4 system with $\kappa_1 = \kappa_2 = 0$ nor with $\kappa_1 M = 0.02$, $\kappa_2 = 0$ because of the appearance of numerical instabilities (see Fig. 5). For higher values of κ_1 and κ_2, we obtain stable black hole evolutions. In these cases, the difference between the AH mass for BSSN and fCCZ4 is less than 0.005% at the end of the simulation ($t = 1875M$), while the error with respect to the initial ADM mass is ~0.7%. We note, however, that the black hole mass continues to drift for the fCCZ4 formulation, while it remains constant after an initial transition for the BSSN formulation. For the CCZ4 formulation, similar results for the BH mass were obtained by [12], who report errors in the range from 0.1% to 2.8%. In contrast, the error is smaller for the Z4c formulation, around 0.03% of the initial ADM mass (see also [12]).

In Fig. 5 we plot the L2 norm of the Hamiltonian constraint violations. The upper panel displays the L2-norm evolution in the whole computational domain, while in the lower panel, we plot the L2-norm evolution only in the region outside the AH. Clearly, the larger violation of the

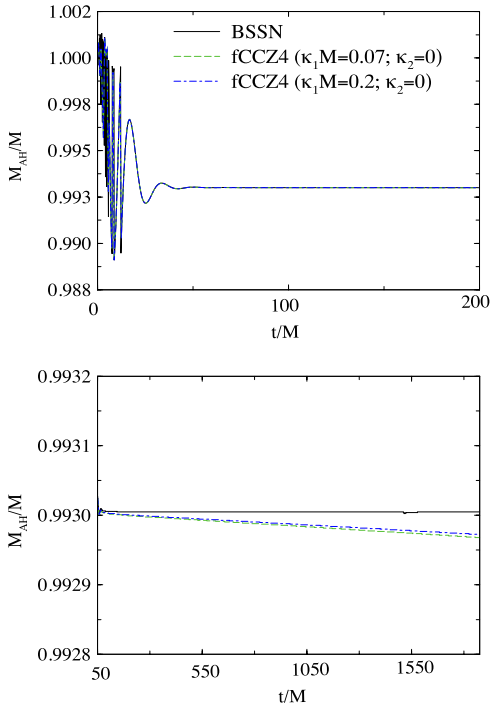

FIG. 4 (color online). Time evolution of the mass of the AH in the single puncture black hole simulation. The lower panel shows the evolution of the AH mass during the stationary phase.

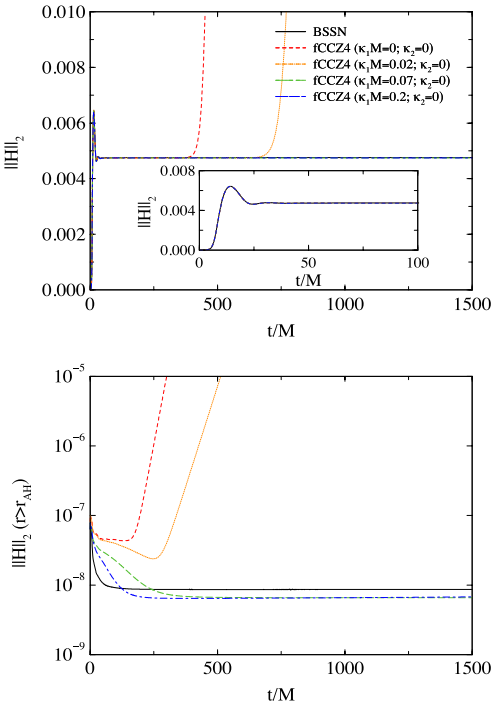

FIG. 5 (color online). (Upper panel) L2 norm of the Hamiltonian constraint in the single puncture black hole simulation. The inset shows a magnified view of the initial $100M$ in the evolution. (Lower panel) Same quantity but computed outside the AH.

Hamiltonian constraint takes place due to the finite differencing close to the puncture, for both formulations of the Einstein equations. However, the L2 norm of the Hamiltonian constraint violation computed outside the AH shows that there are some differences between the two formulations that also depend on the values for the damping coefficients. We observe that the numerical evolutions develop instabilities for $\kappa_2 = 0$ and $\kappa_1 M = (0, 0.02)$. Selecting $\kappa_1 M = 0.07$ and $\kappa_2 = 0.5$ leads to an overdamped behavior that is responsible for the exponential growth of the constraint violation at late times, while we obtain stable simulations with $\kappa_1 M = 0.07$ and $\kappa_2 = -0.5$ (not shown in the plots for clarity). We find that $\kappa_2 = 0$ with $\kappa_1 M = 0.07$ or $\kappa_1 M = 0.2$ gives the best results, leading to constraint violations that are comparable to those achieved with BSSN.

Our numerical experiments with black hole initial data indicate that choosing the damping parameter κ_2 different from zero does not help in reducing violations of the Hamiltonian constraint. We therefore choose $\kappa_2 = 0$ for the remainder of the paper.

C. Stable spherical relativistic star

In this section we turn to nonvacuum spacetimes and describe results for the coupled system formed by the Einstein equations and the equations of general relativistic hydrodynamics. We construct spherically symmetric initial data by solving the Tolman-Oppenheimer-Volkoff (TOV) equations for a polytropic equation of state

$$P = K\rho^{1+1/N}, \tag{5.5}$$

where K is the polytropic constant and N the polytropic index, and evolve these data with the Gamma-law equation of state (3.27) with $\Gamma = 1 + 1/N$. Throughout the remainder of the paper, we adopt $N = 1$. We also adopt code units in which $M_\odot = 1$; we then choose $K = 100$ in these units. In this section we consider a star with a central density of $\rho_c = 1.28 \times 10^{-3}$. Solving the TOV equations then results in star of gravitational mass $M = 1.4M_\odot$, baryon rest-mass $M_* = 1.5M_\odot$, and radius $R = 14.15$ km. We evolve these initial data with $N_r = 2000$ grid points and a grid resolution

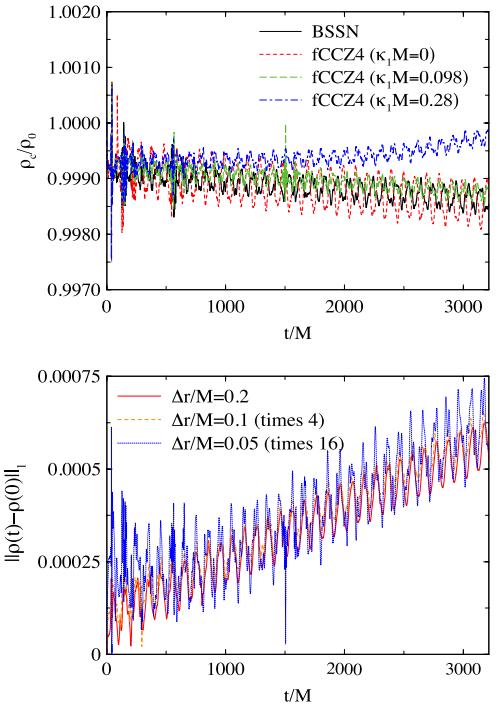

FIG. 6 (color online). (Upper panel) Time evolution of the normalized central density with fCCZ4 for different values of κ_1 and BSSN. (Lower panel) The L1 norm between the evolved rest-mass density and the initial density as a function of time, rescaled for three different resolutions $\Delta r = \{0.2, 0.1, 0.05\}$ for the fCCZ4 system.

of $\Delta r = 0.05$ (so that the interior of the star is covered by approximately 200 grid points) until a final time $t = 4500$ (corresponding to 45 light crossing times).

We investigate the effect of the damping parameter κ_1 during the time evolution of the TOV solution and explore the parameter space choosing $\kappa_1 = \{0, 0.07, 0.2\}$ in our code units or $\kappa_1 M = \{0, 0.098, 0.28\}$. In the upper panel of Fig. 6, we show the time evolution of the normalized central rest-mass density of the star. This figure shows the distinctive periodic radial oscillations which are triggered by finite-difference errors. These oscillations behave differently depending on the evolution formalism and the choices of the damping parameters in fCCZ4. We find that the amplitude of the oscillations is reduced when the damping parameter is increased (compare the red dashed line and the green dashed line). Choosing too large of a value, $\kappa_1 = 0.2$, causes overdamping effects which lead to a drift in the central rest-mass density and a growth in the L2 norm of the Hamiltonian constraint (see Fig. 7). For smaller values of $\kappa_1 M$ (i.e., $\kappa_1 M = 0$ or 0.098), the secular drift in the central

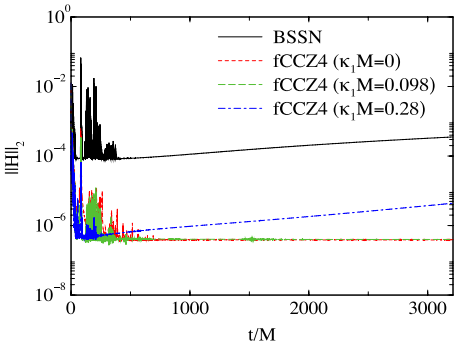

FIG. 7 (color online). Comparison of the time evolution of the L2 norm of the Hamiltonian constraint for the stable spherical relativistic star for BSSN (solid line) and fCCZ4 (dashed lines) with $\kappa_1 = \{0, 0.07, 0.2\}$ (in our code units).

density at late times is very similar for fCCZ4 and BSSN. We observe that the amplitude of the oscillations decreases slightly faster for the fCCZ4 system than for BSSN, indicating that BSSN has a slightly smaller numerical viscosity.

The Fourier transform of the time evolution of the central rest-mass density for the fCCZ4 formulation, with $\kappa_1 M = 0.098$, agrees well with the fundamental frequency and the radial normal mode frequencies obtained with linear perturbation techniques [35]. The relative error is less than 0.1% for the fundamental mode and less than 0.4% for the first three overtones.

We also performed a convergence test of the fCCZ4 implementation for the stable spherical star. In the lower panel of Fig. 6, we show three different curves corresponding to three different resolutions for the L1 norm of the difference between the evolved rest-mass density and the initial value of the density inside the star. These findings again demonstrate second-order convergence, as expected.

Finally, in Fig. 7, we plot the L2 norm of the Hamiltonian constraint, and we find that the constraint violations for fCCZ4 are several orders of magnitude (at least 2) smaller than for BSSN. The influence of the damping parameter $\kappa_1 M$ is not significant in the range $\{0, 0.098\}$, but for larger values, e.g., $\kappa_1 M = 0.28$, we find an exponential growth in the L2 norm. At a reference time $t = 3000$, the L2 norm is roughly 1 order of magnitude larger than with $\kappa_1 M = \{0, 0.098\}$ but still 2 orders of magnitude smaller than for BSSN.

D. Migration test

Our next test of fCCZ4 is the so-called migration test of an unstable relativistic star in hydrostatic equilibrium [35]. For this test we choose as initial data a TOV solution on the unstable branch, meaning with a density larger than that of the maximum mass configuration. Depending on the initial

perturbation, this unstable model may either collapse to a black hole or perform initially large oscillations about a stable TOV configuration with smaller central density. As in Sec. V C, we adopt $N = 1$ and $K = 100$ (in our code units), but we now choose a central rest-mass density of $\rho_c = 8 \times 10^{-3}$. The resulting star has a gravitational mass $M = 1.447$, a baryon rest-mass $M_* = 1.535$, and a radius $R = 8.62$ km. We evolve these data with $N_r = 2000$ grid points and a resolution $\Delta r = 0.025$.

In an ideal gas, the gravitational binding energy is gradually converted into internal energy via shock heating. Therefore, the high-amplitude oscillations around the new equilibrium configuration are damped, and the heated stable equilibrium model approaches a central density slightly smaller than the rest-mass density of a zero temperature star of the same rest mass ($\rho_c = 1.35 \times 10^{-3}$). This is shown in the upper panel of Fig. 8, which displays the evolution of the normalized central density. After the star has migrated to the stable branch, it undergoes a series of strong expansions and contractions around the new stable configuration. During the contraction phase, shock waves are formed inside the star. When these shock waves reach the surface, small amounts of mass are expelled from the object.

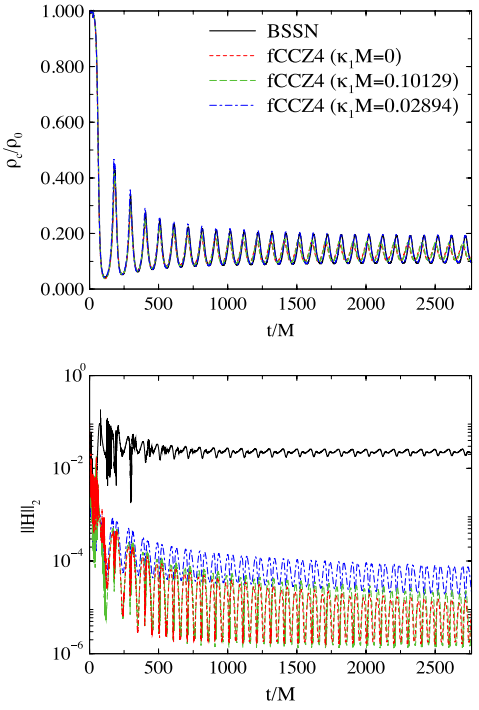

FIG. 8 (color online). Time evolution of the normalized central density (upper panel) and of the L2 norm of the Hamiltonian constraint (lower panel) for the migration test for both BSSN and fCCZ4 with $\kappa_1 = \{0, 0.07, 0.2\}$ (in our code units).

Taking $\kappa_1 = 0.2$, fCCZ4 and BSSN provide very similar results for the evolution of the central density. However, with $\kappa_1 = \{0, 0.07\}$ or $\kappa_1 M = \{0, 0.10129\}$, differences become visible at late times. The oscillations become more damped for these values of the damping parameter (slightly more for the undamped fCCZ4 with $\kappa_1 M = 0$), and a phase lag appears in the oscillations. Nevertheless, the differences are not significant. The lower panel of Fig. 8 shows that for the higher value of the damping parameter, the L2 norm of the Hamiltonian constraint is reduced by 2 orders of magnitude with respect to BSSN, while for the other values of $\kappa_1 M$, the reduction is approximately 3 orders of magnitude. Another difference between BSSN and fCCZ4 is that for the latter, the violations slightly decrease with time while they remain constant for BSSN. We take this as an indication that the numerical viscosity is slightly smaller in BSSN, consistent with our findings in Sec. V C. We obtain the smallest constraint violations for the smallest value of $\kappa_1 M$, but this value also leads to the strongest damping of the oscillations.

E. Gravitational collapse of a marginally stable neutron star

The last numerical experiment is the gravitational collapse of a marginally stable spherical relativistic star to a black hole. As before, we adopt a polytropic start with $K = 100$ and $N = 1$ as initial data, but we now consider a star with central rest-mass density $\rho_c = 3.15 \times 10^{-3}$. This initial model has a gravitational mass $M = 1.64$ and a baryon rest-mass $M_* = 1.77$. At $t = 0$ we artificially decrease the pressure by 0.5% in order to induce the collapse. We perform this test with a spatial resolution of $\Delta r = 0.0125$ and $N_r = 8000$, which places the outer boundary at $r_{\max} = 100$.

In Fig. 9, we plot the evolution of the normalized central density and the mass of the AH after it forms at a time $t_{\rm AH}$. We find that $t_{\rm AH}$ depends slightly on the formulation used and, for fCCZ4, on the coefficient $\kappa_1 M$: for BSSN, we found $t_{\rm AH} \sim 167$, while for fCCZ4 with $\kappa_1 M = 0$, we found $t_{\rm AH} \sim 177$ (all in our code units). Increasing $\kappa_1 M$ slightly reduces $t_{\rm AH}$, as shown in Fig. 9. This behavior is again consistent with our observations in Sec. V C and Sec. V D and suggests that the numerical viscosity of the BSSN scheme is slightly smaller than that of fCCZ4. It also suggests that the numerical viscosity of fCCZ4 decreases with increasing $\kappa_1 M$. For $\kappa_1 M = 0.82$ (not shown in Fig. 9), $t_{\rm AH}$ agrees well with that of BSSN, although this choice of $\kappa_1 M$ leads to nonnegligible overdamped results (an important drift for the black hole mass appears).

In the lower panel of Fig. 9 we show the horizon mass as a function of time, as obtained with the different evolution schemes. The difference between the initial ADM mass of the system and the mass of the AH at $t = 500$ for the BSSN formulation is about 0.5%. We find a slightly higher

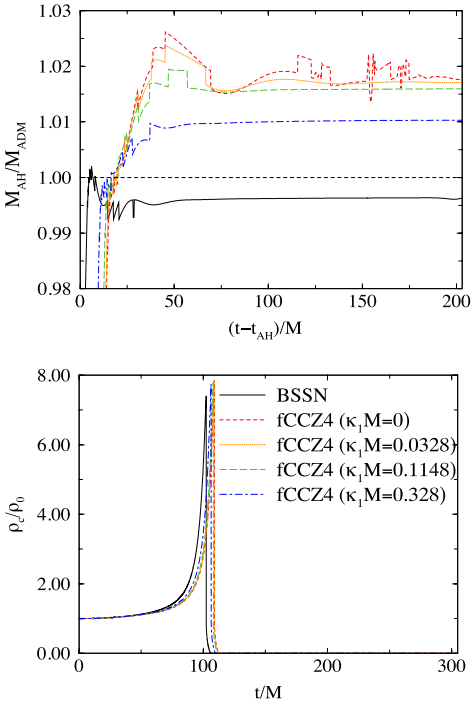

FIG. 9 (color online). Time evolution of the normalized central density (upper panel) and of the irreducible mass of the black hole (lower panel) for BSSN and fCCZ4 with $\kappa_1 = \{0, 0.02, 0.07, 0.2\}$ until $t = 500$ (in our code units).

deviation, around 1.6%–1.7% for fCCZ4 with $\kappa_1 M = \{0.0, 0.1148\}$ and 1% for $\kappa_1 M = 0.328$.

Finally, in Fig. 10 we show the L2 norm of the Hamiltonian constraint violation computed in the region

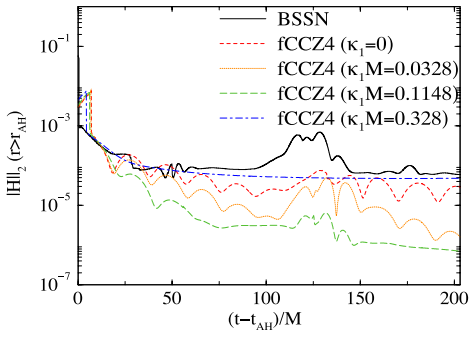

FIG. 10 (color online). Time evolution of the L2 norm of the Hamiltonian constraint for BSSN and fCCZ4 computed outside of the AH. The time coordinate is relative to the time $t_{AH} \sim 167$ when an apparent horizon forms for the BSSN formulation.

outside the AH. As expected, the constraint violations obtained with the fCCZ4 formulation are smaller than those obtained with the BSSN formulation. The difference in the constraint violations between the two formulations is at most 3 orders of magnitude when we take $\kappa_1 M = 0.1148$ (green dashed line in Fig. 10). Increasing the value of κ_1 does not reduce the L2 norm further. Instead, it increases again and approaches a value similar to that obtained with BSSN.

VI. SUMMARY

In this paper, we generalize the covariant and conformal Z4 system [9] of the Einstein equations originally proposed by Alic *et al.* [11] using a reference-metric approach [21] (see [18–20] for the derivation of the BSSN system using the same approach). The resulting system, which we refer to as fCCZ4, allows us to write the evolution equations in a fully covariant form suitable for curvilinear coordinate systems. As a first step, we implement the fCCZ4 system in spherical coordinates under the assumption of spherical symmetry. We adopt a PIRK scheme for the time evolution and obtain stable evolutions— without regularization of the equations—for both vacuum and nonvacuum spacetimes.

The CC4Z formalism of [11,12] shares some properties with a similar approach, Z4c, developed by [10]. In agreement with [11,12], we find that using Sommerfeld outer boundary conditions is as accurate as it is for the BSSN system. Unlike in the Z4c formalism, we therefore find stable evolutions even without implementing constraint-preserving boundary conditions [36]. Unlike reported in [11], we did not need to introduce a third parameter κ_3 in order to obtain stable evolutions for black hole spacetimes (see [12] for an alternative modification of the equations).

We performed a number of tests to compare the accuracy of the fCCZ4 formulation with that of the BSSN system. As in previous experiments with Z4c and CCZ4, we find that constraint violations in neutron-star spacetimes are significantly smaller in fCCZ4 than in BSSN, often by 2 or 3 orders of magnitude. We find similar improvements for the pure gauge-wave test. This test also demonstrates that fCCZ4 can reduce errors introduced by the coordinate singularities in spherical polar coordinates, even though this effect was less visible in our other simulations. We note, however, that these results depend on the choices for the free parameters κ_1 and κ_2. Poor choices may introduce overdamping, thereby increasing errors, or may make the code unstable. We also note that our findings suggest that the fCCZ4 scheme introduces a slightly larger numerical viscosity than the BSSN scheme.

For black hole spacetimes, we find that, even for the best choices for the free parameters, fCCZ4 reduces the constraint violations only very moderately and only at late times. At least for the resolutions that we employed in our

tests, BSSN was slightly more accurate in computing the black hole mass (compare [10,11]).

We found that choosing κ_2 different from zero did not lead to significant improvements; in fact, poor choices may lead to overdamping effects. On the other hand, the damping parameter κ_1 plays an important role in the reduction of the violations of the constraints. Increasing the value of this parameter tends to reduce constraint violations (except in the migration test) but may also introduce a damping that is too large, thereby making the code unstable and causing it to crash. For all examples considered in this paper, we have been able to find suitable choices for κ_1, but for more general applications, it may be difficult to identify an optimal choice for this parameter. Since κ_1 has units of inverse length, its optimal choice depends on typical length scales in the simulation. For a single black hole, for example, a good choice appears to be $\kappa_1 \simeq 0.07/M$. In simulations of black hole binaries with unequal masses, on the other hand, it may be hard to find a single parameter κ_1 that is well suited for both black holes. Similar issues may arise in other mixed systems, e.g., black hole-neutron star binaries or black holes surrounded by accretion disks. An optimal choice of κ_1 for the matter component, for example, might lead to overdamping for the black hole. Should this issue indeed prove to be a problem, a possible solution might be to allow κ_1 to take different values in different regions of the spacetime.

In a future project, we implement the fCCZ4 formalism in three spatial dimensions without any symmetry assumptions, and we plan to explore the issues discussed above with that code.

ACKNOWLEDGMENTS

N. S. G. thanks the Max-Planck-Institut für Astrophysik for its hospitality during the development of part of this project. P M. thanks Sebastiano Bernuzzi and David Hilditch for helpful discussions. T. W. B. gratefully acknowledges support from the Alexander-von-Humboldt Foundation. This work was supported in part by the Spanish MICINN (AYA 2010-21097-C03-01), by the Generalitat Valenciana (PROMETEO-2009-103), by the Deutsche Forschungsgesellschaft (DFG) through its Transregional Center SFB/TR 7 "Gravitational Wave Astronomy," and by NSF grant PHY-1063240 to Bowdoin College.

APPENDIX: DETAILED SOURCE TERMS INCLUDED IN THE PIRK OPERATORS FOR THE EVOLUTION EQUATIONS

The evolution equations (3.2)–(3.4), (3.7), (3.8), (3.10), (3.14), and ((2.25)–(2.27) are evolved using a second-order PIRK method, described in Sec. III. In this Appendix, we provide a complete listing of the source terms included in the explicit or partially implicit operators.

First, the hydrodynamic conserved quantities and the spacetime fields a, b, X, α, and β^r are evolved explicitly; i.e., all of the source terms of the evolution equations of these variables are included in the L_1 operator of the second-order PIRK method.

Second, A_a, K, and Θ are evolved partially implicitly, using updated values of α, a, and b; more specifically, the corresponding L_2 and L_3 operators associated with the evolution equations for A_a, K, and Θ are

$$L_{2(A_a)} = -\left(\nabla^r\nabla_r\alpha - \frac{1}{3}\nabla^2\alpha\right) + \alpha\left(R^r_r - \frac{1}{3}R\right) + \alpha\left(\mathcal{D}^r Z_r + \mathcal{D}_r Z^r - \frac{2}{3}\mathcal{D}_m Z^m\right), \tag{A1}$$

$$L_{3(A_a)} = \alpha(K - 2\Theta)A_a - 16\pi\alpha(S_a - S_b) + \beta^r\partial_r A_a, \tag{A2}$$

$$L_{2(K)} = -\mathcal{D}^2\alpha + \alpha(R + 2\mathcal{D}_m Z^m), \tag{A3}$$

$$L_{3(K)} = \beta^r\partial_r K + \alpha(K^2 - 2\Theta K) - 3\alpha\kappa_1(1+\kappa_2)\Theta + 4\pi\alpha(S_a + 2S_b - 3E), \tag{A4}$$

$$L_{2(\Theta)} = -Z^r\partial_r\alpha + \frac{1}{2}\alpha(R + 2\mathcal{D}_m Z^m), \tag{A5}$$

$$L_{3(\Theta)} = \beta^r\partial_r\Theta + \frac{1}{2}\alpha\left(A_a^2 + 2A_b^2 + \frac{2}{3}K^2 - 2\Theta K\right) - \alpha\kappa_1(2+\kappa_2)\Theta - 8\pi\alpha E. \tag{A6}$$

Next, $\tilde{\Lambda}^r$ is evolved partially implicitly, using updated values of α, a, b, β^r, ϕ, A_a, K, and Θ; more specifically, the corresponding L_2 and L_3 operators associated with the evolution equation for $\tilde{\Lambda}^r$ are

$$\begin{aligned} L_{2(\tilde{\Lambda}^r)} =& \frac{1}{a}\partial_r^2\beta^r + \frac{2}{b}\partial_r\left(\frac{\beta^r}{r}\right) + \frac{\sigma}{3a}\partial_r(\hat{\nabla}_m\beta^m) \\ & - \frac{2}{a}(A_a\partial_r\alpha + \alpha\partial_r A_a) - \frac{4\alpha}{rb}(A_a - A_b) \\ & + \frac{2\alpha}{a}\left[\partial_r A_a - \frac{2}{3}\partial_r K + 6A_a\partial_r\chi + (A_a - A_b)\left(\frac{2}{r} + \frac{\partial_r b}{b}\right)\right] \\ & + 2\alpha A_a\tilde{\Lambda}^r - \tilde{\Lambda}^r\partial_r\beta^r + \frac{2\sigma}{3}\tilde{\Lambda}^r\hat{\nabla}_m\beta^m \\ & + \frac{2}{a}\left(\alpha\partial_r\Theta - \Theta\partial_r\alpha - \frac{2}{3}\alpha K Z_r\right) \\ & + \frac{2}{a}\left(\frac{2}{3}Z_r\tilde{D}_m\beta^m - Z_r\partial_r\beta^r\right) - \frac{2}{a}\kappa_1 Z_r, \end{aligned} \tag{A7}$$

$$L_{3(\tilde{\Lambda}^r)} = \beta^r\partial_r\tilde{\Lambda}^r - 8\pi j_r\frac{\xi\alpha}{a}. \tag{A8}$$

Finally, B^r is evolved partially implicitly, using updated values of $\tilde{\Lambda}^r$; i.e., $L_{2(B^r)} = \frac{3}{4}\partial_t\tilde{\Lambda}^r$ and $L_{3(B^r)} = 0$.

[1] G. M. Harry, Classical Quantum Gravity **27**, 084006 (2010).
[2] Virgo Collaboration, Advanced Virgo Baseline Design, Report No. VIR-0027A-09 2009; available from https://pub3.ego-gw.it/itf/tds/.
[3] Y. Aso, Y. Michimura, K. Somiya, M. Ando, O. Miyakawa, T. Sekiguchi, D. Tatsumi, and H. Yamamoto (KAGRA Collaboration), Phys. Rev. D **88**, 043007 (2013).
[4] T. Nakamura, K. Oohara, and Y. Kojima, Prog. Theor. Phys. Suppl. **90**, 1 (1987).
[5] M. Shibata and T. Nakamura, Phys. Rev. D **52**, 5428 (1995).
[6] T. W. Baumgarte and S. L. Shapiro, Phys. Rev. D **59**, 024007 (1998).
[7] C. Bona, J. Massó, E. Seidel, and J. Stela, Phys. Rev. D **56**, 3405 (1997).
[8] M. Alcubierre, B. Brügmann, P. Diener, M. Koppitz, D. Pollney, E. Seidel, and R. Takahashi, Phys. Rev. D **67**, 084023 (2003).
[9] C. Bona, T. Ledvinka, C. Palenzuela, and M. Zacek, Phys. Rev. D **67**, 104005 (2003).
[10] S. Bernuzzi and D. Hilditch, Phys. Rev. D **81**, 084003 (2010).
[11] D. Alic, C. Bona-Casas, C. Bona, L. Rezzolla, and C. Palenzuela, Phys. Rev. D **85**, 064040 (2012).
[12] D. Alic, W. Kastaun and L. Rezzolla, Phys. Rev. D **88**, 064049 (2013).
[13] C. Gundlach, J. M. Martin-Garcia, G. Calabrese, and I. Hinder, Classical Quantum Gravity **22**, 3767 (2005).
[14] M. Ruiz, D. Hilditch, and S. Bernuzzi, Phys. Rev. D **83**, 024025 (2011).
[15] A. Weyhausen, S. Bernuzzi, and D. Hilditch, Phys. Rev. D **85**, 024038 (2012).
[16] D. Hilditch, S. Bernuzzi, M. Thierfelder, Z. Cao, W. Tichy, and B. Brügmann, Phys. Rev. D **88**, 084057 (2013).
[17] W. Kastaun, F. Galeazzi, D. Alic, L. Rezzolla, and J. A. Font, Phys. Rev. D **88**, 021501 (2013).
[18] E. Gourgoulhon, arXiv:gr-qc/0703035.
[19] J. D. Brown, Phys. Rev. D **79**, 104029 (2009).
[20] E. Gourgoulhon, *3+1 Formalism in General Relativity* (Springer-Verlag, Berlin, Heidelberg, 2012).
[21] S. Bonazzola, E. Gourgoulhon, P. Grandclément, and J. Novak, Phys. Rev. D **70**, 104007 (2004).
[22] I. Cordero-Carrión, P. Cerdá-Durán, and J. M. Ibáñez, Phys. Rev. D **85**, 044023 (2012).
[23] P. J. Montero and I. Cordero-Carrión, Phys. Rev. D **85**, 124037/1 (2012).
[24] T. W. Baumgarte, P. J. Montero, I. Cordero-Carrión, and E. Müller, Phys. Rev. D **87**, 044026 (2013).
[25] P. J. Montero, T. W. Baumgarte, and E. Müller, Phys. Rev. D **89**, 084043 (2014).
[26] M. Hannam, S. Husa, N. Ó. Murchadha, B. Brügmann, J. A. González, and U. Sperhake, J. Phys. Conf. Ser. **66**, 012047 (2007).
[27] M. Alcubierre and M. D. Mendez, Gen. Relativ. Gravit. **43**, 2769 (2011).
[28] F. Banyuls, J. A. Font, J. M. Ibánez, J. M. Martí, and J. A. Miralles, Astrophys. J. **476**, 221 (1997).
[29] L. Pareschi and G. Russo, J. Sci. Comput. **25**, 129 (2005).
[30] I. Cordero-Carrión and P. Cerdá-Durán, arXiv:1211.5930.
[31] H.-O. Kreiss and J. Oliger, in *Methods for the Approximate Solution of the Time Dependent Problems*, edited by Global Atmospheric Research Programme publications series (International Council of Scientific Unions, World Meteorological Organization, Geneva, 1973).
[32] A. Harten, P. D. Lax, and B. van Leer, SIAM Rev. **25**, 35 (1983).
[33] B. Einfeldt, SIAM J. Numer. Anal. **25**, 294 (1988).
[34] T. W. Baumgarte and S. G. Naculich, Phys. Rev. D **75**, 067502 (2007).
[35] J. A. Font, T. Goodale, S. Iyer, M. Miller, L. Rezzolla, E. Seidel, N. Stergioulas, W. Suen, and M. Tobias, Phys. Rev. D **65**, 084024 (2002).
[36] M. Ruiz, D. Hilditch, and S. Bernuzzi, Phys. Rev. D **83**, 024025 (2011).

PHYSICAL REVIEW D **91,** 043005 (2015)

Quasistationary solutions of self-gravitating scalar fields around black holes

Nicolas Sanchis-Gual,[1] Juan Carlos Degollado,[2] Pedro J. Montero,[3] and José A. Font[1,4]

[1]*Departamento de Astronomía y Astrofísica, Universitat de València, Dr. Moliner 50, 46100 Burjassot (València), Spain*

[2]*Departamento de Ciencias Computacionales, Centro Universitario de Ciencias Exactas e Ingeniería, Universidad de Guadalajara, Avenida Revolución 1500, Colonia Olímpica C.P. 44430, Guadalajara, Jalisco, Mexico*

[3]*Max-Planck-Institute für Astrophysik, Karl-Schwarzschild-Strasse 1, 85748 Garching bei München, Germany*

[4]*Observatori Astronòmic, Universitat de València, C/Catedrático José Beltrán 2, 46980 Paterna (València), Spain*

(Received 29 December 2014; published 23 February 2015)

Recent perturbative studies have shown the existence of long-lived, quasistationary configurations of scalar fields around black holes. In particular, such configurations have been found to survive for cosmological time scales, which is a requirement for viable dark matter halo models in galaxies based on such types of structures. In this paper we perform a series of numerical relativity simulations of dynamical nonrotating black holes surrounded by self-gravitating scalar fields. We solve numerically the coupled system of equations formed by the Einstein and the Klein-Gordon equations under the assumption of spherical symmetry using spherical coordinates. Our results confirm the existence of oscillating, long-lived, self-gravitating scalar field configurations around nonrotating black holes in highly dynamical spacetimes with a rich scalar field environment. Our numerical simulations are long-term stable and allow for the extraction of the resonant frequencies to make a direct comparison with results obtained in the linearized regime. A by-product of our simulations is the existence of a degeneracy in plausible long-lived solutions of Einstein equations that would induce the same motion of test particles, either with or without the existence of quasibound states.

DOI: 10.1103/PhysRevD.91.043005 PACS numbers: 95.30.Sf, 04.70.Bw, 04.25.dg

I. INTRODUCTION

Scalar fields play an important role in different areas of theoretical physics. For instance, recent models for the evolution of the Universe, dark energy, and string theory require the existence of ultralight scalar degrees of freedom [1–3]. In a cosmological context, scalar fields have been suggested as the constituents of dark matter halos in galaxies [4–9]. There is large observational evidence that points to the presence of supermassive black holes in the centers of most nearby galaxies. Furthermore, the evolution of these black holes is directly connected to their host galaxy evolution [10]. It has been suggested that in order to consider scalar fields as plausible candidates for dark matter halos they must survive for cosmological time scales in the presence of black holes [11].

There are several studies in the literature investigating the dynamics of scalar fields around black holes within the linearized regime, i.e., in the test field regime in which the black hole spacetime is taken as a background where the scalar field evolves [12–16]. One of the key results of linearized studies concerning massive scalar fields surrounding stationary black holes is that as a result of the presence of a potential well due to the mass term, two types of modes are possible depending on the boundary conditions at infinity: non-normalizable quasinormal modes and quasibound states, which decay at infinity and thus are localized around the black hole. If the black hole is spinning the latter class can yield exponentially growing modes [17–21] and lead to hairy black hole solutions [22].

Quasibound states are scalar field configurations around black holes that may be very long lived [14]. Many of their characteristics can be derived in the test field approximation. For instance, it is possible to determine their complex frequency by imposing ingoing boundary conditions at the black hole horizon and an asymptotic decay behavior at infinity. The problem of obtaining the frequencies of the quasibound states reduces to an eigenvalue problem which can be solved in several efficient ways (see, e.g., Refs. [23,24]). The real part represents the oscillation frequency, and the imaginary part gives their rate of decay or the growth rate, if a mode is superradiantly unstable.

While the test field approximation is valid as long as the energy content of the field is small it will break down eventually as the energy increases. At some point, the backreaction of the scalar field onto the spacetime dynamics becomes non-negligible and nonlinear simulations of self-gravitating scalar field configurations are necessary. There are recent studies in this direction [25,26]. In Ref. [26] a fully 3D evolution of scalar fields around black holes was performed. In such work the authors made a

thorough study of scalar field configurations around stationary and rotating black holes finding quasibound states when the amount of scalar field contributes to some fraction of the mass of the black hole. Here we focus on the cases in which the mass of the scalar field cloud may be *greater* than the mass of the black hole and therefore constitutes a strong deviation from the linearized regime. Stated in a different way, our setup involves a large scalar field environment in a highly dynamical spacetime. These scenarios may be framed as the final stage of a violent process such as the bosenova explosion [27] or as a Kerr hairy solution in which the black hole has lost its spin. Notice, however, that there are some recent works in which the test field regime is suitable to investigate realistic parameters for the scalar field configuration [28,29].

The use of spherical symmetry allows us to follow accurately the evolution of the system and describe the development of a single mode without interference effects from other modes. Furthermore, the significantly long runs we can afford ($t \sim 10^5 M$, where M is the bare mass of the black hole) allow us to obtain very precise figures for the frequencies of the bound states. A comment on orders of magnitude becomes necessary at this point as it should be noted that the frequency of the quasibound states for very small values of the scalar field mass $M\mu$ compatible with dark matter models is of the order of $M\omega \sim 10^{-6}$ in geometrized units.[1] According to our results, in order to capture accurately the values of the corresponding frequencies one would have to evolve the system at least for $t \sim 10^{10} M$. Such a time scale, however, cannot be reached even at the linear level. For this reason we will consider values of μ in the range from 0.08 to 0.3 as we discuss below.

For this work we have coupled the Klein-Gordon equation to the Einstein equations taking advantage of the computational framework recently proposed by Montero and Cordero-Carrión [31] in which a second-order partially implicit Runge-Kutta (PIRK) method is applied to the Baumgarte-Shapiro-Shibata-Nakamura (BSSN) formulation of the Einstein equations [32–34]. This approach has been shown to lead to long-term stable numerical simulations of both vacuum and nonvacuum (with fluids) spacetimes using spherical coordinates without the need for a regularization algorithm at the origin.

The paper is organized as follows: Sec. II describes the formulation of the coupled Einstein-Klein-Gordon system and the construction of the initial data. Section III focuses on the time integration of the system of evolution equations. Our results are presented and discussed in Sec. IV. Finally, we end with a summary of our findings in Sec. V. In the following sections greek indices $\alpha, \beta, \ldots$ run over spacetime indices, while latin indices $i, j, \ldots$ run over space indices only. Throughout this article we use geometrized units $c = G = 1$.

[1] In physical units this corresponds to $\hbar\mu \sim 10^{-24}$ eV [6,30].

II. BASIC EQUATIONS

We investigate the dynamics of a self-gravitating scalar field configuration around a black hole by solving numerically the coupled Einstein-Klein-Gordon system

$$R_{\alpha\beta} - \frac{1}{2} g_{\alpha\beta} R = 8\pi T_{\alpha\beta}, \tag{1}$$

with matter content given by the stress-energy tensor

$$T_{\alpha\beta} = \partial_\alpha \Phi \partial_\beta \Phi - \frac{1}{2} g_{\alpha\beta} (\partial^\sigma \Phi \partial_\sigma \Phi + \mu^2 \Phi^2). \tag{2}$$

The conservation of this stress-energy tensor implies that the field obeys the Klein-Gordon equation

$$\Box \Phi - \mu^2 \Phi = 0, \tag{3}$$

where the d'Alembertian operator is defined by $\Box := (1/\sqrt{-g})\partial_\alpha(\sqrt{-g} g^{\alpha\beta}\partial_\beta)$. We follow the convention that Φ is dimensionless and μ has dimensions of $(\text{length})^{-1}$.

A. Einstein's equations in spherical symmetry

We assume that the spacetime $\mathcal{M}$ can be foliated by a family of spatial slices Σ_t that coincide with level surfaces of a coordinate time t. We denote the future-pointing unit normal on Σ_t with n^α and write the spacetime metric $g_{\alpha\beta}$ as

$$\begin{aligned} ds^2 &= g_{\alpha\beta} dx^\alpha dx^\beta \\ &= -\alpha^2 dt^2 + \gamma_{ij}(dx^i + \beta^i dt)(dx^j + \beta^j dt), \end{aligned} \tag{4}$$

where α is the lapse function, β^i the shift vector, and γ_{ij} the spatial metric induced on Σ

$$\gamma_{\alpha\beta} = g_{\alpha\beta} + n_\alpha n_\beta. \tag{5}$$

In terms of the lapse and the shift, the normal vector n^α can be expressed as

$$n^\alpha = (1/\alpha, -\beta^i/\alpha) \quad \text{or} \quad n_\alpha = (-\alpha, 0, 0, 0). \tag{6}$$

We adopt a conformal decomposition of the spatial metric γ_{ij}

$$\gamma_{ij} = e^{4\chi} \hat{\gamma}_{ij}, \tag{7}$$

where $\psi = e^\chi = (\gamma/\hat{\gamma})^{1/12}$ is the conformal factor, $\hat{\gamma}_{ij}$ the conformally related metric, and $\hat{\gamma}$ its determinant.

Under the assumption of spherical symmetry the line element may be written as

$$ds^2 = e^{4\chi}(a(t,r)dt^2 + r^2 b(t,r) d\Omega^2), \tag{8}$$

with $d\Omega^2 = \sin^2\theta d\varphi^2 + d\theta^2$ being the solid angle element and $a(t,r)$ and $b(t,r)$ the metric functions.

We set the value of $\hat{\gamma}$ at $t = 0$ as that of the determinant of the flat metric in spherical coordinates $\overset{\circ}{\gamma}$. The evolution equations for the conformal factor and for the conformal metric components take the form

$$\partial_t X = \beta^r \partial_r X - \frac{1}{3} X \hat{\nabla}_m \beta^m + \frac{1}{3} X \alpha K, \tag{9}$$

$$\partial_t a = \beta^r \partial_r a + 2a \partial_r \beta^r - \frac{2}{3} a \hat{\nabla}_m \beta^m - 2\alpha a A_a, \tag{10}$$

$$\partial_t b = \beta^r \partial_r b + 2b \frac{\beta^r}{r} - \frac{2}{3} b \hat{\nabla}_m \beta^m - 2\alpha b A_b, \tag{11}$$

where $X \equiv e^{-2\chi}$, K is the trace of the extrinsic curvature, $\hat{\nabla}_m \beta^m$ is the divergence of the shift vector β^i, $\hat{A}_{ij}$ is the traceless part of the conformal extrinsic curvature, and

$$A_a \equiv \hat{A}^r_r, \qquad A_b \equiv \hat{A}^\theta_\theta. \tag{12}$$

The evolution equation for K is

$$\partial_t K = \beta^r \partial_r K - \nabla^2 \alpha + \alpha \left(A_a^2 + 2A_b^2 + \frac{1}{3} K^2 \right) + 4\pi\alpha(\rho + S_a + 2S_b). \tag{13}$$

Next, the evolution equation for the independent component of the traceless part of the conformal extrinsic curvature A_a is given by

$$\partial_t A_a = \beta^r \partial_r A_a - \left(\nabla^r \nabla_r \alpha - \frac{1}{3} \nabla^2 \alpha \right) + \alpha \left(R^r_r - \frac{1}{3} R \right) + \alpha K A_a - \frac{16}{3} \pi \alpha (S_a - S_b), \tag{14}$$

where R^r_r is the mixed radial component of the Ricci tensor and R is its trace.

Finally, the evolution equation for $\hat{\Delta}^r$, the radial component of the additional BSSN variables [35] $\hat{\Delta}^i = \hat{\gamma}^{mn} \hat{\Delta}^i_{mn}$ with $\hat{\Delta}^a_{bc} = \hat{\Gamma}^a_{bc} - \overset{\circ}{\Gamma}{}^a_{bc}$, is given by

$$\begin{aligned} \partial_t \hat{\Delta}^r = {} & \beta^r \partial_r \hat{\Delta}^r - \hat{\Delta}^r \partial_r \beta^r + \frac{1}{a} \partial_r^2 \beta^r + \frac{2}{b} \partial_r \left(\frac{\beta^r}{r} \right) \\ & + \frac{\sigma}{3} \left(\frac{1}{a} \partial_r (\hat{\nabla}_m \beta^m) + 2 \hat{\Delta}^r \hat{\nabla}_m \beta^m \right) \\ & - \frac{2}{a} (A_a \partial_r \alpha + \alpha \partial_r A_a) + 2\alpha \left(A_a \hat{\Delta}^r - \frac{2}{rb} (A_a - A_b) \right) \\ & + \frac{2\alpha}{a} \left[\partial_r A_a - \frac{2}{3} \partial_r K + 6 A_a \partial_r \chi \right. \\ & \left. + (A_a - A_b) \left(\frac{2}{r} + \frac{\partial_r b}{b} \right) - 8\pi j_r \right]. \end{aligned} \tag{15}$$

The matter source terms ρ, S_a, S_b, and j_r appearing in the previous equations are components of the energy-momentum tensor (2) given by

$$\rho \coloneqq n^\alpha n^\beta T_{\alpha\beta} = \frac{1}{2} \left(\Pi^2 + \frac{\Psi^2}{a e^{4\chi}} \right) + \frac{1}{2} \mu^2 \Phi^2, \tag{16}$$

$$j^r \coloneqq -P^{r\alpha} n^\beta T_{\alpha\beta} = -\Pi\Psi, \tag{17}$$

$$S_a \coloneqq T^r_r = \frac{1}{2} \left(\Pi^2 + \frac{\Psi^2}{a e^{4\chi}} \right) - \frac{1}{2} \mu^2 \Phi^2, \tag{18}$$

$$S_b \coloneqq T^\theta_\theta = \frac{1}{2} \left(\Pi^2 - \frac{\Psi^2}{a e^{4\chi}} \right) - \frac{1}{2} \mu^2 \Phi^2, \tag{19}$$

where Π and Ψ are defined below. The Hamiltonian and momentum constraints are given by the following two equations that we compute to monitor the accuracy of the numerical evolutions:

$$\mathcal{H} \equiv R - (A_a^2 + 2A_b^2) + \frac{2}{3} K^2 - 16\pi\rho = 0, \tag{20}$$

$$\mathcal{M}^r \equiv \partial_r A_a - \frac{2}{3} \partial_r K + 6 A_a \partial_r \chi + (A_a - A_b) \left(\frac{2}{r} + \frac{\partial_r b}{b} \right) - 8\pi S_r = 0. \tag{21}$$

1. Gauge conditions

In addition to the BSSN spacetime variables, there are two more variables left undetermined: the lapse function α and the shift vector β^i. Our code can handle arbitrary gauge conditions, and for the simulations reported in this paper we use the so called "nonadvective 1 + log" condition [36] for the lapse and a variation of the "Gamma-driver" condition for the shift vector [35,37].

The form of this slicing condition is expressed as

$$\partial_t \alpha = -2\alpha K. \tag{22}$$

For the radial component of the shift vector, we choose the Gamma-driver condition, which is written as

$$\partial_t B^r = \frac{3}{4} \partial_t \hat{\Delta}^r, \tag{23}$$

$$\partial_t \beta^r = B^r, \tag{24}$$

where the auxiliary variable B^r is introduced.

B. Klein-Gordon equation

In order to solve the Klein-Gordon equation we use two first-order variables defined as

$$\Pi \coloneqq n^\alpha \partial_\alpha \Phi = \frac{1}{\alpha} (\partial_t \Phi - \beta^r \partial_r \Phi), \tag{25}$$

$$\Psi \coloneqq \partial_r \Phi. \tag{26}$$

Therefore, using Eq. (3) we obtain the following system of first-order equations:

$$\partial_t \Phi = \beta^r \partial_r \Phi + \alpha \Pi, \tag{27}$$

$$\partial_t \Psi = \beta^r \partial_r \Psi + \Psi \partial_r \beta^r + \partial_r (\alpha \Pi), \tag{28}$$

$$\partial_t \Pi = \beta^r \partial_r \Pi + \frac{\alpha}{a e^{4\chi}} \left[\partial_r \Psi + \Psi \left(\frac{2}{r} - \frac{\partial_r a}{2a} + \frac{\partial_r b}{b} + 2\partial_r \chi \right) \right] + \frac{\Psi}{a e^{4\chi}} \partial_r \alpha + \alpha K \Pi - \alpha \mu^2 \Phi. \tag{29}$$

C. Initial data: Solving the constraints

It has been shown in Ref. [26] that choosing the maximal slicing condition and a vanishing scalar field Φ, the momentum constraint is satisfied trivially and the Hamiltonian constraint can be solved analytically. In order to explore a different dynamical scenario, we choose instead as initial data a Gaussian distribution for the scalar field of the form

$$\Phi = A_0 e^{-(r-r_0)^2/\lambda^2}, \tag{30}$$

with A_0 the initial amplitude, r_0 the center of the Gaussian, and λ its width. The auxiliary first-order quantities are initialized as follows:

$$\Pi(t=0, r) = 0, \tag{31}$$

$$\Psi(t=0, r) = -2 \frac{(r-r_0)}{\lambda^2} A_0 e^{-(r-r_0)^2/\lambda^2}. \tag{32}$$

We choose a conformally flat metric with $a = b = 1$ together with a time symmetry condition $K_{ij} = 0$. With these choices and $\Pi(t=0, r) = 0$ the momentum constraint is satisfied trivially and the Hamiltonian constraint (20) gives an equation for the conformal factor $\psi = e^{\chi}$

$$\partial_{rr} \psi + \frac{2}{r} \partial_r \psi + 2\pi \psi^5 \rho = 0. \tag{33}$$

In order to solve this equation for a black hole, we assume that the conformal factor can be written in a puncturelike form as

$$\psi = 1 + \frac{M}{2r} + u(r), \tag{34}$$

and we then substitute this form in the Hamiltonian constraint (20) to obtain

$$\partial_{rr} u(r) + \frac{2}{r} \partial_r u(r) + 2\pi \psi^5 \rho = 0. \tag{35}$$

Given a distribution of the scalar field density ρ, we solve this ordinary differential equation for u using a standard four-order Runge-Kutta integrator, assuming that $u \to 0$ as $r \to \infty$ and regularity at the origin.

III. TIME INTEGRATION

We employ the second-order PIRK method developed by Refs. [38,39] to integrate the evolution equations in time (from time t^n to t^{n+1}) and to handle the singular terms that appear in the evolution equations due to our choice of curvilinear coordinates. Writing a system of partial differential equations as follows

$$\begin{cases} u_t = \mathcal{L}_1(u, v), \\ v_t = \mathcal{L}_2(u) + \mathcal{L}_3(u, v), \end{cases} \tag{36}$$

where $\mathcal{L}_1$, $\mathcal{L}_2$, and $\mathcal{L}_3$ represent general nonlinear differential operators, the second-order PIRK method takes the following form:

$$\begin{cases} u^{(1)} = u^n + \Delta t L_1(u^n, v^n), \\ v^{(1)} = v^n + \Delta t \left[\frac{1}{2} L_2(u^n) + \frac{1}{2} L_2(u^{(1)}) + L_3(u^n, v^n) \right], \end{cases} \tag{37}$$

$$\begin{cases} u^{n+1} = \frac{1}{2} [u^n + u^{(1)} + \Delta t L_1(u^{(1)}, v^{(1)})], \\ v^{n+1} = v^n + \frac{\Delta t}{2} [L_2(u^n) + L_2(u^{n+1}) \\ \qquad + L_3(u^n, v^n) + L_3(u^{(1)}, v^{(1)})], \end{cases} \tag{38}$$

where we denote by L_1, L_2, and L_3 the corresponding discrete operators. In particular, we note that L_1 and L_3 will be treated in an explicit way, whereas the L_2 operator will contain the singular terms appearing in the sources of the equations and, therefore, will be treated partially implicitly.

This scheme is applied to the Klein-Gordon equation and to the BSSN evolution equations. We include all the problematic terms appearing in the sources of the equations, that is, stiff source terms that can lead to the development of numerical instabilities (e.g., $1/r$ factors due to spherical coordinates close to $r = 0$ even when regular data are evolved), in the L_2 operator. First, the conformal metric components a and b, the quantity X (function of the conformal factor), the lapse function α, the radial component of the shift β^r, and the scalar field Φ are evolved explicitly, i.e., as the generic variable u is evolved in the previous PIRK scheme. Second, the traceless part of the extrinsic curvature A_a and the trace of the extrinsic curvature K are evolved partially implicitly, using updated values of α, a, and b. Then, the quantity $\hat{\Delta}^r$ and the auxiliary first-order quantities of the scalar field Ψ and Π are evolved partially implicitly, using the updated values of α, a, b, β^r, ψ, A_a, K, and Φ. Finally, B^r is evolved partially implicitly, using the updated values of $\hat{\Delta}^r$. We note that the matter source terms are always included in the explicitly treated parts. In the Appendix, we give the exact form of the source terms included in each operator.

IV. NUMERICAL RESULTS

A. Initial models and convergence

We set up puncturelike initial data representing a stationary black hole with a surrounding scalar field cloud. Whereas part of the initial scalar field is absorbed by the black hole, another part lingers for a long time in the form of a long-lived quasibound state which continuously falls into the black hole. We have set up and evolved 25 different models exploring different values of the initial amplitude of the pulse $A_0 = \{0.0005, 0.005, 0.05, 0.1\}$ and different values of the scalar field mass $M\mu = \{0.08 : 0.3\}$ to study their influence in the evolution. Regarding the initial pulse, all models are placed at the same initial location $r_0 = 10M$ and share the same width $\lambda = 5$. The values for the amplitude are chosen so that the self-gravitation of the scalar field becomes important, far away from the test field regime. The bare mass of the black hole is initially set to $M = 1$.

The grid resolution is set to $\Delta r = 0.2M$, and the step time is given by $\Delta t = 0.5\Delta r$ or $\Delta t = 0.3\Delta r$. The second choice is needed to obtain long-term stable simulations for the models with larger amplitude. The final time of the numerical evolutions varies between $2 \times 10^4 M$ for the large amplitude models and about $6 \times 10^4 M$ for the small amplitude ones. The outer boundary of the computational domain is placed at $r = 6 \times 10^4 M$, far enough so it does not affect the dynamics in the inner region.

In Table I we present the different choices for the initial parameters of the models we have evolved, that is, the mass of the scalar field particle $M\mu$ and the amplitude of the pulse A_0. The frequencies $M\omega$ refer to the real part of the dominant modes and are labeled according to their strength on the power spectrum. The table also contains the mass of the apparent horizon (AH) at the end of the simulation $M_{\rm AH}$, defined as $M_{\rm AH} = \sqrt{\mathcal{A}/16\pi}$, where $\mathcal{A}$ is the area of the AH, the Arnowitt-Deser-Misner (ADM) mass $M_{\rm ADM}$ of the whole system

$$M_{\rm ADM} = -\frac{1}{2\pi}\lim_{r\to\infty}\oint_S \partial_j \psi dS^j, \tag{39}$$

and the initial energy of the scalar field E_0

$$E = \int_{2M}^{\infty} \rho dV, \tag{40}$$

TABLE I. Initial parameters for the scalar field around the black hole with initial bare mass $M = 1$. The initial Gaussian is located at $r_0 = 10M$ with half-width $\lambda = 5$. In all cases the extraction radius is $r_{\rm ext} = 100M$. $M_{\rm AH}$ corresponds to the final mass of the apparent horizon of the black hole, $M_{\rm ADM}$ is the initial ADM mass of the system, and E_0 is the initial energy of the scalar field. We show the real part of the oscillation frequencies of the scalar field. The subheadings 1, 2, and 3 correspond to the overtone modes.

			$M\omega$					
Model	$M\mu$	A_0	1	2	3	$M_{\rm AH}$	$M_{\rm ADM}$	E_0
1	0.08	0.1	0.09608	0.09772	⋯	2.03	3.23	2.28
2	0.09	0.1	0.10876	0.11063	⋯	2.07	3.31	2.37
3	0.10	0.0005	0.09946	0.09985	⋯	1.0	1.000062	6.4E-6
4	0.10	0.005	0.09948	0.09989	⋯	1.0	1.0062	6.4E-6
5	0.10	0.05	0.09984	0.10455	0.10535	1.20	1.614	0.64
6	0.10	0.1	0.12117	0.12412	⋯	2.18	3.40	2.46
7	0.11	0.1	0.13382	⋯	⋯	2.23	3.50	2.56
8	0.12	0.1	0.15253	⋯	⋯	2.36	3.61	2.66
9	0.13	0.1	0.16734	⋯	⋯	2.48	3.73	2.79
10	0.14	0.1	0.18266	⋯	⋯	2.55	3.85	2.91
11	0.15	0.0005	0.14797	0.14951	0.14981	1.0	1.00008	8.2E-5
12	0.15	0.005	0.14806	0.14957	0.14981	1.0	1.008	8.2E-3
13	0.15	0.05	0.15062	0.15983	0.16043	1.37	1.77	0.8
14	0.15	0.1	0.19865	⋯	⋯	2.68	3.98	3.04
15	0.16	0.1	0.21529	⋯	⋯	2.82	4.13	3.19
16	0.17	0.1	0.23257	⋯	⋯	2.96	4.27	3.34
17	0.18	0.1	0.25079	⋯	⋯	3.01	4.43	3.49
18	0.19	0.1	0.26980	⋯	⋯	3.25	4.59	3.65
19	0.20	0.0005	0.19508	0.19883	0.19949	1.0	1.0001	1.1E-4
20	0.20	0.005	0.19513	0.19902	0.19973	1.0	1.010	1.1E-2
21	0.20	0.05	0.20147	0.21867	⋯	1.57	1.99	1.03
22	0.20	0.1	0.28959	⋯	⋯	3.46	4.76	3.82
23	0.30	0.0005	0.29812	⋯	⋯	1.0	1.00017	1.8E-4
24	0.30	0.005	0.29843	⋯	⋯	1.0	1.017	1.8E-2
25	0.30	0.05	0.34413	⋯	⋯	2.14	2.61	1.67

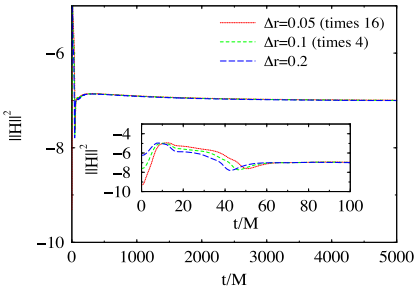

FIG. 1 (color online). Time evolution of the L2 norm of the Hamiltonian constraint for an initial scalar field pulse with $A_0 = 0.1$ and mass $M\mu = 0.1$. The plot shows results for three different resolutions, rescaled by the factors corresponding to second-order convergence. The inset shows a magnified view of the initial $100M$ in the evolution. At $t = 0$ the convergence is to fourth order.

where ρ is defined in Eq. (16). We have checked that the total ADM mass of the system M_{ADM} computed at the initial time slice using Eq. (39) is equal to the sum of the initial black hole mass plus the initial energy of the scalar field Eq. (40). The discrepancy is at most 2% of the ADM mass.

In order to test the convergence of the code we performed three simulations with different resolutions $\Delta r = \{0.2M, 0.1M, 0.05M\}$. In Fig. 1 we plot the rescaled evolution of the L2 norm of the Hamiltonian constraint for the particular choice of the initial amplitude $A_0 = 0.1$ and the scalar field mass $M\mu = 0.1$, obtaining the expected second-order convergence of our PIRK time-evolution scheme. The same result is achieved irrespective of the model.

Comparing simulations with different resolutions, we estimate that the error in the final mass is around 5% while the errors in the scalar field energy and ADM mass estimates are around 2%. Those errors decrease when we increase the resolution. We also compared the frequency using observers located at different positions, and the error in the frequency estimation is negligible. Taking into account that we are performing simulations up to $3 - 6 \times 10^4 M$, the error bars for the oscillation frequencies are $\sim 1 - 5 \times 10^{-5} M$.

B. Nonlinear quasibound states

We evolve the Einstein-Klein-Gordon system using the initial data given by Eqs. (30)–(32). In order to analyze the results of the simulations we extract a time series for the scalar field amplitude at an observation point with a fixed radius r_{ext}. Thus, to identify the frequencies at which the field oscillates we perform a fast Fourier transform after a given number of time steps and obtain the power spectrum. For some models we were able to obtain not only the fundamental frequency of oscillation but also some of the overtones.

It is well known that the frequency resolution is inversely proportional to the simulation time, and hence longer runs yield to more accurate frequencies. Thanks to the computational advantage provided by spherical symmetry and to the use of the PIRK method we were able to compute the frequencies at which the scalar field oscillates, confirming the existence of long-lived spherical states in our nonlinear evolutions even for large initial amplitudes of the scalar field.

The power spectrum obtained from the Fourier transform shows a set of distinct frequencies. In order to validate our results we contrast the numerical values of the frequency of the small amplitude configurations with the ones obtained using Leaver's continued fraction technique [40] in the frequency domain in the test field approximation.

In Figs. 2–5 we plot the evolution of the scalar field seen by an observer at $r_{\mathrm{ext}} = 100M$ for models 3–6 of our sample along with their corresponding Fourier transforms. In all of the plots the field is seen to be clearly oscillating. Moreover, all of these models show a distinctive beating pattern due to the presence of overtones, as described in

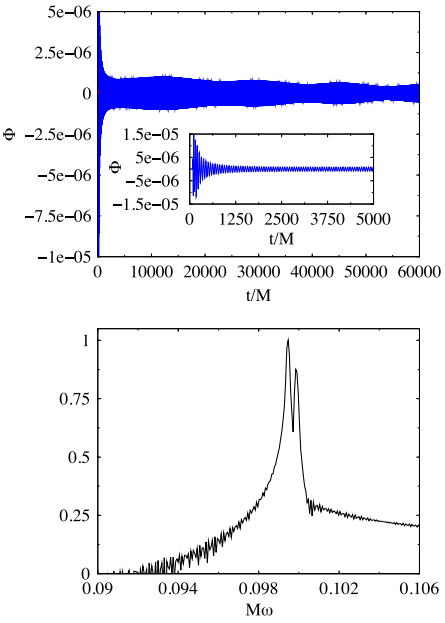

FIG. 2 (color online). Upper panel: Time evolution of the scalar field with mass $M\mu = 0.1$ and $A_0 = 0.0005$ corresponding to model 3 for an observer at $r_{\mathrm{ext}} = 100M$. The inset shows a magnified view of the initial $5000M$ in the evolution. Lower panel: Fourier transform of the evolution of the scalar field. $M\omega$ refers to the real part of the oscillation frequencies. The units in the vertical axis are arbitrary; we have normalized them by the amplitude of the fundamental mode.

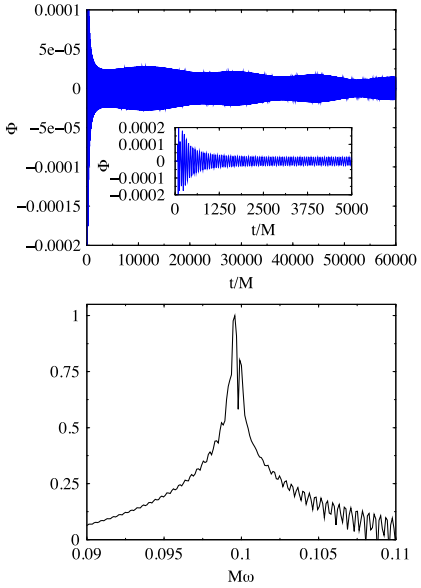

FIG. 3 (color online). Same as Fig. 2 but for model 4.

Refs. [12,15,41,42] for the case of fixed background computations and in Ref. [26] in the nonlinear regime. Within the computational times we can afford, such beatings and overtones cannot be resolved only in models 7–10,

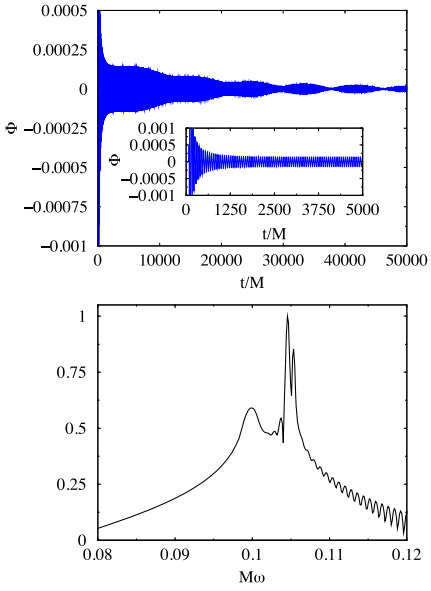

FIG. 4 (color online). Same as Fig. 2 but for model 5.

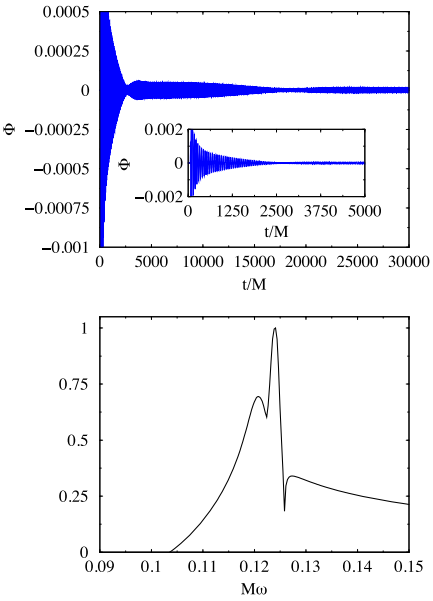

FIG. 5 (color online). Same as Fig. 2 but for model 6.

14–18, and 22–25. For the small amplitude models 3–12, 14, 19, 20, and 23 the frequencies are very close to the values obtained in the test field regime. As shown in Table I the frequency grows as the amplitude is increased.

By using a matching technique, Furuhashi and Nambu showed analytically in Ref. [43] that in the limit $M\mu \ll 1$ the real part of the frequency of quasibound states ω_{qbs} depends on the mass parameter μ as

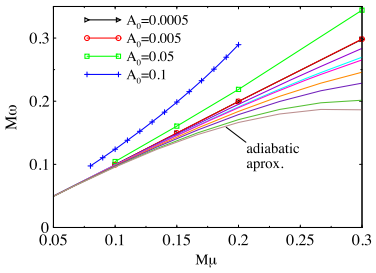

FIG. 6 (color online). Frequency ω as a function of the scalar field mass μ for the models shown in Table I. The semianalytic relation (41) for several values of $M = \{1.1, 1.5, 1.6, 2.0, 2.3, 2.7, 2.9\}$ is also plotted. For models with small initial A_0 the numerical frequencies match the values of the semianalytical values for $M = 1$ showing consistency with the test field approximation and the limit $M\mu \ll 1$.

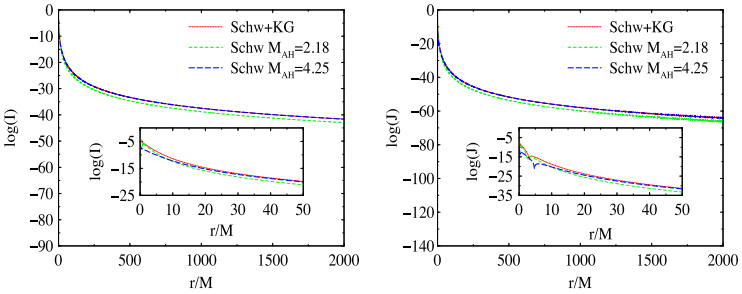

FIG. 7 (color online). Radial profiles of the Weyl invariants I (left) and J (right) for model 6 in Table I at $t = 9000M$. The red curve corresponds to our numerically evolved spacetime while the green and blue curves correspond to analytic (static) Schwarzschild spacetimes of mass $M_{\rm AH} = 2.18$ and 4.25, respectively. The inset shows a region close to the black hole horizon where the numerical solution differs considerably from a stationary Schwarzschild black hole.

$$\mathrm{Re}(\omega_{qbs}) \approx \mu\left[1 - \frac{1}{2}(M\mu)^2\right]. \tag{41}$$

In Fig. 6 we show a plot of the frequencies of all the configurations of Table I as a function of μ. We also consider in this plot the adiabatic approximation for the frequency given by Eq. (41) for different values of the mass of the black hole M. For small values of A_0, the corresponding curve is indistinguishable from the one of the test field approximation. However, for greater values, the results from the nonlinear approach not only deviate from the quasiadiabatic approximation but they also follow the opposite trend: the frequency is greater than the frequency of the test field limit. This discrepancy may be due to the violation of the condition $M\mu \ll 1$ used in the analytical approximation and due to a breakdown of the adiabatic approximation. Nevertheless, the extrapolation of our results for the scalar field mass μ in the regime compatible with scalar field dark matter models $M\mu \sim 10^{-6}$ supports the validity of the model.

C. Spacetime characterization

Spacetime invariants are useful quantities to compare numerical solutions with known exact solutions; see, for instance, Ref. [44] for an instructive way to use them during the formation of a single black hole. With this aim we have used the invariants I and J defined as [45]

$$I = \frac{1}{2}[(E_{ij}E^{ij} - B_{ij}B^{ij}) - 2iE_{ij}B^{ij}],$$
$$J = -\tfrac{1}{6}[(E^i{}_kE^{jk} - 3B^i{}_kB^{jk})E_{ij} \quad + i(B^i_kB^{jk} - 3E^i_kE^{jk})B_{ij}]$$

to characterize our numerical spacetime. In these expressions E_{ij} and B_{ij} are the electric and magnetic parts of the Weyl tensor. We have computed these two quantities to use them as a measure of the deviation of our numerical solution from that corresponding to a Schwarzschild black hole. As expected, the numerical spacetime for the cases with a scalar field pulse of sufficiently small amplitude resembles the Schwarzschild solution once most of the scalar field has accreted on the black hole. The situation changes in a significant way when the amplitude increases. In the two plots of Fig. 7 the solid red curves correspond to the invariants I (left panel) and J (right panel) for our model 6 at $t = 9000M$. These radial profiles are compared with the corresponding purely Schwarzschild invariants for a black hole with the same final mass ($M_{\rm AH} = 2.18$), as indicated by the dashed green curves in the same figure. The deviation of our numerical spacetime from an analytic Schwarzschild black hole spacetime with equivalent mass is evident. An important remark is that both invariants may, however, be superimposed, at sufficiently large distances, if we choose a larger Schwarzschild black hole mass. The dashed blue curve in Fig. 7 shows that is indeed the case if the mass of the Schwarzschild black hole is chosen to be $M_{\rm AH} = 4.25$. The discrepancy is still noticeable near the black hole horizon, as the inset in Fig. 7 clearly makes visible.

This difference may have important implications when studying the motion of test particles around black holes. In particular, there would be a degeneracy in the characterization of the underlying spacetime generating the gravitational attraction of a test particle. One observer at infinity might infer, due to the movement of a test particle, that the central object is either one isolated Schwarzschild black hole with mass M_1 or a transient (nonstatic) state made up of a scalar cloud around a black hole with mass M_2. These two possibilities can be regarded as well as two different, very long-lived solutions of Einstein equations that induce the same motion of test particles, either the vacuum Schwarzschild solution or that of a dynamical spherically symmetric black hole surrounded by a scalar field.

In Table II we summarize the results for all six cases of our sample of models with the largest initial amplitudes and for which the aforementioned degeneracy is most apparent. The third column corresponds to the final numerical black hole mass $M_{\rm AH1}$. The fourth column reports the equivalent Schwarzschild mass $M_{\rm AH2}$ that would induce the same

TABLE II. Mass of the black hole spacetimes corresponding to the six largest amplitude models of our sample. Columns three and four indicate, respectively, the masses of our numerically evolved spacetimes and those of the analytic Schwarzschild black holes that would induce the same radial profiles (degeneracy) in the Weyl invariants.

Model	$M\mu$	$M_{\rm AH1}$	$M_{\rm AH2}$	$M_{\rm AH1}/M_{\rm AH2}$
6	0.10	2.18	4.25	1.95
8	0.12	2.36	5.0	2.12
10	0.14	2.55	6	2.35
15	0.16	2.82	7.25	2.57
17	0.18	3.1	8.75	2.82
22	0.20	3.46	11.0	3.18

radial profiles of the Weyl invariants at large distances. The second mass is extracted by fitting the invariants at large distances, and therefore it does not have to be taken as an accurate measure but rather as an approximate value. The ratio $M_{\rm AH1}/M_{\rm AH2}$ grows with $M\mu$, as shown in the fifth column of the table. We note that it remains to be seen whether the spacetime degeneracy found in our simulations is still important or even exists in the first place for values of the scalar field mass μ compatible with dark matter models, namely, $M\mu \sim 10^{-6}$. As mentioned in the Introduction, the time scales needed to computationally disclose the answer cannot be reached even with linear perturbation codes.

V. CONCLUSIONS

In this paper we have solved numerically the Einstein-Klein-Gordon system in spherical symmetry using spherical coordinates with a PIRK numerical scheme. Our study has been focused on investigating within a fully nonlinear setup whether quasistationary scalar field configurations may be found in the form of clouds (or hairy "wigs") surrounding dynamical black holes. Such configurations have been recently put forward by Refs. [13,14] as a plausible model to describe dark matter halos in galaxies. Through a computational study based on perturbative approaches, these authors found indeed such configurations to be long lived.

In our nonlinear study we have performed a large number of (second-order) accurate and long-term stable simulations of dynamical nonrotating black holes surrounded by self-gravitating scalar fields. The models of our sample have been suitably parametrized to span a broad range of cases from the test field regime to the fully nonlinear regime. Confirming earlier findings from perturbation theory we have found that also in the case of highly dynamical spacetimes (i.e., those consisting of a black hole and a rich scalar field environment) there are states which closely resemble the quasibound states in the test field approximation of Refs. [13,14]. In addition, we have been able to characterize the resulting spacetimes by analyzing the Weyl invariants I and J and have compared them to analytical values of Schwarzschild black hole spacetimes. Our results have revealed a degeneracy in plausible long-lived solutions of Einstein equations that induce the same motion of test particles, either with or without the existence of quasibound states. By performing a Fourier transform of the time series of our numerical data we have been able to characterize the scalar field states by their distinctive oscillation frequencies. It has been found that the scalar field oscillates with different well-defined frequencies and that its time evolution produces in most of our models a characteristic beating pattern due to the nonlinear combination of two frequencies with close enough values. Such scalar field oscillations may have important imprints in a number of astrophysical scenarios. For instance, the fully three-dimensional dynamical evolutions performed in Ref. [26] showed that the interaction of the scalar field with the central black hole results in both scalar field and gravitational radiation. Recently, Ref. [46], using first-order perturbation theory, found that the gravitational response is already present even at the linear level. Since our current study is limited to spherical symmetry, we could not perform such analysis in the present work, a task which we defer to a future investigation.

ACKNOWLEDGMENTS

The authors would like to thank the anonymous referee for his/her useful suggestions that improved the content of the manuscript. We also thank Isabel Cordero-Carrión and Olivier Sarbach for useful discussions and suggestions. This work has been supported by Consejo Nacional de Ciencia y Tecnología-México, by the Deutsche Forschungsgemeinschaft (DFG) through its Transregional Center SFB/TR7 "Gravitational Wave Astronomy," by the Spanish Ministerio de Economía y Competitividad (AYA2013-40979-P), and by the Generalitat Valenciana (PROMETEOII-2014-069). Partial support to NSG comes from "NewCompStar", COST Action MP1304. The computations have been performed at the Servei d'Informàtica de la Universitat de València.

APPENDIX: SOURCE TERMS

The evolution equations (9)–(11), (13)–(15), and (22)–(24) are evolved using a second-order PIRK method, described in Sec. III. In this Appendix, the source terms included in the explicit or partially implicit operators are detailed.

First, a, b, X, α, β^r, and Φ are evolved explicitly; i.e., all the source terms of the evolution equations of these variables are included in the L_1 operator of the second-order PIRK method.

Second, A_a and K are evolved partially implicitly, using updated values of α, a, and b. More precisely, the corresponding L_2 and L_3 operators associated with the evolution equations for A_a and K read

$$L_{2(A_a)} = -\left(\nabla^r\nabla_r\alpha - \frac{1}{3}\nabla^2\alpha\right) + \alpha\left(R^r_r - \frac{1}{3}R\right), \quad \text{(A1)}$$

$$L_{3(A_a)} = \beta^r\partial_r A_a + \alpha K A_a - 16\pi\alpha(S_a - S_b), \quad \text{(A2)}$$

$$L_{2(K)} = -\nabla^2\alpha, \tag{A3}$$

$$L_{3(K)} = \beta^r\partial_r K + \alpha\left(A_a^2 + 2A_b^2 + \frac{1}{3}K^2\right) + 4\pi\alpha(\rho + S_a + 2S_b). \tag{A4}$$

Next, $\hat{\Delta}^r$, Ψ, and Π are evolved partially implicitly, using the updated values of α, a, b, β^r, ψ, A_a, K, and Φ. Specifically, the corresponding L_2 and L_3 operators associated with the evolution equation for $\hat{\Delta}^r$, Ψ, and Π are given by

$$L_{2(\hat{\Delta}^r)} = \frac{1}{a}\partial_r^2\beta^r + \frac{2}{b}\partial_r\left(\frac{\beta^r}{r}\right) + \frac{\sigma}{3a}\partial_r(\hat{\nabla}_m\beta^m) - \frac{2}{a}(A_a\partial_r\alpha + \alpha\partial_r A_a) - \frac{4\alpha}{rb}(A_a - A_b) + \frac{\xi\alpha}{a}\left[\partial_r A_a - \frac{2}{3}\partial_r K + 6A_a\partial_r\chi + (A_a - A_b)\left(\frac{2}{r} + \frac{\partial_r b}{b}\right)\right], \tag{A5}$$

$$L_{3(\hat{\Delta}^r)} = \beta^r\partial_r\hat{\Delta}^r - \hat{\Delta}^r\partial_r\beta^r + \frac{2\sigma}{3}\hat{\Delta}^r\hat{\nabla}_m\beta^m + 2\alpha A_a\hat{\Delta}^r - 8\pi j_r\frac{\xi\alpha}{a}, \tag{A6}$$

$$L_{2(\Psi)} = \partial_r(\alpha\Pi), \tag{A7}$$

$$L_{3(\Psi)} = \beta^r\partial_r\Psi + \Psi\partial_r\beta^r, \tag{A8}$$

$$L_{2(\Pi)} = \frac{\alpha}{ae^{4\chi}}\left[\partial_r\Psi + \Psi\left(\frac{2}{r} - \frac{\partial_r a}{2a} + \frac{\partial rb}{b} + 2\partial_r\chi\right)\right] + \frac{\Psi}{ae^{4\chi}}\partial_r\alpha - \alpha\mu^2\Phi, \tag{A9}$$

$$L_{3(\Pi)} = \beta^r\partial_r\Pi + \alpha K\Pi. \tag{A10}$$

Finally, B^r is evolved partially implicitly, using the updated values of $\hat{\Delta}^r$, i.e., $L_{2(B^r)} = \frac{3}{4}\partial_t\hat{\Delta}^r$ and $L_{3(B^r)} = 0$.

[1] A. Arvanitaki, S. Dimopoulos, S. Dubovsky, N. Kaloper, and J. March-Russell, Phys. Rev. D **81**, 123530 (2010).
[2] A. Arvanitaki and S. Dubovsky, Phys. Rev. D **83**, 044026 (2011).
[3] M. Kamionkowski, J. Pradler, and D. G. E. Walker, Phys. Rev. Lett. **113**, 251302 (2014).
[4] J.-c. Hwang, Phys. Lett. B **401**, 241 (1997).
[5] T. Matos, F. S. Guzman, and L. A. Urena-Lopez, Classical Quantum Gravity **17**, 1707 (2000).
[6] T. Matos and L. A. Urena-Lopez, Phys. Rev. D **63**, 063506 (2001).
[7] T. Matos and L. A. Urena-Lopez, Classical Quantum Gravity **17**, L75 (2000).
[8] D. J. E. Marsh and P. G. Ferreira, Phys. Rev. D **82**, 103528 (2010).
[9] W. Hu, R. Barkana, and A. Gruzinov, Phys. Rev. Lett. **85**, 1158 (2000).
[10] J. Kormendy and K. Gebhardt, AIP Conf. Proc. **586**, 363 (2001).
[11] J. Barranco, A. Bernal, J. C. Degollado, A. Diez-Tejedor, M. Megevand, M. Alcubierre, D. Núñez, and O. Sarbach, Phys. Rev. D **84**, 083008 (2011).
[12] H. Witek, V. Cardoso, A. Ishibashi, and U. Sperhake, Phys. Rev. D **87**, 043513 (2013).
[13] J. Barranco, A. Bernal, J. C. Degollado, A. Diez-Tejedor, M. Megevand, M. Alcubierre, D. Núñez, and O. Sarbach, Phys. Rev. Lett. **109**, 081102 (2012).
[14] J. Barranco, A. Bernal, J. C. Degollado, A. Diez-Tejedor, M. Megevand, M. Alcubierre, D. Núñez, and O. Sarbach, Phys. Rev. D **89**, 083006 (2014).
[15] S. R. Dolan, Phys. Rev. D **87**, 124026 (2013).
[16] A. Cruz-Osorio, F. S. Guzman, and F. D. Lora-Clavijo, J. Cosmol. Astropart. Phys. 06 (2011) 029.
[17] S. L. Detweiler, Phys. Rev. D **22**, 2323 (1980).
[18] S. R. Dolan, Phys. Rev. D **76**, 084001 (2007).
[19] T. Damour, N. Deruelle, and R. Ruffini, Nuovo Cimento Lett. **15**, 257 (1976).
[20] T. Zouros and D. Eardley, Ann. Phys. (N.Y.) **118**, 139 (1979).
[21] P. Pani, V. Cardoso, L. Gualtieri, E. Berti, and A. Ishibashi, Phys. Rev. D **86**, 104017 (2012).
[22] C. A. R. Herdeiro and E. Radu, Phys. Rev. Lett. **112**, 221101 (2014).
[23] E. Berti, V. Cardoso, and A. O. Starinets, Classical Quantum Gravity **26**, 163001 (2009).
[24] R. Konoplya and A. Zhidenko, Rev. Mod. Phys. **83**, 793 (2011).
[25] F. Guzman and F. Lora-Clavijo, Phys. Rev. D **85**, 024036 (2012).
[26] H. Okawa, H. Witek, and V. Cardoso, Phys. Rev. D **89**, 104032 (2014).
[27] H. Yoshino and H. Kodama, Prog. Theor. Phys. **128**, 153 (2012).
[28] R. Brito, V. Cardoso, and P. Pani, arXiv:1411.0686.
[29] A. Arvanitaki, M. Baryakhtar, and X. Huang, arXiv:1411.2263.

[30] A. P. Lundgren, M. Bondarescu, R. Bondarescu, and J. Balakrishna, Astrophys. J. **715**, L35 (2010).
[31] P. J. Montero and I. Cordero-Carrión, Phys. Rev. D **85**, 124037 (2012).
[32] T. Nakamura, K. Oohara, and Y. Kojima, Prog. Theor. Phys. Suppl. **90**, 1 (1987).
[33] M. Shibata and T. Nakamura, Phys. Rev. D **52**, 5428 (1995).
[34] T. W. Baumgarte and S. L. Shapiro, Phys. Rev. D **59**, 024007 (1998).
[35] M. Alcubierre and M. D. Mendez, Gen. Relativ. Gravit. **43**, 2769 (2011).
[36] C. Bona, J. Massó, E. Seidel, and J. Stela, Phys. Rev. D **56**, 3405 (1997).
[37] M. Alcubierre, B. Brügmann, P. Diener, M. Koppitz, D. Pollney, E. Seidel, and R. Takahashi, Phys. Rev. D **67**, 084023 (2003).
[38] I. Cordero-Carrión and P. Cerdá-Durán, arXiv:1211.5930.
[39] F. Casas and V. Martinez, *Advances in Differential Equations and Applications*, SEMA SIMAI Springer Series Vol. 4 (Springer, New York, 2014).
[40] E. Leaver, Proc. R. Soc. A **402**, 285 (1985).
[41] Z. Zhang, E. Berti, and V. Cardoso, Phys. Rev. D **88**, 044018 (2013).
[42] J. C. Degollado and C. A. R. Herdeiro, Phys. Rev. D **89**, 063005 (2014).
[43] H. Furuhashi and Y. Nambu, Prog. Theor. Phys. **112**, 983 (2004).
[44] J. G. Baker and M. Campanelli, Phys. Rev. D **62**, 127501 (2000).
[45] M. Alcubierre, *Introduction to 3+1 Numerical Relativity* (Oxford University Press, New York, 2008).
[46] J. C. Degollado and C. A. R. Herdeiro, Phys. Rev. D **90**, 065019 (2014).

PHYSICAL REVIEW D **92,** 083001 (2015)

Quasistationary solutions of self-gravitating scalar fields around collapsing stars

Nicolas Sanchis-Gual,[1] Juan Carlos Degollado,[2] Pedro J. Montero,[3] José A. Font,[1,4] and Vassilios Mewes[1]

[1]*Departamento de Astronomía y Astrofísica, Universitat de València, Dr. Moliner 50, 46100, Burjassot (València), Spain*

[2]*Departamento de Ciencias Computacionales, Centro Universitario de Ciencias Exactas e Ingeniería, Universidad de Guadalajara Av. Revolución 1500, Colonia Olímpica C.P. 44430, Guadalajara, Jalisco, Mexico*

[3]*Max-Planck-Institute für Astrophysik, Karl-Schwarzschild-Str. 1, 85748, Garching bei München, Germany*

[4]*Observatori Astronòmic, Universitat de València, C/ Catedrático José Beltrán 2, 46980, Paterna (València), Spain*

(Received 30 July 2015; published 2 October 2015)

Recent work has shown that scalar fields around black holes can form long-lived, quasistationary configurations surviving for cosmological time scales. Scalar fields thus cannot be discarded as viable candidates for dark matter halo models in galaxies around central supermassive black holes (SMBHs). One hypothesized formation scenario of most SMBHs at high redshift is the gravitational collapse of supermassive stars (SMSs) with masses of $\sim 10^5$ $M_\odot$. Any such scalar field configurations must survive the gravitational collapse of a SMS in order to be a viable model of physical reality. To check for the postcollapse survival of these configurations and to follow the dynamics of the black hole–scalar field system we present in this paper the results of a series of numerical relativity simulations of gravitationally collapsing, spherically symmetric stars surrounded by self-gravitating scalar fields. We use an ideal fluid equation of state with adiabatic index $\Gamma = 4/3$ which is adequate to simulate radiation-dominated isentropic SMSs. Our results confirm the existence of oscillating, long-lived, self-gravitating scalar field configurations around nonrotating black holes after the collapse of the stars.

DOI: 10.1103/PhysRevD.92.083001 PACS numbers: 95.30.Lz, 04.25.dg, 04.70.Bw, 95.30.Sf

I. INTRODUCTION

The nature of the formation process of galactic black holes is a fundamental issue in the study of galaxy formation. Observations indicate that most galaxies host black holes in their nuclei and that some are formed at redshift $z > 6$ with masses as large as $\sim 10^9$ $M_\odot$ [1,2]. However, it is still unknown how such supermassive black holes (SMBHs) can form and how they grow to their observed masses today.

One possible scenario for the formation of SMBHs in the center of galaxies is that they were formed through accretion and merging of the first stellar remnants [3,4]. Another scenario assumes that central black holes formed via direct collapse (see [5–7]). This route assumes that fragmentation, which depends on efficient cooling, is suppressed. Depending on the rate and radiative efficiency of the inflowing mass, there may be different outcomes. A low rate of mass accumulation would favor the formation of isentropic supermassive stars (SMSs), with masses $\geq 5 \times 10^4$ $M_\odot$, which then would evolve as equilibrium configurations dominated by radiation pressure before collapsing to form a SMBH seed [8,9].

Scalar fields have been considered in cosmology to provide inflationary solutions in the early Universe [10] and as an alternative explanation for dark energy [11]. In addition, they have also been proposed as strong candidates for dark matter [12–15]. In these models one assumes that dark matter is composed of bosonic particles which may condensate into macroscopic objects forming boson stars or forming halos around black holes. The fact that most galaxies host a SMBH at their centers has raised many questions regarding the dynamics of the whole system.

The issue of whether scalar field halos are able to survive around black holes for cosmological time scales has been addressed on several occasions (see, e.g., [16] and references therein). It has been shown in the test-field limit in the background spacetime of a Schwarzschild black hole that scalar field configurations do remain around SMBHs for cosmological time scales, provided the mass of the scalar particle is of the order of 10^{-22}–10^{-24} eV. Further studies considered also the backreaction of spacetime [17–19] and confirmed the existence of such long-lived states. These gravitationally trapped, scalar field configurations are states characterized by well-defined complex frequencies, the real part representing the oscillation frequencies of the scalar field amplitude and the imaginary part the decay rate. It has been proved that these states are generic in the sense that they appear after some time in the evolution of the scalar field even when arbitrary initial data are used [20]. This observation seems to be enough to guarantee (as we show

below) that any choice of initial data will create a scalar field environment around the black hole.

The main objective of this work is to assess the impact of black hole formation on the scalar field configurations and show to what extent the final systems resemble the quasi-bound states found in previous investigations where the black hole is assumed to exist from the start. To accomplish this goal we perform numerical relativity simulations which track the gravitational collapse of a polytropic star in the presence of a scalar field environment. The numerical techniques and the code used are those already described in [17]. We shall refer to that work as paper 1. In this work we also take into account the evolution of the relativistic hydrodynamic equations. In order to simplify our model, we consider that the scalar field and the matter of the star are coupled only through gravity.

The paper is organized as follows: In Sec. II we present the basic equations and discuss the initial data used in our simulations. Section III briefly describes our numerical approach. In Sec. IV we discuss our findings and describe some properties of the solutions. Finally in Sec. V we sum up our concluding remarks. Throughout the paper greek indices run over spacetime indices (0–3), while latin indices run over space indices only (1–3). We use units in which $c = G = M_\odot = 1$.

II. BASIC EQUATIONS

We investigate the dynamics of a self-gravitating scalar field configuration around a polytropic star collapsing to a black hole by solving numerically the coupled Einstein-Klein-Gordon system and the general relativistic hydrodynamics equations. The Einstein equations in covariant form read

$$R_{\alpha\beta} - \frac{1}{2} g_{\alpha\beta} R = 8\pi T_{\alpha\beta}, \tag{1}$$

where $R_{\alpha\beta}$ is the Ricci tensor of the four-dimensional spacetime, $g_{\alpha\beta}$ is the spacetime metric, R is the Ricci scalar, and the matter content is given for our system by a combined stress-energy tensor

$$T_{\alpha\beta} = T^{\mathrm{F}}_{\alpha\beta} + T^{\mathrm{SF}}_{\alpha\beta}, \tag{2}$$

where $T^{\mathrm{F}}_{\alpha\beta}$ is the stress-energy tensor of the (perfect) fluid defined by

$$T^{\mathrm{F}}_{\alpha\beta} = \rho h u_\alpha u_\beta + p g_{\alpha\beta}, \tag{3}$$

and $T^{\mathrm{SF}}_{\alpha\beta}$ is the part corresponding to the scalar field, given by

$$T^{\mathrm{SF}}_{\alpha\beta} = \partial_\alpha \Phi \partial_\beta \Phi - \frac{1}{2} g_{\alpha\beta} (\partial^\sigma \Phi \partial_\sigma \Phi + \mu^2 \Phi^2). \tag{4}$$

In Eq. (3) ρ is the rest-mass density, p is the pressure, u_α is the fluid four velocity, and $h = 1 + \varepsilon + p/\rho$ is the relativistic specific enthalpy, with ε being the specific internal energy. We will assume that each type of matter obeys their own conservation law, in other words, that the coupling between them comes purely from gravity. The equations of motion for the scalar field are obtained from the Klein-Gordon equation

$$\Box \Phi - \mu^2 \Phi = 0, \tag{5}$$

where the d'Alembertian operator is defined by $\Box := (1/\sqrt{-g})\partial_\alpha(\sqrt{-g} g^{\alpha\beta}\partial_\beta)$. We follow the convention that Φ is dimensionless and μ has dimensions of $(\text{length})^{-1}$.

In the following we present the different systems of evolution (and constraint) equations we solve to carry out our study. While we mainly include this information to make the paper self-contained, we keep these sections as concise as possible, and refer the interested reader to our previous papers [17,21,22] for further details.

A. Einstein's equations

Under the assumption of spherical symmetry, the $1+1$ line element may be written as

$$ds^2 = e^{4\chi}(a(t,r)dt^2 + r^2 b(t,r) d\Omega^2), \tag{6}$$

with $d\Omega^2 = \sin^2\theta d\varphi^2 + d\theta^2$ being the solid angle element and $a(t,r)$ and $b(t,r)$ two nonvanishing metric functions. Moreover χ is related to the conformal factor ψ as $\psi = e^\chi = (\gamma/\hat{\gamma})^{1/12}$, with γ and $\hat{\gamma}$ being the determinants of the physical and conformal 3-metrics, respectively. They are conformally related by $\gamma_{ij} = e^{4\chi}\hat{\gamma}_{ij}$.

In particular we adopt the Baumgarte-Shapiro-Shibata-Nakamura formalism of Einstein's equations [23,24], where the evolved fields are the conformally related 3-dimensional metric, the conformal exponent χ, the trace of the extrinsic curvature K, the independent component of the traceless part of the conformal extrinsic curvature, and the radial component of the conformal connection functions (we refer to [21,25] for further details).

The matter fields appearing on the right-hand side of the evolution equations for the gravitational fields (see [21,25]), $\mathcal{E}$, j_i, S_i, and S_{ij} include the contribution of both the fluid and the scalar field, i.e., $\mathcal{E} = \mathcal{E}^{\mathrm{F}} + \mathcal{E}^{\mathrm{SF}}$, etc. The matter source terms for the fluid given by the stress-energy tensor of Eq. (3) read

$$\mathcal{E}^{\mathrm{F}} \equiv n^\alpha n^\beta T^{\mathrm{F}}_{\alpha\beta}, \tag{7}$$

$$j^{\mathrm{F}}_r \equiv -\gamma^\alpha_r n^\beta T^{\mathrm{F}}_{\alpha\beta}, \tag{8}$$

$$S^{\mathrm{F}}_a \equiv (T^{\mathrm{F}})^r_r, \tag{9}$$

$$S^{\mathrm{F}}_b \equiv (T^{\mathrm{F}})^\theta_\theta. \tag{10}$$

The Hamiltonian and momentum constraints are given by the following two equations that we compute to monitor the accuracy of the numerical evolutions:

$$\mathcal{H} \equiv R - (A_a^2 + 2A_b^2) + \frac{2}{3}K^2 - 16\pi\mathcal{E} = 0, \quad (11)$$

$$\mathcal{M}_r \equiv \partial_r A_a - \frac{2}{3}\partial_r K + 6A_a\partial_r\chi + (A_a - A_b)\left(\frac{2}{r} + \frac{\partial_r b}{b}\right) - 8\pi j_r = 0, \quad (12)$$

where A_a and A_b are the contraction of the traceless part of the conformal extrinsic curvature, $A_a \equiv \hat{A}^r_r$, $A_b \equiv \hat{A}^\theta_\theta$. In addition to the evolution fields, there are two more variables left undetermined, the lapse function α, and the shift vector β^i. Our code can handle arbitrary gauge conditions and for the simulations reported in this paper we use the same conditions of paper 1, namely, the so-called "nonadvective $1 + \log$" condition [26] for the lapse, and a variation of the "gamma-driver" condition for the shift vector [25,27].

B. Klein-Gordon equation

To solve the Klein-Gordon equation we introduce two first-order variables defined as

$$\Pi \coloneqq n^\alpha\partial_\alpha\Phi = \frac{1}{\alpha}(\partial_t\Phi - \beta^r\partial_r\Phi), \quad (13)$$

$$\Psi \coloneqq \partial_r\Phi. \quad (14)$$

Therefore, using Eq. (5) we obtain the following system of first-order equations:

$$\partial_t\Phi = \beta^r\partial_r\Phi + \alpha\Pi, \quad (15)$$

$$\partial_t\Psi = \beta^r\partial_r\Psi + \Psi\partial_r\beta^r + \partial_r(\alpha\Pi), \quad (16)$$

$$\partial_t\Pi = \beta^r\partial_r\Pi + \frac{\alpha}{ae^{4\chi}}\left[\partial_r\Psi + \Psi\left(\frac{2}{r} - \frac{\partial_r a}{2a} + \frac{\partial rb}{b} + 2\partial_r\chi\right)\right] + \frac{\Psi}{ae^{4\chi}}\partial_r\alpha + \alpha K\Pi - \alpha\mu^2\Phi. \quad (17)$$

The matter source terms for the scalar field read

$$\mathcal{E}^{\rm SF} \equiv n^\alpha n^\beta T^{\rm SF}_{\alpha\beta} = \frac{1}{2}\left(\Pi^2 + \frac{\Psi^2}{ae^{4\chi}}\right) + \frac{1}{2}\mu^2\Phi^2, \quad (18)$$

$$j_r^{\rm SF} \equiv -\gamma^\alpha_r n^\beta T^{\rm SF}_{\alpha\beta} = -g_{rr}\Pi\Psi, \quad (19)$$

$$S_a^{\rm SF} \equiv (T^{\rm SF})^r_r = \frac{1}{2}\left(\Pi^2 + \frac{\Psi^2}{ae^{4\chi}}\right) - \frac{1}{2}\mu^2\Phi^2, \quad (20)$$

$$S_b^{\rm SF} \equiv (T^{\rm SF})^\theta_\theta = \frac{1}{2}\left(\Pi^2 - \frac{\Psi^2}{ae^{4\chi}}\right) - \frac{1}{2}\mu^2\Phi^2. \quad (21)$$

C. Hydrodynamics equations

The general relativistic hydrodynamics equations, expressed through the conservation laws of the stress-energy tensor $T^{\mu\nu}$ and the continuity equation, are

$$\nabla_\alpha T^{\alpha\beta} = 0, \qquad \nabla_\alpha(\rho u^\alpha) = 0. \quad (22)$$

Following [28], we write the equations of general relativistic hydrodynamics as a first-order, flux-conservative system. We define the fluid 3-velocity as seen by a normal (Eulerian) observer as

$$v^r \equiv \frac{u^r}{\alpha u^t} + \frac{\beta^r}{\alpha}, \quad (23)$$

and the Lorentz factor between the fluid and the normal observer as $W \equiv \alpha u^t$. We also define the relativistic densities of mass, momentum, and energy for the normal observer as

$$D = \rho W, \quad (24)$$

$$S_r = \rho h W^2 v_r, \quad (25)$$

$$\tau = \rho h W^2 - p - D. \quad (26)$$

We then assemble these variables into a vector $\mathbf{U}$ of conserved fluid variables

$$\mathbf{U} = \sqrt{\gamma}(D, S_r, \tau). \quad (27)$$

By defining the corresponding vector of fluxes $\mathbf{F}^r$ and the vector of source terms $\mathbf{S}$ we can cast Eqs. (22) in flux-conservative form

$$\partial_t\mathbf{U} + \partial_r\mathbf{F}^r = \mathbf{S}. \quad (28)$$

We refer to [21] where the explicit form of vectors $\mathbf{F}^r$ and $\mathbf{S}$ is given. To close the system of hydrodynamics equations, we choose a gamma-law equation of state (EOS)

$$P = (\Gamma - 1)\rho\epsilon, \quad (29)$$

where Γ is the adiabatic index.

D. Scalar field initial data

As in paper 1 our choice of initial data for the scalar field is a Gaussian distribution of the form

$$\Phi = A_0 e^{-(r-r_0)^2/\lambda^2}, \quad (30)$$

where A_0 is the initial amplitude of the pulse, r_0 is the center of the Gaussian, and λ is its width. The auxiliary first-order quantities are initialized as follows:

$$\Pi(t=0,r)=0, \tag{31}$$

$$\Psi(t=0,r)=-2\frac{(r-r_0)}{\lambda^2}A_0 e^{-(r-r_0)^2/\lambda^2}. \tag{32}$$

Likewise, we choose a conformally flat metric with $a=b=1$ together with a time symmetry condition $K_{ij}=0$. With these choices and $\Pi(t=0,r)=0$ the momentum constraint is satisfied trivially and the Hamiltonian constraint, Eq. (11), yields the following equation for the conformal factor $\psi=e^{\chi}$,

$$\partial_{rr}\psi+\frac{2}{r}\partial_r\psi+2\pi\psi^5\mathcal{E}=0. \tag{33}$$

In order to solve this equation for our collapsing stars, we assume that the conformal factor can be written as

$$\psi=\psi^{\mathrm{TOV}}+u(r), \tag{34}$$

where ψ^{TOV} is the part of the conformal factor associated with the stellar Tolman-Oppenheimer-Volkoff (TOV) model. By substituting this ansatz in the Hamiltonian constraint we obtain

$$\partial_{rr}u(r)+\frac{2}{r}\partial_r u(r)+2\pi\psi^5\mathcal{E}^{\mathrm{SF}} +2\pi(\psi^5-(\psi^{\mathrm{TOV}})^5)\mathcal{E}^{\mathrm{TOV}}=0. \tag{35}$$

Given a distribution of the scalar field density $\mathcal{E}^{\mathrm{SF}}$, we solve this ordinary differential equation for u using a standard fourth-order Runge-Kutta integrator, assuming that $u\to 0$ as $r\to\infty$ and regularity at the origin.

III. NUMERICS

The time update of the different systems of evolution equations we have to solve in our code (Einstein, Klein-Gordon, and Euler) is done using the same types of techniques we have extensively used in our previous work (see in particular [17,21]). We refer the interested reader to those references for full details on the particular numerical techniques implemented in the code. Here, we simply mention that the evolution equations are integrated using the second-order PIRK method developed by [29,30]. This method allows us to handle the singular terms that appear in the evolution equations due to our choice of curvilinear coordinates. The derivatives in the spacetime evolution are computed using a fourth-order centered finite difference approximation on a uniform grid except for advection terms for which we adopt a fourth-order upwind scheme. We also use fourth-order Kreiss-Oliger dissipation to avoid high frequency noise appearing near the outer boundary. The difference with our previous work [17] is that we are also evolving the hydrodynamics conserved quantities explicitly. Correspondingly, the equations of hydrodynamics are solved using the Harten-Lax-van Leer-Einfeldt approximate Riemann solver in tandem with the second-order monotonized central reconstruction scheme [21].

IV. RESULTS

A. Stellar models and code convergence

We construct spherically symmetric stellar models by solving the Tolman-Oppenheimer-Volkoff (TOV) equations for a polytropic EOS,

$$p=\kappa\rho^{1+1/N}, \tag{36}$$

where κ is the polytropic constant and N the polytropic index. These data are evolved in our code with the gamma-law EOS, Eq. (29), with $\Gamma=1+1/N$. We adopt $N=3$ ($\Gamma=4/3$), which is the appropriate value for a SMS. Moreover, we select the value of $\kappa=0.48773$ in our code units. The polytropic constant is set to this value to keep the mass of the star close to 1, namely, in the range $M=\{0.8,1.43\}$ for our four different TOV models. These models are gravitationally unstable spherical relativistic stars that collapse to black holes in dynamical time scales by artificially decreasing the pressure by a small amount (typically 5%) at $t=0$. The main characteristics of our sample of stellar models are reported in Table I. Their corresponding location in the mass vs central density diagram is displayed in Fig. 1. The models are constructed using the RNS code [31].

The collapsing polytropic stars are surrounded by a scalar field cloud whose functional form is given by Eq. (30). We investigate the behavior of the scalar field in a highly dynamical evolution in which the stars undergo gravitational collapse. The end result of the collapse is the formation of a Schwarzschild black hole whose mass is the sum of the mass of the corresponding original star and a portion of the scalar field mass, the part that is accreted. The aim of this investigation is to find out whether in such a dynamical scenario part of the scalar field can still survive in the form of long-lived quasibound states.

To carry out our study we set up and evolve 80 different initial scalar field models. These models are characterized by different values of the initial energy of the scalar

TABLE I. Stellar TOV models: $N=3$ ($\Gamma=4/3$) polytropes with $\kappa=0.48773$. From left to right the columns indicate the model number, the central rest-mass density ρ_c, the central energy density e_c, the radius of the star R, the gravitational mass of the star M, and the compactness M/R.

Model	ρ_c	e_c	R	M	M/R
1	3.11×10^{-6}	3.17×10^{-6}	185.8	1.43	0.008
2	3.11×10^{-5}	3.25×10^{-5}	86.3	1.31	0.015
3	3.11×10^{-4}	3.41×10^{-4}	39.9	1.01	0.025
4	3.11×10^{-3}	3.77×10^{-3}	19.2	0.80	0.042

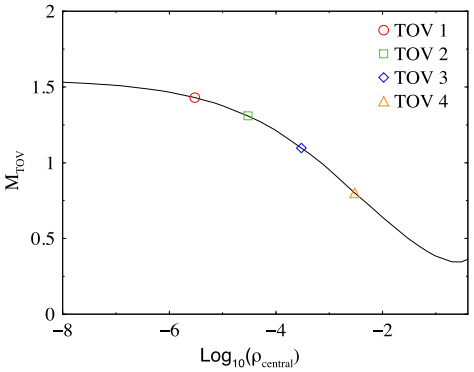

FIG. 1 (color online). Mass of the polytropic TOV stars as function of their initial central rest-mass density. All models are in the unstable branch of the diagram.

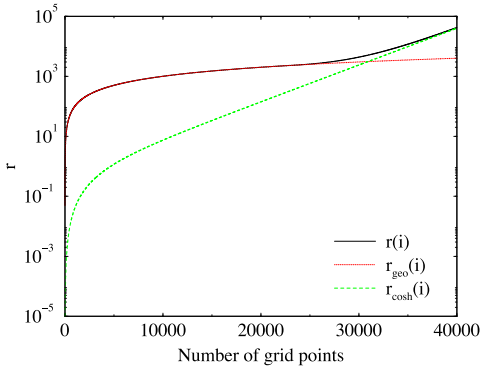

FIG. 2 (color online). Extent of the radial grid as a function of the number of grid points. The black solid line represents the radial coordinate profile of the composite grid, the red dotted line the geometric progression patch and the green dashed line the hyperbolic cosine patch.

field, namely, $E_0 = \{3.2\times10^{-5}, 0.50, 2.85, 4.3\}$ and different values of the scalar field mass $\mu = \{0.05, 0.08, 0.1, 0.15, 0.2\}$. The choice of the values for the energy is made to span all regimes of interest, from the test-field regime to that for which the self-gravity of the scalar field becomes important. For all models, the distribution of the scalar field pulse is placed at the same initial location $r_0 = 100$ and they all share the same initial width $\lambda = 50$.

We have used a logarithmic radial grid in our simulations setting to $\Delta r = 0.1$ the minimum radial resolution at the origin. This is different from the grid we used in paper 1. The reason behind this choice is to reduce the number of radial points without losing accuracy in the inner region and placing the outer boundary sufficiently far away to avoid unwanted reflections from the scalar field. Our grid is composed of two patches, a geometrical progression in the interior and a hyperbolic cosine outside. Using the inner grid alone requires too many grid points to place the outer boundary sufficiently far from the origin, while the hyperbolic cosine patch produces very small grid spacings in the inner region of the grid, leading to prohibitively small time steps due to the Courant-Friedrich-Lewy condition. The two patches are defined at each radial point as

$$r_{\rm geo}(i) = i\Delta r g^{i}_{\rm prog} - r_{\rm min} \tag{37}$$

$$r_{\rm cosh}(i) = \cosh\Big[i(-\log((1+r_{\rm max}) + \sqrt{2r_{\rm max}+r^2_{\rm max}})/(N_r))\Big] - 1, \tag{38}$$

where Δr is the minimum resolution; $r_{\rm min}$ and $r_{\rm max}$ are the inner and outer boundary, respectively; and N_r the total number of radial points. The outer boundary of the computational domain is placed at $r_{\rm max} = 4\times10^4$, far enough so as to not affect the dynamics in the inner region during the entire simulation. For the matching of the two patches, we compute the grid spacings Δr_i for the two patches $r_{\rm geo}(i)$ and $r_{\rm cosh}(i)$ at each grid point and when the difference between the grid spacings is at a minimum, we change from the interior grid to the hyperbolic cosine grid from the corresponding radial point onwards. In Fig. 2 we plot the two patches and the resulting grid as a function of the number of grid points. The time step is given by $\Delta t = 0.5\Delta r$ in order to obtain long-term stable simulations. The final time of the numerical evolutions is 3.5×10^4.

While the convergence of the code was already satisfactorily tested in paper 1, we nevertheless need to assess it again here since we now deal with an augmented system of equations compared to paper 1 due to the presence of the hydrodynamical terms. In order to test the convergence of the code we performed three simulations with different resolutions $\Delta r = \{0.2, 0.1, 0.05\}$. In Fig. 3 we plot the rescaled evolution of the L2 norm of the Hamiltonian constraint for a particular choice of the initial energy, $E_0 = 4.3$, scalar field mass, $\mu = 0.1$, and for the TOV model 4, obtaining the expected second-order convergence of our PIRK time-evolution scheme. We note that the same result is achieved irrespective of the combination of parameters considered and of the TOV model.

Comparing simulations with different resolutions, we estimate that the error in the final black hole mass is ∼2%, while the error estimates for the scalar field energy and ADM mass at the end of the simulations are ∼2%–3%. Those errors decrease as $(\Delta r)^2$ with increasing resolution. Taking into account that our simulations are performed up to a (significantly long) final time of 3.5×10^4, the error bars for our main quantifiable quantity, the frequencies of oscillation of the scalar field (see next section), are $\sim3\times10^{-5}$.

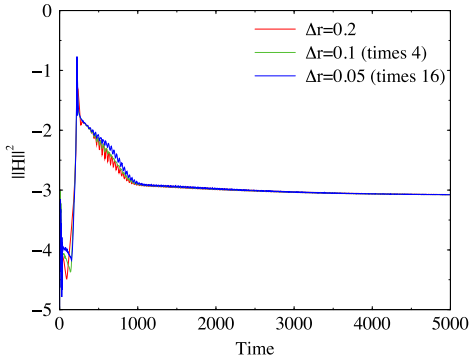

FIG. 3 (color online). Time evolution of the L2 norm of the Hamiltonian constraint for an initial scalar field pulse with $E_0 = 5 \times 10^{-3}$ and mass $M\mu = 0.1$ for the TOV model 4. The plot shows results for three different resolutions, rescaled by the factors corresponding to second-order convergence.

B. Nonlinear quasibound states

We solve the Einstein-Klein-Gordon-Euler system using the initial data given by Eqs. (30)–(32) and let the scalar field evolve in the rapidly changing gravitational field of a collapsing polytropic star. As in paper 1 we analyze the results of the simulations by extracting a time series for the scalar field amplitude at a set of observation points located at fixed radii $r_{\rm ext}$ (typically at three radii located at $r_{\rm ext} = 100$, 200, and 300). To identify the frequencies at which the scalar field oscillates we perform a fast Fourier transform after a given number of time steps and obtain the corresponding power spectrum. The very existence of these frequencies for the long-term simulations we perform is the main indicator we use to demonstrate the presence of quasibound states.

The main results of our simulations are summarized in Tables II–V. These four tables contain for each TOV model the different choices for the scalar field mass μ; the initial amplitude of the pulse A_0; the Arnowitt-Deser-Misner (ADM) mass $M_{\rm ADM}$ of the whole system, defined as

$$M_{\rm ADM} = -\frac{1}{2\pi}\lim_{r\to\infty}\oint_S \partial_j \psi dS^j; \tag{39}$$

and the initial energy of the scalar field E_0

$$E = \int_{2M}^{\infty} \mathcal{E}^{\rm SF} dV, \tag{40}$$

TABLE II. Initial parameters and most relevant quantities for the scalar field and collapsing TOV model 1 ($M = 1.43$). From left to right the columns report the name of the model; the initial amplitude of the pulse, A_0; the scalar field mass, μ; the real part of the angular frequency ω for the fundamental mode of oscillation and the first overtone; the time of the collapse of the TOV star and the formation of the black hole, $t_{\rm col}$; the final mass of the apparent horizon of the black hole, $M_{\rm AH}$; the initial ADM mass of the system, $M_{\rm ADM}$; and the initial and final energy of the scalar field, E_0 and $E_{\rm final}$, respectively. The initial Gaussian pulse is located at $r_0 = 100$ with half-width $\lambda = 50$.

			ω						
Model	A_0	μ	1	2	$t_{\rm col}$	$M_{\rm AH}$	$M_{\rm ADM}$	E_0	$E_{\rm final}$
1.1a	5.00×10^{-5}	0.05	0.04990	...	2494	1.40	1.43	3.2×10^{-5}	3.1×10^{-5}
1.1b	3.30×10^{-5}	0.08	0.07935	0.07988	2494	1.40	1.43	3.2×10^{-5}	2.0×10^{-5}
1.1c	2.65×10^{-5}	0.10	0.09874	0.09964	2494	1.40	1.43	3.2×10^{-5}	1.2×10^{-5}
1.1d	1.80×10^{-5}	0.15	0.14901	0.14954	2494	1.40	1.43	3.2×10^{-5}	1.2×10^{-5}
1.1e	1.35×10^{-5}	0.20	0.19783	0.19927	2494	1.40	1.43	3.2×10^{-5}	5.0×10^{-6}
1.2a	6.30×10^{-3}	0.05	0.05009	...	1706	1.40	1.92	0.50	0.49
1.2b	4.12×10^{-3}	0.08	0.07953	0.08007	1582	1.67	1.92	0.50	0.22
1.2c	3.33×10^{-3}	0.10	0.09859	0.09999	1508	1.76	1.92	0.50	0.15
1.2d	2.25×10^{-3}	0.15	0.15008	...	1376	1.77	1.92	0.50	0.14
1.2e	1.70×10^{-3}	0.20	0.20017	...	1306	1.90	1.92	0.50	0.02
1.3a	1.50×10^{-2}	0.05	0.05099	...	774	1.49	4.20	2.85	2.71
1.3b	9.82×10^{-3}	0.08	0.07909	0.08115	748	3.38	4.19	2.84	0.81
1.3c	7.95×10^{-3}	0.10	0.10197	...	738	3.47	4.19	2.84	0.70
1.3d	5.36×10^{-3}	0.15	0.15314	...	728	4.10	4.19	2.84	0.07
1.3e	4.04×10^{-3}	0.20	0.20412	...	730	4.13	4.20	2.84	0.02
1.4a	1.85×10^{-2}	0.05	0.05153	...	606	1.83	5.72	4.31	3.81
1.4b	1.22×10^{-2}	0.08	0.08276	...	608	4.49	5.77	4.36	1.18
1.4c	9.85×10^{-3}	0.10	0.10341	...	612	5.06	5.75	4.34	0.54
1.4d	6.65×10^{-3}	0.15	0.15512	...	626	5.53	5.76	4.35	0.07
1.4e	5.00×10^{-3}	0.20	0.20665	...	642	5.60	5.73	4.33	0.007

TABLE III. Same as Table II but for TOV model 2.

			ω						
Model	A_0	μ	1	2	$t_{\rm col}$	$M_{\rm AH}$	$M_{\rm ADM}$	E_0	$E_{\rm final}$
2.1a	5.00×10^{-5}	0.05	0.04991	...	750	1.28	1.31	3.2×10^{-5}	3.1×10^{-5}
2.1b	3.30×10^{-5}	0.08	0.07953	...	750	1.28	1.31	3.2×10^{-5}	2.1×10^{-5}
2.1c	2.65×10^{-5}	0.10	0.09909	0.09981	750	1.28	1.31	3.2×10^{-5}	1.0×10^{-5}
2.1d	1.80×10^{-5}	0.15	0.14650	0.14918	750	1.28	1.31	3.2×10^{-5}	9.9×10^{-6}
2.1e	1.35×10^{-5}	0.20	0.19802	0.19927	750	1.28	1.31	3.2×10^{-5}	2.7×10^{-6}
2.2a	6.30×10^{-3}	0.05	0.05009	...	640	1.28	1.80	0.50	0.49
2.2b	4.12×10^{-3}	0.08	0.07971	0.08025	650	1.54	1.80	0.50	0.23
2.2c	3.33×10^{-3}	0.10	0.09859	0.10008	654	1.64	1.80	0.50	0.16
2.2d	2.25×10^{-3}	0.15	0.14936	0.15009	660	1.67	1.80	0.50	0.10
2.2e	1.70×10^{-3}	0.20	0.20017	...	666	1.76	1.80	0.50	0.03
2.3a	1.50×10^{-2}	0.05	0.05117	...	438	1.36	4.07	2.84	2.71
2.3b	9.82×10^{-3}	0.08	0.07918	0.08170	472	3.20	4.07	2.83	0.90
2.3c	7.95×10^{-3}	0.10	0.10197	...	488	3.39	4.07	2.83	0.65
2.3d	5.36×10^{-3}	0.15	0.15314	...	516	3.98	4.07	2.83	0.09
2.3e	4.04×10^{-3}	0.20	0.20412	...	536	4.01	4.07	2.83	0.02
2.4a	1.85×10^{-2}	0.05	0.05170	...	386	1.58	5.60	4.30	3.92
2.4b	1.22×10^{-2}	0.08	0.08276	...	426	4.32	5.65	4.35	1.18
2.4c	9.85×10^{-3}	0.10	0.10341	...	444	5.05	5.63	4.33	0.44
2.4d	6.65×10^{-3}	0.15	0.15512	...	478	5.40	5.63	4.33	0.08
2.4e	5.00×10^{-3}	0.20	0.20678	...	500	5.48	5.62	4.32	0.008

TABLE IV. Same as Table II but for TOV model 3.

			ω						
Model	A_0	μ	1	2	$t_{\rm col}$	$M_{\rm AH}$	$M_{\rm ADM}$	E_0	$E_{\rm final}$
3.1a	5.00×10^{-5}	0.05	0.04991	...	228	1.09	1.10	3.2×10^{-5}	3.1×10^{-5}
3.1b	3.30×10^{-5}	0.08	0.07971	...	228	1.09	1.10	3.2×10^{-5}	2.6×10^{-5}
3.1c	2.65×10^{-5}	0.10	0.09928	0.09982	228	1.09	1.10	3.2×10^{-5}	1.4×10^{-5}
3.1d	1.80×10^{-5}	0.15	0.14758	0.14936	228	1.09	1.10	3.2×10^{-5}	1.1×10^{-5}
3.1e	1.35×10^{-5}	0.20	0.19855	0.19945	228	1.09	1.10	3.2×10^{-5}	3.1×10^{-6}
3.2a	6.30×10^{-3}	0.05	0.05009	...	226	1.10	1.60	0.50	0.49
3.2b	4.12×10^{-3}	0.08	0.07989	...	228	1.22	1.60	0.50	0.36
3.2c	3.33×10^{-3}	0.10	0.09928	0.10018	228	1.40	1.60	0.50	0.16
3.2d	2.25×10^{-3}	0.15	0.14953	0.15026	228	1.50	1.60	0.50	0.09
3.2e	1.70×10^{-3}	0.20	0.19827	0.20017	228	1.53	1.60	0.50	0.04
3.3a	1.50×10^{-2}	0.05	0.05117	...	220	1.13	3.91	2.82	2.71
3.3b	9.82×10^{-3}	0.08	0.07953	0.08133	226	2.94	3.91	2.82	0.91
3.3c	7.95×10^{-3}	0.10	0.10197	...	226	3.22	3.91	2.82	0.61
3.3d	5.36×10^{-3}	0.15	0.15314	...	228	3.72	3.90	2.81	0.11
3.3e	4.04×10^{-3}	0.20	0.20412	...	228	3.82	3.91	2.82	0.03
3.4a	1.85×10^{-2}	0.05	0.05170	...	218	1.23	5.35	4.28	4.02
3.4b	1.22×10^{-2}	0.08	0.08276	...	226	4.15	5.39	4.32	1.15
3.4c	9.85×10^{-3}	0.10	0.10341	...	226	4.82	5.35	4.30	0.43
3.4d	6.65×10^{-3}	0.15	0.15512	...	228	5.17	5.38	4.31	0.08
3.4e	5.00×10^{-3}	0.20	0.20682	...	228	5.29	5.37	4.29	0.01

TABLE V. Same as Table II but for TOV model 4.

			ω						
Model	A_0	μ	1	2	$t_{\rm col}$	$M_{\rm AH}$	$M_{\rm ADM}$	E_0	$E_{\rm final}$
4.1a	5.00×10^{-5}	0.05	0.04991	...	72	0.75	0.80	3.2×10^{-5}	3.1×10^{-5}
4.1b	3.30×10^{-5}	0.08	0.07989	...	72	0.75	0.80	3.2×10^{-5}	3.1×10^{-5}
4.1c	2.25×10^{-5}	0.10	0.09963	...	72	0.75	0.80	2.3×10^{-5}	1.9×10^{-5}
4.1d	1.80×10^{-5}	0.15	0.14882	0.14973	72	0.75	0.80	3.2×10^{-5}	1.4×10^{-5}
4.1e	1.35×10^{-5}	0.20	0.19927	0.19963	72	0.75	0.80	3.2×10^{-5}	7.5×10^{-5}
4.2a	6.30×10^{-3}	0.05	0.05009	...	72	0.75	1.29	0.50	0.49
4.2b	4.12×10^{-3}	0.08	0.08007	...	72	0.77	1.29	0.50	0.47
4.2c	3.33×10^{-3}	0.10	0.09982	0.10035	72	0.89	1.28	0.49	0.35
4.2d	2.25×10^{-3}	0.15	0.14829	0.15008	72	1.09	1.29	0.50	0.19
4.2e	1.70×10^{-3}	0.20	0.19908	0.20035	72	1.24	1.29	0.50	0.04
4.3a	1.50×10^{-2}	0.05	0.05117	...	72	0.84	3.60	2.80	2.72
4.3b	9.82×10^{-3}	0.08	0.08078	0.08168	72	2.61	3.59	2.79	0.91
4.3c	7.95×10^{-3}	0.10	0.10214	...	72	2.63	3.60	2.80	0.88
4.3d	5.36×10^{-3}	0.15	0.15314	...	72	3.38	3.59	2.79	0.11
4.3e	4.04×10^{-3}	0.20	0.20412	...	72	3.48	3.60	2.80	0.04
4.4a	1.85×10^{-2}	0.05	0.05182	...	72	0.86	5.03	4.24	4.08
4.4b	1.22×10^{-2}	0.08	0.08029	0.08276	72	3.53	5.04	4.29	1.45
4.4c	9.85×10^{-3}	0.10	0.10341	...	72	4.30	5.06	4.27	0.64
4.4d	6.65×10^{-3}	0.15	0.15512	...	72	4.82	5.06	4.27	0.10
4.4e	5.00×10^{-3}	0.20	0.20681	...	72	4.93	5.05	4.26	0.01

where $\mathcal{E}^{\rm SF}$ is defined in Eq. (18). As the second-to-last column of each table shows, we vary the initial amplitude for the different μ in order to keep the initial scalar field energy constant for four different scenarios, from the test-field approximation to the nonlinear regime where the scalar field is self-gravitating. This is presented as the four subdivisions of each table. The oscillation frequencies of the scalar field are reported in columns 4 and 5 for the fundamental mode and first overtone, respectively.

Figures 4–6 show the time evolution of the scalar field amplitude extracted at three different radii, $r_{\rm ext} = \{100, 200, 300\}$. In the left panels of Fig. 4 we plot the evolution for the initial scalar field energy $E_0 = 3.2 \times 10^{-5}$ for the TOV model 2 and for three scalar field masses, namely, $\mu = \{0.05, 0.1, 0.2\}$ from top to bottom. The three panels show a moderately rapid decay of the amplitude of the oscillations of the scalar field. However, the field amplitudes by the end of the simulations have not totally vanished, especially for the $\mu = 0.05$ model shown in the top panel. Correspondingly, the right panels of Fig. 4 present the power spectra, showing the well-defined oscillation frequencies of the quasistationary states. It is worth stressing that the values of the frequencies do not depend on the location of the observer, as it is shown in the right panels of Fig. 4 for three different observers.

Similar time evolution plots are displayed in Fig. 5 but, in this case, for the larger initial scalar field energy of our sample, $E_0 = 4.3$, for the same TOV model as in Fig. 4 and for two scalar field masses $\mu = \{0.05, 0.2\}$. The evolution for the same initial parameters corresponding to the TOV model 4 can be found in Fig. 6. The comparison among these time evolution plots shows that for the smallest scalar field mass, $\mu = 0.05$, the differences among the evolutions for the different TOV models are more evident. The TOV model 2 shows an increase in the amplitude of the oscillations at the end of the simulation due to the presence of two close frequencies giving rise to a beating pattern, while TOV model 4 does not show this behavior. However, for larger scalar field masses, the differences in the time evolutions become qualitatively less important.

The power spectra obtained from the Fourier transforms of these time series show a set of distinct frequencies, exemplified in the right panels of Fig. 4 for a particular set of models. The frequency resolution is inversely proportional to the simulation time and hence the longer the runs the more accurate the frequencies. The presence of these frequencies confirms the existence of long-lived spherical quasibound states of scalar fields surrounding black holes even if these are formed *dynamically* through the gravitational collapse of spherical stars. During the nonlinear evolution of the system, part of the scalar field survives the gravitational collapse and remains in the form of trapped states. These results extend the validity of our previous model, put forward in [32] and paper 1, in the linear and nonlinear regimes respectively, to a significantly more dynamical scenario.

In columns 4 and 5 of Tables II–V we show the frequencies ω of the scalar field oscillations. These

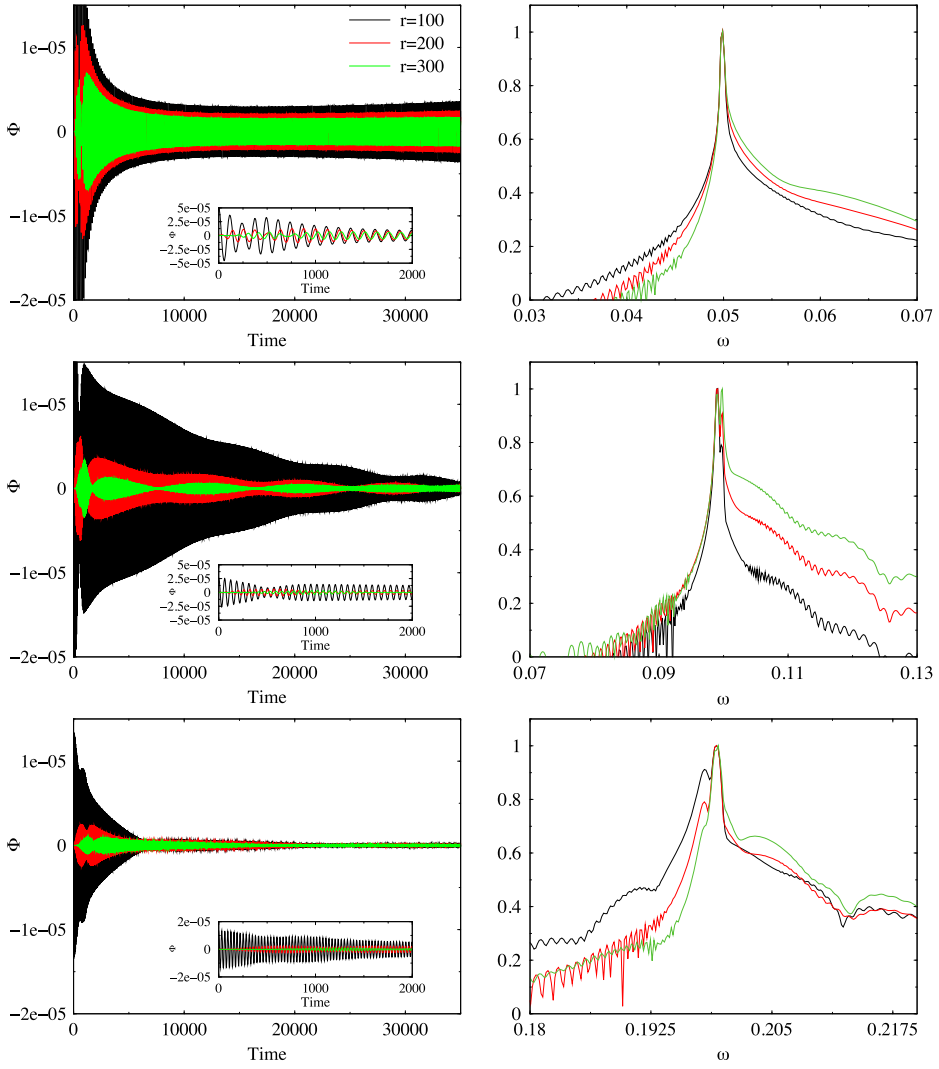

FIG. 4 (color online). Left column: Time evolution of the scalar field with initial energy $E_0 = 3.2 \times 10^{-5}$ for the TOV model 2 and three different scalar field masses $\mu = \{0.05, 0.1, 0.2\}$ (from top to bottom). The inset shows a magnified view of the initial 2000 units of time in the evolution. Right column: Fourier transform of the evolution of the scalar field. ω refers to the real part of the frequencies. The units in the vertical axis are arbitrary and are normalized by the amplitude of the fundamental mode. Each curve corresponds to a different extraction radius, as indicated in the legend of the top left plot.

frequencies refer only to the real part of the dominant modes and are labeled according to their strength on the power spectrum. For some models we are able to obtain several frequencies of oscillation. Tables II–V also report the mass of the apparent horizon (AH) at the end of the simulation $M_{\rm AH}$, defined as $M_{\rm AH} = \sqrt{\mathcal{A}/16\pi}$, where $\mathcal{A}$ is the area of the AH, $t_{\rm col}$ is the time of collapse at which the AH is first found, and $E_{\rm final}$ is the scalar field energy at the end of the simulation. In Fig. 7 we plot the time evolution of the central rest-mass density of the TOV model 1 for different values of the scalar field amplitude. This figure shows that the time at which the TOV collapses decreases

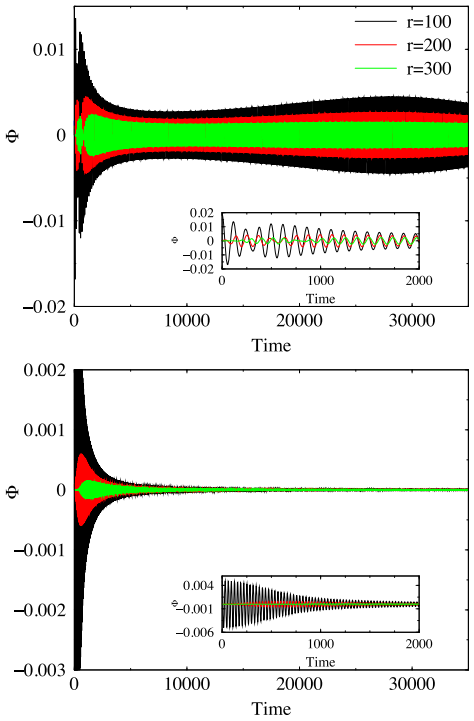

FIG. 5 (color online). Time evolution of the scalar field with initial energy $E_0 = 4.3$ for the TOV model 2 and two different scalar field masses $\mu = \{0.05, 0.2\}$ (from top to bottom). The inset shows a magnified view of the initial 2000 units of time in the evolution.

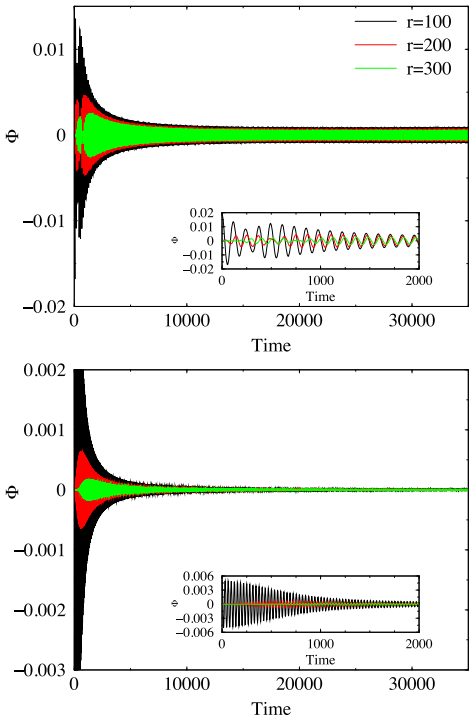

FIG. 6 (color online). Time evolution of the scalar field with initial energy $E_0 = 4.3$ for the TOV model 4 and two different scalar field masses $\mu = \{0.05, 0.2\}$ (from top to bottom). The inset shows a magnified view of the initial 2000 units of time in the evolution.

monotonically when the initial scalar field amplitude increases. We note that $t_{\rm col}$ for the case of the test-field scalar field energy ($A_0 = 5 \times 10^{-5}$) coincides perfectly with the corresponding time for the case with no scalar field affecting the density evolution of the TOV star (as both lines overlap in the figure).

From Tables II–V we see that the time of collapse shows a clear dependence with the initial energy of the scalar field E_0 only for the less compact TOV models of our sample, models 1 and 2 for which the values of the compactness parameter M/R are 0.008 and 0.015, respectively. The collapse time becomes shorter the larger E_0 becomes. Model 3, with $M/R = 0.025$, has significantly shorter values of $t_{\rm col}$ and, moreover, $t_{\rm col}$ barely shows any dependence on E_0. Finally, for the TOV model 4 with $M/R = 0.042$ the time of collapse is the shortest of the whole sample and constant, $t_{\rm col} = 72$ irrespective of E_0. This result is explained by the fact that in this case the star collapses to form a black hole even before the scalar field pulse can reach the collapsing star. Therefore, the presence

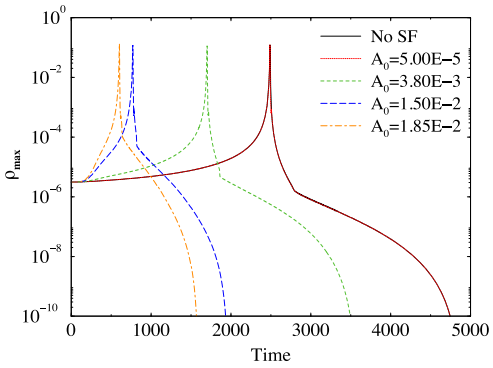

FIG. 7 (color online). Time evolution of the maximum (central) rest-mass density of the TOV model 1 for different initial values of the amplitude of the scalar field pulse with mass $\mu = 0.05$. Notice that the black and red solid lines overlap.

of the scalar field does not influence the collapse dynamics at all, even for the highest scalar field energies we consider in our sample.

The oscillation frequencies for the same scalar field parameters vary slightly from one TOV model to another due to the different initial mass of the black hole when it is formed. For most cases we find that the smaller the black hole mass the higher the frequencies. This trend, however, does not apply for the larger energy models, for which the frequencies are essentially identical for all the TOV stars. This behavior might be simply a numerical artifact due to the lack of sufficient time resolution, as with increasing evolution time the frequencies could be better resolved and differences may appear.

In general our results show that when we consider large enough values of the scalar field mass μ, a significantly large amount of the initial scalar field energy falls onto the black hole, and this amount increases with μ (see the last columns of Tables II–V). This behavior is found for all initial scalar field energies considered. On the other hand, the amount of scalar field absorbed by the black hole changes depending on the TOV model, that is, on the initial mass of the black hole when it is formed. We find that it is slightly smaller for the models for which the TOV mass is smaller (and the compactness of the star is correspondingly larger). For the models with the largest mass μ and largest amplitude A_0, the energies at the end of the simulations are just a tiny fraction of the initial values (see the last row of the last columns of Tables II–V). Even if long-lived quasistationary states can be found in such cases, their energies may be too small to question the actual survival of the scalar field. Nevertheless, for smaller values of μ this trend is reversed and only a small fraction of the initial energy of the scalar field is absorbed by the black hole.

Our results cannot be directly extrapolated to the case of a typical $10^6 M_\odot$ SMS collapsing to a black hole. However, we may still put forward an educated guess of what actually might happen. On the one hand, SMS are less compact ($M/R \sim 10^{-3}$) than our TOV models and their gravity is almost Newtonian. Taking this into account, if the quasistationary states survive to the collapse of a more compact star, it could be expected that they will also persist after the collapse of a SMS. On the other hand, SMS collapse occurs at $t_{\rm col} \sim 10^5$ s [9], which in our units is about $t_{\rm col}/M \sim 1000$–40000, depending on the compactness of the star. Our results yield $t_{\rm col}/M \sim 90$–1750, and the simulations show that the scalar field survives at least for 2 to 3 orders of magnitude beyond the collapse time scale. In the context of a SMS, quasistationary states may then exist for long times.

The time evolution of the scalar field energy corresponding to the TOV model 2 and for all scalar field masses is shown in Fig. 8. The top panel corresponds to $E_0 = 3.2 \times 10^{-5}$ and the bottom panel to $E_0 \sim 4.3$ (the precise values are given in the second to last column of Table III, models

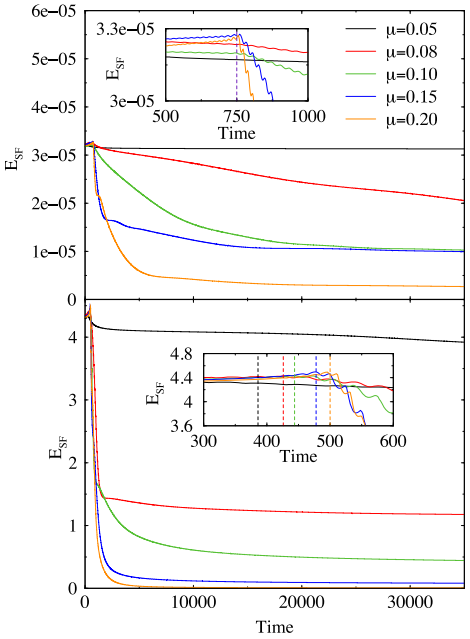

FIG. 8 (color online). Time evolutions of the scalar field energy from the initial value $E_0 = 3.2 \times 10^{-5}$ (top panel) and from the initial value $E_0 \sim 4.3$ (bottom panel). The evolutions are shown for the TOV model 2 and for all scalar field masses $\mu = \{0.05, 0.08, 0.1, 0.15, 0.2\}$. The insets show magnified views around the time of collapse in the corresponding evolutions. The times at which the black holes are formed are displayed as vertical dashed lines. The different colors are related to the different scalar field masses as indicated in the legend of the top panel.

2.4a–2.4e). In the case of the test-field regime, the energy decay is smooth and varies monotonically with the increasing mass. In the nonlinear regime, there is a significant leap (better seen in the inset of the bottom panel) in the amount of scalar field energy due to the initial accretion onto the black hole when it is formed. The decay of the energy after black hole formation (signaled by the dashed vertical lines in the figure) is in general fairly abrupt for all scalar field masses except for $\mu = 0.05$. After the scalar field first interacts with the black hole, the energy reaches a phase during which the accretion rate is importantly reduced, allowing the survival of the scalar field for long time scales (but again notice the drastic reduction in the scalar field energy for $E_0 \sim 4.3$ and $\mu = 0.15$ and $\mu = 0.2$). This response of the system happens faster the larger the initial energy of the scalar field.

In Fig. 9 we plot the evolution of the scalar field energy $E_{\rm SF}$ (red curves) and the mass of the apparent horizon $M_{\rm AH}$ (black curves) for the TOV model 2 and the largest initial

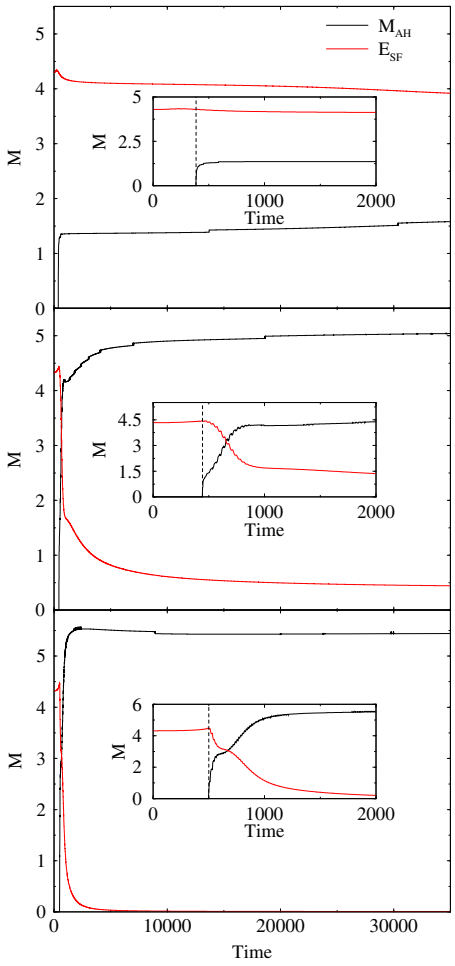

FIG. 9 (color online). Time evolution of the mass of the apparent horizon $M_{\rm AH}$ and of the scalar field energy for the initial $E_0 \sim 4.3$ and the scalar field masses $\mu = \{0.05, 0.1, 0.2\}$ from top to bottom corresponding to the TOV model 2. The inset shows a magnified view of the initial 2000 units of time in the evolution. The time at which the black hole is formed is displayed as a vertical dashed line.

energy ($E_0 \sim 4.3$) for three scalar field masses, $\mu = \{0.05, 0.1, 0.2\}$ from top to bottom. The scalar field energy remains mostly constant until the time of collapse, when it begins to decrease (see the corresponding insets). The decrease is more significant and faster the larger the scalar field mass is. Similarly, the mass of the black hole starts to increase as soon as the apparent horizon emerges for the first time, as a response to the accretion of the scalar field. It becomes clear from this figure that the amount of the scalar

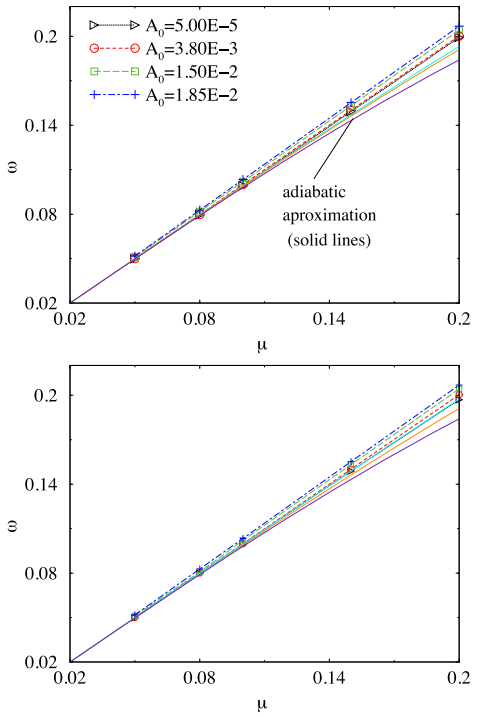

FIG. 10 (color online). Top panel: Frequency ω as a function of the scalar field mass μ for the models shown in Table III. The semianalytic relation given by Eq. (41) is also plotted for $M = \{1.31, 1.5, 2.0\}$ (solid lines). The semianalytic values for $M = 1.31$ correspond to the cyan line. Bottom panel: Same as the top panel but for the models shown in Table V. The semianalytic relation is plotted for $M = \{0.8, 1.5, 2.0\}$. The semianalytic values for $M = 0.80$ correspond to the cyan line.

field lost in the process is absorbed by the black hole, becoming the only contribution to its growth when the fluid mass has been completely accreted by the black hole. The evolutions of both quantities are almost perfect mirror images of each other.

By using a matching technique, Furuhashi and Nambu showed analytically in [33] that in the limit $M\mu \ll 1$ the real part of the frequency of quasibound states, $\omega_{\rm qbs}$, depends on the mass parameter μ as

$$\mathrm{Re}(\omega_{\rm qbs}) \approx \mu\left[1 - \frac{1}{2}(M\mu)^2\right]. \tag{41}$$

In Fig. 10 we show a plot of the frequencies of all the configurations of Tables III and V as a function of μ (similar behavior is found for the other models). Our numerical results are plotted with nonsolid lines. We also consider in this plot the adiabatic approximation for the frequency

TABLE VI. Same as Tables II–V but for evolutions of scalar fields in spacetimes containing initially a Schwarzschild black hole. Only the fundamental frequency is shown.

Model	A_0	μ	ω	$(M_{\rm AH})_0$	$(M_{\rm AH})_{\rm final}$	$M_{\rm ADM}$	E_0	$E_{\rm final}$
1_4a_bh	1.85×10^{-2}	0.05	0.05116	1.43	3.70	5.73	4.31	1.88
1_4c_bh	9.85×10^{-3}	0.10	0.10341	1.43	5.32	5.75	4.34	0.31
1_4e_bh	5.00×10^{-3}	0.20	0.20681	1.43	5.62	5.75	4.33	0.007
2_4a_bh	1.85×10^{-2}	0.05	0.05170	1.31	2.67	5.59	4.30	2.88
2_4c_bh	9.85×10^{-3}	0.10	0.10341	1.31	5.18	5.62	4.33	0.34
2_4e_bh	5.00×10^{-3}	0.20	0.20681	1.31	5.44	5.61	4.32	0.008
3_4a_bh	1.85×10^{-2}	0.05	0.05170	1.10	1.34	5.36	4.28	3.93
3_4c_bh	9.85×10^{-3}	0.10	0.10341	1.10	4.87	5.39	4.30	0.41
3_4e_bh	5.00×10^{-3}	0.20	0.20681	1.10	5.26	5.38	4.29	0.01
4_4a_bh	1.85×10^{-2}	0.05	0.05188	0.80	0.86	5.04	4.24	4.08
4_4c_bh	9.85×10^{-3}	0.10	0.10341	0.80	4.32	5.06	4.27	0.64
4_4e_bh	5.00×10^{-3}	0.20	0.20681	0.80	4.93	5.05	4.26	0.01

given by Eq. (41) for different values of the mass of the black hole M. These analytic results are plotted with solid lines in the figure.

For the TOV model 4 (bottom panel), we find that for the smallest value of A_0, indicated in the legend in the top panel of the figure, the corresponding semianalytic curve (black dotted line) is indistinguishable from the one of the test-field approximation for $M = 0.8$ (cyan solid line), showing consistency with the test-field approximation and the limit $M\mu \ll 1$. For the TOV model 2 (top panel), while the results are similar, for the larger scalar field mass the adiabatic approximation is not matched even in the test-field approximation for $M = 1.31$ (cyan solid line). For all the models, we find that for greater values of A_0, the results from the nonlinear approach not only deviate from the adiabatic approximation but they also follow the opposite trend: the frequency is greater than the frequency of the test-field limit. This discrepancy may be due to the violation of the condition $M\mu \ll 1$ used in the analytical approximation and due to a breakdown of the adiabatic approximation.

These results agree with our findings in paper 1. When the initial amplitude is increased and the model is far from the test-field regime, the frequencies become higher. A similar trend is found when the scalar field mass is small, the frequencies becoming closer to those of the test-field regime. However, in this case we find that for the larger amplitudes the frequencies do not differ as much as in paper 1 from the frequencies matching the adiabatic approximation. This may be due to the fact that depending on the initial profile and position of the scalar field pulse, there can be a variable amount of scalar field that ends up being part of the quasibound states.

C. Comparison with a BH-scalar field system

In order to further understand the influence of the collapse of the stars in the evolution of the scalar field, we also evolve an additional set of 12 models corresponding to purely Schwarzschild-like black hole spacetimes. These black holes have initial masses equal to those of the different TOV stars considered in the simulations we have just discussed. Likewise, the initial distributions of the scalar field clouds are the same as in the previous simulations. Therefore, the scalar field interacts from the beginning with an already existing black hole. This is the same situation we analyzed in paper 1, only the initial black hole masses have now been adapted to match those of the TOV stars. We choose only three scalar field masses, $\mu = \{0.05, 0.1, 0.2\}$, and the largest value of the initial energy, $E_0 \sim 4.3$. The grid resolution, time-step, and final evolution time remain unchanged. Table VI summarizes the results corresponding to this scenario.

In this set of simulations, as we showed in paper 1, part of the scalar field is immediately accreted onto the black hole while part forms the quasibound states. The determination of the oscillation frequencies of those states reveals that, for $\mu = 0.1$ and 0.2, some of the frequencies are equal to those of the collapsing star scenario. On the other hand, the final scalar field energy is, for the majority of models, smaller than that for the TOV setup, but the difference is reduced either if the scalar field mass is increased or if the initial black hole mass is lowered. This discrepancy, most noticeable for TOV model 2, can be due to the fact that for the TOV a larger fraction of the scalar field may escape before the black hole forms and starts accreting. There is almost no difference between the two setups for TOV model 4 because, as mentioned before, the time of collapse is short enough to form a black hole before most of scalar field reaches the star. We also note that for the black hole models 1 and 2 and $\mu = 0.05$ the amount of scalar field that falls onto the black hole is larger than for the other models and scalar field masses. As a result, the mass of the final black holes increases significantly and the oscillation frequencies change. The dynamics of the scalar field in

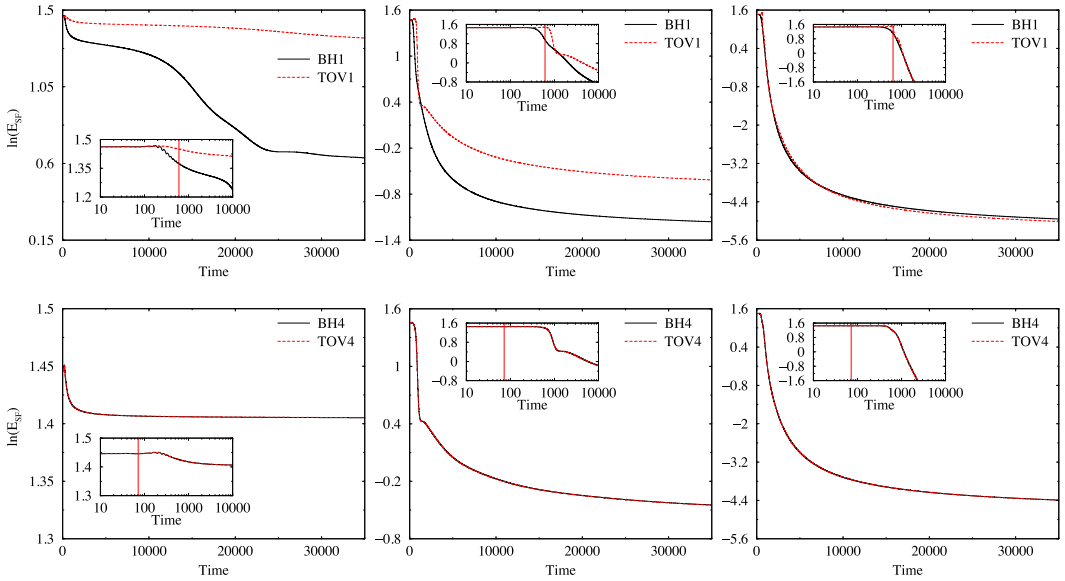

FIG. 11 (color online). Comparison of the time evolution of the scalar field energy for the collapsing TOV star models 1 and 4, and for Schwarzschild black holes with the same initial mass. The initial energy density is $E_0 \sim 4.3$. The insets show magnified views in the logarithm scale of the initial 10000 units of time in the evolution. Left column: $\mu = 0.05$. Middle column: $\mu = 0.1$. Right column: $\mu = 0.2$.

the BH and TOV setups is markedly different for this particular set of models.

This is clearly visible in Fig. 11 where we plot the evolution of the scalar field energy for the initial parameters described in Table VI for both the TOV and BH models 1 and 4. As the mass of the scalar field increases from $\mu = 0.05$ (left column of panels) to $\mu = 0.2$ (right column of panels) the evolution of the energy becomes progressively similar, and the presence of a black hole from the start or at later times is unimportant for the dynamics. The same trend is found as the initial black hole mass or TOV mass is reduced (see the bottom row of panels in Fig. 11). In this case the dynamics also becomes identical irrespective of the scalar field mass. The major differences are found in the upper left corner of the composite of panels in Fig. 11, i.e., when μ is the smallest and the black hole and TOV initial masses are largest. In any event, the influence of the gravitational collapse on the dynamics of the scalar field and on the eventual presence of quasibound states is not as potentially threatening as we might have expected before conducting this research. The initial (rapid) phase of accretion by an already formed black hole seems to overcome any dynamical effect from the collapse of the star which might have affected the survival of the scalar field, even for the smaller scalar field masses and the larger initial black hole masses considered in our study, where different evolutions are observed.

V. CONCLUSIONS

In this paper we have discussed the feasibility of the existence of quasistationary states of self-gravitating scalar fields in the form of clouds (or hairy "wigs") around collapsing, black-hole-forming stars. For our analysis we have solved numerically the Einstein-Klein-Gordon coupled system of equations further coupled to the Euler equations of general relativistic hydrodynamics. Our numerical approach has been limited to spherical symmetry and has been based on spherical coordinates and a PIRK numerical scheme for the time update. This research extends our previous work where the same issue was investigated for black holes already existing at $t = 0$ to a much more dynamical scenario where the black holes are formed as the result of the gravitational collapse of unstable (polytropic) stars.

In our nonlinear study we have performed a large number of (second-order) accurate and long-term stable simulations of dynamical nonrotating collapsing stars, with an EOS corresponding to SMSs, surrounded by self-gravitating scalar fields. The models of our sample have been suitably parametrized to span a broad range of scalar field cases, from the test-field regime to the fully nonlinear regime, along with different initial masses for the star. We have found that in the case of highly dynamical spacetimes there are states which closely resemble the quasibound

states in the test-field approximation of [20,32], surviving the stellar collapse and black hole formation.

By performing a Fourier transform of the time series of our numerical data we have been able to characterize the scalar field states by their distinctive oscillation frequencies. It has been found that the scalar field oscillates with different well-defined frequencies, and that its time evolution produces in most of our models a characteristic beating pattern due to the nonlinear combination of two oscillations with close frequencies. Such scalar field oscillations may have important imprints in a number of astrophysical scenarios such as gravitational wave astronomy. In particular, Refs. [18,34] have shown recently that the frequency of oscillation of the scalar field leaves a distinctive signature in the late time behavior of the gravitational wave signal.

We have also compared the evolutions of the scalar field in collapsing, black-hole-forming spacetimes with spacetimes that already contain a nonrotating black hole. This comparison has provided a better understanding of the influence of the stellar collapse on the scalar field dynamics. Our results have shown that the differences are mainly due to the initial (or lack of) accretion phase onto the black hole that contributes to the growth of its mass and to the different dynamics, in the case of self-gravitating scalar fields.

Furthermore, our results indicate that for certain values of μ, the formation of the black hole during the collapse of the star enhances the chances of the scalar field to remain in a quasibound state. This result may have important implications for models of black hole formation together with dark matter halos in the early epochs of the Universe. For instance, large galaxies in the scalar field model can already be formed at high redshift [35].

The collapse of the $\sim 1\ M_\odot$ stars considered in this work and the subsequent formation of the black holes modify the dynamics of the scalar field, but for the range of TOV masses these types of events have a very short duration. While our results cannot be directly extrapolated to the case of a typical $10^6\ M_\odot$ SMS collapsing to a black hole, it could perhaps be expected, on the basis of their smaller compactness and almost Newtonian gravity, that quasistationary states might still persist after the collapse of a SMS star. Actual numerical simulations are however necessary to validate the viability of this scenario and the survival of quasibound states of scalar fields around SMBH for cosmological time scales. In addition to such simulations it is worth studying the evolution of scalar fields around accreting black holes during significantly longer evolutionary times than those attempted in [17], a task we defer for the near future.

Finally, we note that the dynamical scenario presented here can also be generalized to rotating stars where the final state may be a rotating Kerr black hole surrounded by a scalar field cloud yielding a hairy black hole solution [36,37]. It has been argued that these solutions may act as dynamical attractors in a highly dynamical process [38] and thus simulations as the ones performed here would be able to describe their formation.

ACKNOWLEDGMENTS

P. M. thanks Ewald Müller for comments on the manuscript. This work has been supported by the Spanish MINECO (AYA2013-40979-P), by the Generalitat Valenciana (PROMETEOII-2014-069), by the CONACyT-México, and by the Max Planck Institute for Astrophysics. The computations have been performed at the Servei d'Informàtica de la Universitat de València.

[1] D. J. Mortlock, S. J. Warren, B. P. Venemans, M. Patel, P. C. Hewett, R. G. McMahon, C. Simpson, T. Theuns, E. A. Gonzales-Solares, A. Adamson *et al.*, Nature (London) **474**, 616 (2011).
[2] B. P. Venemans, E. Bañados, R. Decarli, E. P. Farina, F. Walter, K. C. Chambers, X. Fan, H.-W. Rix, E. Schlafly, R. G. McMahon *et al.*, Astrophys. J. Lett. **801**, L11 (2015).
[3] V. Bromm and A. Loeb, Astrophys. J. **596**, 34 (2003).
[4] Z. Haiman and A. Loeb, Astrophys. J. **552**, 459 (2001).
[5] M. C. Begelman, M. Volonteri, and M. J. Rees, Mon. Not. R. Astron. Soc. **370**, 289 (2006).
[6] M. C. Begelman, Mon. Not. R. Astron. Soc. **402**, 673 (2010).
[7] L. Mayer, S. Kazantzidis, A. Escala, and S. Callegari, Nature (London) **466**, 1082 (2010).
[8] M. Shibata and S. L. Shapiro, Astrophys. J. **572**, L39 (2002).
[9] P. J. Montero, H.-T. Janka, and E. Müller, Astrophys. J. **749**, 37 (2012).
[10] J. E. Lidsey, A. R. Liddle, E. W. Kolb, E. J. Copeland, T. Barreiro, and M. Abney, Rev. Mod. Phys. **69**, 373 (1997).
[11] T. Padmanabhan, Phys. Rep. **380**, 235 (2003).
[12] V. Sahni and L.-M. Wang, Phys. Rev. D **62**, 103517 (2000).
[13] W. Hu, R. Barkana, and A. Gruzinov, Phys. Rev. Lett. **85**, 1158 (2000).
[14] T. Matos and L. A. Urena-Lopez, Classical Quantum Gravity **17**, L75 (2000).
[15] T. Matos and L. A. Urena-Lopez, Phys. Rev. D **63**, 063506 (2001).
[16] J. Barranco, A. Bernal, J. C. Degollado, A. Diez-Tejedor, M. Megevand, M. Alcubierre, D. Núñez, and O. Sarbach, Phys. Rev. D **84**, 083008 (2011).

[17] N. Sanchis-Gual, J. C. Degollado, P. J. Montero, and J. A. Font, Phys. Rev. D **91**, 043005 (2015).
[18] H. Witek, V. Cardoso, A. Ishibashi, and U. Sperhake, Phys. Rev. D **87**, 043513 (2013).
[19] J. Barranco, A. Bernal, J. C. Degollado, A. Diez-Tejedor, M. Megevand *et al.* (to be published).
[20] J. Barranco, A. Bernal, J. C. Degollado, A. Diez-Tejedor, M. Megevand, M. Alcubierre, D. Núñez, and O. Sarbach, Phys. Rev. D **89**, 083006 (2014).
[21] P. J. Montero and I. Cordero-Carrion, Phys. Rev. D **85**, 124037 (2012).
[22] N. Sanchis-Gual, P. J. Montero, J. A. Font, E. Müller, and T. W. Baumgarte, Phys. Rev. D **89**, 104033 (2014).
[23] T. W. Baumgarte and S. L. Shapiro, Phys. Rev. D **59**, 024007 (1998).
[24] M. Shibata and T. Nakamura, Phys. Rev. D **52**, 5428 (1995).
[25] M. Alcubierre and M. D. Mendez, Gen. Relativ. Gravit. **43**, 2769 (2011).
[26] C. Bona, J. Massó, E. Seidel, and J. Stela, Phys. Rev. D **56**, 3405 (1997).
[27] M. Alcubierre, B. Brügmann, P. Diener, M. Koppitz, D. Pollney, E. Seidel, and R. Takahashi, Phys. Rev. D **67**, 084023 (2003).
[28] F. Banyuls, J. A. Font, J. M. Ibánez, J. M. Martí, and J. A. Miralles, Astrophys. J. **476**, 221 (1997).
[29] I. Cordero-Carrión and P. Cerdá-Durán, arXiv:1211.5930.
[30] F. Casas and V. Martinez, *Advances in Differential Equations and Applications*, SEMA SIMAI Springer Series Vol. 4 (Springer International Publishing Switzerland, Switzerland, 2014).
[31] N. Stergioulas and J. L. Friedmann, Astrophys. J. **444**, 306 (1995).
[32] J. Barranco, A. Bernal, J. C. Degollado, A. Diez-Tejedor, M. Megevand, M. Alcubierre, D. Núñez, and O. Sarbach, Phys. Rev. Lett. **109**, 081102 (2012).
[33] H. Furuhashi and Y. Nambu, Prog. Theor. Phys. **112**, 983 (2004).
[34] J. C. Degollado and C. A. R. Herdeiro, Phys. Rev. D **90**, 065019 (2014).
[35] J. Magaña, T. Matos, A. Suárez, and F. J. Sanchez-Salcedo, J. Cosmol. Astropart. Phys. 10 (2012) 003.
[36] C. A. R. Herdeiro and E. Radu, Phys. Rev. Lett. **112**, 221101 (2014).
[37] C. Herdeiro and E. Radu, Classical Quantum Gravity **32**, 144001 (2015).
[38] C. L. Benone, L. C. B. Crispino, C. Herdeiro, and E. Radu, Phys. Rev. D **90**, 104024 (2014).

PHYSICAL REVIEW D **94,** 043004 (2016)

Quasistationary solutions of scalar fields around accreting black holes

Nicolas Sanchis-Gual,[1] Juan Carlos Degollado,[2] Paula Izquierdo,[3] José A. Font,[1,4] and Pedro J. Montero[5]

[1]*Departamento de Astronomía y Astrofísica, Universitat de València, Dr. Moliner 50, 46100 Burjassot, València, Spain*

[2]*Instituto de Ciencias Físicas, Universidad Nacional Autónoma de México, Apdo. Postal 48-3, 62251 Cuernavaca, Morelos, Mexico*

[3]*Universidad de la Laguna (ULL), Av. Astrofísico Francisco Sánchez S/N, 38206 San Cristóbal de La Laguna, Santa Cruz de Tenerife, Spain*

[4]*Observatori Astronòmic, Universitat de València, C/ Catedrático José Beltrán 2, 46980 Paterna, València, Spain*

[5]*Max-Planck-Institute für Astrophysik, Karl-Schwarzschild-Str. 1, 85748 Garching bei München, Germany*

(Received 17 June 2016; published 8 August 2016)

Massive scalar fields can form long-lived configurations around black holes. These configurations, dubbed quasibound states, have been studied both in the linear and nonlinear regimes. In this paper, we show that quasibound states can form in a dynamical scenario in which the mass of the black hole grows significantly due to the capture of infalling matter. We solve the Klein-Gordon equation numerically in spherical symmetry, mimicking the evolution of the spacetime through a sequence of analytic Schwarzschild black hole solutions of increasing mass. It is found that the frequency of oscillation of the quasibound states decreases as the mass of the black hole increases. In addition, accretion leads to an increase of the exponential decay of the scalar field energy. We compare the black hole mass growth rates used in our study with estimates from observational surveys and extrapolate our results to values of the scalar field masses consistent with models that propose scalar fields as dark matter in the universe. We show that, even for unrealistically large mass accretion rates, quasibound states around accreting black holes can survive for cosmological time scales. Our results provide further support to the intriguing possibility of the existence of dark matter halos based on (ultralight) scalar fields surrounding supermassive black holes in galactic centers.

DOI: 10.1103/PhysRevD.94.043004

I. INTRODUCTION

There is compelling evidence that most nearby galaxies host supermassive black holes (SMBHs) in their centers, with masses in the range 10^6–$10^9 M_\odot$ [1,2]. Such SMBHs are expected to be the evolutionary result of the growth of seed black holes (BHs) in high redshift galaxies through accretion episodes and mergers of massive BH (MBH) binaries with masses somewhere in between those of stellar-origin BHs and SMBHs [3,4]. The discovery of supermassive luminous quasars at redshifts of $z > 6$ has shown that SMBHs with masses $\sim 10^9 M_\odot$ must form extremely early on in the history of the universe [5–7]. These SMBHs must grow rapidly in order to acquire their mass within a short period of $\sim$1 Gyr. Explaining the formation and evolution of SMBHs dwelling in the most powerful quasars when the Universe was less than 1 Gyr old (and of the regular and much smaller MBHs hidden in 13 Gyr old galaxies) is a pressing open issue [8]. Proposed models involve the gravitational collapse of gas clouds or the collapse of supermassive stars in the early universe (a model hampered by the low masses of the initial seeds of first-generation Pop III stars [9]), the runaway growth by accretion onto Pop III BH, or mergers of smaller size BHs. In either scenario, the formation of SMBHs is a highly dynamical event amenable to gravitational wave investigations. Indeed, it is expected that eLISA will probe MBH binaries in the 10^3–$10^7 M_\odot$ range out to redshift $z > 10$ through the detection of their gravitational waves in the mHz frequency band [10].

While one can make a convincing case that SMBHs have grown largely through accretion, with the consequent energy emission observed in electromagnetic output, it has been argued that even an exponential growth at the Eddington-limited e-folding time is too slow to grow stellar-mass BH seeds into the supermassive luminous quasars that are observed at $z \sim 7$ [7]. Some proposals to circumvent this issue invoke super-Eddington accretion for brief periods of time [11–13], the formation through accretion and merging of the first stellar remnants [14,15], or via more massive seeds from the collapse of pregalactic disks at high redshifts [16–18].

In light of these proposals, it is worth considering if rapid BH accretion may have any effect on the distribution of the associated dark matter halo when the latter is modeled as a scalar field. In the absence of accretion, the existence of long-lasting scalar field configurations surrounding a

(nonrotating) BH has been investigated in a number of recent papers, either in the test-field limit [19–21] or employing self-gravitating scalar fields [22,23]. These papers have shown that SMBHs at galactic centers do not represent a serious threat to dark matter models based on (ultralight) scalar fields as a viable alternative to the usual description of dark matter in terms of weakly interacting massive particles. For both scalar fields around SMBHs and axionlike scalar fields around primordial BHs, it has been found that scalar fields can survive for cosmological timescales [20]. Despite these findings, and due to the rapid growth of accretion-powered SMBHs, it is worth investigating the chances of survival of the scalar field within such a dynamical situation. This is the purpose of this paper. Here, we study the properties of scalar field quasibound states in the background of an accreting spherically symmetric BH. Assuming that the BH mass grows adiabatically due to infalling matter, we show that, indeed, long-lasting, quasibound states can still form in such a scenario.

This paper is organized as follows. In Sec. II, we lay out the mathematical and physical approach we use to carry out our investigation. In particular, Sec. II E contains a brief synopsis of our numerical methodology. The results are presented and discussed in Sec. III, while Sec. IV contains the summary of our findings. Throughout the paper, we employ geometrized units ($c = G = 1$). Latin indices indicate spatial indices and hence run from 1 to 3, while Greek indices run from 0 to 3.

II. PROBLEM SETUP

A. Klein-Gordon equation

Our setup considers a scalar field distribution Φ of sufficiently small energy to neglect its self-gravity; i.e. the field can be regarded as a test field. This configuration surrounds a BH which is assumed to be continuously accreting matter. The dynamics of the scalar field is governed by the Klein-Gordon equation,

$$\Box\Phi - \mu^2\Phi = 0, \tag{1}$$

where the d'Alembertian operator is defined by $\Box \coloneqq (1/\sqrt{-\bar{g}})\partial_\alpha(\sqrt{-\bar{g}}g^{\alpha\beta}\partial_\beta)$. We follow the convention that Φ is dimensionless and μ, the mass of the scalar field, has dimensions of $(\text{length})^{-1}$.

We write the spacetime metric $g_{\alpha\beta}$ as

$$\begin{aligned} ds^2 &= g_{\alpha\beta}dx^\alpha dx^\beta \\ &= -\alpha^2dt^2 + \gamma_{ij}(dx^i + \beta^i dt)(dx^j + \beta^j dt), \end{aligned} \tag{2}$$

where α is the lapse function, β^i is the shift vector, and γ_{ij} is the spatial metric. We adopt a conformal decomposition of the spatial metric γ_{ij},

$$\gamma_{ij} = e^{4\chi}\hat{\gamma}_{ij}, \tag{3}$$

where $\psi \coloneqq e^\chi$ is the conformal factor, $\hat{\gamma}_{ij}$ is the conformally related metric, and $\hat{\gamma}$ is its determinant. By assuming spherical symmetry, the line element may be written as

$$dl^2 = e^{4\chi}(a(t,r)dr^2 + r^2b(t,r)d\Omega^2), \tag{4}$$

with $d\Omega^2 = \sin^2\theta d\varphi^2 + d\theta^2$ being the solid angle element and $a(t,r)$ and $b(t,r)$ being two independent metric functions.

To solve the Klein-Gordon equation in spherical symmetry, we introduce two first-order fields, Π and Ψ, defined as

$$\Pi \coloneqq n^\alpha\partial_\alpha\Phi = \frac{1}{\alpha}(\partial_t\Phi - \beta^r\partial_r\Phi), \tag{5}$$

$$\Psi \coloneqq \partial_r\Phi, \tag{6}$$

where n^α is the unit vector normal to the surfaces of constant t. Therefore, using Eq. (1), we obtain the following system of first-order equations,

$$\partial_t\Phi = \beta^r\partial_r\Phi + \alpha\Pi, \tag{7}$$

$$\partial_t\Psi = \beta^r\partial_r\Psi + \Psi\partial_r\beta^r + \partial_r(\alpha\Pi), \tag{8}$$

$$\begin{aligned} \partial_t\Pi = \beta^r\partial_r\Pi + \frac{\alpha}{ae^{4\chi}}\Bigg[&\partial_r\Psi \\ &+ \Psi\left(\frac{2}{r} - \frac{\partial_r a}{2a} + \frac{\partial rb}{b} + 2\partial_r\chi\right)\Bigg] \\ &+ \frac{\Psi}{ae^{4\chi}}\partial_r\alpha + \alpha K\Pi - \alpha\mu^2\Phi, \end{aligned} \tag{9}$$

where K is the trace of the extrinsic curvature. The stress-energy tensor of the scalar field reads

$$T_{\alpha\beta} = \partial_\alpha\Phi\partial_\beta\Phi - \frac{1}{2}g_{\alpha\beta}(\partial^\sigma\Phi\partial_\sigma\Phi + \mu^2\Phi^2). \tag{10}$$

From this tensor, we can compute the energy of the scalar field E,

$$E_{\text{SF}} = \int_{r_{\text{AH}}}^{\infty}\mathcal{E}_{\text{SF}}dV, \tag{11}$$

where r_{AH} is the radius of the apparent horizon and $\mathcal{E}^{\text{SF}}$ is given by

$$\mathcal{E}_{\text{SF}} \coloneqq n^\alpha n^\beta T_{\alpha\beta} = \frac{1}{2}\left(\Pi^2 + \frac{\Psi^2}{ae^{4\chi}}\right) + \frac{1}{2}\mu^2\Phi^2. \tag{12}$$

B. Analytic black hole solution

The numerical evolution of a single BH using the so-called "moving puncture" technique leads to a well-known time-independent, maximal slicing solution of Schwarzschild [24]. It was shown in Ref. [25] that this

solution can also be constructed analytically and be used as a test for numerical codes. We take advantage of this result to put forward the defining characteristic of the procedure we employ in the current investigation. Namely, we avoid evolving numerically the BH, computing instead a sequence of analytical solutions at each time step for different BH masses to mimic the BH growth for different accretion rates. This procedure allows us to simulate long episodes of accretion.

The analytic solution is constructed by defining all quantities as a function of the gauge-invariant areal radius R. We have to transform the solution into isotropic coordinates, as the latter are used in our numerical procedure, comparing the spatial metrics as a function of R and the isotropic radius r,

$$\alpha^{-2}dR^2 + R^2 d\Omega^2 = \psi^4(dr^2 + r^2 d\Omega^2). \tag{13}$$

Thus, the isotropic radius r is given as a function of R by

$$\begin{aligned} r &= \left[\frac{2R + M + (4R^2 + 4MR + 3M^2)^{1/2}}{4}\right] \\ &\times \left[\frac{4 + 3\sqrt{2})(2R - 3M)}{8R + 6M + 3(8R^2 + 8MR + 6M^2)^{1/2}}\right]^{1/\sqrt{2}} \\ &= R\left[1 - \frac{M}{R} - \frac{M^2}{2R^2} + \cdots\right]. \end{aligned} \tag{14}$$

In the limiting case $R \to 3M/2$, $r \to 0$. Correspondingly, the conformal factor is obtained from

$$\begin{aligned} \psi &= \left[\frac{4R}{2R + M + (4R^2 + 4MR + 3M^2)^{1/2}}\right] \\ &\times \left[\frac{8R + 6M + 3(8R^2 + 8MR + 6M^2)^{1/2}}{4 + 3\sqrt{2})(2R - 3M)}\right]^{1/2\sqrt{2}}. \end{aligned} \tag{15}$$

Finally, the lapse function and the isotropic shift vector are, respectively, given by

$$\alpha = \left(1 - \frac{2M}{R} + \frac{27M^4}{16R^4}\right)^{1/2}, \tag{16}$$

$$\beta^r = \frac{3\sqrt{3}M^2}{4}\frac{r}{R^3}. \tag{17}$$

C. Adiabatic growth of the BH mass

We assume that the mass of the BH grows due to the capture of matter as, e.g., falling in from an accretion disk. This infalling matter is assumed to interact with the scalar field only gravitationally; that is, the quasibound states surrounding the BH can only be affected by the increase of the mass of the BH. We will employ a simple phenomenological law based on observational and theoretical grounds which allows us to reasonably incorporate the growth of the BH mass in our model. As mentioned before, the observational evidence of the existence of very luminous quasars, which implies BH masses of $\sim 10^8$–$10^9 M_\odot$ at $z \sim 6$–7 [7,26,27] demonstrates that SMBHs grow rapidly in a short span of time ($\sim 10^9$ years). Moreover, cosmological simulations [28–30] suggest that SMBH seeds undergo an exponential growth phase at early times, $z \gtrsim 4$. Therefore, given a growth rate $\dot{M}_{\rm BH}$, the mass of the BH will increase as

$$M = M_0 e^{\dot{M}_{\rm BH} t}, \tag{18}$$

where M_0 is the initial BH mass and t is the time in our simulations. The actual mechanism that produces the growth of the BH mass is not actually relevant for our study since we are interested in describing the evolution of the scalar field. Thus, assuming that it grows according to Eq. (18) seems a reasonable first step. Variations in the growth rate could be investigated in a future work.

We first consider five different values for $\dot{M}_{\rm BH}$, namely, $\dot{M}_{\rm BH} = \{0, 5\times10^{-7}, 5\times10^{-6}, 5\times10^{-5}, \text{and } 10^{-4}\}$. The time evolution of the BH mass for the different growth (accretion) rates considered is plotted in Fig. 1. We note that our values of $\dot{M}_{\rm BH}$, while small, are nevertheless orders of magnitude higher than realistic values inferred from observations, which are at most $\dot{M}_{\rm BH} \sim 10^{-11}$ in our units [31]. (We further expound on this issue in Sec. III C below.) Using such values would, however, render the numerical investigation prohibitively expensive. The first set of simulations reported in this paper evolves the scalar fields up to a final time $t = 4\times10^4 M$, which is ~ 0.2 s for $M = 1\ M_\odot$. Despite evolutions being fairly long from the

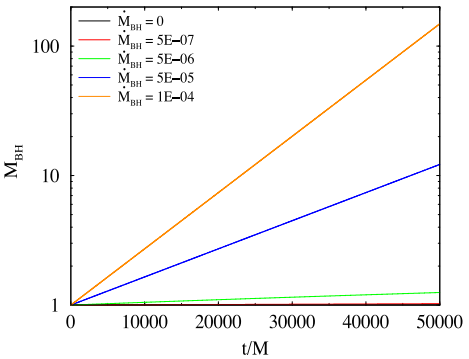

FIG. 1. Evolution of the BH mass for the different accretion rates indicated in the legend. Note that the cases $\dot{M}_{\rm BH} = 0$ and $\dot{M}_{\rm BH} = 5\times10^{-7}$ practically overlap in the plot. Unless stated otherwise, the same color criterion for $\dot{M}_{\rm BH}$ is employed in the remaining figures of this paper.

computational point of view, they are certainly not so on astrophysical grounds. Therefore, in order to study the effect of accretion on the scalar field evolution in affordable computational times, we have to resort to large enough growth rates. As we show below, our simulations indicate that, even for the smaller $\dot{M}_{\rm BH}$ considered, some slight differences appear by the end of the simulation. Nevertheless, longer, and computationally more expensive, simulations would be necessary to show the influence of the growth rate for the smaller values of $\dot{M}_{\rm BH}$.

In the second part of our study, we change the computational setup of the problem by placing reflecting boundary conditions for the scalar field at some radius, i.e., placing a *mirror* beyond which the scalar field is required to vanish, as we did in Ref. [32]. While evolving the scalar field in a cavity is certainly an unrealistic situation, it has some practical advantages as it allows us to investigate lower values of $\dot{M}_{\rm BH}$ and perform longer runs since the computational grid is significantly smaller than in the "natural" setup (with outgoing boundary conditions at the outermost radial grid zone). Within this idealized setup, the initial value of $\dot{M}_{\rm BH}$ can be as low as $\dot{M}_{\rm BH} = 5 \times 10^{-9}$. Despite this reduction only bringing in practice about a 1 order of magnitude gain in the final evolution time, it is nevertheless significant to better quantify the exponential decay in the energy of the scalar field, as we show below.

D. Initial data

For initial data for the scalar field, we set a Gaussian distribution of the form

$$\Phi = A_0 e^{-(r-r_0)^2/\lambda^2}, \tag{19}$$

where A_0 is the initial amplitude, r_0 is the center of the Gaussian, and λ is its width. The auxiliary first-order quantities are initialized as follows:

$$\Pi(t=0,r) = 0, \tag{20}$$

$$\Psi(t=0,r) = -2\frac{(r-r_0)}{\lambda^2} A_0 e^{-(r-r_0)^2/\lambda^2}. \tag{21}$$

Likewise, we choose a conformally flat metric with $a = b = 1$ together with a time symmetry condition, i.e., a vanishing extrinsic curvature, $K_{ij} = 0$.

For the BH, we compute the Schwarzschild solution using the moving puncture technique from Eqs. (14)–(17) for the initial mass $M_0 = 1$.

E. Numerical approach

The solution of the Klein-Gordon evolution equation is computed with the same type of numerical techniques we have used in previous works. The reader is referred in particular to Refs. [22,33] for full details on those techniques. For a succinct summary, we mention that the evolution equations are integrated using the second-order partially implicit Runge-Kutta method introduced in Refs. [34,35], which allows one to handle singular terms that appear due to our choice of curvilinear coordinates. The spatial derivatives in the evolution equations are computed using a fourth-order centered finite difference approximation on a logarithmic grid except for the advection terms for which we adopt a fourth-order upwind scheme. We also use fourth-order Kreiss-Oliger dissipation to avoid high frequency noise appearing near the outer boundary. Again, we stress that in the approach adopted in this work only the scalar field needs to be evolved numerically. The spacetime is updated following the algebraic equations from Sec. II B.

Our simulations employ a logarithmic radial grid, as described in Ref. [23]. We set the finest radial resolution close to the origin, and a grid spacing of $\Delta r = 0.1M$. In the first set of simulations, the outer boundary of the computational domain is placed at $r_{\rm max} = 4 \times 10^4 M$, far enough as to not affect the dynamics of the scalar field in the inner region during the entire simulation. The time step is chosen to be $\Delta t = 0.5\Delta r$, which guarantees long-term stable simulations. The final time of the numerical evolutions is $4 \times 10^4 M$. In the second set of simulations, corresponding to the mirrored states, the radial extension of the numerical domain can be significantly reduced. Specifically, we place the outer boundary at $r_{\rm max} = 250M$, which allows us to use ten times fewer grid points than in the first setup. Finally, the time in the second set of simulations extends up to $8 \times 10^5 M$.

III. RESULTS

A. Time evolution of the scalar field amplitude

1. Quasi-bound frequencies

Quasi-bound states of scalar fields around BHs in the test-field approximation are configurations that have well-defined (complex) frequencies. The real part gives the oscillation of the field, and the imaginary part gives the rate of decay of the configuration. As mentioned in the Introduction, there is a growing body of work which has shown that for some choices of parameters quasibound states may survive for cosmological time scales around SMBHs and, thus, they are consistent with dark matter models based on (ultralight) scalar fields [19–23]. Such long-lasting, quasibound states have also been found to exist in the nonlinear regime [36].

We turn next to discuss the effect of accretion on the quasibound states. We solve the Klein-Gordon system (9) using the initial data given by Eqs. (19)–(21) in the rapidly changing gravitational field of an accreting BH. As done in Refs. [22,23], we analyze the results of the simulations by extracting a time series for the scalar field amplitude at a set of observation points located at fixed radii $r_{\rm ext}$ (typically at

$r_{\rm ext} = 100M$). We identify the frequencies at which the scalar field oscillates by performing a fast Fourier transform. It is worth mentioning that the values of the frequencies do not depend on the location of the observer.

Our main results are summarized in Table I. The first three columns report our different choices for the growth rate of the mass of the BH, $\dot{M}_{\rm BH}$; the five different scalar field masses, $M\mu$, considered in this work; and the initial amplitude of the Gaussian pulse, A_0. The reason we vary the initial amplitude of the pulse for the different values of μ is to keep the initial scalar field energy (almost) constant for the different accretion rates considered, namely $E^0_{\rm SF} = 1.12 \times 10^{-4}$. The oscillation frequencies of the scalar field are reported in columns 4 and 5 for the fundamental mode and the first overtone, respectively. The imaginary part of the frequencies, shown in columns 6 to 8, is the decay rate of the oscillations of the scalar field. From left to right, these three columns report the linear, quadratic, and cubic parts of analytic fits to numerical data for the different models. The last column of Table I also reports the mass of the BH at the end of the simulation, $M_{\rm BH}$, computed from Eq. (18), the evolution of which is displayed in Fig. 1.

Figure 2 shows the time evolution of the scalar field amplitude and spectra extracted at $r_{\rm ext} = 100M$. In the left panels, we plot the evolution for two representative scalar field masses, namely $M\mu = 0.1$ (top) and $M\mu = 0.2$ (bottom), and for the different BH mass growth rates. The criterion for the color of the different curves and its relation to $\dot{M}_{\rm BH}$ follows from Fig. 1. For each panel, the decay of the amplitude of the oscillations of the scalar field is seen to depend strongly on $\dot{M}_{\rm BH}$, regardless of $M\mu$. For the higher growth rates (orange and blue curves), the field amplitudes by the end of the simulations have almost practically vanished. Large field amplitudes and long-lasting oscillations are most noticeable for the three lower accretion rate models of our sample. The differences for $\dot{M}_{\rm BH} = 5 \times 10^{-7}$ with respect to the nonaccreting case become barely visible only for late times. The right panels of Fig. 2 display the corresponding power spectra. They show well-defined oscillation frequencies, best seen in the insets, of the quasistationary states for the models with smaller BH mass growth rate (black, red, and green curves), as expected from the bandwidth theorem, while the other two models attain wider peaks.

TABLE I. Initial parameters and most relevant quantities for the different distributions of scalar fields considered. From left to right, the columns report the BH mass growth rate, $\dot{M}_{\rm BH}$; the scalar field mass, $M\mu$; the initial amplitude of the pulse, A_0; the real part of the angular frequency ω for the fundamental mode of oscillation and the first overtone; the linear, quadratic, and cubic numerical fits of the decay rate of the modes (coefficients a, b, and c in the text), Ms; and the final BH mass, $M_{\rm BH}$. The initial Gaussian pulse is located at $r_0 = 100M$ with half-width $\lambda = 50$.

			$M\omega$		Ms			
$\dot{M}_{\rm BH}$	$M\mu$	A_0	1	2	a	b	c	$M_{\rm BH}$
0.00	0.05	9.42E-05	0.04998	···	3.257E-08	0	0	1.00
5E-07	0.05	9.42E-05	0.04993	...	3.272E-08	···	···	1.02
5E-06	0.05	9.42E-05	0.04989	···	2.390E-08	2.263E-13	···	1.22
5E-05	0.05	9.42E-05	0.04914	0.04951	4.426E-06	-4.755E-10	1.548E-14	7.39
1E-04	0.05	9.42E-05	0.04844	0.04908	9.826E-06	-1.787E-09	9.803E-14	54.60
0.00	0.08	6.18E-05	0.07969	···	2.179E-06	0	0	1.00
5E-07	0.08	6.18E-05	0.07969	···	2.284E-06	···	···	1.02
5E-06	0.08	6.18E-05	0.07959	···	1.886E-06	4.773E-11	···	1.22
5E-05	0.08	6.18E-05	0.07905	0.07942	2.571E-05	-4.547E-09	3.318E-13	7.39
1E-04	0.08	6.18E-05	0.07825	0.07895	5.309E-05	-1.541E-08	1.693E-12	54.60
0.00	0.10	5.00E-05	0.09945	0.09989	1.494E-05	0	0	1.00
5E-07	0.10	5.00E-05	0.09944	0.09988	1.551E-05	···	···	1.02
5E-06	0.10	5.00E-05	0.09928	0.09978	1.935E-05	7.147E-11	···	1.22
5E-05	0.10	5.00E-05	0.09878	0.09929	6.962E-05	-1.255E-08	1.455E-12	7.39
1E-04	0.10	5.00E-05	0.09808	0.09873	1.054E-04	-2.974E-08	5.194E-12	54.60
0.00	0.15	3.37E-05	0.14801	0.14950	3.394E-04	0	0	1.00
5E-07	0.15	3.37E-05	0.14793	0.14954	3.399E-04	···	···	1.02
5E-06	0.15	3.37E-05	0.14778	0.14943	3.450E-04	···	···	1.22
5E-05	0.15	3.37E-05	0.14785	0.14892	3.950E-04	···	···	7.39
1E-04	0.15	3.37E-05	0.14745	0.14807	4.360E-04	···	···	54.60
0.00	0.20	2.54E-5	0.19879	0.19948	6.800E-04	0	0	1.00
5E-07	0.20	2.54E-5	0.19882	0.19955	6.800E-04	···	···	1.02
5E-06	0.20	2.54E-5	0.19868	0.19943	6.830E-04	···	···	1.22
5E-05	0.20	2.54E-5	0.19830	0.19855	7.000E-04	···	···	7.39
1E-04	0.20	2.54E-5	0.19707	0.19787	7.197E-04	···	···	54.60

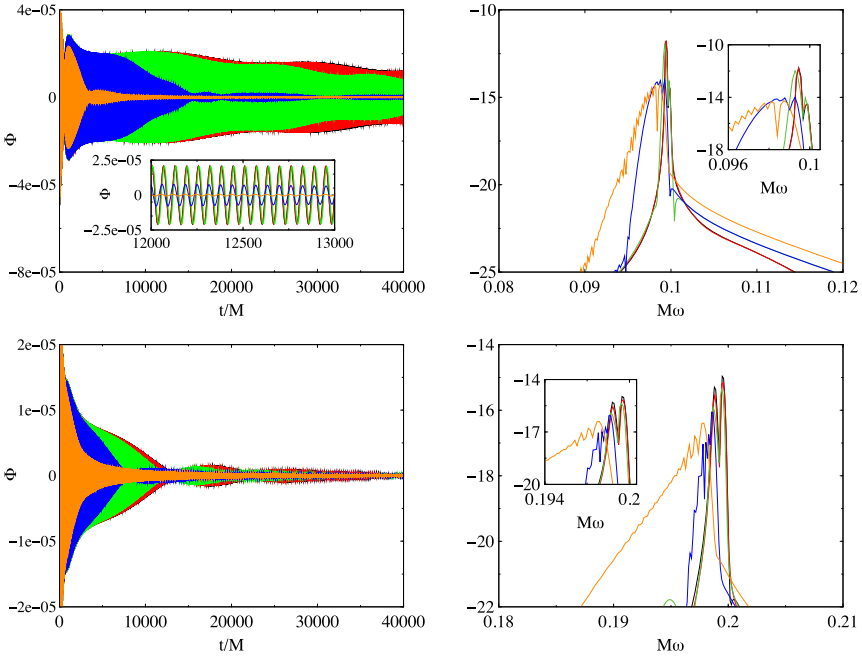

FIG. 2. *Left column*: Time evolution of the scalar field with mass $M\mu = 0.1$ (top) and $M\mu = 0.2$ (bottom) and for different BH growth rates, $\dot{M}_{\rm BH}$. *Right column*: Corresponding power spectra obtained from Fourier transforming the time series shown on the left. The units in the vertical axis are arbitrary.

As expected, in the nonaccreting BH case, the oscillation frequencies shown in Fig. 2 and reported in Table I are in very good agreement with those found in Ref. [22] in the test-field regime and for the same scalar field masses. Despite the fact that in the current work we are not evolving the spacetime, while we did in Ref. [22], the discarded backreaction on the evolution of the scalar field is negligible because of the small energy of the scalar field in our models.

Our results also indicate that the frequencies of the quasibound states decrease as the mass of the BH increases. One may infer such behavior from a classical mechanics analogy. Let us consider the solution of the one-dimensional wave equation in flat spacetime with moving boundaries. If the boundary moves with a constant velocity v, an explicit solution can be obtained. Let us consider the oscillation of a string along the x direction. The string is constrained at two points, $x = 0$ and $x = vt$, and the amplitude of the wave is given by $h(t, x)$. We are interested in the solution of the equation

$$\partial_{tt}h(t,x) - \partial_{xx}h(t,x) = 0, \tag{22}$$

in the interval $0 \le x \le vt$, with the boundary conditions, $h(0,t) = h(vt,t) = 0$, and initial data, $h(x,0) = h_0(x)$ $\partial_t h(0,x) = u_0(x)$.

The general solution of Eq. (22) is a periodic function in $\log[(1-v)t]$ with period $T = \log(\frac{1+v}{1-v})$ of the form

$$h(t,x) = \sum_{n=-\infty}^{+\infty} C_n \left\{ \exp\left[i \frac{2n\pi}{T} \tilde{\alpha} \right] - \exp\left[i \frac{2n\pi}{T} \tilde{\beta} \right] \right\}, \tag{23}$$

where $\tilde{\alpha} = \log(t+x)$ and $\tilde{\beta} = \log(t-x)$ and the coefficients C_n are determined by the initial conditions. What is important to notice in this solution is that the frequency decreases as the velocity of the boundary increases. One may think that a similar process happens when the mass of the BH increases since that implies the displacement of the position of the horizon and, thus, the displacement of the position of the boundary that confines the scalar field.

2. Scalar field energy

The time evolution of the energy of the scalar field, computed with Eq. (11), is shown in solid lines in Figs. 3 and 4 for all scalar field masses, $M\mu = \{0.05, 0.08, 0.10, 0.15, 0.20\}$. The dashed lines in the three panels of Fig. 3 correspond to analytic fits of the numerical data, that we discuss below. These two figures show that the initial energy of the scalar field is (almost) the same for all models considered. Both figures show that the decrease of

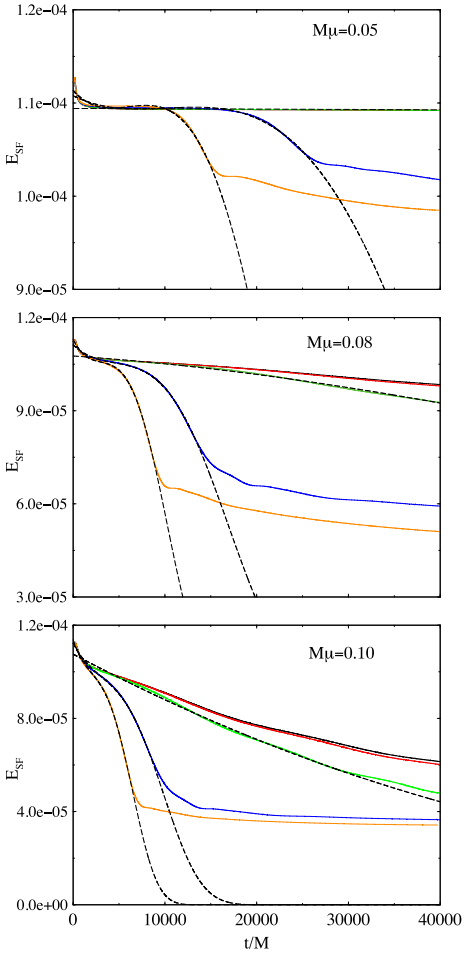

FIG. 3. Time evolution of the scalar field energy for different values of the BH mass growth rate and for the scalar field masses $M\mu = \{0.05, 0.08, 0.10\}$, from top to bottom. The dashed black lines correspond to the exponential fit for the three models with a higher BH mass growth rate.

the initial energy is more significant and faster the larger the scalar field mass and the larger the BH growth.

Let us first discuss the lightest scalar field models. In Fig. 3, corresponding to $M\mu = \{0.05, 0.08, 0.10\}$, we see that for the smallest, nonzero value of $\dot{M}_{\rm BH}$ the decay of the scalar field energy is very close to the nonaccreting case (compare red and black curves). For the higher values of the mass flux, the energy at early times begins decaying exponentially with a small slope, but at some point, the falling of scalar field energy onto the BH speeds up. The appearance of this effect depends on the BH mass growth

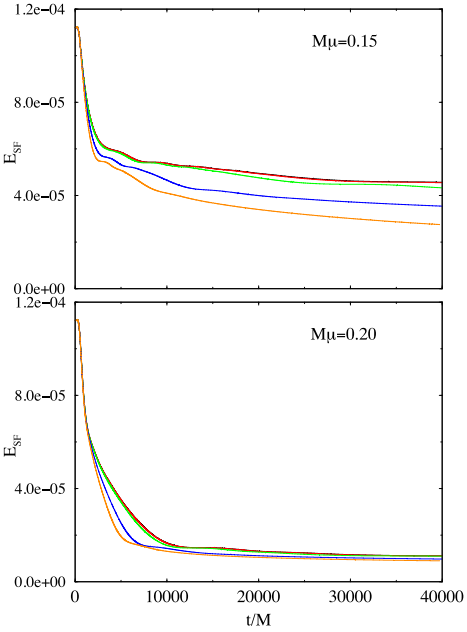

FIG. 4. Time evolution of the scalar field energy for the masses $M\mu = \{0.15, 0.20\}$.

rate, appearing earlier for higher $\dot{M}_{\rm BH}$. After some time, the process stops, and the scalar field energy settles to an almost constant value, given by the energy of the part of the scalar field that has escaped to infinity. There is, however, part of the scalar field still localized around the BH in the form of quasistationary bound states.

On the other hand, Fig. 4 shows that for $M\mu = 0.15$ and 0.2 the decay rate of the energy of the scalar field is much faster than for the lightest models and the energy decreases almost identically regardless of the BH mass growth rate. This becomes clear if we check the imaginary part of the frequency reported in column 6 of Table I for these scalar field masses. The imaginary part of the frequency does not vary significantly when the growth of the BH mass is faster.

However, as we mentioned before for the smaller values of the scalar field mass displayed in Fig. 3, the energy decay changes from an exponential decay with a linear exponent (the usual feature of a quasistationary state around a nonaccreting Schwarzschild BH) to an exponential decay with both *quadratic* and *cubic* exponents, as shown by the analytic fits. These parts are entirely due to the growth of the BH and are orders of magnitude smaller than the linear part of the exponential decay. Therefore, they are only significant for sufficiently long times. Columns 6, 7, and 8 of Table I report the values of the rate of decay according to the fit $\exp[-ct^3 - bt^2 - at]$, where a, b, and c are the linear, quadratic, and cubic

coefficients, respectively. The dashed black lines in Fig. 3 fit part of the time evolution of the scalar field energy for the three models with a higher BH growth rate. The values of the cubic, quadratic, and linear coefficients increase with the scalar field mass, as can be inferred from Table I.

B. Mirrored states

In order to further understand the influence of the growth of the BH mass in the evolution of the scalar field, we turn now to describe the results corresponding to the evolution of an additional set of 21 models. These models correspond to Schwarzschild BH spacetimes with seven different BH mass growth rates, namely $\dot{M}_{\rm BH} = \{0, 5\times10^{-9}, 5\times10^{-8}, 5\times10^{-7}, 5\times10^{-6}, 5\times10^{-5}, 10^{-4}\}$, and we impose reflecting boundary conditions for the scalar field at some radius, as done in Ref. [32]. At the location of the mirror, $r = r_{\rm m}$, and beyond, the scalar field Φ is required to vanish. This leads to a discontinuity in the Φ derivatives. In our simulations, the mirror is located at $r_{\rm m} = 200M$, and the boundary conditions for the scalar field are

$$\Phi(r_{\rm m}) = \Psi(r_{\rm m}) = \Pi(r_{\rm m}) = 0,$$
$$\partial_r\Phi(r_{\rm m}) = \partial_r\Psi(r_{\rm m}) = \partial_r\Pi(r_{\rm m}) = 0. \qquad (24)$$

We consider again a Gaussian distribution for the scalar field, with $r_0 = 50M$ and $\lambda = 25$. As mentioned before, using a mirror is an idealized setup, it has pragmatic advantages since it allows us to perform longer runs and to study smaller growth rates. The spacetime is still given by the analytic solution of Sec. II B (hence, there are no reflections of the spacetime variables coming in from the outer boundary), and since the scalar field is now enclosed in a cavity, no part of the scalar field propagates away from the BH. Therefore, all the oscillatory modes will be trapped in this case, not only those with $\omega^2 < \mu^2$, and the energy evolution will not be dominated by the asymptotic, scalar field energy minimum. In this idealized situation, the entire scalar field will fall into the BH with time.

The results of this new set of simulations are similar to those discussed in the preceding section. They are summarized in Table II for the lightest scalar field models analyzed, namely $M\mu = \{0.05, 0.08, 0.10\}$. Again, the scalar field oscillates with a fundamental frequency and higher overtones (of which Table II only reports the first one), but since the higher frequencies decay faster, we end up with only the fundamental mode of oscillation. As for the cases without a mirror, the real part of the frequency decreases with $\dot{M}_{\rm BH}$. In the case of a nonaccreting BH, the decay of the energy (and of the amplitude of the oscillations) is exponential with a single linear exponent as expected. As done before, in the case of accreting BHs and long evolution times, we fit the energy decay to the analytic formula $\exp[-dt^4 - ct^3 - bt^2 - at]$, with linear, quadratic, cubic, and quartic terms. These parameters seem to depend on the BH mass growth rate, and, probably, we could fit it to even higher-order polynomials if we could reach even longer simulations. Indeed, some of the models reported in

TABLE II. Same as Table I but for the simulation setup corresponding to a scalar field enclosed in a cavity. The initial Gaussian pulse is, in this case, located at $r_0 = 50M$ with half-width $\lambda = 25$.

		$M\omega$		Ms							
$\dot{M}_{\rm BH}$	$M\mu$	1	2	a	b	c	d	e	f	$M_{\rm BH}$	$t_{\rm final}$
0.00	0.05	0.05168	0.05781	1.593E-05	0	0	0	0	0	1.000	8.0E05
5E-09	0.05	0.05168	0.05781	1.591E-05	9.738E-14	···	···	···	···	1.004	8.0E05
5E-08	0.05	0.05167	0.05780	1.590E-05	1.041E-12	···	···	···	···	1.040	8.0E05
5E-07	0.05	0.05163	0.05776	1.647E-05	7.612E-12	9.051E-18	···	···	···	1.221	4.0E05
5E-06	0.05	0.05137	0.05754	5.837E-06	6.122E-10	-5.102E-15	2.179E-20	···	···	3.201	2.4E05
5E-05	0.05	0.05076	0.05688	-2.713E-05	2.762E-08	-1.928E-12	4.847E-17	···	···	6.686	3.8E04
1E-04	0.05	0.05055	0.05655	8.341E-05	4.054E-08	-6.348E-12	3.415E-16	···	···	9.025	2.2E04
0.00	0.08	0.08039	0.08431	3.265E-05	0	0	0	0	0	1.000	4.0E05
5E-09	0.08	0.08039	0.08431	3.260E-05	2.455E-13	···	···	···	···	1.002	4.0E05
5E-08	0.08	0.08038	0.08430	3.272E-05	2.358E-12	···	···	···	···	1.020	4.0E05
5E-07	0.08	0.08034	0.08426	3.368E-05	2.042E-11	3.407E-17	···	···	···	1.221	4.0E05
5E-06	0.08	0.08012	0.08406	5.378E-05	2.742E-10	-3.517E-15	5.500E-20	···	···	2.226	1.6E05
5E-05	0.08	0.07936	0.08337	2.912E-04	-2.237E-08	5.539E-13	5.264E-17	···	···	3.857	2.7E04
1E-04	0.08	0.07981	0.08293	-6.087E-04	5.364E-07	-1.377E-10	1.577E-14	-7.606E-19	1.332E-23	6.050	1.8E04
0.00	0.10	0.09975	0.10287	6.355E-05	0	0	0	0	0	1.000	4.0E05
5E-09	0.10	0.09975	0.10287	6.348E-05	6.340E-13	···	···	···	···	1.002	4.0E05
5E-08	0.10	0.09974	0.10286	6.361E-05	6.300E-12	···	···	···	···	1.020	4.0E05
5E-07	0.10	0.09969	0.10281	6.898E-05	2.991E-11	1.283E-16	···	···	···	1.191	3.5E05
5E-06	0.10	0.09945	0.10262	9.451E-05	1.602E-10	4.284E-15	9.373E-20	···	···	1.733	1.1E05
5E-05	0.10	0.09864	0.10179	6.781E-04	-1.537E-07	1.690E-11	-5.78E-16	7.136E-21	···	3.490	2.5E04
1E-04	0.10	0.09828	0.10151	7.818E-04	-3.295E-07	6.964E-11	-4.692E-15	1.153E-19	···	5.474	1.7E04

Table II can already be fitted with higher-order terms (even up to fifth or sixth, coefficients e and f, respectively) for the current evolution times considered. The sixth-order term is considered for only one particular model, even if it is very small, in order to keep the highest-order term always positive and, therefore, drive the fit to tend to zero for $t \to \infty$. The coefficients also depend on the scalar field mass, decreasing for smaller values of μ.

In Fig. 5, we plot (solid lines) time evolutions of the scalar field energy for the mirrored states of models with masses $M\mu = \{0.05, 0.08, 0.10\}$ (from top to bottom) together with their corresponding fits (black dashed lines). The results discussed in the previous section become more clear in this idealized setup. Increasing the BH growth rate speeds up the decay of the energy. Moreover, the decay is longer than for the case of quasibound states without a mirror, and, contrary to what happens when there is an outgoing boundary, the energy does not relax to the value corresponding to that part of the scalar field that escapes to infinity.

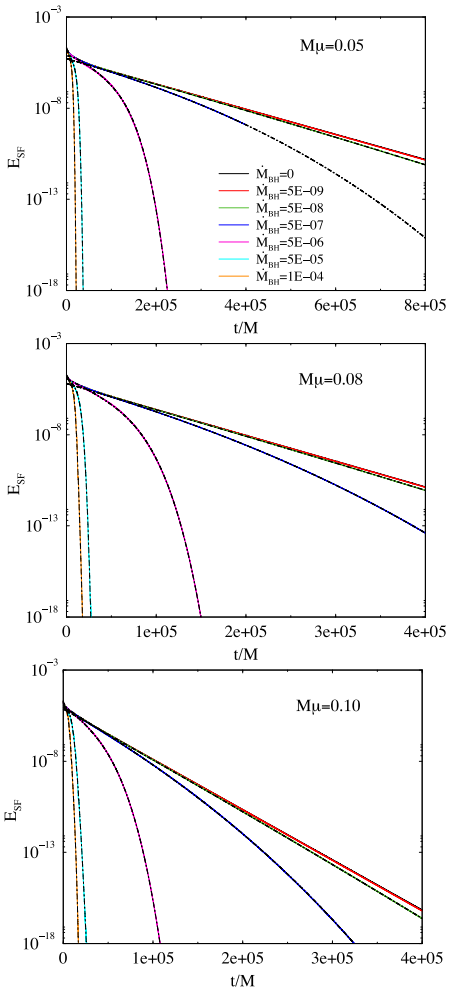

FIG. 5. Time evolutions (solid lines) of the scalar field energy for three scalar field masses $M\mu = \{0.05, 0.08, 0.10\}$ (from top to bottom) and seven different values of $\dot{M}_{BH}$ (stated in the legend). The black dashed lines indicate the analytic fits. Notice that the scale of the horizontal axis is different in the top panel (the simulation is twice as long) and that the color criterion is different to that of Fig. 1 due to the larger sample of $\dot{M}_{BH}$ included in this figure.

C. Comparison with realistic BH mass growth rates

We can estimate the rate of the BH mass growth due to accretion using the bolometric luminosity of an active galaxy nuclei (AGN) as [31,37]

$$L_{\rm bol} = \frac{\eta \dot{M}_{\rm BH}}{(1-\eta)} c^2, \tag{25}$$

where $L_{\rm bol}$ is the bolometric luminosity, $\dot{M}_{\rm BH}$ is the BH mass growth rate, c is the speed of light, and η is the radiative efficiency, for which we take the commonly adopted empirical value of 0.1 [38]. Recently, bolometric luminosities larger than $10^{14} L_\odot$ have been discovered [31]. According to Eq. (25), this corresponds to $\dot{M}_{\rm BH} \sim 10^{-11}$ in our units.

In Fig. 6, we plot several BH growth rates in geometrized units of AGN bolometric luminosities as a function of the redshift z. We use data from two different samples, namely

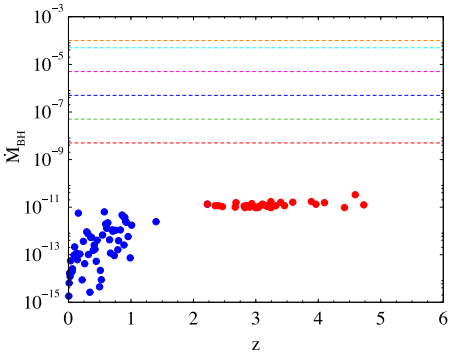

FIG. 6. AGN BH growth rates in geometrized units as a function of redshift. The dashed horizontal lines indicate the values of $\dot{M}_{\rm BH} = \{5\times10^{-9}(\text{red}), 5\times10^{-8}(\text{green}), 5\times10^{-7}(\text{blue}), 5\times10^{-6}(\text{magenta}), 5\times10^{-5}(\text{cyan}), 1\times10^{-4}(\text{orange})\}$ considered in our numerical study. The symbols correspond to observational data from Refs. [31,39] (red and blue points, respectively). Our values are about 2 orders of magnitude larger than the largest observational value.

that of Ref. [39], for redshifts between 0.01 and 2.224, and the luminosities of Wide-field Infrared Survey Explorer-selected galaxies reported recently in Ref. [31], which include redshifts up to $z = 4.593$. The larger luminosities are obtained precisely for the higher redshifts, corresponding to the growth phase of SMBHs. Figure 6 shows that the maximum growth rate is only about 2 orders of magnitude smaller than the smallest $\dot{M}_{\rm BH}$ we can afford in our simulations.

The influence of the accretion rate on the energy decay depends on the scalar field mass and decreases for smaller $M\mu$. Therefore, for the expected value of scalar field dark matter models, the actual value of $\dot{M}_{\rm BH}$ is expected to be fairly small. However, the growth of SMBH seeds to their actual masses, $\sim 10^9 M_\odot$, is believed to take place only during 1% of their lifetime, i.e., about 10^9 years. Therefore, the role played by high-order terms in the evolution of the energy could become significant during this phase and increase the amount of scalar field that may end up being absorbed by the BH during this period.

Finally, we can extrapolate our results to the realistic case of ultralight scalar field masses. In the case of a test field, the decay rate of the dynamical resonances is related to the imaginary part of the quasiresonant frequencies, and thus its half-life time $t_{1/2}$ is inversely proportional to $\mathrm{Im}(M\omega)$ [20]. For an accreting BH and the long evolution times reported in this work, we have shown that terms higher than linear are important to capture the decay rate of the energy of the scalar field. We can then use the relation $E_{\rm SF} = E^0_{\rm SF} \exp\left[-(at + bt^2 + ct^3)\right]$ to solve for $t_{1/2}$, which corresponds to the time when the energy of the scalar field has decreased to half its initial value. The result of this exercise is depicted in Fig. 7, which shows $t_{1/2}$ as a function of $M\mu$ for all five values of $\dot{M}_{\rm BH}$ used in the "unmirrored" setup simulations. (We use in this figure the same color criterion for $\dot{M}_{\rm BH}$ as defined in Fig. 1.) The symbols in the figure indicate the values of $t_{1/2}$ for the lighter values of the scalar field mass ($M\mu = 0.05$, 0.08, and 0.1) used in our simulations. Following Ref. [20], we do a least-squares fit to these data and extrapolate our results to lower values of $M\mu$. Figure 7 shows that, even for high mass accretion rates, e.g., $\dot{M}_{\rm BH} = 5 \times 10^{-7}$ (red curve) quasibound states around accreting BHs can survive for time scales significantly longer than the age of the Universe.

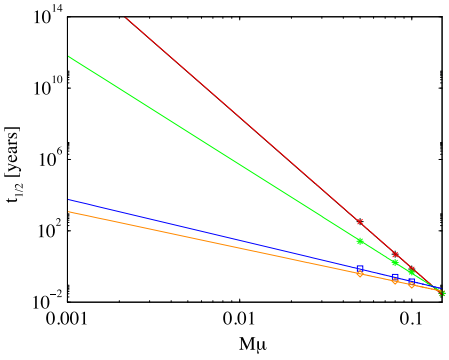

FIG. 7. Half-life of the quasiresonant frequencies of the quasibound states for different scalar field masses and different BH growth rates. The solid lines are least-square fits to the numerical data.

IV. CONCLUSIONS

We have studied the properties of scalar field quasibound states in the background of an accreting, spherically symmetric BH. We have assumed that the BH mass grows due to matter accretion, describing the effect of the increase of the BH mass on the properties of the quasibound states of the surrounding scalar field distribution. For our study, we have solved the Klein-Gordon equation numerically, mimicking the evolution of the spacetime through a sequence of exact Schwarzschild BH solutions of increasing mass, using analytic expressions which depend only on the BH mass parameter. Our numerical approach has been limited to spherical symmetry and has been based on spherical coordinates and a partially implicit Runge-Kutta numerical scheme for the time update of the Klein-Gordon equation. To study the effect of accretion on the scalar field evolution in affordable computational times, we have resorted to large growth rates, at best 2 orders of magnitude larger than the largest observational estimations.

By performing a Fourier transform of the time series of our numerical data, we have been able to characterize the scalar field states by their distinctive oscillation frequencies. It has been found that the frequencies decrease with increasing BH mass. Moreover, accretion results in a significative increase of the exponential decay of the scalar field energy due to the presence of terms of order higher than linear in the exponent. These terms are zero in the nonaccreting Schwarzschild BH case, resulting in a linear exponential fit. Our computational setup has considered both outgoing and reflecting boundary conditions at the outer radial boundary, the latter describing a scalar field enclosed in a cavity. By imposing reflecting boundary conditions at a finite distance, the scalar field does not escape to infinity, and we can isolate the influence of accretion. Such configuration, albeit artificial, has helped us to study the higher-order terms that appear in the exponential decay of the energy. Finally, we have compared our BH mass growth rates with estimates from observational surveys, and we have been able to extrapolate our results to realistic values of the scalar field mass $M\mu$. We have found thats, even for the high mass accretion rates considered in this work, e.g., $\dot{M}_{\rm BH} = 5 \times 10^{-7}$, quasibound states around accreting BHs can survive for cosmological time scales. The results obtained in this paper add further support to the intriguing possibility of the existence of dark

matter halos based on (ultralight) scalar fields surrounding SMBHs at galactic centers.

ACKNOWLEDGMENTS

This work was supported in part by the Spanish MINECO (Grant No. AYA2013-40979-P), by the Generalitat Valenciana (Grant No. PROMETEOII-2014-069), by the CONACyT-México Grant No. 233137 by Instituto de Ciencias Fisicas-UNAM, and by the Max-Planck-Institut für Astrophysik. The computations have been performed at the Servei d'Informàtica de la Universitat de València.

[1] L. Ferrarese and H. Ford, Space Sci. Rev. **116**, 523 (2005).
[2] J. Kormendy and L. C. Ho, Annu. Rev. Astron. Astrophys. **51**, 511 (2013).
[3] G. Kauffmann and M. Haehnelt, Mon. Not. R. Astron. Soc. **311**, 576 (2000).
[4] M. Volonteri, F. Haardt, and P. Madau, Astrophys. J. **582**, 559 (2003).
[5] A. J. Barth, P. Martini, C. H. Nelson, and L. C. Ho, Astrophys. J. **594**, L95 (2003).
[6] C. J. Willott, W. J. Percival, R. J. McLure, D. Crampton, J. B. Hutchings, M. J. Jarvis, M. Sawicki, and L. Simard, Astrophys. J. **626**, 657 (2005).
[7] D. J. Mortlock *et al.*, Nature (London) **474**, 616 (2011).
[8] M. Volonteri, Astron. Astrophys. Rev. **18**, 279 (2010).
[9] P. Madau and M. J. Rees, Astrophys. J. Lett. **551**, L27 (2001).
[10] E. Barausse, J. Bellovary, E. Berti, K. Holley-Bockelmann, B. Farris, B. Sathyaprakash, and A. Sesana, J. Phys. Conf. Ser. **610**, 012001 (2015).
[11] M. C. Begelman, Mon. Not. R. Astron. Soc. **187**, 237 (1979).
[12] T. Alexander and P. Natarajan, Science **345**, 1330 (2014).
[13] J. C. McKinney, A. Tchekhovskoy, A. Sadowski, and R. Narayan, Mon. Not. R. Astron. Soc. **441**, 3177 (2014).
[14] V. Bromm and A. Loeb, Astrophys. J. **596**, 34 (2003).
[15] Z. Haiman and A. Loeb, Astrophys. J. **552**, 459 (2001).
[16] M. C. Begelman, M. Volonteri, and M. J. Rees, Mon. Not. R. Astron. Soc. **370**, 289 (2006).
[17] M. C. Begelman, Mon. Not. R. Astron. Soc. **402**, 673 (2010).
[18] L. Mayer, S. Kazantzidis, A. Escala, and S. Callegari, Nature (London) **466**, 1082 (2010).
[19] J. Barranco, A. Bernal, J. C. Degollado, A. Diez-Tejedor, M. Megevand, M. Alcubierre, D. Núñez, and O. Sarbach, Phys. Rev. D **84**, 083008 (2011).
[20] J. Barranco, A. Bernal, J. C. Degollado, A. Diez-Tejedor, M. Megevand, M. Alcubierre, D. Núñez, and O. Sarbach, Phys. Rev. Lett. **109**, 081102 (2012).
[21] J. Barranco, A. Bernal, J. C. Degollado, A. Diez-Tejedor, M. Megevand, M. Alcubierre, D. Núñez, and O. Sarbach, Phys. Rev. D **89**, 083006 (2014).
[22] N. Sanchis-Gual, J. C. Degollado, P. J. Montero, and J. A. Font, Phys. Rev. D **91**, 043005 (2015).
[23] N. Sanchis-Gual, J. C. Degollado, P. J. Montero, J. A. Font, and V. Mewes, Phys. Rev. D **92**, 083001 (2015).
[24] M. Hannam, S. Husa, D. Pollney, B. Brügmann, and N. O. Murchadha, Phys. Rev. Lett. **99**, 241102 (2007).
[25] T. W. Baumgarte and S. G. Naculich, Phys. Rev. D **75**, 067502 (2007).
[26] C. J. Willott, L. Albert, D. Arzoumanian, J. Bergeron, D. Crampton, P. Delorme, J. B. Hutchings, A. Omont, C. Reylé, and D. Schade, Astron. J. **140**, 546 (2010).
[27] X. Fan, M. A. Strauss, R. H. Becker, R. L. White, J. E. Gunn, G. R. Knapp, G. T. Richards, D. P. Schneider, J. Brinkmann, and M. Fukugita, Astron. J. **132**, 117 (2006).
[28] V. Springel, T. Di Matteo, and L. Hernquist, Mon. Not. R. Astron. Soc. **361**, 776 (2005).
[29] J. Hu, Y. Shen, Y.-Q. Lou, and S. Zhang, Mon. Not. R. Astron. Soc. **365**, 345 (2006).
[30] T. Di Matteo, J. Colberg, V. Springel, L. Hernquist, and D. Sijacki, Astrophys. J. **676**, 33 (2008).
[31] C.-W. Tsai *et al.*, Astrophys. J. **805**, 90 (2015).
[32] N. Sanchis-Gual, J. C. Degollado, P. J. Montero, J. A. Font, and C. Herdeiro, Phys. Rev. Lett. **116**, 141101 (2016).
[33] P. J. Montero and I. Cordero-Carrion, Phys. Rev. D **85**, 124037 (2012).
[34] I. Cordero-Carrión and P. Cerdá-Durán, arXiv:1211.5930.
[35] I. Cordero-Carrión and P. Cerdá-Durán, *Advances in Differential Equations and Applications*, SEMA SIMAI Springer Series Vol. 4 (Springer International, Switzerland, 2014).
[36] H. Okawa, H. Witek, and V. Cardoso, Phys. Rev. D **89**, 104032 (2014).
[37] B. Weihao and Z. Yongheng, arXiv:astro-ph/0305095.
[38] Q. Yu and S. Tremaine, Mon. Not. R. Astron. Soc. **335**, 965 (2002).
[39] J.-H. Woo and C. M. Urry, Astrophys. J. **579**, 530 (2002).

Explosion and Final State of an Unstable Reissner-Nordström Black Hole

Nicolas Sanchis-Gual,[1] Juan Carlos Degollado,[2,3] Pedro J. Montero,[4] José A. Font,[1,5] and Carlos Herdeiro[6]
[1]Departamento de Astronomía y Astrofísica, Universitat de València, Doctor Moliner 50, 46100, Burjassot (València), Spain
[2]Instituto de Ciencias Físicas, Universidad Nacional Autónoma de México, Apartado Postal 48-3, 62251 Cuernavaca, Morelos, México
[3]Departamento de Ciencias Computacionales, Centro Universitario de Ciencias Exactas e Ingeniería, Universidad de Guadalajara Avenida Revolución 1500, Colonia Olímpica C.P. 44430 Guadalajara, Jalisco, Mexico
[4]Max-Planck-Institut für Astrophysik, Karl-Schwarzschild-Strasse 1, 85748 Garching bei München, Germany
[5]Observatori Astronòmic, Universitat de València, C/ Catedrático José Beltrán 2, 46980 Paterna (València), Spain
[6]Departamento de Física da Universidade de Aveiro and CIDMA, Campus de Santiago, 3810-183 Aveiro, Portugal
(Received 22 December 2015; revised manuscript received 26 February 2016; published 7 April 2016)

A Reissner-Nordström black hole (BH) is superradiantly unstable against spherical perturbations of a charged scalar field enclosed in a cavity, with a frequency lower than a critical value. We use numerical relativity techniques to follow the development of this unstable system—dubbed *a charged BH bomb*—into the nonlinear regime, solving the full Einstein-Maxwell-Klein-Gordon equations, in spherical symmetry. We show that (i) the process stops before all the charge is extracted from the BH, and (ii) the system settles down into a hairy BH: a charged horizon in equilibrium with a scalar field condensate, whose phase is oscillating at the (final) critical frequency. For a low scalar field charge q, the final state is approached smoothly and monotonically. For large q, however, the energy extraction overshoots, and an explosive phenomenon, akin to a *bosenova*, pushes some energy back into the BH. The charge extraction, by contrast, does not reverse.

DOI: 10.1103/PhysRevLett.116.141101

Introduction.—A remarkable feature of rotating (Kerr) black holes (BHs) is that they may, classically, give away energy and angular momentum. A bosonic field can be the extraction mediator. Its waves, with sufficiently slowly rotating phases, are amplified when scattering off a corotating BH [1–9]. Trapping these *superradiantly scattered* waves around the BH, the bosonic field piles up exponentially into a gravitating macroscopic Bose-Einstein-type condensate. It has been conjectured that an explosive phenomenon ensues, dubbed *a BH bomb* [3]. Understanding the explosion and final state of the BH bomb has been an open issue since the 1970s [10].

The BH bomb proposal was based on linear studies of the superradiant instability. The conjectured explosive regime, however, is nonlinear, and numerical evolutions using the full Einstein equations are mandatory to probe it. Unfortunately, the growth rates of superradiant instabilities for rotating BHs are too small [7,11], rendering the numerical evolution of the rotating BH bomb a *tour de force* with current numerical relativity (NR) technology [12,13]. But suggestive progress has come from two other types of nonlinear studies. First, considering a test bosonic field with nonlinear dynamics on the Kerr BH [14,15] produced evidence that an explosive event indeed occurs, akin to the *bosenova* observed in condensed matter systems [16]. Second, *hairy BH* solutions with a stationary geometry of the fully nonlinear Einstein-bosonic field system were found precisely at the threshold of the instability [17,18].

In the absence of the NR technology to address the rotating BH bomb, we are led to the more favorable situation that occurs for charged (Reissner-Nordström) BHs. An analogue process to superradiant scattering can take place, by which Coulomb energy and charge are extracted from the BH by a *charged* bosonic field [19,20]. This occurs for sufficiently small frequency waves and for a field with the same charge (sign) as the BH. Introducing a trapping mechanism, a *charged BH bomb* forms. On the one hand, linear studies show that the growth rates of such charged superradiant instability can be much larger than for their rotating counterparts [21–23]. On the other hand, the instability can occur within spherical symmetry, in contrast with the rotating case that breaks even axial symmetry. These features make the study of the charged BH bomb amenable with current NR techniques.

In this Letter, we report NR simulations, using the full Einstein equations, of the charged BH bomb. As a simple model, we take a charged scalar field (SF) as the bosonic mediator and enclose the BH-SF system in a cavity, as a trapping mechanism. We find that the nonlinear regime may be, albeit needs not be, explosive. Moreover, we establish that, regardless of how explosive the nonlinear regime is, the generic final state is a *hairy* BH: a charged horizon surrounded by a SF condensate storing part of the charge and energy of the initial BH and with a phase oscillating at the threshold frequency of the superradiant instability. Hairy BHs of this sort have been recently constructed and shown to be stable [24].

Framework.—We consider the Einstein-Maxwell-Klein-Gordon (EMKG) system described by the action $\mathcal{S} = \int d^4x\sqrt{-g}\mathcal{L}$, with Lagrangian density

$$\mathcal{L} = \frac{R - F_{\alpha\beta}F^{\alpha\beta}}{16\pi} - \frac{1}{2}D_\alpha\Phi(D^\alpha\Phi)^* - \frac{\mu^2}{2}|\Phi|^2, \quad (1)$$

where R is the Ricci scalar, $F_{\alpha\beta} \equiv \nabla_\alpha A_\beta - \nabla_\beta A_\alpha$, A_α is the electromagnetic potential, D_α is the gauge covariant derivative, $D_\alpha \equiv \nabla_\alpha - iqA_\alpha$, and q and μ are the charge and the mass of the scalar field. Newton's constant, the speed of light, and $4\pi\epsilon_0$ are set to 1 in our units.

To address numerically the EMKG system, we use a generalized BSSN formulation [25,26] adapted to spherical symmetry [27–29], and the code described in Refs. [30,31]. This code was upgraded to account for Maxwell's equations and energy-momentum tensor. The $3+1$ metric split reads $ds^2 = -(\alpha^2 + \beta^r\beta_r)dt^2 + 2\beta_r dtdr + e^{4\chi}[adr^2 + br^2 d\Omega_2]$, where the lapse α, shift component β^r, and the (spatial) metric functions χ, a, b depend on t, r. The electric field $E^\mu = F^{\mu\nu}n_\nu$ has only a radial component, and the magnetic field $B^\mu = \star F^{\mu\nu}n_\nu$ vanishes, where n^μ is the 4-velocity of the Eulerian observer [32]. Spherical symmetry implies we only have to consider the equations for the electric potential ${}^{(3)}\varphi = -A^\mu n_\mu$ and the radial component of both the vector potential A^r and the electric field E^r.

At $r = r_{\rm m}$ (mirror) and beyond, the SF Φ is required to vanish. This leads to a discontinuity in the Φ derivatives. In our scheme, however, the consequent constraint violation does not propagate towards $r < r_m$. We further impose parity boundary conditions at the origin (puncture) for the SF.

Initial data and parameters.—The EMKG system admits as a solution the Reissner-Nordström BH with Arnowitt, Deser and Misner mass M and charge Q together with a vanishing SF. We take the initial data to describe one such BH with $M = 1$ and $Q = 0.9$. The former will set the main scale in the problem. Perturbing such a BH with a spherical scalar wave $\Phi = e^{-iwt}f(r)$ yields a superradiant instability if (i) $w < w_c \equiv q\phi_H$, where ϕ_H is the electric potential at the horizon, and (ii) the perturbation is trapped by imposing reflecting boundary conditions for the SF at the spherical surface $r = r_m$ (sufficiently) outside the horizon.

To trigger the instability, we set as the SF initial data a Gaussian distribution of the form $\Phi = A_0 e^{-(r-r_0)^2/\lambda^2}$, with $A_0 = 3\times10^{-4}$, $r_0 = 7M$, and $\lambda = \sqrt{2}$ and set the mirror at $r_m = 14.2M$. The SF mass is fixed to $\mu = 0.1/M$, and we focus on models with different values of the SF charge qM, namely, $qM = 0.8$, 5, 20, and 40.

The logarithmic numerical grid extends from the origin to $r = 10^4 M$ and uses a maximum resolution of $\Delta r = 0.025M$. Simulations with varying resolutions have shown the expected second-order convergence of the code. An analysis of constraint violations, which we have observed to be always around 10^{-5} outside the horizon and converging away at the expected second-order rate together with a broader survey of the parameter space is presented as Supplemental Material [33].

Physical quantities.—The extraction of energy and charge from the BH by the superradiant instability is compatible with the second law of thermodynamics. This can be checked by monitoring the irreducible mass [35] of the BH computed in terms of the apparent horizon (AH) area $A_{\rm AH}$ on each time slice as $M_{\rm irr} = \sqrt{A_{\rm AH}/(16\pi)}$. For the initial RN BH, $M_{\rm irr}^{\rm ini} \simeq 0.718M$, and we will see that the final BH has a larger $M_{\rm irr}$ for all cases.

The energy transfer from the BH to the SF can be established by computing the energy stored in the latter. This is given by the (spatial) volume integral

$$E_{\rm SF} = \int_{r_{\rm AH}}^{r_m} \mathcal{E}^{\rm SF} dV, \quad (2)$$

where $\mathcal{E}^{\rm SF}$ is the projection of the stress-energy tensor of the scalar field along the normal direction to the $t =$ constant surfaces [36].

The charge transfer, on the other hand, is monitored by tracking both the SF charge using a formula similar to Eq. (2) replacing $\mathcal{E}^{\rm SF}$ by the charge density and the BH charge $Q_{\rm BH}$ evaluated at the AH as [32]

$$Q_{\rm BH} = (r^2 e^{6\chi}\sqrt{ab^2}E^r)|_{\rm AH}. \quad (3)$$

Finally, to establish the nature of the final BH, we compute the electric potential at the AH and the corresponding critical frequency $w_c = q\phi_H$ as $\phi_H = \alpha^{(3)}\varphi - \beta^r a_r|_{r=r_{\rm AH}}$, where $a_r = \gamma_{rr}A^r$ and γ_{rr} is the corresponding component of the spatial metric [37].

Numerical evolutions and final state.—Solving numerically the EMKG system, we obtain a time series for the evolution of the SF real and imaginary parts at a chosen observation point, say, $r_{\rm obs} = 10M$. This is illustrated in Fig. 1 for two values of qM.

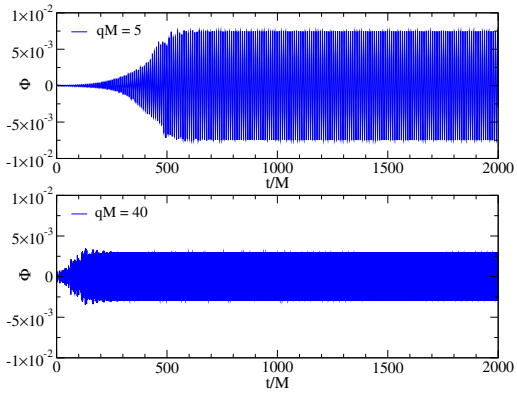

FIG. 1. Time evolution of the SF real part extracted at $r_{\rm obs} = 10M$, for $qM = 5$ (top) and 40 (bottom). The imaginary part is analogous (but with opposite phase at late times).

TABLE I. Summary of physical quantities for the runs with different qM (first column): e-folding time during the growth phase (second column), final oscillation frequency of the SF phase and final critical frequency (third and fourth columns), initial and final SF energy and their ratio (fifth to seventh columns), and final BH irreducible mass and ratio of the final to initial BH and SF charge (eighth to tenth columns).

qM	τ/M	$M\omega_{\rm SF}^{\rm fin}$	$M\omega_{c}^{\rm fin}$	$E_{\rm SF}^{\rm ini}/M$	$E_{\rm SF}^{\rm fin}/M$	$E_{\rm SF}^{\rm fin}/E_{\rm SF}^{\rm ini}$	$M_{\rm irr}^{\rm fin}/M$	$Q_{\rm BH}^{\rm fin}/Q$	$Q_{\rm SF}^{\rm fin}/Q$
0.8	4.8E02	0.277	0.278	3.00E-05	1.32E-01	4.40E03	0.728	45%	55%
5.0	1.1E02	0.642	0.642	4.31E-05	3.93E-02	9.12E02	0.875	6.0%	94%
20.0	4.8E01	1.756	1.757	3.13E-04	1.31E-02	4.19E01	0.924	1.0%	99%
40.0	2.9E01	3.130	3.129	8.95E-04	8.02E-03	8.96E00	0.942	0.1%	99.9%

Figure 1 demonstrates the existence of two distinct phases in the SF evolution. The first phase is the *superradiant growth phase* known from linear theory. During this phase, the SF is amplified, extracting energy and charge from the BH, and its amplitude grows exponentially $|\Phi| \sim e^{t/\tau}$; a numerical fit for the e-folding time τ is reported in Table I. The second phase, however, is outside the scope of linear or test field theory. It is the *saturation and equilibrium phase*: superradiant extraction stalls at $t/M \sim 500$ ($\sim$100) for $qM = 5$ (40), and the amplification stops. Then, after a more or less tumultuous period—to be addressed below—the SF amplitude remains constant for arbitrarily long evolution times. An equilibrium state between the SF and the BH is reached.

To establish the nature of this equilibrium state, we perform a fast Fourier transform to obtain the oscillating frequency spectrum. The angular frequency $\omega_{\rm SF}^{\rm fin}$ for the *single* mode of oscillation in the final SF condensate is $M\omega_{\rm SF}^{\rm fin} = 0.642$ (3.130) for $qM = 5$ (40). Then, computing the critical frequency $\omega_{\rm c}^{\rm fin}$ from the horizon electric potential of the final BH, we obtain *precisely* the same value; see Table I. Thus, these configurations are *hairy* BHs that exist at the threshold of the superradiant instability.

Charged hairy BHs in a cavity at the threshold of the superradiant instability have been recently constructed by Dolan *et al.* [24] for the model (1) with $\mu = 0$. Therein, it was established the existence of different families of such hairy BHs with different numbers of nodes N for the SF amplitude between the horizon and the mirror. But only the solutions with $N = 0$ are stable against perturbations. In Fig. 2, we exhibit snapshots of the SF amplitude radial profile at different time steps for $qM = 40$. It can be observed that whereas during the evolution the scalar amplitude exhibits several maxima and minima (and nodes exist), the final configuration has no nodes. A qualitative difference between the final state hairy BHs presented here and the stationary solutions in Ref. [24] is that the radial profiles here have a local maximum between the horizon and the mirror, which is due to the nonzero mass term. Indeed, simulations with $\mu = 0$ show no such maximum (cf. the Supplemental Material [33]). Nevertheless, the evolutions presented here, together with the results in Ref. [24], establish that the hairy BHs *dynamically* obtained in this work are stable configurations.

Charge and energy extraction.—We now consider in more detail the energy and charge transfer from the initial BH to the SF. The second column in Table I shows that the e-folding time of the instability during the growth phase decreases with increasing qM. This is in agreement with what can be observed in the top panel of Fig. 3 exhibiting the time evolution of the SF energy: comparing the curves for $qM = 0.8$ and 5 during the superradiant growth phase, the slope is larger for larger qM. For both these cases, the SF energy increase is essentially monotonic until the saturation and equilibrium phase is reached. Also, one observes that the final SF energy is larger for *smaller* qM. The corresponding quantitative values are given in the sixth column of Table I. Considering that the initial perturbation has larger energy for large qM (cf. the fifth column of Table I), the ratio between the final to initial SF energy

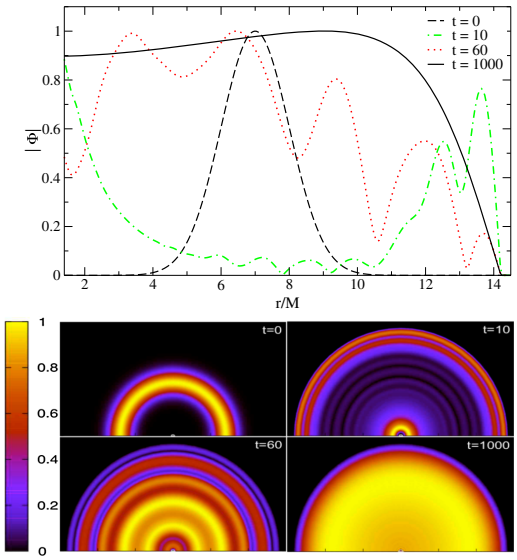

FIG. 2. One-dimensional (top panel) and 2D (bottom panels) snapshots of the normalized SF radial profile for $qM = 40$ at times $t/M = 0$, 10, 60, 1000. The small white circles near the origin in the 2D panels mark the AH.

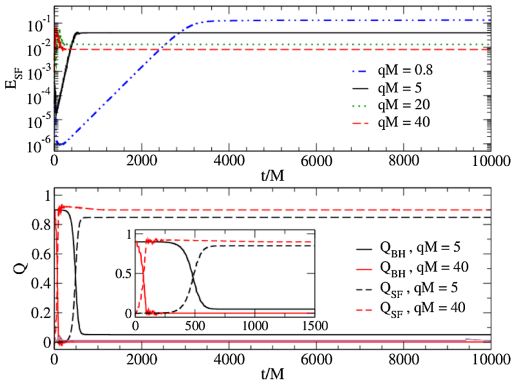

FIG. 3. Top panel: Time evolution of the SF energy displayed in logarithmic scale. Bottom panel: Time evolution of the charge for both the SF and the BH. The inset enlarges the early phase of the evolution, for clarity.

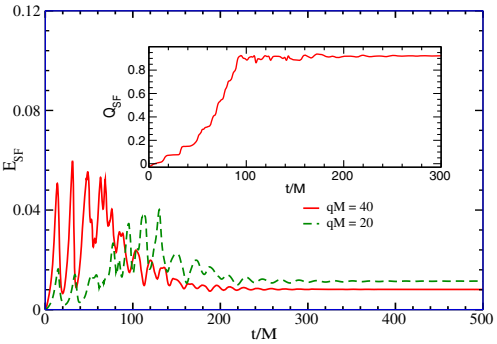

FIG. 4. Bosenova of the $qM = 20$, 40 models. The extracted energy overshoots the final equilibrium value and strong oscillations follow. The inset shows the SF charge for $qM = 40$.

varies from $\sim 4.4 \times 10^3$ to ~ 9.0, when qM increases from $qM = 0.8$ to 40. Thus, energy extraction is more efficient for lower charge coupling corresponding to a longer and smoother superradiant growth.

An opposite trend is observed for the charge, as exhibited in the last two columns of Table I and the bottom panel of Fig. 3. This figure shows a perfect charge exchange between the BH and the SF. Furthermore, the final charge in the scalar field (BH) increases (decreases) with increasing qM, in agreement with the last two columns of Table I. Thus, the charge extraction is more efficient for higher charge coupling. This observation, together with the remarks on the energy, are consistent with the computation of the irreducible mass shown in the eighth column of Table I, where one observes that $M_{\rm irr}^{\rm fin}$ approaches M as qM grows.

Bosenova.—The superradiant growth phase for $qM = 20$, 40 is detailed in Fig. 4. Whereas for models with small enough electric charge (up to $qM \sim 10$), the equilibrium phase is reached under a monotonic trend of energy extraction; for larger values of qM, the energy extracted clearly overshoots the final equilibrium value. Strong oscillations of the SF energy follow before they get damped and the system relaxes to the equilibrium phase. In this process, some of the extracted energy is pushed back into the BH. But the charge extraction is never reversed (Fig. 4, inset). This agitated and reversed (relatively steady) behavior of the SF energy (charge), mimics that described in Refs. [14,15] for the energy (angular momentum) of a test, but nonlinear, SF on the Kerr background, where it was argued that it is an explosion of the amplified SF—akin to a bosenova—that pushes some energy back to the BH. A more detailed analysis of this phenomenon will appear somewhere else, but we show in the Supplemental Material [33] that changing the values of μ and r_m does not change qualitatively the results above.

Implications.—We have reported the first fully nonlinear evolution of a BH bomb. Our numerical simulations establish dynamically that the final state of the superradiant instability in our setup is a hairy BH: a charged horizon surrounded by a scalar field condensate, whose real and imaginary parts oscillate with opposite phases at the critical frequency determined by the horizon electric potential. Together with the frequency domain perturbation analysis of Ref. [24], our results have demonstrated that these BHs are stable against superradiance, despite having $w_c \neq 0$, i.e., nonzero horizon charge. Thus, for these hairy BHs, perturbations with $w < w_c$ of the *same bosonic field* that constitutes the background hair are not unstable modes.

These hairy BHs may be considered as the charged counterparts of the hairy rotating solutions found in Refs. [17,18]. The major difference between the mirror imposed here and the mass term therein is that the latter is only reflective for $w < \mu$. Thus, if there are sufficiently low-frequency modes (which are the ones amplified by superradience anyway), these are gravitationally trapped, and the mirror is a good model for the mass term. A further parallelism between the two cases is the bosenovalike explosion exhibited here and the one discussed for a nonlinear field on the Kerr background. This supports the proposal that such rotating hairy BHs play a decisive role in the nonlinear development of the rotating BH bomb in asymptotically flat spacetimes, either as long-lived intermediate states or as end points. Dis(proving) it is an outstanding open question (see also [38]).

This work has been supported by the Spanish MINECO (Grant No. AYA2013-40979-P), by the Generalitat Valenciana (Grant No. PROMETEOII-2014-069), by the CONACyT-México, by the Max-Planck-Institut für Astrophysik, by the FCT (Portugal) IF program, by the

CIDMA (FCT) strategic Project No. UID/MAT/04106/2013, and by the EU Grants No. NRHEP–295189-FP7-PEOPLE-2011-IRSES, No. H2020-MSCA-RISE-2015, and No. StronGrHEP-690904. Computations have been performed at the Servei d'Informàtica de la Universitat de València.

[1] J. M. Bardeen, W. H. Press, and S. A. Teukolsky, Astrophys. J. **178**, 347 (1972).
[2] A. A. Starobinsky, Zh. Eksp. Teor. Fiz. **64**, 48 (1973) [Sov. Phys. JETP **64**, 48 (1973)].
[3] W. H. Press and S. A. Teukolsky, Nature (London) **238**, 211 (1972).
[4] T. Damour, N. Deruelle, and R. Ruffini, Lett. Nuovo Cimento **15**, 257 (1976).
[5] T. Zouros and D. Eardley, Ann. Phys. (N.Y.) **118**, 139 (1979).
[6] S. L. Detweiler, Phys. Rev. D **22**, 2323 (1980).
[7] V. Cardoso, O. J. C. Dias, J. P. S. Lemos, and S. Yoshida, Phys. Rev. D **70**, 044039 (2004).
[8] S. R. Dolan, Phys. Rev. D **76**, 084001 (2007).
[9] J. Rosa, J. High Energy Phys. 06 (2010) 015.
[10] R. Brito, V. Cardoso, and P. Pani, Lect. Notes Phys. **906**, 1 (2015).
[11] S. R. Dolan, Phys. Rev. D **87**, 124026 (2013).
[12] H. Okawa, H. Witek, and V. Cardoso, Phys. Rev. D **89**, 104032 (2014).
[13] W. E. East, F. M. Ramazanoğlu, and F. Pretorius, Phys. Rev. D **89**, 061503 (2014).
[14] H. Yoshino and H. Kodama, Prog. Theor. Phys. **128**, 153 (2012).
[15] H. Yoshino and H. Kodama, Classical Quantum Gravity **32**, 214001 (2015).
[16] S. L. Cornish, N. R. Claussen, J. L. Roberts, E. A. Cornell, and C. E. Wieman, Phys. Rev. Lett. **85**, 1795 (2000).
[17] C. A. R. Herdeiro and E. Radu, Phys. Rev. Lett. **112**, 221101 (2014).
[18] C. Herdeiro and E. Radu, Classical Quantum Gravity **32**, 144001 (2015).
[19] J. D. Bekenstein, Phys. Rev. D **7**, 2333 (1973).
[20] S. Hod, Phys. Lett. B **713**, 505 (2012).
[21] J. C. Degollado, C. A. R. Herdeiro, and H. F. Rúnarsson, Phys. Rev. D **88**, 063003 (2013).
[22] S. Hod, Phys. Rev. D **88**, 064055 (2013).
[23] J. C. Degollado and C. A. R. Herdeiro, Phys. Rev. D **89**, 063005 (2014).
[24] S. R. Dolan, S. Ponglertsakul, and E. Winstanley, Phys. Rev. D **92**, 124047 (2015).
[25] T. W. Baumgarte and S. L. Shapiro, Phys. Rev. D **59**, 024007 (1998).
[26] M. Shibata and T. Nakamura, Phys. Rev. D **52**, 5428 (1995).
[27] J. D. Brown, Phys. Rev. D **79**, 104029 (2009).
[28] M. Alcubierre and M. D. Mendez, Gen. Relativ. Gravit. **43**, 2769 (2011).
[29] P. J. Montero and I. Cordero-Carrion, Phys. Rev. D **85**, 124037 (2012).
[30] N. Sanchis-Gual, J. C. Degollado, P. J. Montero, and J. A. Font, Phys. Rev. D **91**, 043005 (2015).
[31] N. Sanchis-Gual, J. C. Degollado, P. J. Montero, J. A. Font, and V. Mewes, Phys. Rev. D **92**, 083001 (2015).
[32] J. M. Torres and M. Alcubierre, Gen. Relativ. Gravit. **46**, 1773 (2014).
[33] See the Supplemental Material http://link.aps.org/supplemental/10.1103/PhysRevLett.116.141101, which includes Refs. [24,34], for an overview regarding the initial data and constraints violation, the expected second order convergence for this code and the sensitivity of the results to the scalar field mass and the position of the mirror.
[34] N. Sanchis-Gual, P. J. Montero, J. A. Font, E. Muller, and T. W. Baumgarte, Phys. Rev. D **89**, 104033 (2014).
[35] D. Christodoulou, Phys. Rev. Lett. **25**, 1596 (1970).
[36] M. Alcubierre, *Introduction to 3+1 Numerical Relativity* (Oxford University Press, New York, 2008), ISBN.
[37] M. Alcubierre, J. C. Degollado, and M. Salgado, Phys. Rev. D **80**, 104022 (2009).
[38] P. Bosch, S. R. Green, and L. Lehner, Phys. Rev. Lett. **116**, 141102 (2016).

PHYSICAL REVIEW D **94,** 044061 (2016)

Dynamical formation of a Reissner-Nordström black hole with scalar hair in a cavity

Nicolas Sanchis-Gual,[1] Juan Carlos Degollado,[2] Carlos Herdeiro,[3] José A. Font,[1,4] and Pedro J. Montero[5]

[1]*Departamento de Astronomía y Astrofísica, Universitat de València, Dr. Moliner 50, 46100 Burjassot (València), Spain*

[2]*Instituto de Ciencias Físicas, Universidad Nacional Autónoma de México, Apartado Postal 48-3, 62251 Cuernavaca, Morelos, Mexico*

[3]*Departamento de Física da Universidade de Aveiro and CIDMA, Campus de Santiago, 3810-183 Aveiro, Portugal*

[4]*Observatori Astronòmic, Universitat de València, C/ Catedrático José Beltrán 2, 46980 Paterna (València), Spain*

[5]*Max-Planck-Institut für Astrophysik, Karl-Schwarzschild-Strasse 1, 85748 Garching bei München, Germany*

(Received 26 July 2016; published 30 August 2016)

In a recent *Letter* [Sanchis-Gual *et al.*, Phys. Rev. Lett. **116**, 141101 (2016)], we presented numerical relativity simulations, solving the full Einstein–Maxwell–Klein-Gordon equations, of superradiantly unstable Reissner-Nordström black holes (BHs), enclosed in a cavity. Low frequency, spherical perturbations of a charged scalar field trigger this instability. The system's evolution was followed into the nonlinear regime, until it relaxed into an equilibrium configuration, found to be a *hairy* BH: a charged horizon in equilibrium with a scalar field condensate, whose phase is oscillating at the (final) critical frequency. Here, we investigate the impact of adding self-interactions to the scalar field. In particular, we find sufficiently large self-interactions suppress the exponential growth phase, known from linear theory, and promote a nonmonotonic behavior of the scalar field energy. Furthermore, we discuss in detail the influence of the various parameters in this model: the initial BH charge, the initial scalar perturbation, the scalar field charge, the mass, and the position of the cavity's boundary (mirror). We also investigate the "explosive" nonlinear regime previously reported to be akin to a bosenova. A mode analysis shows that the "explosions" can be interpreted as the decay into the BH of modes that exit the superradiant regime.

DOI: 10.1103/PhysRevD.94.044061

I. INTRODUCTION

In an attempt to summarize the astonishing simplicity of electrovacuum black holes (BHs), John Wheeler famously coined the *dictum*: "black holes have no hair" [1]. This catchy statement is, obviously, vague and needs to be contextualized. In fact, it is useful to introduce the following terminology, which clearly separates two different interpretations of Wheeler's statement.

The *strong no-hair hypothesis*, on the one hand, asserts that stationary, regular (on and outside a horizon), BH solutions described by parameters other than "charges" associated with Gauss laws *do not exist*. This is a commonly found interpretation in the current literature. Unfortunately for the believers in such enormous simplicity, decades of research considering different matter fields showed that BHs can indeed have hair—see [2,3] for recent reviews. The strong no-hair hypothesis has been falsified, even if one requires physically reasonable matter (obeying all energy conditions) and asymptotically flat spacetimes.

The *weak no-hair hypothesis*, on the other hand, demands only that stationary, regular (on and outside a horizon), BH solutions described by parameters other than "charges" associated with Gauss laws *cannot form dynamically*. This is certainly what the proponents of the no-hair hypothesis had in mind (in the context of astrophysics and asymptotically flat spacetimes). The status of this version of the hypothesis is less definite. In particular, in asymptotically flat spacetimes and to the best of our knowledge, no stationary "hairy" BH solution has been shown to form dynamically. Indeed, often, but not always, the stationary solutions that have been found as counterexamples to the strong no-hair hypothesis are unstable against perturbations, and hence unlikely to form dynamically (see an early discussion of this version of the conjecture in [4]).

An interesting new angle concerning the weak no-hair hypothesis arises in the context of an instability of the paradigmatic BH solution of vacuum general relativity—the Kerr solution [5]—which is triggered by fields that can, potentially, form BH hair.

Bosonic fields scattering off Kerr BHs can extract energy through the classical process of *superradiance* [6]. For concreteness, let us focus on a scalar field. This occurs when such a field, oscillating with frequency ω and with an azimuthal quantum number m, fulfills the condition $\omega < m\Omega_H$ [7–12], where Ω_H is the horizon angular velocity.

By introducing a mass term for the scalar field, or a mirrorlike boundary condition, superradiant modes can become trapped, "mining" energy from the BH and growing exponentially in time, thus triggering an instability of the combined BH-scalar field system. Consequently, in this setup, the *bald* Kerr BH is unstable and the scalar field (which is not associated with a Gauss law) grows in time outside the BH. This growth could, in principle, approach an equilibrium configuration, in which the BH becomes hairy, because stationary solutions describing Kerr BHs with (this type of) scalar hair have been recently discovered [13–15]. So, is the end point of the superradiant instability triggered by a massive scalar field a hairy Kerr BH? In other words, does a stationary, asymptotically flat hairy BH form dynamically in this setup, thus falsifying the weak no-hair hypothesis?

While the initial growth of the superradiant instability described in the previous paragraph can be captured at the linear level, a fully nonlinear approach is required to address its saturation and end point. This is, however, a remarkably challenging undertaking with current numerical relativity (NR) technology [16,17]. Linear analysis studies for Kerr BHs [11,18] have shown that the maximum growth rate of the instability is so small that it may remain indistinguishable from numerical errors when performing nonlinear numerical simulations [16]. Whereas the first nonlinear simulations of superradiant scattering of gravitational waves off nearly extremal Kerr BHs have been recently carried out [17], following the evolution of the superradiant instability presents another level of difficulty.

In view of the difficulties just described, is there a technically simpler model that presents similar features to the superradiant instability of the Kerr BH in the presence of massive bosonic fields? Indeed, an analogous, but technically simpler setup exists. A superradiant instability appears in the case of a charged, i.e., Reissner-Nordström (RN), BH. In this case, superradiance occurs when a charged scalar field with frequency ω and charge q, scattering off a charged BH with charge Q and horizon electric potential ϕ_H, obeys the condition, $\omega < \omega_c \equiv q\phi_H$ [19]. Unlike the Kerr case, mirrorlike boundary conditions are necessary to trigger superradiance in the RN BH; i.e., a mass term is not sufficient [20,21] (or necessary). Studies in the linearized regime have shown that the growth time scale of unstable modes in the RN case is significantly shorter than for the Kerr BH and that those unstable modes may be spherically symmetric [22–25]. These features suggest taking charge as a surrogate for rotation and studying the nonlinear growth of the superradiant instability in the RN BH in a cavity, sometimes dubbed *charged BH bomb*.

In a recent *Letter* [26], we reported NR simulations, using the full Einstein equations, of the charged BH bomb. We found that, indeed, the generic final state is a *hairy* BH: a charged horizon, surrounded by a scalar field condensate storing part of the charge and energy of the initial BH. This condensate's phase oscillates at the threshold frequency of the superradiant instability, thus realizing dynamically charged hairy BHs analogous to Kerr BHs with scalar hair [13–15]. The former have recently been constructed as stationary solutions, and a subset was shown to be perturbatively stable [27]. Similar results for the superradiantly unstable RN–anti–de Sitter (AdS) BH were found in [28], considering reflecting boundary conditions at the AdS timelike boundary.

The purpose of this paper is to further the investigation of the dynamics of the coupled BH-scalar field system in a cavity, initiated in [26]. Whereas our *Letter* provided the generic picture, here we will pay careful attention to the variation of the hair growth process with the different parameters in the setup, namely, the BH initial charge, the initial scalar perturbation, the scalar field charge and mass, as well as the radius of the mirror. Moreover, we consider the effect of adding a (nonlinear) self-interaction term to the scalar field. We shall also investigate in more detail the behavior of the "explosive" regime, described in [26] to be akin to a bosenova, following [29,30]. As we shall discuss, a mode analysis renders a simple and clear interpretation of the observed behavior, confirming the results found in [28], for the asymptotically AdS case. To accomplish these goals, we have performed a number of NR simulations, which will be detailed below. The numerical techniques and the code used are those already described in [31].

The paper is organized as follows: In Sec. II we present the basic equations and discuss the initial data used in our simulations. Section III briefly describes our numerical approach. In Sec. IV we discuss our findings and describe some properties of the solutions. Finally, in Sec. V we sum up our concluding remarks. Appendix describes some technical details. Throughout the paper Greek indices run over spacetime indices (0 to 3), while Latin indices run over space indices only (1 to 3). We use units in which $c = G = \hbar = 4\pi\epsilon_0 = 1$.

II. BASIC EQUATIONS

We shall investigate the dynamics of a complex scalar field, with charge q and mass μ, around a RN BH, by solving numerically the fully nonlinear Einstein–Maxwell–Klein-Gordon (EMKG) equations, described by the action $\mathcal{S} = \int d^4x\sqrt{-g}\mathcal{L}$, where the Lagrangian density is

$$\mathcal{L} = \frac{R - F_{\alpha\beta}F^{\alpha\beta}}{16\pi} - \frac{1}{2}D_\alpha\Phi(D^\alpha\Phi)^* - \frac{\mu^2}{2}|\Phi|^2 - V_{\rm int}, \qquad (1)$$

where $V_{\rm int} = \frac{1}{4}\lambda|\Phi|^4$ is a quartic self-interaction potential with coupling λ. We have denoted by R the Ricci scalar, $F_{\alpha\beta} \equiv \nabla_\alpha A_\beta - \nabla_\beta A_\alpha$, A_α is the electromagnetic potential, D_α is the gauge covariant derivative, $D_\alpha \equiv \nabla_\alpha + iqA_\alpha$, and q and μ are the charge and the mass of the scalar field.

Varying the above action with respect to the metric yields the Einstein equations, $G_{\alpha\beta} = 8\pi(T^{\rm SF}_{\alpha\beta} + T^{\rm EM}_{\alpha\beta})$, with the following energy-momentum tensors:

$$T^{\rm SF}_{\alpha\beta} = \frac{1}{2}(D_\alpha\Phi)^*(D_\beta\Phi) + \frac{1}{2}(D_\alpha\Phi)(D_\beta\Phi)^* - \frac{1}{2}g_{\alpha\beta}(D^\sigma\Phi)^*(D_\sigma\Phi) - \frac{\mu^2}{2}g_{\alpha\beta}|\Phi\Phi^*| - \frac{1}{4}\lambda g_{\alpha\beta}|\Phi\Phi^*|^2, \quad (2)$$

$$T^{\rm EM}_{\alpha\beta} = \frac{1}{4\pi}F_{\alpha\sigma}F^{\sigma}_{\beta} - \frac{1}{16\pi}g_{\alpha\beta}F_{\sigma\delta}F^{\sigma\delta}. \quad (3)$$

Varying (1) with respect to the scalar field yields the Klein-Gordon equation

$$\nabla^\alpha\nabla_\alpha\Phi + iqA^\alpha(2\nabla_\alpha\Phi + iqA_\alpha\Phi) + iq\Phi\nabla_\alpha A^\alpha - \mu^2\Phi - \lambda|\Phi|^2\Phi = 0. \quad (4)$$

Finally, varying the action with respect to the Maxwell potential yields the Maxwell equations

$$\nabla^\alpha F_{\alpha\beta} = 2\pi iq[\Phi^* D_\beta\Phi - \Phi(D_\beta\Phi)^*] \coloneqq 4\pi(j_{em})_\beta. \quad (5)$$

We follow the convention that Φ is dimensionless and μ has dimensions of $(\text{length})^{-1}$.

In the following we present the explicit evolution equations we solve in our simulations. While we mainly include this information to make the paper self-contained, we keep these sections as concise as possible and refer the interested reader to [31] for further details. The equations are presented for the particular case of spherical symmetry.

A. Spacetime and electromagnetic split

The $3+1$ metric split takes the form

$$ds^2 = (-\alpha^2 + \beta^r\beta_r)dt^2 + 2\beta_r dt dr + e^{4\chi}[a dr^2 + br^2 d\Omega^2], \quad (6)$$

where the lapse α, shift component β^r, and the (spatial) metric functions, χ, a, b depend only on t and r.

We use the following $3+1$ decomposition of the vector field A^α:

$$\varphi \coloneqq -n_\nu A^\nu, \quad (7)$$

$$a^r \coloneqq {}^{(3)}A^r = \gamma^r_\mu A^\mu, \quad (8)$$

where n^μ is the 4-velocity of the Eulerian observer [32] and $\gamma_{\mu\nu} = g_{\mu\nu} + n^\mu n_\nu$ is the metric on the spatial slices (first fundamental form). This split defines the scalar and vector electromagnetic potentials measured by Eulerian observers. In our spherically symmetric setup, the electric field $E^\mu = F^{\mu\nu}n_\nu$ has only a radial component, and the magnetic field $B^\mu = {}_\star F^{\mu\nu}n_\nu$ vanishes. Spherical symmetry implies we only have to consider the equations for the electric potential, φ, for the radial component of the vector potential, a^r, and for the radial component of the electric field, E^r. The evolution equations for these fields and the electric field take the form

$$\partial_t\varphi = \beta^r\partial_r\varphi + \alpha K\varphi - \frac{\alpha}{ae^{4\chi}}\left[\partial_r a_r + a_r\left(\frac{2}{r} - \frac{\partial_r a}{2a} + \frac{\partial_r b}{b} + 2\partial_r\chi\right)\right] - \frac{a_r}{ae^{4\chi}}\partial_r\alpha, \quad (9)$$

$$\partial_t a_r = \beta^r\partial_r a_r + a_r\partial_r\beta^r - \alpha a e^{4\chi}E^r - \partial_r(\alpha\varphi), \quad (10)$$

$$\partial_t E^r = \beta^r\partial_r E^r - E^r\partial_r\beta^r + \alpha K E^r - 4\alpha\pi j^r_e, \quad (11)$$

where K is the trace of the extrinsic curvature K_{ij} (the second fundamental form) and j^r_e is the electric current density measured by Eulerian observers.

B. Charged Klein-Gordon equation

To solve the Klein-Gordon equation we introduce two first-order variables, defined as

$$\Pi \coloneqq n^\alpha\partial_\alpha\Phi = \frac{1}{\alpha}(\partial_t\Phi - \beta^r\partial_r\Phi), \quad (12)$$

$$\Psi \coloneqq \partial_r\Phi. \quad (13)$$

Therefore, using Eq. (4) we obtain the following system of first-order equations:

$$\partial_t\Phi = \beta^r\partial_r\Phi + \alpha\Pi, \quad (14)$$

$$\partial_t\Psi = \beta^r\partial_r\Psi + \Psi\partial_r\beta^r + \partial_r(\alpha\Pi), \quad (15)$$

$$\partial_t\Pi = \beta^r\partial_r\Pi + \frac{\alpha}{ae^{4\chi}}\left[\partial_r\Psi + \Psi\left(\frac{2}{r} - \frac{\partial_r a}{2a} + \frac{\partial_r b}{b} + 2\partial_r\chi\right)\right] - \alpha\left[\mu^2 + \lambda|\Phi|^2 + q^2\left(\frac{a_r^2}{ae^{4\chi}} - \varphi^2\right)\right]\Phi + \alpha K\Pi + \frac{\Psi}{ae^{4\chi}}\partial_r\alpha + 2iq\alpha\left[\frac{a_r\Psi}{ae^{4\chi}} + \varphi\Pi\right]. \quad (16)$$

C. Energy-momentum tensor

We define the gauge invariant versions of the variables Π and Ψ as

$$\tilde{\Pi} \coloneqq n^\mu\mathcal{D}_\mu\Phi^* = \Pi - iq\varphi\Phi, \quad (17)$$

$$\tilde{\Psi} \coloneqq \gamma_r^\mu \mathcal{D}_\mu \Phi = \Psi + iqa_r\Phi. \tag{18}$$

The matter source terms for the scalar field read

$$\mathcal{E}^{\mathrm{SF}} \coloneqq n^\alpha n^\beta T^{\mathrm{SF}}_{\alpha\beta} = \frac{1}{2}\left(|\tilde{\Pi}|^2 + \frac{|\tilde{\Psi}|^2}{ae^{4\chi}}\right) + \frac{1}{2}\mu^2|\Phi|^2 + \frac{1}{4}\lambda|\Phi|^4, \tag{19}$$

$$j_r^{\mathrm{SF}} = -\gamma_r^\alpha n^\beta T^{\mathrm{SF}}_{\alpha\beta} = -\frac{1}{2}(\tilde{\Pi}^*\tilde{\Psi} + \tilde{\Psi}^*\tilde{\Pi}), \tag{20}$$

$$S_a^{\mathrm{SF}} \coloneqq (T_r^r)^{\mathrm{SF}} = \frac{1}{2}\left(|\tilde{\Pi}|^2 + \frac{|\tilde{\Psi}|^2}{ae^{4\chi}}\right) - \frac{1}{2}\mu^2|\Phi|^2 - \frac{1}{4}\lambda|\Phi|^4, \tag{21}$$

$$S_b^{\mathrm{SF}} \coloneqq (T_\theta^\theta)^{\mathrm{SF}} = \frac{1}{2}\left(|\tilde{\Pi}|^2 - \frac{|\tilde{\Psi}|^2}{ae^{4\chi}}\right) - \frac{1}{2}\mu^2|\Phi|^2 - \frac{1}{4}\lambda|\Phi|^4, \tag{22}$$

and for the electric field

$$\mathcal{E}^{\mathrm{em}} = \frac{1}{8\pi}ae^{4\chi}(E^r)^2, \tag{23}$$

$$S_a^{\mathrm{em}} = -\frac{1}{8\pi}ae^{4\chi}(E^r)^2, \tag{24}$$

$$S_b^{\mathrm{em}} = \frac{1}{8\pi}ae^{4\chi}(E^r)^2. \tag{25}$$

The momentum density j_r^{em} vanishes because there is no magnetic field in spherical symmetry.

D. Initial data

As in our *Letter* [26], we choose the initial data for the scalar field to be a Gaussian distribution, of the form

$$\Phi = A_0 e^{-(r-r_0)^2/\sigma^2}, \tag{26}$$

where A_0 is the initial amplitude of the pulse, r_0 is the center of the Gaussian, and σ is its width. This scalar field will always be contained within a cavity, whose boundary we call "the mirror."

The auxiliary first order quantities are initialized as follows:

$$\Pi(t=0,r) = 0, \tag{27}$$

$$\Psi(t=0,r) = -2\frac{(r-r_0)}{\sigma^2}A_0 e^{-(r-r_0)^2/\sigma^2}. \tag{28}$$

As the geometrical initial data, we choose a conformally flat metric with $a = b = 1$ together with a time symmetry condition $K_{ij} = 0$. This describes a time slice of a RN BH, in isotropic coordinates, if the 3-metric is written as

$$dl^2 = \psi^4(dr^2 + r^2 d\Omega^2), \tag{29}$$

and the conformal factor is given by

$$\psi = \left[\left(1 + \frac{M}{2r}\right)^2 - \frac{Q^2}{4r^2}\right]^{1/2}, \tag{30}$$

where M is the BH mass and Q its charge.

At $t = 0$, we choose a "precollapsed" lapse

$$\alpha = \psi^{-2}, \tag{31}$$

and a vanishing shift $\beta^r = 0$. Initially, the electric field is given by

$$E^r = \frac{Q}{r^2\psi^6}. \tag{32}$$

The mirrorlike boundary conditions are

$$\Phi(r_{\mathrm{m}}) = \Psi(r_{\mathrm{m}}) = \Pi(r_{\mathrm{m}}) = 0, \quad \partial_r\Phi(r_{\mathrm{m}}) = \partial_r\Psi(r_{\mathrm{m}}) = \partial_r\Pi(r_{\mathrm{m}}) = 0. \tag{33}$$

To summarize, the model (background plus field properties) to be studied contains five parameters,

$$M, Q, r_{\mathrm{m}}, \mu, q. \tag{34}$$

In the following we take $M = 1$ for all the simulations, which fixes the energy scale of the problem, but will vary the value of Q, focusing on the sample

$$Q = \{0, 0.3, 0.5, 0.7, 0.9\}M. \tag{35}$$

The mirror shall be considered at three different positions, with radial coordinates

$$r_{\mathrm{m}} = \{9, 14.2, 19\}M, \tag{36}$$

in order to study its influence in the evolution of the superradiant instability. For the scalar field mass we shall consider both a massless and a massive field,

$$\mu M = \{0, 0.1\}, \tag{37}$$

and we consider seven models with different values of the scalar field charge qM, namely,

$$qM = \{0.8, 1, 1.2, 2, 5, 10, 20, 40\}. \tag{38}$$

The initial data for the scalar field cloud introduce three other parameters, as described above. For all models,

except those in Sec. IV C 4, we choose $A_0 = 3 \times 10^{-4}$, $\sigma = \sqrt{2}$. In Sec. IV C 4 we also consider $A_0 = 2.1 \times 10^{-5}$, $\sigma = 0.01$ and $A_0 = 2.0 \times 10^{-4}$, $\sigma = 1.8$. The center of the Gaussian is $r_0 = 7M$, when we set the mirror at $r_{\rm m} = 14.2M$ and $r_{\rm m} = 19M$; on the other hand, $r_0 = 5M$ for $r_{\rm m} = 9M$. In all simulations below, with the exception of Sec. IV C 5, we take the self-interaction coupling $\lambda = 0$. In Sec. IV C 5 we consider the values

$$\lambda = \{0, 1.5, 5.0, 7.5\} \times 10^4. \tag{39}$$

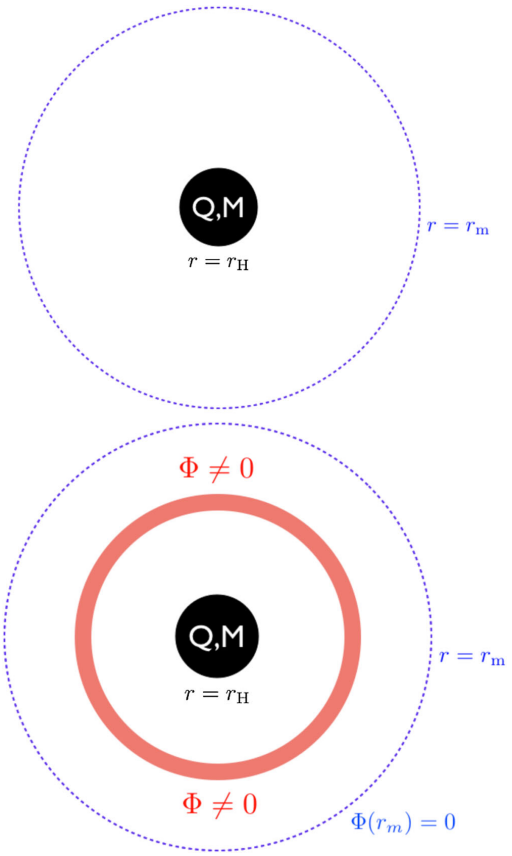

FIG. 1. Schematic representation of the RN BH with mass M and charge Q in a cavity with boundary at $r = r_{\rm m}$, where mirror boundary conditions for the scalar field are imposed. Top panel: The unperturbed setup. In this case the cavity is irrelevant since neither the gravitational nor the electromagnetic field have special boundary conditions at the cavity's boundary. Bottom panel: The perturbed setup, setting a Gaussian scalar cloud around the BH. The scalar field obeys reflective boundary conditions at the cavity's boundary (hence called *mirror*).

A schematic representation of the unperturbed and perturbed RN BH in a cavity is exhibited in Fig. 1.

III. NUMERICS

The time update of the different systems of evolution equations we have to solve in our code (Einstein, Klein-Gordon, and Maxwell) is done using the same type of techniques we have extensively used in previous work (see, in particular, [31,33,34]). We refer the interested reader to those references for full details on the particular numerical techniques implemented in the code. Here, we simply mention that the evolution equations are integrated using the second-order partially implicit Runge Kutta (PIRK) method developed by [35,36]. This method allows one to handle the singular terms that appear in the evolution equations due to our choice of curvilinear coordinates. The derivatives in the spacetime evolution are computed using a fourth-order centered finite difference approximation on a log grid except for advection terms for which we adopt a fourth-order upwind scheme. We also use fourth-order Kreiss-Oliger dissipation to avoid high frequency noise appearing near the outer boundary. In this work we are also evolving the electric field explicitly and the electric potentials implicitly.

IV. RESULTS

A. Initial setup, convergence, and constraint violations

The EMKG system admits as a solution the RN BH with Arnowitt-Deser-Misner mass M and charge Q, together with a vanishing scalar field. We perturb the RN BH by surrounding it with a charged scalar field cloud whose initial form is given by Eq. (26)—see Fig. 1, bottom panel. The superradiant instability, which leads to the growth of the scalar field outside the horizon, and the loss of energy/charge by the BH, is triggered if the scalar cloud oscillations include modes with frequency $w < w_{\rm c} \equiv q\phi_H$, where ϕ_H is the electric potential at the horizon. The trapping of the superradiant modes, which is fundamental for the instability, is guaranteed by imposing reflecting boundary conditions for the scalar field at the spherical mirror, located at $r = r_{\rm m}$.

In the numerical simulations performed to follow the development of the instability, we have used a logarithmic radial grid that extends from the origin to $r = 10^4 M$ and uses a maximum resolution close to the origin of $\Delta r = 0.025M$. In order to test the convergence of the code we performed three simulations with different resolutions $\Delta r = \{0.025, 0.0125, 0.00625\}$ M. In [26] (see supplemental material therein) we have already shown the rescaled evolution of the L2 norm of the Hamiltonian constraint for a particular choice of the scalar field charge, $qM = 40$, and mirror position $r_{\rm m} = 14.2M$, obtaining the expected second-order convergence of our PIRK time-evolution scheme. We note that the same result is

achieved irrespective of the combination of parameters considered.

We remark that in our setup, the initial data do not satisfy the constraints. Nevertheless, as discussed in detail in the supplemental material in [26], this fact does not introduce significant errors in the simulations.

B. System's evolution: General picture

We solve numerically the EMKG system using the initial data given by Eqs. (26)–(33) and let the superradiant instability grow. As in [26] we analyze the results of the simulations by extracting a time series for the scalar field amplitude at an observation point located at one fixed radii, here taken to be at $r_{\rm obs} = 5M$ (a different value from that used in [26]). Typical behaviors are shown in Fig. 2. To identify the frequencies at which the scalar field oscillates we perform a fast Fourier transform after a given number of time steps and obtain the corresponding power spectrum.

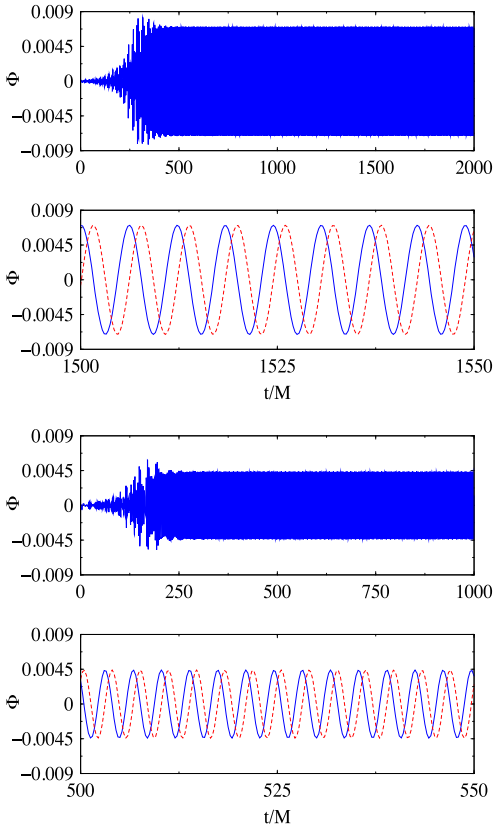

FIG. 2. First (top) panel: Time evolution of the scalar field real part, extracted at $r_{\rm obs} = 5M$, for $qM = 10$, $Q = 0.9M$, $\mu M = 0.1$, and for $r_{\rm m} = 14.2M$. Second panel: Detail of the time evolution of the scalar field real (blue solid line) and imaginary (red dashed line) parts. Third and bottom panels: Same as first and second rows, but for $qM = 20$.

The time evolution of the scalar field amplitude exhibited in Fig. 2 shows two distinct phases. During the first phase—the *superradiant growth phase*—the amplitude of the oscillations of the scalar field grow exponentially (at the observation point), which is the expected behavior due to the superradiant instability, well known from the linear theory analysis [22–24]. During a second phase—the *saturation and equilibrium phase*—the exponential growth of the scalar field stops and an equilibrium between the scalar field and the BH is attained, during which the amplitude of the scalar field remains constant and the real and imaginary parts of the scalar field oscillate with a single frequency and with opposite phases (i.e., when one is at a maximum of the magnitude of the amplitude, the other one has a vanishing amplitude—Fig. 2, second and fourth rows). These plots show the power spectra obtained from the Fourier transforms of the time series.

The true nature of this final equilibrium state is revealed by computing also the critical frequency $\omega_{\rm c}^{\rm fin} \equiv q\phi_H^{\rm fin}$, from the horizon electric potential of the final BH. The latter is computed at the apparent horizon (AH) of the final BH as [37]

$$\phi_H = \alpha\varphi - \beta^r a_r|_{r=r_{\rm AH}}. \tag{40}$$

We obtain *precisely* the same value as that of the final frequency of the scalar field—see Table I, fourth and fifth columns. The condition $\omega = \omega_c$ is thus fulfilled, implying these configurations are *hairy* BHs that exist at the threshold of the superradiant instability. These solutions were first discussed for rotating BHs bifurcating from the Kerr solution in [13], and for charged BHs in a cavity bifurcating from the RN solution in [27]. In particular, the latter paper established that solutions with no nodes in the scalar field profile (like the ones obtained here) are stable against radial perturbations. This provides strong evidence that the equilibrium state obtained herein is the end point of the evolution.

To summarize: a RN BH, perturbed by a charged scalar field confined within a cavity around the BH, containing low frequency modes, such that $w < q\Phi_H$, is unstable. During a first phase, the BH transfers part of its energy and charge into the scalar field, and the scalar field grows exponentially while the horizon electric potential, ϕ_H, of the BH decreases. In a second phase this growth stops when a single mode of the scalar field remains, with precisely the critical frequency of the BH, $q\Phi_H^{\rm final}$. This is the general picture observed in all simulations. Now we shall discuss how this general picture is sensitive to the different parameters of the system.

TABLE I. Summary of physical quantities for the runs with different values of qM and $r_{\rm m} = 9M$ (top table), $r_{\rm m} = 14.2M$ (middle table), and $r_{\rm m} = 19M$ (bottom table). Each model (first column) a–h corresponds to the values in Eq. (38), which are shown in the second column; (third column) e-folding time during the growth phase; (fourth and fifth columns) final oscillation frequency of the scalar field phase and final critical frequency; (sixth to eighth columns) initial and final scalar field energy, and their ratio; (ninth to eleventh columns) final BH irreducible mass and ratio of the final to initial BH and scalar field charge.

Model	qM	τ/M	$M\omega_{\rm SF}^{\rm fin}$	$M\omega_{\rm c}^{\rm fin}$	$E_{\rm SF}^{\rm ini}/M$	$E_{\rm SF}^{\rm fin}/M$	$E_{\rm SF}^{\rm fin}/E_{\rm SF}^{\rm ini}$	$M_{\rm irr}^{\rm fin}/M$	$Q_{\rm BH}^{\rm fin}/Q$	$Q_{\rm SF}^{\rm fin}/Q$
1a	0.8	3.3×10^{02}	0.376	0.377	1.66×10^{-05}	1.29×10^{-01}	7.77×10^{03}	0.721	60%	40%
1b	1.0	2.4×10^{02}	0.405	0.405	1.67×10^{-05}	1.33×10^{-01}	7.96×10^{03}	0.723	48%	52%
1c	1.2	2.0×10^{02}	0.435	0.436	1.69×10^{-05}	1.29×10^{-01}	7.63×10^{03}	0.732	41%	59%
1d	2.0	1.3×10^{02}	0.546	0.546	1.81×10^{-05}	1.01×10^{-01}	5.58×10^{03}	0.766	24%	76%
1e	5.0	6.5×10^{01}	0.928	0.928	2.79×10^{-05}	5.29×10^{-02}	1.90×10^{03}	0.838	8.0%	92%
1f	10.0	4.3×10^{01}	1.513	1.514	6.27×10^{-05}	3.11×10^{-02}	4.96×10^{02}	0.870	3.0%	97%
1g	20.0	3.3×10^{01}	2.607	2.608	2.02×10^{-04}	1.84×10^{-02}	9.11×10^{01}	0.881	2.0%	98%
1h	40.0	2.0×10^{01}	4.676	4.676	7.59×10^{-04}	1.15×10^{-02}	1.52×10^{01}	0.900	0.6%	99.4%

Model	qM	τ/M	$M\omega_{\rm SF}^{\rm fin}$	$M\omega_{\rm c}^{\rm fin}$	$E_{\rm SF}^{\rm ini}/M$	$E_{\rm SF}^{\rm fin}/M$	$E_{\rm SF}^{\rm fin}/E_{\rm SF}^{\rm ini}$	$M_{\rm irr}^{\rm fin}/M$	$Q_{\rm BH}^{\rm fin}/Q$	$Q_{\rm SF}^{\rm fin}/Q$
2a	0.8	4.8×10^{02}	0.277	0.278	3.00×10^{-05}	1.32×10^{-01}	4.40×10^{03}	0.728	45%	55%
2b	1.0	3.7×10^{02}	0.296	0.297	3.01×10^{-05}	1.22×10^{-01}	4.05×10^{03}	0.742	36%	64%
2c	1.2	3.4×10^{02}	0.315	0.316	3.04×10^{-05}	1.11×10^{-01}	3.65×10^{03}	0.764	31%	69%
2d	2.0	2.1×10^{02}	0.389	0.390	3.17×10^{-05}	8.02×10^{-02}	2.53×10^{03}	0.815	18%	82%
2e	5.0	1.1×10^{02}	0.642	0.642	4.31×10^{-05}	3.93×10^{-02}	9.12×10^{02}	0.875	6.0%	94%
2f	10.0	7.1×10^{01}	1.030	1.031	8.37×10^{-05}	2.25×10^{-02}	2.69×10^{02}	0.903	2.0%	98%
2g	20.0	4.8×10^{01}	1.756	1.756	3.13×10^{-04}	1.31×10^{-02}	4.19×10^{01}	0.924	1.0%	99%
2h	40.0	2.9×10^{01}	3.130	3.129	8.95×10^{-04}	8.02×10^{-03}	8.96×10^{00}	0.942	0.1%	99.9%

Model	qM	τ/M	$M\omega_{\rm SF}^{\rm fin}$	$M\omega_{\rm c}^{\rm fin}$	$E_{\rm SF}^{\rm ini}/M$	$E_{\rm SF}^{\rm fin}/M$	$E_{\rm SF}^{\rm fin}/E_{\rm SF}^{\rm ini}$	$M_{\rm irr}^{\rm fin}/M$	$Q_{\rm BH}^{\rm fin}/Q$	$Q_{\rm SF}^{\rm fin}/Q$
3a	0.8	6.3×10^{02}	0.231	0.232	2.99×10^{-05}	1.19×10^{-01}	3.98×10^{03}	0.773	40.5%	59.5%
3b	1.0	4.8×10^{02}	0.244	0.244	3.01×10^{-05}	1.10×10^{-01}	3.65×10^{03}	0.777	31%	69%
3c	1.2	4.2×10^{02}	0.257	0.259	3.04×10^{-05}	9.87×10^{-02}	3.25×10^{03}	0.796	26%	74%
3d	2.0	2.7×10^{02}	0.313	0.314	3.17×10^{-05}	6.89×10^{-02}	2.17×10^{03}	0.846	15%	85%
3e	5.0	1.6×10^{02}	0.506	0.507	4.31×10^{-05}	3.27×10^{-02}	7.59×10^{02}	0.902	5.0%	95%
3f	10.0	1.1×10^{02}	0.802	0.802	8.37×10^{-05}	1.84×10^{-02}	2.20×10^{02}	0.927	2.0%	98%
3g	20.0	7.4×10^{01}	1.355	1.355	2.46×10^{-04}	1.06×10^{-02}	4.30×10^{01}	0.935	0.9%	99.1%
3h	40.0	5.0×10^{01}	2.402	2.401	8.95×10^{-04}	6.41×10^{-03}	7.16×10^{00}	0.950	0.02%	99.98%

C. System's evolution: Detailed description

The most relevant dynamics of our system concerns the energy and charge transfers between the BH and the scalar field. The energy in the scalar field can be computed by the (spatial) volume integral

$$E_{\rm SF} = \int_{r_{\rm AH}}^{r_{\rm m}} \mathcal{E}^{\rm SF} dV, \tag{41}$$

where $\mathcal{E}^{\rm SF}$ is the projection of the energy-momentum tensor of the scalar field along the normal direction to the $t =$ constant surfaces [38]; cf. Eq. (19). In Fig. 3 we plot the evolution of this scalar field energy for different values of the BH initial charge, Q (and also of the scalar field charge q). The first important feature, manifest on the bottom panel, is that for the vanishing BH charge the scalar field energy *does not grow*. In other words, there is no superradiant instability of uncharged BHs. The second important trend is that for a fixed scalar field charge, the instability is stronger—both in terms of a shorter time scale and in terms of a larger energy transfer into the scalar field—for larger Q (top and middle panels). Finally, observe that even if both the scalar field and the BH are charged, but if there are no superradiant modes in the scalar field cloud, there is no growth of the scalar field. This is seen in one of the examples in the bottom panel, for which the choice of parameters (q and Q), leads to $\omega_{\rm SF} > \omega_{\rm c}$.

Having clarified the essential trends when varying the BH charge, we fix this charge to a large value $Q = 0.9$ to make the superradiant instability strong and focus on the variation of the scalar field charge and the mirror radius. We have evolved $8 \times 3 = 24$ different models to study the variation of these parameters corresponding to the values shown in Eqs. (38) and (36). A summary of the physical quantities obtained in these evolutions is shown in Table I.

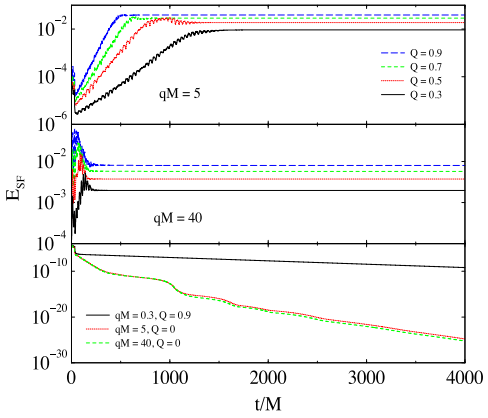

FIG. 3. Time evolution of the scalar field energy, displayed in logarithmic scale, for $r_{\rm m} = 14.2M$, different values of the initial BH charge Q and (top panel), $qM = 5$; (middle panel) $qM = 40$; (bottom panel) different values of the scalar field charge q.

For each model studied, Table I shows the following: the e-folding time (third column) obtained as the best fit of the form $|\Phi| \sim e^{t/\tau}$ during the growth phase; the final scalar field frequency obtained from a fast Fourier transform and the final critical frequency, obtained from (40); the initial and final scalar field energy, obtained from (41), as well as their ratio; the final BH irreducible mass, computed in terms of the AH area $A_{\rm AH}$, [39], on each time slice, as

$$M_{\rm AH} = \sqrt{\frac{A_{\rm H}}{16\pi}}; \tag{42}$$

and the final scalar field and BH charge, the former being obtained from a formula similar to (41) replacing $\mathcal{E}^{\rm SF}$ by the charge density, and the latter, $Q_{\rm BH}$, evaluated at the AH as [32]

$$Q_{\rm BH} = (r^2 e^{6\chi}\sqrt{ab^2}E^r)|_{\rm AH}. \tag{43}$$

In the following subsections we describe various trends that can be observed from the results in Table I.

1. Entropy growth

As a first observation we note that, for the initial RN BH, the irreducible mass is $M_{\rm irr}^{\rm ini} \simeq 0.718M$. Inspection of Table I shows that the final BH has a larger $M_{\rm irr}$, for all cases. This confirms that the evolution abides with the area law and, in this respect, charged superradiance can be regarded as a classical process in BH physics. It can also be concluded that the final irreducible mass grows with the scalar field charge. This is a consequence of two factors: (i) scalar fields with a larger charge are more efficient in

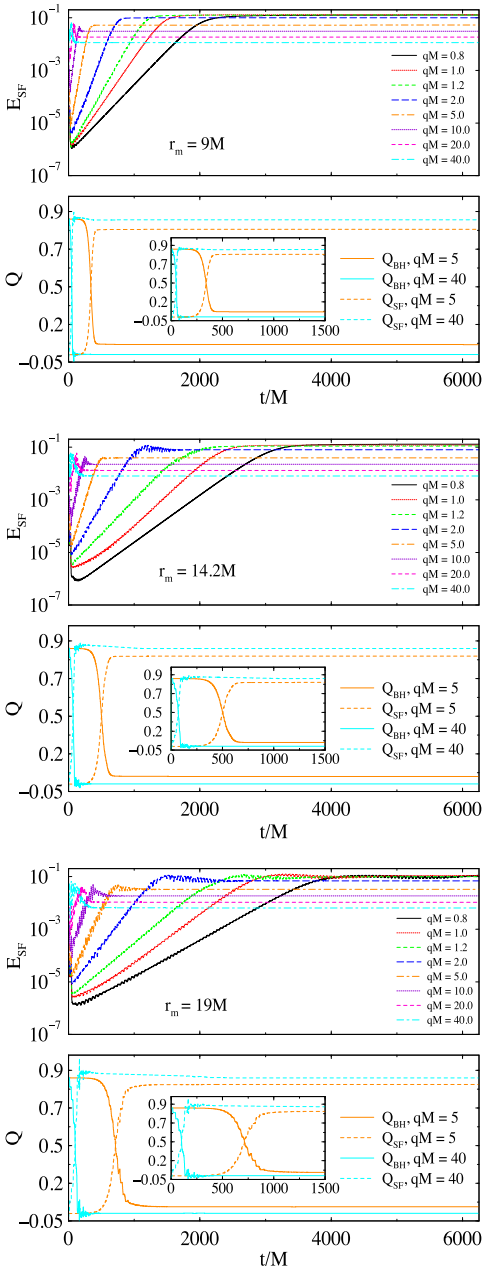

FIG. 4. Time evolution of the scalar field energy and charge and the BH charge, displayed in logarithmic scale, for the following: (top panels) $r_{\rm m} = 9M$; (middle panels) $r_{\rm m} = 14.2M$; (bottom panels) $r_{\rm m} = 19M$. The inset zooms in the early phase of the evolution for clarity.

discharging the BH, transferring its charge to the scalar field; (ii) by contrast, the scalar field energy grows less, in terms of the final-to-initial energy ratio, with increasing scalar field charge.

2. Impact of the mirror radius and scalar field charge

The first consequence of varying the mirror radius is a variation in the time scale of the process (for all other parameters fixed): the larger the mirror radius, the larger the e-folding time. This is an intuitive behavior, as the recurrent scattering that leads to the exponential pileup of the superradiant modes takes longer in a larger cavity. This behavior had already been noticed in linear studies [22]. Such a trend is more easily visualized in Fig. 4, where the time evolution of the scalar field is exhibited for the various values of q and for the three values of the mirror radius.

Another clear trend when increasing the mirror radius is that the critical frequency at which equilibrium is achieved is smaller. Naively this is associated with a larger wavelength of the dominant superradiant mode, which is allowed in a larger cavity. A smaller critical frequency implies a smaller horizon electric potential and thus a larger charge to energy ratio transfer to the scalar field. This is in agreement with what can be observed from the table. Concerning the charge, the relevant information is in the last two columns of Table I: for the same q, a larger radius implies a larger (smaller) fraction of charge in the scalar field (BH). Note that the corresponding panels of Fig. 4 show a perfect charge exchange between the BH and the scalar field. Concerning the energy transfer, inspection of the sixth to eighth columns of Table I shows that increasing the mirror radius leads to a smaller energy growth of the scalar cloud. This inverse correlation between charge transfer and energy transfer had already been observed in [26] and also occurs when varying q. Increasing the scalar field charge (likewise increasing the mirror radius) leads to a higher charge transfer to the scalar field but lower energy growth of the scalar field cloud. In terms of the strength of the instability, however, measured by the e-folding time, increasing the scalar field charge leads to the opposite trend to that of increasing the mirror radius: a larger scalar field charge leads to a faster growth of the instability.

3. Impact of scalar field mass

In our simulations presented in [26] we chose to discuss a massive scalar field, as it seems far-fetched to consider a massless, but charged, scalar field (all charged particles are massive, in the Standard Model of particle physics). Still, for the sake of completeness, we here discuss the effect of the mass, by comparing simulations of a massive ($\mu M = 0.1$) and a massless scalar field, and by focusing on a particular feature of the field distribution in the equilibrium state.

In Fig. 5 we plot the scalar field magnitude, at two different time slices, for the evolution of the massive and the massless scalar field. As can be observed from the various panels, at the first time slice plotted, $t = 50M$, the scalar field distribution is "bumpy," with several maxima and minima, and possibly with nodes. In the final time slice, however, $t = 2000M$, corresponding to a late time at which equilibrium has been attained, there are no nodes. Moreover, whereas for the massless case the scalar field magnitude profile is monotonically decreasing from the horizon to the mirror, for the massive case there is a maximum.

Charged hairy BHs in a cavity at the threshold of the superradiant instability were constructed in [27], for the

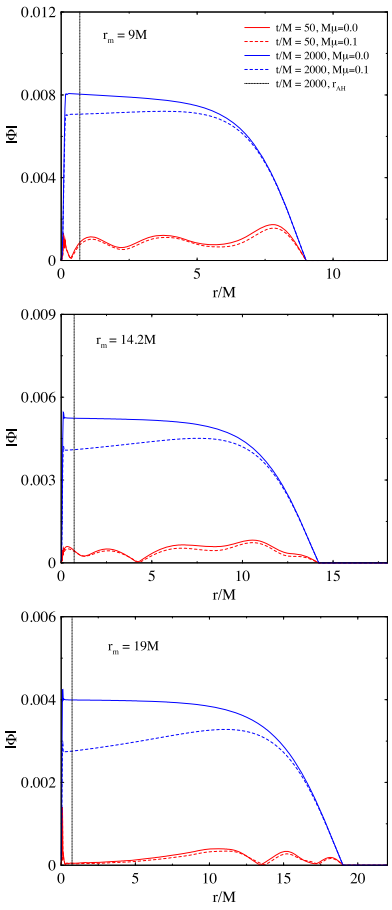

FIG. 5. Scalar field magnitude at two different time slices, for two different values of the scalar field mass, in terms of the radial coordinate, for $qM = 20$ and $r_m = 9M$ (top panel), $r_m = 14.2M$ (central panel), $r_m = 19M$ (bottom panel). The vertical line marks the location of the AH at the final time.

model (1) with $\mu = 0$. Therein it was established that, amongst the different families of such hairy BHs, with different numbers of nodes for the scalar field magnitude between the horizon and the mirror, only the nodeless solutions are stable against perturbations (and hence could be the true end point of the instability process). This is exactly what we find for our hairy BHs—the scalar field magnitude is nodeless when equilibrium is reached. We remark that the stationary solutions in [27] were obtained for a massless scalar field; consequently the scalar field magnitude for the stable solutions was monotonically decreasing from the BH to the mirror, in agreement with what is found *dynamically* in our simulations and exhibited in Fig. 5.

4. Impact of the initial cloud parameters

In Fig. 6 we investigate the dependence of the evolution on the initial scalar perturbation. We compare three different perturbations. The black solid line corresponds to the default Gaussian, used in all other simulations presented in this paper ($A_0 = 3 \times 10^{-4}$, $\sigma = \sqrt{2}$); the green dashed line corresponds to a scalar perturbation with a lower amplitude but slightly more spread ($A_0 = 2.0 \times 10^{-4}$, $\sigma = 1.8$); finally the red dotted line corresponds to a much lower amplitude perturbation and is very narrow ($A_0 = 2.1 \times 10^{-5}$, $\sigma = 0.01$). The corresponding Gaussians are plotted, for comparison, in the top panel of Fig. 6. The

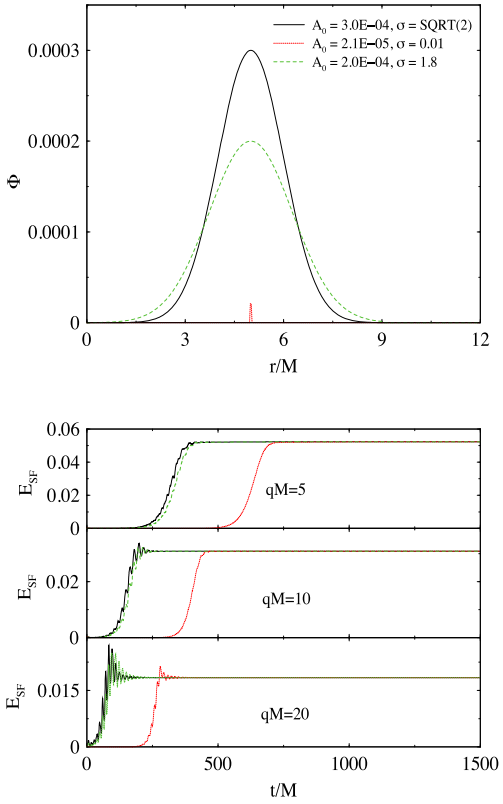

FIG. 6. The three different Gaussians used as initial data (top panel). The corresponding time evolutions, for three different values of qM (bottom panels).

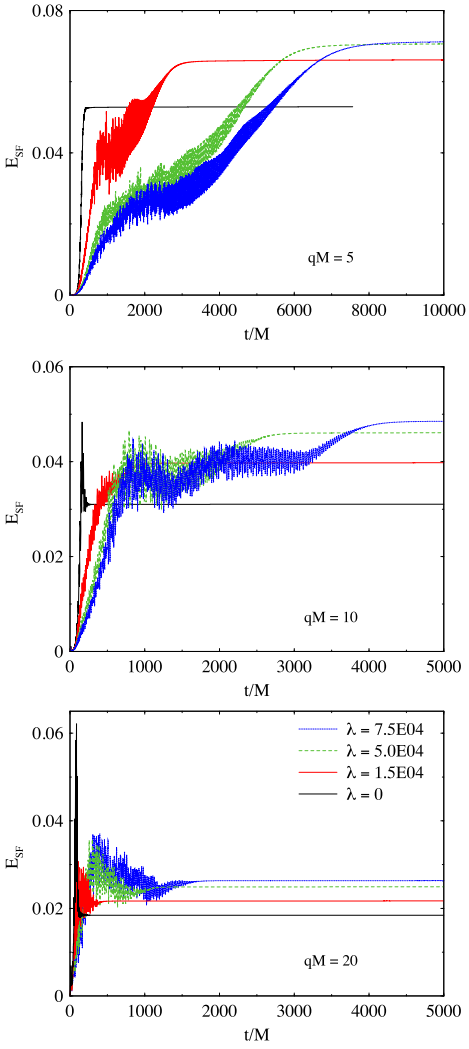

FIG. 7. Time evolutions of the scalar field energy for different values of the quartic self-coupling and $qM = 5$, 10, 20 (top, middle, and bottom panels).

bottom panel shows the corresponding time evolutions of the scalar field energy, using the same color convention, from which one can extract three observations. First, smaller perturbation amplitudes lead to a longer superradiant growth phase. Second, the final scalar field energy is insensitive to the initial perturbation. Third, the scalar field energy overshoot (see Sec. IV D for a discussion of this overshooting behavior) observed in the $qM = 10$, 20 cases is larger for larger perturbations. These features can be interpreted as the need to attain a certain threshold in the scalar cloud energy for the saturation phase to kick in. Naturally this threshold takes longer, when starting with a smaller perturbation. Still, the final hairy BH obtained is essentially insensitive to the perturbation parameters, as long as the perturbation approximation remains valid.

5. Impact of the scalar field self-interactions

We now tackle the effect of adding a quartic self-interaction to the scalar field, by taking $\lambda \neq 0$ in the model described by action (1). In Fig. 7 we show the time evolution of the scalar field energy for three nonzero values of the quartic self-coupling together with the case with no self-interactions, for three different values of qM.

The overall trends revealed by inspection of Fig. 7 is as follows. Increasing the self-coupling leads to a slower growth of the scalar field energy outside the horizon. But the final state corresponds to a hairy BH with more energy in the scalar field. Moreover, the self-interactions promote more energy exchange between the BH and the scalar field outside the horizon; i.e., the evolution is never monotonic, even for small qM values. This is likely associated with the mode conversion allowed by the self-interactions, a suggestion supported by the mode analysis discussed below, in Sec. IV D 1.

As in all previous cases, the increase in the ability to transfer energy from the BH into the scalar field is accompanied by a decrease in the ability to transfer charge from the BH to the scalar field. This is illustrated in Fig. 8 for the simulations with $qM = 20$.

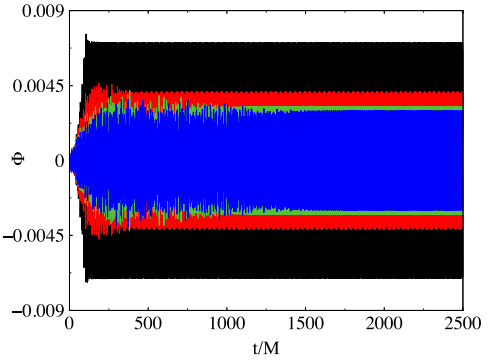

FIG. 9. Time series for the (real part of the) scalar field for different values of the quartic self-coupling (same color coding as in Fig. 8) and $qM = 20$.

Interestingly, the larger scalar field energy obtained for larger self-couplings is not associated with a larger scalar field amplitude outside the horizon. This can be concluded from Fig. 9, where the oscillations of the (real part of the) scalar field are shown for $qM = 20$. It can be observed that these oscillations are larger for *smaller* self-coupling. This result is confirmed in Fig. 10, where the magnitude of the final scalar field profile is shown as a function of the radial coordinate. Figure 10 clarifies, moreover, that the scalar field *spatial gradients* become larger when increasing the self-coupling. Thus, the larger gradients, rather than a larger scalar field magnitude, yield the larger scalar field energy outside the horizon, for larger self-coupling.

As we saw before, the presence of a mass term leads to an extremum in the scalar field magnitude radial profile (as

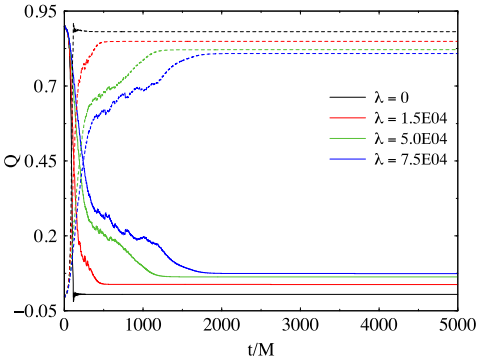

FIG. 8. Time evolution of the electric charge in the scalar field outside the horizon, for different values of the quartic self-coupling and $qM = 20$.

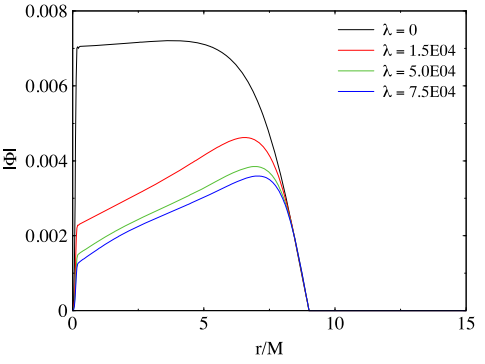

FIG. 10. Magnitude of the scalar field, in terms of the radial coordinate, for the final BH configuration, for different values of the quartic self-coupling and $qM = 20$.

opposed to a monotonic function for the massless case; cf. Sec. IV C 3), and hence a larger radial second derivative of that magnitude. The self-interactions term, from Fig. 10, tends to further increase this second derivative, in the neighborhood of the extremum.

D. Bosenova and mode analysis

Analysis of Fig. 4 reveals a qualitative difference in the evolution of the scalar field energy between low and high scalar field charge simulations. Whereas the former exhibits an essentially monotonic growth, the latter displays a more turbulent evolution before the equilibrium phase, wherein the energy extraction overshoots the equilibrium value and some energy is returned to the BH. This behavior is detailed in Fig. 11 (top panel) for $qM = 20$ and for the three different positions of the mirror. Figure 11 shows strong oscillations in the scalar field energy contained outside the horizon, before the system relaxes into an equilibrium configuration. Observe also that when the mirror is set closer to the BH, the relaxation is faster.

During the oscillations observed in Fig. 11, some of the energy in the scalar field is pushed back into the BH, before being extracted again, in a process that can last several cycles. In [26], it was suggested that this process resembles the bosenova explosion, described in [29,30]. Such an explosion, resulting from the nonlinear interactions of the scalar field, would push the energy of a test, but nonlinear, scalar field on the Kerr background, back into the BH. A simpler explanation, moreover not needing to invoke nonlinear effects, was put forward in [28], by studying the growth of the superradiant instability in charged AdS BHs, a setup with analogous physics to the one studied herein. These authors argued that oscillations such as the ones observed in Fig. 11 result from modes that become nonsuperradiant, as the horizon electric potential (and hence the critical frequency) decreases, and consequently fall back into the BH. In order to test this hypothesis in our setup, we have performed the mode analysis shown in Fig. 12. These figures show that for q just above the instability threshold (the smallest q value, $qM = 0.8$), the system only has a single superradiant mode, and the evolution consists of a very smooth transition to the stationary equilibrium state, in agreement with the low q curves in Fig. 4. For larger q ($qM = 5$ and 20), one

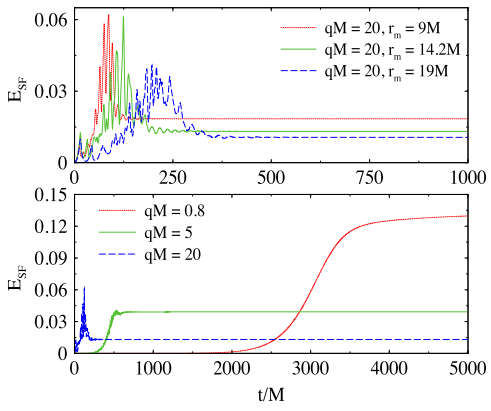

FIG. 11. Top panel: Details of the oscillations of the energy density during the "explosive" phase, for the $qM = 20$ models and three different positions of the mirror. The extracted energy overshoots the final equilibrium value, and strong oscillations follow. Bottom panel: Variation of the scalar field energy density for three models for which the mode analysis is performed in Fig. 12.

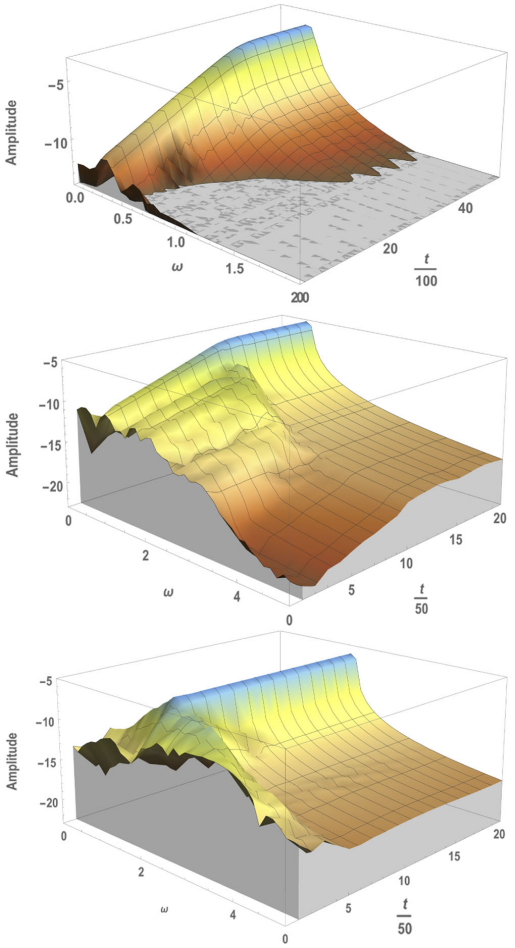

FIG. 12. Mode analysis for (top panel) $qM = 0.8$, (central panel) $qM = 5$, (bottom panel) $qM = 20$. For all three cases $\mu M = 0.1$ and $r_m = 14.2M$.

observes more than one initially superradiant mode growing, since they are in the superradiant range, but decay before the end state is reached, as they exit the superradiant window. This qualitatively explains the oscillations seen in Fig. 11. In this case, the only mode that does not decay is the fundamental mode, which matches the critical frequency as the system relaxes into the hairy BH solution.

1. Mode analysis with $\lambda \neq 0$

The mode analysis of the previous subsection suggests that despite the nonlinear nature of the process leading to

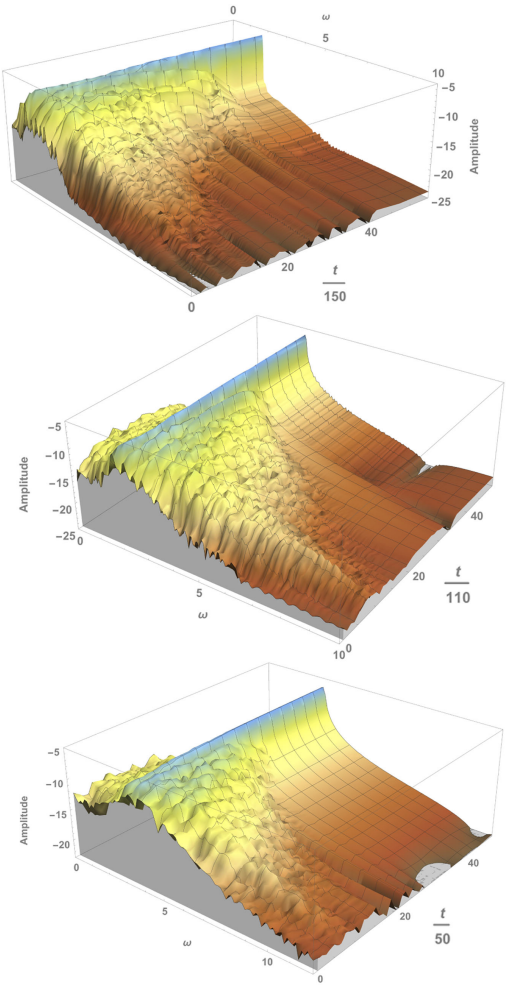

FIG. 13. Mode analysis for the model with self-interactions, with $\lambda = 7.5 \times 10^4$ and (top panel) $qM = 5$, (central panel) $qM = 10$, (bottom panel) $qM = 20$. For all three cases $\mu M = 0.1$ and $r_m = 9M$.

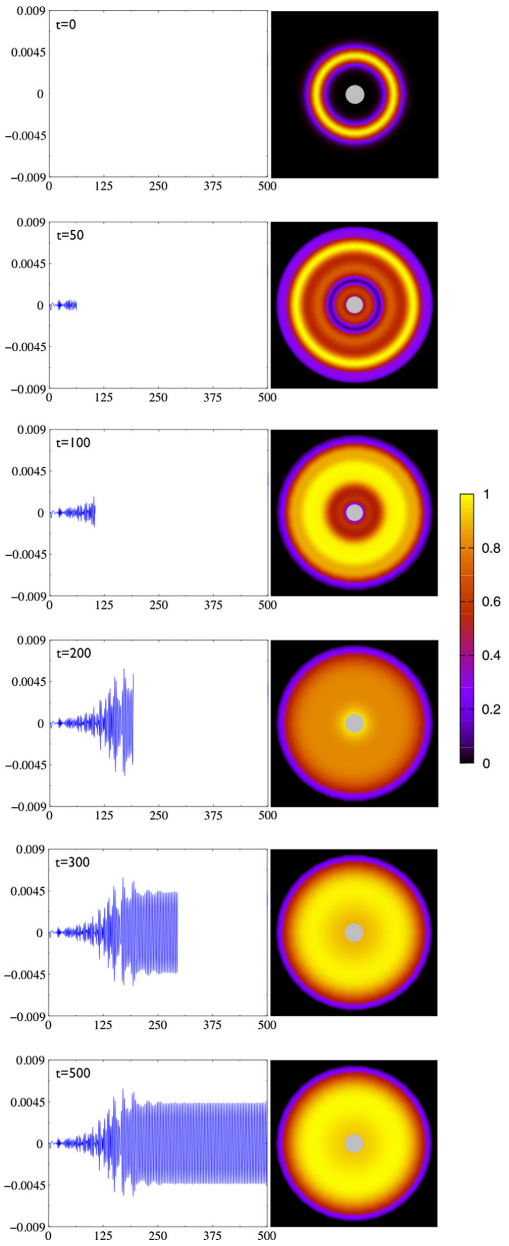

FIG. 14. Illustration of the formation of a hairy BH for $qM = 20$, $\lambda = 0$. The left panels show the time series until a certain time, and the right (two-dimensional) panels show the corresponding snapshot, at that time, of the normalized scalar field profile magnitude (cf. color bar). The inner white circle denotes the BH region, bounded by the apparent horizon.

the hairy BH formation, different scalar field modes evolve in an essentially independent way and, moreover, in the way predicted by the linear (test field) theory. A natural question is how the scalar field self-interactions affect such evolution. To address this question we plot in Fig. 13 a mode analysis for the evolution with $\lambda = 7.5 \times 10^4$ and $qM = 5, 10, 20$. Some differences with respect to the cases without self-interactions shown in Fig. 12 are notorious. A first difference is that the dominant mode, which ends up defining the final BH hair, is essentially unchanged during the evolution. In particular the growth phase, expected from linear theory, is suppressed. The reason is that for the (large) values of λ (and small mass μ) considered, the self-interacting (quartic) term is almost of the order of the (quadratic) mass term from the very beginning and hence the linear approximation never holds. A second difference is that the remaining modes, which end up decaying into the BH, are now more turbulent. It is plausible that this is a manifestation of mode conversion, promoted by the self-interactions. Of course, such mode conversion can also occur, even without the manifest scalar self-coupling, due to the implicit self-coupling induced via the coupling to gravity. Nonetheless, our findings are that, for the setups and parameters considered herein, the effect is clearer in the presence of a nonvanishing self-interaction term.

V. CONCLUSIONS

In this paper we have extended and complemented the results presented in a recent *Letter* [26] on the nonlinear development of the superradiant instability for a RN BH in a cavity. Following the development of this instability, we have shown it leads to the dynamical formation of a hairy RN BH, of the type studied in [27] as stationary solutions. This falsifies the weak version of the no-hair hypothesis, albeit not for a truly asymptotically flat spacetime. In Fig. 14 we provide an illustration of the dynamical formation of the hairy BH.

We have examined the sensitivity of the hair growth process to the BH charge, to the mirror radius, to the scalar charge and mass, to the parameters of the initial scalar perturbation, and to the introduction of a scalar self-coupling. In a nutshell, the energy extraction is *more* efficient for lower scalar field charge, for larger BH charge, and for smaller mirror radius. The trend with the charge extraction is opposite: it is *less* efficient for lower charge coupling, for larger BH charge, and for a smaller mirror radius. Concerning the existence, or not, of scalar field mass we have confirmed that this leads to a qualitative difference in the final scalar field magnitude profile, which is monotonically decreasing, from the horizon to the mirror, for massless scalar fields, but has a maximum for massive scalar fields. Introducing a scalar field quartic self-coupling, the final scalar field magnitude profile acquires larger spatial gradients, which justifies the larger energy transferred from the BH to the scalar field, despite the lower amplitude of the final scalar field profile, as compared to the non-self-interacting case. We have also observed that the final hairy BH is essentially insensitive to varying the initial perturbation, even though the details of the evolution depend on it.

We have clarified the oscillating behavior for the scalar field energy outside the horizon which is observed for the larger scalar field charges. A mode analysis reveals that various modes contribute to the superradiant growth in the early states of the process. However, a single mode remains at the end, in equilibrium with the BH; thus the other modes became nonsuperradiant and decay back into the BH before equilibrium is attained. This is in contrast with the smaller q simulations, for which a single mode is superradiantly growing from the early stages of the process, and hence the equilibrium phase is achieved essentially monotonically. This analysis confirms the observations in [28], for our setup. Such mode analysis lends support to the linear approximation and even to the use of an adiabatic approximation, such as in [40], for taking into account the backreaction. Indeed, individual modes evolve essentially independently, exchanging their energy with the horizon. When turning on self-interactions, however, the picture changes. For sufficiently large self-coupling, the regime predicted by the linear theory is essentially unobserved, and each mode, except the dominant one, fluctuates noticeably until it completely decays. Not surprisingly, therefore, turning on self-interactions limits the validity of a linear approximation.

Finally, we remark that the hairy BHs we have dynamically shown to form in this paper can be interpreted as a bound state of a RN BH and a charged scalar soliton in a cavity. This latter class of solutions was recently studied in detail in [41]. It was shown in this work that, amongst these solitonic solutions, some are unstable. An interesting question is, thus, what is the development of the instability for such unstable solitons, and in particular, if they evolve into a hairy BH. The technology described herein can be used to tackle this question. We hope to report on it in the near future.

ACKNOWLEDGMENTS

This work has been supported by the Spanish MINECO (AYA2013-40979-P), by the Generalitat Valenciana (PROMETEOII-2014-069), by the CONACyT-México Grant No. 233137, by the Max-Planck-Institut für Astrophysik, by the FCT (Portugal) IF programme, by the CIDMA (FCT) strategic project UID/MAT/04106/2013 and by the H2020-MSCA-RISE-2015 Grant No. StronGrHEP-690904. Computations have been performed at the Servei d'Informàtica de la Universitat de València.

APPENDIX: SOURCE TERMS

In this Appendix the source terms included in the explicit or partially implicit operators are detailed.

First, a, b, $X=\psi^{-1/2}$, α, β^r, Φ, and E^r are evolved explicitly; i.e., all the source terms of the evolution equations of these variables are included in the L_1 operator of the second-order PIRK method.

Second, A_a and K are evolved partially implicitly, using updated values of α, a, and b. More precisely, the corresponding L_2 and L_3 operators associated with the evolution equations for A_a and K read

$$L_{2(A_a)}=-\left(\nabla^r\nabla_r\alpha-\frac{1}{3}\nabla^2\alpha\right)+\alpha\left(R^r_r-\frac{1}{3}R\right), \quad \text{(A1)}$$

$$L_{3(A_a)}=\beta^r\partial_r A_a+\alpha K A_a-16\pi\alpha(S_a-S_b), \quad \text{(A2)}$$

$$L_{2(K)}=-\nabla^2\alpha, \quad \text{(A3)}$$

$$L_{3(K)}=\beta^r\partial_r K+\alpha\left(A_a^2+2A_b^2+\frac{1}{3}K^2\right)+4\pi\alpha(\rho+S_a+2S_b). \quad \text{(A4)}$$

Next, $\hat{\Delta}^r$, Ψ, Π, φ, and a_r are evolved partially implicitly, using the updated values of α, a, b, β^r, ψ, A_a, K, Φ, and E^r. Specifically, the corresponding L_2 and L_3 operators associated with the evolution equation for $\hat{\Delta}^r$, Ψ, Π, φ, and a_r are given by

$$L_{2(\hat{\Delta}^r)}=\frac{1}{a}\partial_r^2\beta^r+\frac{2}{b}\partial_r\left(\frac{\beta^r}{r}\right)+\frac{\sigma}{3a}\partial_r(\hat{\nabla}_m\beta^m)-\frac{2}{a}(A_a\partial_r\alpha+\alpha\partial_r A_a)-\frac{4\alpha}{rb}(A_a-A_b)+\frac{\xi\alpha}{a}\left[\partial_r A_a-\frac{2}{3}\partial_r K+6A_a\partial_r\chi+(A_a-A_b)\left(\frac{2}{r}+\frac{\partial_r b}{b}\right)\right], \quad \text{(A5)}$$

$$L_{3(\hat{\Delta}^r)}=\beta^r\partial_r\hat{\Delta}^r-\hat{\Delta}^r\partial_r\beta^r+\frac{2\sigma}{3}\hat{\Delta}^r\hat{\nabla}_m\beta^m+2\alpha A_a\hat{\Delta}^r-8\pi j_r\frac{\xi\alpha}{a}, \quad \text{(A6)}$$

$$L_{2(\Psi)}=\partial_r(\alpha\Pi), \quad \text{(A7)}$$

$$L_{3(\Psi)}=\beta^r\partial_r\Psi+\Psi\partial_r\beta^r, \quad \text{(A8)}$$

$$L_{2(\Pi)}=\frac{\alpha}{ae^{4\chi}}\left[\partial_r\Psi+\Psi\left(\frac{2}{r}-\frac{\partial_r a}{2a}+\frac{\partial rb}{b}+2\partial_r\chi\right)\right]+\frac{\Psi}{ae^{4\chi}}\partial_r\alpha-\alpha\left[\mu^2+\lambda|\Phi|^2+q^2\left(\frac{a_r^2}{ae^{4\chi}}\right)\right]\Phi+2iq\alpha\left[\frac{a_r\Psi}{ae^{4\chi}}+\varphi\Pi\right], \quad \text{(A9)}$$

$$L_{3(\Pi)}=\beta^r\partial_r\Pi+\alpha K\Pi, \quad \text{(A10)}$$

$$L_{2(\varphi)}=-\frac{\alpha}{ae^{4\chi}}\left[\partial_r a_r+a_r\left(\frac{2}{r}-\frac{\partial_r a}{2a}+\frac{\partial rb}{b}+2\partial_r\chi\right)\right]-\frac{a_r}{ae^{4\chi}}\partial_r\alpha, \quad \text{(A11)}$$

$$L_{3(\varphi)}=\beta^r\partial_r\varphi+\alpha K\varphi, \quad \text{(A12)}$$

$$L_{2(a_r)}=a_r\partial_r\beta^r-\partial_r(\alpha\varphi), \quad \text{(A13)}$$

$$L_{3(a_r)}=\beta^r\partial_r a_r-\alpha a e^{4\chi}E^r. \quad \text{(A14)}$$

Finally, B^r is evolved partially implicitly, using the updated values of $\hat{\Delta}^r$, i.e., $L_{2(B^r)}=\frac{3}{4}\partial_t\hat{\Delta}^r$ and $L_{3(B^r)}=0$.

[1] R. Ruffini and J. A. Wheeler, Phys. Today **24**, 30 (1971).
[2] C. A. R. Herdeiro and E. Radu, Int. J. Mod. Phys. D **24**, 1542014 (2015).
[3] M. S. Volkov, arXiv:1601.08230.
[4] P. Bizon, Acta Phys. Pol. B **25**, 877 (1994).
[5] R. P. Kerr, Phys. Rev. Lett. **11**, 237 (1963).
[6] R. Brito, V. Cardoso, and P. Pani, Lect. Notes Phys. **906**, 1 (2015).
[7] J. M. Bardeen, W. H. Press, and S. A. Teukolsky, Astrophys. J. **178**, 347 (1972).
[8] A. A. Starobinsky, Zh. Eksp. Teor. Fiz. **64**, 48 (1973).
[9] W. H. Press and S. A. Teukolsky, Nature (London) **238**, 211 (1972).
[10] T. Zouros and D. Eardley, Ann. Phys. (N.Y.) **118**, 139 (1979).
[11] V. Cardoso, O. J. Dias, J. P. S. Lemos, and S. Yoshida, Phys. Rev. D **70**, 044039 (2004).
[12] S. R. Dolan, Phys. Rev. D **76**, 084001 (2007).
[13] C. A. R. Herdeiro and E. Radu, Phys. Rev. Lett. **112**, 221101 (2014).
[14] C. Herdeiro and E. Radu, Classical Quantum Gravity **32**, 144001 (2015).
[15] C. A. R. Herdeiro, E. Radu, and H. Rúnarsson, Phys. Rev. D **92**, 084059 (2015).
[16] H. Okawa, H. Witek, and V. Cardoso, Phys. Rev. D **89**, 104032 (2014).

[17] W. E. East, F. M. Ramazanoğ, and F. Pretorius, Phys. Rev. D **89**, 061503 (2014).
[18] S. R. Dolan, Phys. Rev. D **87**, 124026 (2013).
[19] J. D. Bekenstein, Phys. Rev. D **7**, 2333 (1973).
[20] S. Hod, Phys. Lett. B **713**, 505 (2012).
[21] S. Hod, Phys. Rev. D **91**, 044047 (2015).
[22] C. A. R. Herdeiro, J. C. Degollado, and H. F. Rúnarsson, Phys. Rev. D **88**, 063003 (2013).
[23] S. Hod, Phys. Rev. D **88**, 064055 (2013).
[24] J. C. Degollado and C. A. Herdeiro, Gen. Relativ. Gravit. **45**, 2483 (2013).
[25] J. C. Degollado and C. A. R. Herdeiro, Phys. Rev. D **89**, 063005 (2014).
[26] N. Sanchis-Gual, J. C. Degollado, P. J. Montero, J. A. Font, and C. Herdeiro, Phys. Rev. Lett. **116**, 141101 (2016).
[27] S. R. Dolan, S. Ponglertsakul, and E. Winstanley, Phys. Rev. D **92**, 124047 (2015).
[28] P. Bosch, S. R. Green, and L. Lehner, Phys. Rev. Lett. **116**, 141102 (2016).
[29] H. Yoshino and H. Kodama, Prog. Theor. Phys. **128**, 153 (2012).
[30] H. Yoshino and H. Kodama, Classical Quantum Gravity **32**, 214001 (2015).
[31] N. Sanchis-Gual, J. C. Degollado, P. J. Montero, and J. A. Font, Phys. Rev. D **91**, 043005 (2015).
[32] J. M. Torres and M. Alcubierre, Gen. Relativ. Gravit. **46**, 1773 (2014).
[33] P. J. Montero and I. Cordero-Carrion, Phys. Rev. D **85**, 124037 (2012).
[34] N. Sanchis-Gual, J. C. Degollado, P. J. Montero, J. A. Font, and V. Mewes, Phys. Rev. D **92**, 083001 (2015).
[35] I. Cordero-Carrión and P. Cerdá-Durán, arXiv:1211.5930.
[36] I. Cordero-Carrión and P. Cerdá-Durán, *Advances in Differential Equations and Applications*, SEMA SIMAI Springer Series, Vol. 4 (Springer International Publishing, Switzerland, 2014).
[37] M. Alcubierre, J. C. Degollado, and M. Salgado, Phys. Rev. D **80**, 104022 (2009).
[38] M. Alcubierre, *Introduction to 3+1 Numerical Relativity* (Oxford University Press, New York, 2008).
[39] D. Christodoulou, Phys. Rev. Lett. **25**, 1596 (1970).
[40] R. Brito, V. Cardoso, and P. Pani, Classical Quantum Gravity **32**, 134001 (2015).
[41] S. Ponglertsakul, E. Winstanley, and S. R. Dolan, Phys. Rev. D **94**, 024031 (2016).

IOP Publishing Classical and Quantum Gravity

Class. Quantum Grav. **34** (2017) 165001 (18pp) https://doi.org/10.1088/1361-6382/aa7d1f

Dynamical formation of a hairy black hole in a cavity from the decay of unstable solitons

Nicolas Sanchis-Gual[1], Juan Carlos Degollado[2], José A Font[1,3], Carlos Herdeiro[4] and Eugen Radu[4]

[1] Departamento de Astronomía y Astrofísica, Universitat de València, Dr. Moliner 50, 46100, Burjassot (València), Spain
[2] Instituto de Ciencias Físicas, Universidad Nacional Autónoma de México, Apdo. Postal 48-3, 62251, Cuernavaca, Morelos, Mexico
[3] Observatori Astronòmic, Universitat de València, C/ Catedrático José Beltrán 2, 46980, Paterna (València), Spain
[4] Departamento de Física da Universidade de Aveiro and Centre for Research and Development in Mathematics and Applications (CIDMA), Campus de Santiago, 3810-183 Aveiro, Portugal

E-mail: Nicolas.Sanchis@uv.es

Received 11 January 2017, revised 19 June 2017
Accepted for publication 3 July 2017
Published 18 July 2017

Abstract

Recent numerical relativity simulations within the Einstein–Maxwell–(charged-)Klein–Gordon (EMcKG) system have shown that the non-linear evolution of a superradiantly unstable Reissner–Nordström black hole (BH) enclosed in a cavity, leads to the formation of a BH with scalar hair. Perturbative evidence for the stability of such hairy BHs has been independently established, confirming they are the true endpoints of superradiant instability. The same EMcKG system admits also charged scalar soliton-type solutions, which can be either stable or unstable. Using numerical relativity techniques, we provide evidence that the time evolution of some of these *unstable* solitons leads, again, to the formation of a hairy BH. In some other cases, unstable solitons evolve into a (bald) Reissner–Nordström BH. These results establish that the system admits two distinct channels to form hairy BHs at the threshold of superradiance: growing hair from an unstable (bald) BH, or growing a horizon from an unstable (horizonless) soliton. Some parallelism with the case of asymptotically flat boson stars and Kerr BHs with scalar hair is drawn.

Keywords: relativity and gravitation, classical black holes, numerical studies of black holes and black-hole binaries, Einstein–Maxwell spacetimes, spacetimes with fluids, radiation or classical fields

(Some figures may appear in colour only in the online journal)

1. Introduction

In two recent papers [1, 2], we have investigated the non-linear evolution of the superradiant instability of a Reissner–Nordström (RN) black hole (BH), triggered by a charged scalar field confined to a cavity, which surrounds the BH. This system is not only afflicted by superradiant instabilities—unlike asymptotically flat RN BHs [3, 4]—but also allows a sufficiently fast development of the instability [5–8], and hence a fully non-linear numerical treatment of the evolution. Moreover, within this system, superradiant instabilities occur even within spherical symmetry, making their treatment simpler.

Using numerical relativity techniques, we evolved in [1, 2] the Einstein–Maxwell–(charged-)Klein–Gordon (EMcKG) system, and showed that the endpoint of the instability is a hairy BH of the sort first discussed in [9] (see also [10]). In the appropriate gauge, the scalar hair is a stationary state characterized by a real frequency that equals the threshold frequency for the superradiant instability. Thus, these BHs *exist at the threshold of superradiance*, making them charged analogues of the (rotating) Kerr BHs with scalar [11, 12] and Proca hair [13] discovered in asymptotically flat spacetime (see also [14–16] for generalizations with charge and self-interactions and [17–19] for analogue solutions in higher dimensions).

Besides the hairy BHs, the same EMcKG system allows for soliton-like solutions, which are everywhere regular and horizonless [20, 21]. Indeed, the hairy BHs may be regarded as a bound state of these solitons with a horizon, in the same way that Kerr BHs with scalar (or Proca) hair can be regarded as a bound state of rotating boson stars [22] (or rotating Proca stars [23][5]) with a horizon (see, e.g. [26, 27], for discussions of horizons inside solitons). In [20, 21] the linear stability of the EMcKG solitons in a cavity was recently addressed and it was shown that some of these solutions are unstable against linear spherical perturbations. A natural question to ask is what is the end-point of the instability and, in particular, if the decay of these unstable solitons could yield a different channel for the formation of the aforementioned hairy BHs.

In this paper we shall address these questions, by using similar numerical methods to the ones used in [1, 2]. As we shall discuss below, there are different possible schemes to consider when evolving these EMcKG solitons. The reason is that the 'cavity', which is something virtual for the stationary soliton solutions, needs to be made concrete, and imposes a concrete rule in the dynamical evolution of the system. Different schemes result from a different choice of rule, and ultimately, they reflect different dynamical problems. We shall illustrate this explicitly, by considering two different schemes. For these two possibilities, albeit we observe some quantitative and qualitative differences, there is a universal feature: we shall provide numerical evidence that indeed a hairy BH at the threshold of superradiance may form from the decay of an unstable soliton. But we also observe, for both schemes, that some unstable solitons decay into a (bald) RN BH, rather than a hairy one.

This paper is organized as follows. We start in section 2 by briefly describing the stationary solitonic solutions of the EMcKG system in a cavity [20, 21], which we have reproduced,

[5] Static Proca stars have been recently generalized to include charge [24] or a cosmological constant [25].

and that will provide us with the initial data for our numerical evolutions. The framework for these evolutions is briefly reviewed in section 3, wherein both schemes are discussed and the corresponding numerical results are presented. Finally, in section 4, we provide some further discussion of our results and allude to potential issues of our methods. Furthermore, we speculate about the implications of our findings to the rotating, asymptotically flat case.

2. Stationary solitons of the EMcKG system in a cavity

2.1. The framework

We consider the following action, describing the EMcKG system (here we follow precisely the same conventions as in [20, 21], which allows a direct comparison with the results therein): $S = \int \sqrt{-g}\mathcal{L}\mathrm{d}^4x$ with

$$\mathcal{L} = \frac{R}{2} - \frac{1}{4}F_{\mu\nu}F^{\mu\nu} - \frac{1}{2}g^{\mu\nu}D^*_{(\mu}\Phi^* D_{\nu)}\Phi - \frac{\mu^2}{2}|\Phi|^2, \tag{1}$$

where we have used standard notation: g is the metric determinant, R is the Ricci scalar, μ is the scalar field mass and round brackets denote symmetrization, $Y_{(\mu\nu)} = \frac{1}{2}(Y_{\mu\nu} + Y_{\nu\mu})$ for a tensor field $Y_{\mu\nu}$. We use a mostly positive space-time signature, and units in which $8\pi G = c = 1$. The scalar field Φ is complex, and Φ^* is the complex conjugate of Φ. The electromagnetic field strength is denoted $F_{\mu\nu} = \nabla_\mu A_\nu - \nabla_\nu A_\mu$, where A_μ is the electromagnetic potential. In (1), we have introduced the gauge covariant derivative, $D_\mu = \nabla_\mu - \mathrm{i}qA_\mu$, where ∇_μ is the covariant derivative and q is the scalar field charge. These conventions are slightly different from the ones in our previous works [1, 2]. We shall further remark on this in section 3. Observe that the EMcKG system is invariant under the gauge transformation:

$$A_\mu \to \tilde{A}_\mu = A_\mu + \partial_\mu\chi(x)\,, \qquad \Phi \to \tilde{\Phi} = \mathrm{e}^{\mathrm{i}q\chi(x)}\Phi, \tag{2}$$

for a real function $\chi(x)$.

2.2. The solitons

To obtain the stationary solitonic solutions [20, 21], we shall consider an ansatz describing spherical, time-independent configurations. For an isotropic coordinate system, the metric ansatz reads

$$\mathrm{d}s^2 = -f_0(r)\mathrm{d}t^2 + f_1(r)[\mathrm{d}r^2 + r^2(\mathrm{d}\theta^2 + \sin^2\theta\mathrm{d}\varphi^2)], \tag{3}$$

while the matter fields are

$$A = A_0(r)\mathrm{d}t,\ \Phi = \phi(r). \tag{4}$$

In the following we shall be working with ansatz (3) and (4). But we observe that the gauge transformation (2), with $\chi = -\omega t/q$ yields the fields:

$$\tilde{A} = \left(A_0(r) - \frac{\omega}{q}\right)\mathrm{d}t,\ \tilde{\Phi} = \mathrm{e}^{-\mathrm{i}\omega t}\phi(r). \tag{5}$$

In this gauge the scalar field oscillates with frequency ω. We recall that the critical frequency for superradiance, ω_c, around a RN BH, is set by the horizon electric potential as $\omega_c = q\phi(r_H) \equiv -q\tilde{A}_0(r_H)$, where r_H is the radial coordinate of the horizon. This is the condition obeyed by a BH at the threshold of superradiance, which in terms of the 'old' gauge (4) reads $A_0(r_H) = 0$.

With our metric ansatz the EMcKG equations reduce to a set of four second order equations plus a constraint (which is one of the Einstein eqs.). For solitons, these equations are solved starting with the following small-r expansion

$$\begin{aligned} f_0(r) &= f_{00} + \frac{1}{6}(2a_0^2q^2 - f_{00}\mu^2)f_{10}\phi_0^2 r^2 + \mathcal{O}(r^4), \\ f_1(r) &= f_{10} - \frac{f_{10}^2}{12f_{00}}(a_0^2q^2 + f_{00}\mu^2)\phi_0^2 r^2 + \mathcal{O}(r^4), \\ A_0(r) &= a_0 + \frac{1}{6}a_0 f_{10}q^2\phi_0^2 r^2 + \mathcal{O}(r^4), \\ \phi(r) &= \phi_0 - \frac{f_{10}}{6f_{00}}(a_0^2q^2 - f_{00}\mu^2)\phi_0 r^2 + \mathcal{O}(r^4), \end{aligned} \tag{6}$$

with $f_{00}, f_{10}, a_0, \phi_0$ four arbitrary constants and f_{00}, f_{10} strictly positive such that the metric has the correct signature. In the numerical integration one takes $f_{00} = f_{10} = 1$. This can be justified as follows. We notice that the equations of motion possess the following independent scaling symmetries (invariant functions are not shown)

$$(i)\ f_0 \to \lambda^2 f_0,\ A_0 \to \lambda A_0, \tag{7}$$

$$(ii)\ r \to \lambda r,\ f_1 \to \frac{f_1}{\lambda^2}, \tag{8}$$

$$(iii)\ r \to \lambda r,\ q \to \frac{q}{\lambda},\ \mu \to \frac{\mu}{\lambda}, \tag{9}$$

with $\lambda > 0$ an arbitrary number. The symmetries (i) and (ii) are used to set $f_{00} = f_{10} = 1$, while (iii) is used to set $q = 0.1$ (following [20]) without any loss of generality. This choice sets the scale; dimensionful quantities are given in units of q (e.g. ω/q is dimensionless). Then a continuum of solutions is found by varying the remaining parameters a_0, ϕ_0. We shall also focus on the massless scalar field case $\mu = 0$. The field equations are integrated numerically to find solitonic solutions by using a standard Runge-Kutta method. We start the numerical integration at $r = \epsilon$, where ϵ is typically 10^{-8}, using the expansions (6) as initial conditions. One finds that the scalar field ϕ oscillates about zero (see figure 1); the mirror defining the cavity can be placed at any zero of the scalar field, but here we shall always consider the mirror to be located at the first zero of the scalar field, whose radial position is labelled $r = r_m$. Thus, in this model, for the stationary solutions, the mirror is 'virtual' rather than corresponding to a concrete physical object that impacts on the EMcKG equations.

In section 3 we shall evolve eleven initial data sets, namely one which, according to [20], is associated with a stable solution (Model 0) and ten which are associated with unstable solitons (Models 1–10), all with $q = 0.1$ and $\mu = 0$[6]. These models are summarized in table 1, where we also anticipate the outcome of their numerical evolution using our two schemes. To exemplify the behaviour of the various functions $\{f_0(r), f_1(r), \phi(r), A_0(r)\}$ for typical solitons, we display in figure 1 their radial dependence for models 1 and 5 in table 1. According to the results of [20] these are both unstable solitons. Indeed, as we discuss below, we see them evolving in both schemes. In particular, for scheme I, one of these will be shown to decay into a hairy BH (model 1) and the other to decay into a bald BH (model 5).

[6] That these are stable or unstable can be observed by examining figure 11 in [20].

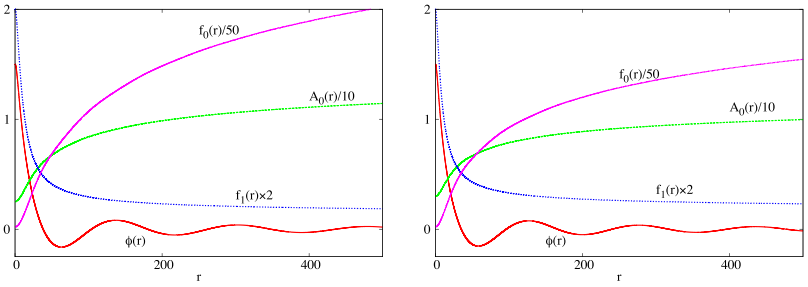

Figure 1. Metric, scalar field and gauge field functions for model 1 (left panel) and model 5 (right panel). Some functions are rescaled for better visualization. Observe the oscillations of the scalar field. The mirror position is at the first zero of the scalar field (see table 1).

3. Numerical evolutions

3.1. The framework

The numerical evolutions of our initial data are performed in the EMcKG system (1) but, following our previous work [1, 2], we use slightly different conventions, corresponding to the following rescaling of the fields shown in (1):

$$A_\mu \longrightarrow \sqrt{2}A_\mu, \qquad \Phi \longrightarrow \sqrt{8\pi}\Phi, \qquad q \longrightarrow \frac{q}{\sqrt{2}}. \tag{10}$$

The metric and mass parameter are unchanged. Rescalings (10) are imposed to all the data in table 1, which the table reports before the rescaling. This change also ensures that we use the same values for a_0, ϕ_0 and q than in [20].

The time update of the different systems of evolution equations we have to solve in our code (Einstein, Klein–Gordon, and Maxwell) is done using the same type of numerical techniques we have extensively used in previous work (see, in particular, [2, 28–30]). We refer the interested reader to those references for full details. In particular see equations (9)–(11) and (14)–(16) in [2] and (9)–(15) in [29]. Here, we simply mention that the evolution equations are integrated using the second-order Partially implicit Runge-Kutta (PIRK) method developed by [31, 32]. This method allows to handle the singular terms that appear in the evolution equations due to our choice of curvilinear coordinates. The derivatives in the spacetime evolution are computed using a fourth-order centered finite-difference approximation on a logarithmic radial grid. We also use fourth-order Kreiss-Oliger dissipation to avoid high-frequency noise appearing near the outer numerical boundary. For the simulations presented in this work we evolve the electric field explicitly and the electric potentials implicitly.

We perform the evolution of the unstable and the stable solitons by rescaling the lapse function of the 3 + 1 formalism [33] in the following way:

$$\tilde{\alpha} = \alpha/\alpha(r_{\max}). \tag{11}$$

where $\alpha = \sqrt{f_0}$. The lapse is rescaled to facilitate our numerical simulations, as it ensures that $\tilde{\alpha} \to 1$ at the outer boundary of our grid, which corresponds to Minkowski spacetime.

Table 1. The eleven soliton models we use as initial data, all with $q = 0.1$ and $\mu = 0$. From left to right the columns report: the model number, the parameters a_0, ϕ_0 and r_m characterizing the corresponding solitons (columns 2 to 4), and the outcome of the evolutions for the two schemes (following columns), in particular if a hairy BH (HBH) forms or if a bald RN BH results from the evolution. In the former case, the critical frequency of the BH, ω_c, and the corresponding frequency of oscillation of the scalar field, ω_Φ, are also indicated. The error in the frequencies ω_Φ is about 5% and is estimated from the convergence test by increasing the resolution of the spatial grid. We observe that the difference between the critical frequency and the scalar-field frequency is reduced with increasing resolution, as expected.

	a_0	ϕ_0	r_m	Scheme I	ω_c	ω_Φ	Scheme IIa	ω_c	ω_Φ	Scheme IIb	ω_c	ω_Φ
0	1.5	1.5	45.2	HBH	0.044	0.050	Stable			Stable		
1	2.5	1.5	38.2	HBH	0.057	0.056	(bald) RN	—	—	(bald) RN	—	—
2	2.6	1.5	37.6	HBH	0.057	0.055	(bald) RN	—	—	(bald) RN	—	—
3	2.7	1.5	37.0	HBH	0.058	0.055	(bald) RN	—	—	(bald) RN	—	—
4	2.8	1.5	36.4	HBH	0.056	0.054	(bald) RN	—	—	(bald) RN	—	—
5	3.0	1.5	35.2	(bald) RN	—	—	(bald) RN	—	—	(bald) RN	—	—
6	3.0	1.8	56.8	HBH	0.040	0.039	HBH	0.004	0.004	HBH	0.004	0.004
7	3.2	1.8	55.8	HBH	0.042	0.042	HBH	0.005	0.004	HBH	0.004	0.004
8	3.4	1.8	54.8	HBH	0.043	0.042	HBH	0.006	0.005	HBH	0.004	0.004
9	4.0	1.8	52.0	HBH	0.048	0.046	(bald) RN	—	—	(bald) RN	—	—
10	4.5	1.8	49.8	(bald) RN	—	—	(bald) RN	—	—	(bald) RN	—	—

3.2. The two schemes

We are interested in the dynamics of the solitons inside the cavity bounded by the mirror at $r = r_m$. Whereas the presence of the mirror in the stationary soliton solution is a matter of perspective, its presence in a dynamical evolution must be enforced by some dynamical rule. In other words, since a generic evolution of the initial data provided by the solitons described in the previous section, will not preserve the node at $r = r_m$, one has to place a mirror at the location of the node, enclosing a cavity. Here we shall consider two different dynamical rules.

In *Scheme I* we shall use the initial data provided by the stationary soliton solutions *only* inside the cavity. That is, scheme I is based on a *truncated soliton*. Outside the cavity we change the initial data by setting the scalar field to zero all along the computational domain, but leaving the metric fields unchanged. Whereas this is the simplest thing to do, within the 'scalar field enclosed in a cavity' perspective, it has the obvious shortcoming that the initial data outside the cavity does not satisfy the field equations. In other words, the initial data is constraint-violating outside the cavity. As we show below, however, the simulation converges to a solution of the field equations within acceptable errors for this system, the endpoint being either a hairy BH or a bald BH, depending on the starting soliton. We remark that this dynamical perspective departs from that encoded in the perturbation theory considered in [20], where the soliton extends to spatial infinity and the perturbations are required to preserve the node at the mirror location. As a consequence of this difference, model 0 in table 1, which according to [20] is a stable soliton, turns out to evolve in scheme I.

In *Scheme II*, on the other hand, we shall use the initial data provided by the stationary soliton solutions *both* inside and outside the cavity. We therefore use the *full soliton*. The presence of the mirror is enforced by not evolving the scalar field value at the mirror, which is initially put to zero. This ensures the presence of the node during the whole evolution and (within numerical error) the absence of scalar energy or charge flux between the inside and outside of the cavity. This enforcement leads to more localized constraint violations, which occur only at the mirror location, and to a closer correspondence with the perturbation problem discussed in [20]. The results of the evolutions, however, are qualitatively similar to those of scheme I, i.e. we see two possible outcomes, *but* the 'same' soliton in both schemes may have a different fate. In scheme II we perturb the soliton inside the cavity by multiplying Φ by a factor slightly larger than one in order to trigger the evolution; then we consider two different perturbation factors leading to two sub-schemes: scheme IIa, with a factor of 1.05, and scheme IIb, with a factor of 1.01.

Our simulations employ a logarithmic radial grid with a maximum resolution of $\Delta r = 0.025$. The outer boundary of the computational domain is placed at $r_{\rm max} = 4.5 \times 10^3$, far enough as to not affect the dynamics in the inner region during the entire extent of the simulations. The (Courant) time step is given by $\Delta t = 0.1\Delta r$ which ensures long-term stable simulations. The definition of the quantities $E_{\rm SF}$ (scalar field energy), $M_{\rm AH}$ (apparent horizon mass), $Q_{\rm T}$ (total charge), $Q_{\rm SF}$ (scalar field charge), and $Q_{\rm BH}$ (black hole charge), that we use to interpret our results below, can be found in [2] and [34].

3.3. Numerical results—scheme I

Let us start by describing the numerical results under scheme I. In figure 2 (left panel) we show the result for the evolution of the energy in the scalar field computed as in [1, 2], for models 1–5. We observe that after an initial period of no remarkable change, all models exhibit a sharp decrease of the energy in the scalar field. For model 5 the drop is at $t \sim 150$ while for the other models the drop in the energy occurs at $t \sim 200$. For models 1–4 what follows is a new, non-zero, equilibrium value of the scalar field energy. However, for model 5 the energy in the scalar field keeps decreasing and tends to vanish asymptotically.

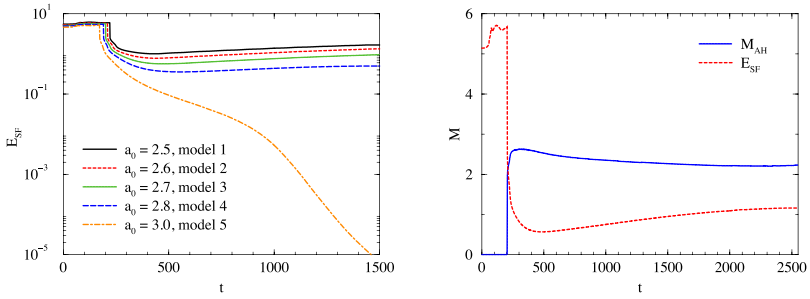

Figure 2. Time evolutions in scheme I: the left panel shows the scalar field energy for models 1–5, while the right panel shows the AH mass and scalar field energy for model 3.

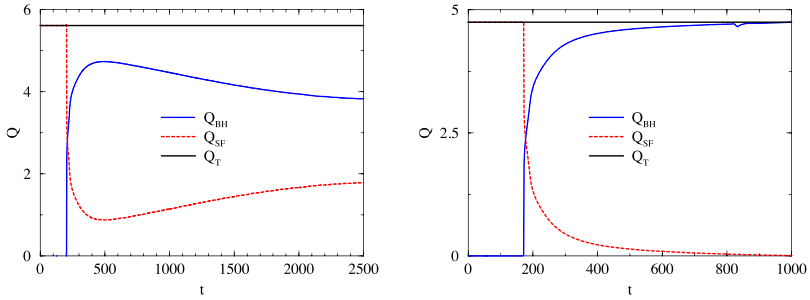

Figure 3. Time evolution of the charge in the scalar field, $Q_{\rm SF}$, in the BH (computed at the AH), $Q_{\rm BH}$, and of the total charge, $Q_{\rm T}$, for models 3 (left panel) and 5 (right panel), in scheme I.

In all models 1–5 we observe the formation of an apparent horizon (AH) at a time which roughly coincides with the sharp decay of the scalar field energy visible in figure 2. This is illustrated in the right panel of the figure for model 3. One can then compute the charge inside the AH and the charge in the scalar field using the expressions described in [1, 2]. The result is exhibited in figure 3 for models 3 and 5[7]. A clear charge transfer from the scalar field (soliton) to the BH is observed, with the total charge (black solid line) remaining constant within an excellent approximation. Whereas in model 3 the charge in the scalar field remains non-zero signaling the formation of a hairy BH, in model 5 the scalar field charge vanishes, signaling the formation of a (bald) RN BH.

To examine in more detail the type of hairy BH that forms in the decay of the soliton we show in the left panel of figure 4 the real part of the scalar field for models 1–5, as a function of time, extracted at a specific radial position $r = 5$. Correspondingly, the right panel of figure 4 displays the real and imaginary parts of the scalar field for model 3 as an illustrative example. It can be seen that for all these models the real and imaginary parts are sinusoidal

[7] There is a visible numerical artifact due to the noise coming from the mirror for model 5, around $t = 800$. It does not appear for model 3 at that time, because the numerical error propagates slower. With higher resolution, the amplitude increases but it becomes thinner.

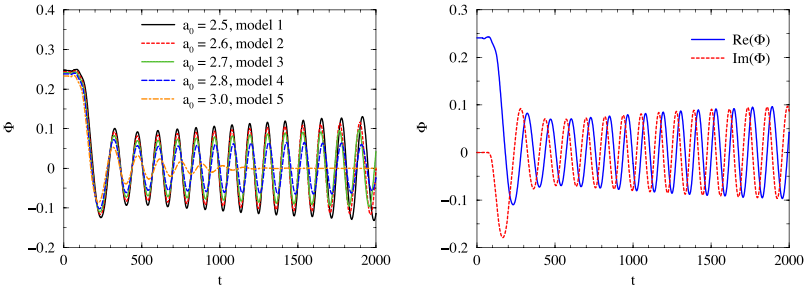

Figure 4. Time evolution of the real part of the scalar field amplitude for models 1–5 (left panel) and of the real (blue solid line) and imaginary (red dashed line) parts of the scalar field amplitude for model 3 (right panel). Data are extracted at $r = 5$. Notice the decay of the field amplitude in model 5.

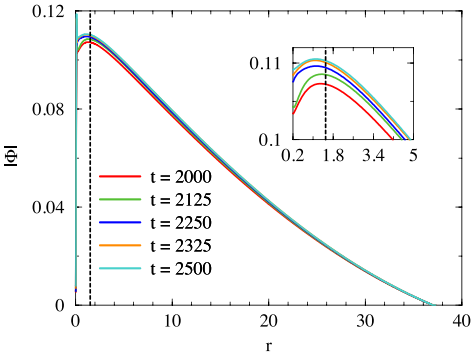

Figure 5. Radial profile of the scalar field magnitude for model 3 at different times of the evolution with scheme I. The vertical dashed line marks the location of the AH.

functions and have a phase difference of $\pi/2$; therefore, they oscillate with an opposite phase. The critical frequency for the BH that forms and the frequency of oscillation of the scalar field, computed as in [1, 2] are shown in table 1. They match within the numerical error, showing that these BHs are hairy BHs at the threshold of superradiance.

Finally, we display in figure 5 the radial profile of the scalar field magnitude for model 3 and at different times of the evolution. It is worth noticing that the maximum value attained by the scalar field (best visible in the inset) is inside the BH horizon (signaled by the dashed vertical line). Therefore, the scalar field decays monotonically from the horizon to the mirror, as one expects for stable hairy BHs [1, 9].

The results we have just discussed establish that a hairy BH can form as the outcome of numerical evolutions of unstable solitons. There are, however, two issues that must be discussed in the current scheme. The first issue is related to the constraint violations of the simulations. These arise due to the choice of initial data in scheme I, in which we set the scalar field to zero outside the mirror, but also due to the coordinate singularity at $r = 0$. Figure 6

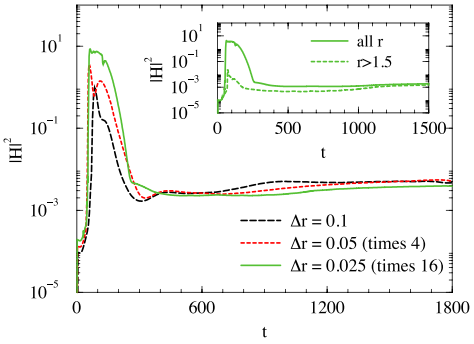

Figure 6. Time evolution of the L2 norm of the Hamiltonian constraint for model 3 using scheme I. The inset shows the evolution when considering the entire radial domain (solid line) and when removing the radial zones that eventually lie within the AH (dashed line). Second-order convergence is approximately achieved in the evolution for $t \gtrsim 400$.

plots the time evolution of the L2 norm of the Hamiltonian constraint for model 3 for three different radial grid resolutions. Whereas relatively large constraint violations are observed at some early phase of the evolution, namely during the formation of the AH and shortly after, the values of the violations decrease significantly for the remaining part of the evolution. We also computed the radial component of the momentum constraint in order to compare with the Hamiltonian constraint. We observe that they do not grow with time, their values are acceptable and comparable at the end of the simulation, and they behave similarly. We note that the values attained in the final state are comparable to those observed in our previous works [1, 2].

The second issue is related to the stable solution—model 0 in table 1. We have checked that the time evolution of this model indicates it is not stable; rather it evolves. What concerns us here is not so much what is the endpoint of this evolution, but the fact that the soliton in our dynamical scheme I is not stable, whereas it is stable in the perturbation scheme considered in [20, 21]. This discrepancy underlines the fact that the dynamical perturbations considered therein are not faithfully represented by our scheme I, and leads us to consider scheme II below.

To argue the generality of the behaviour observed for models 1–5 under scheme I, we display in figure 7 the time evolution of the scalar field energy (left panel) and the oscillations of the real part of the scalar field (right panel) for models 6–10. We observe the same trend to that found in models 1–5, namely, for the same value of ϕ_0 sufficiently small values of a_0 lead to a hairy BH, but for larger values the final state changes and a bald RN BH is obtained instead. Model 10 is the only one whose energy decreases during the rest of the evolution after the BH is formed. The total amount of scalar field energy remaining in the cavity is larger than for the previous five models.

3.4. Numerical results—scheme II

We now turn our attention to scheme II. In figure 8 we plot the evolution of the scalar field energy, for models 0-10 within scheme IIa (the first six models in the left panel and the last five in the right one). The first observation is that model 0 is now stable, in accordance to

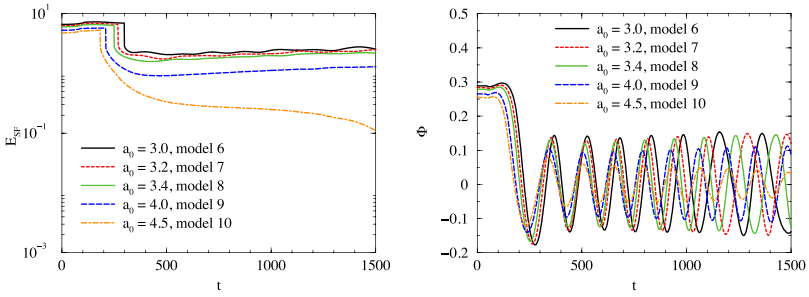

Figure 7. Time evolution of the scalar field energy (left panel) and of the real part of the scalar field amplitude (right panel) for models 6–10 in scheme I. The extraction radius is at $r = 5$.

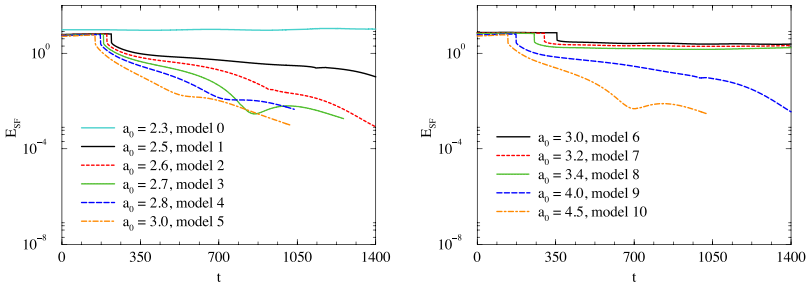

Figure 8. Time evolutions of the scalar field energy for models 0-5 (left panel) and models 6–10 (right panel), using scheme IIa.

[20], and the energy remains almost constant, taking into account that the soliton is slightly perturbed. For the unstable models 1–5, a BH forms at $t \gtrsim 200$ absorbing part of the scalar field energy. For all these models, the energy in the scalar field keeps decreasing with time, tending to vanish rather than approaching an equilibrium state. A different result is found for models 6–8, displayed in the right panel of figure 8. For these models the scalar field energy is almost constant after the formation of the BH. As observed in scheme I, however, increasing a_0 for fixed ϕ_0 beyond a certain value, the scalar field energy keeps decreasing with time, indicating that a bald RN BH, rather than a hairy BH, forms (see models 9 and 10 in the right panel of figure 8).

The charge transfer from the scalar field (soliton) to the BH in scheme II is monitored in figure 9, where we plot the evolution of the charge of the BH, of the scalar field, and of the total charge, for model 8 and for the two perturbations considered (schemes IIa and IIb). A clear charge transfer can be seen from the scalar field to the BH at the time of formation of the AH. The total charge, however, decreases when the BH forms (black curves), signaling an issue. This is in fact due to the amount of perturbation we set up initially. Comparison of both schemes shows that when the initial perturbation to the solution is reduced from 5% (scheme IIa, dashed black lines) to 1% (scheme IIb, solid black lines), then total charge conservation holds at a higher accuracy. Using a large perturbation has the desirable feature that it triggers

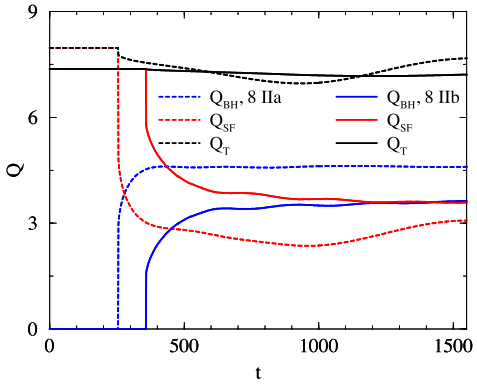

Figure 9. Time evolution of the charge in the scalar field, $Q_{\rm SF}$ (red curves), in the BH (computed at the AH), $Q_{\rm BH}$ (blue curves), and of the total charge $(Q_{\rm T})$ (black curves), for model 8. Dashed curves correspond to scheme IIa (5% perturbation) and solid lines to scheme IIb (1% perturbation).

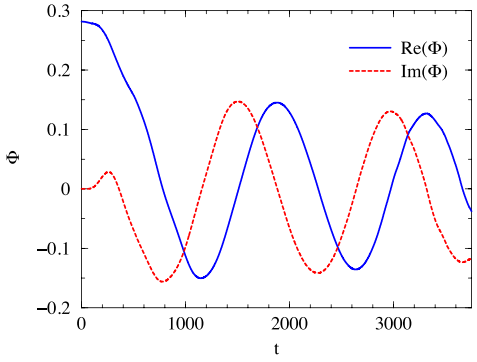

Figure 10. Time evolution of the real (blue solid line) and imaginary (red dashed line) parts of the scalar field amplitude for model 8 and scheme IIb. Data are extracted at $r = 5$.

faster dynamics and hence leads to shorter simulations; however, as this example shows, too large perturbations introduce also undesirable features in the dynamics of the system, as total charge variation.

In figure 10, we show the scalar field amplitude extracted at $r = 5$ for model 8 for scheme IIb. As before we find that the real and imaginary parts of the scalar field oscillate with opposite phases. Moreover, as shown in table 1, the oscillation frequency of the scalar field matches, to a good accuracy, the critical frequency, establishing the formation of a hairy BH at the threshold of superradiance. We observe that, for scheme IIb, the oscillation frequency is an order of magnitude smaller than in scheme I, so we can only capture roughly one period. We note that this already required using a larger computational grid than for the simulations based on scheme I.

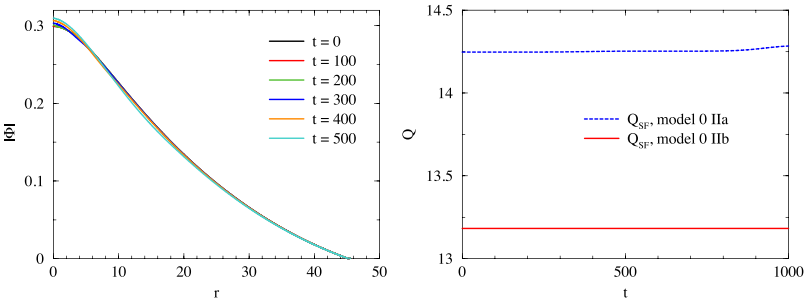

Figure 11. (Left panel): radial profile of the scalar field magnitude for model 0 II without adding a perturbation and for different times. (Right panel): Time evolution of the scalar field charge for models 0 IIa (blue dashed line) and 0 IIb (red solid line). The total charge variation observed for model 0 IIa towards the end of the simulation is related to the use of much too large a perturbations, as discussed in the main text.

Let us focus now in the stable solution, model 0. We have already shown in figure 8 that the evolution of the scalar field energy in this model is stable in scheme II, contrary to what we found when using scheme I. To add further proof of its stable character we plot in figure 11 the radial profile of the scalar field magnitude for different times for model 0 II without initial perturbation (left panel) and the evolution of the scalar field charge (right panel). These results show that this model is indeed stable during our numerical evolutions with scheme II. The solution remains essentially invariant, up to numerical error and the constraint violations induced by the presence of the mirror.

Finally, in figure 12 we show the evolution of the L2 norm of the Hamiltonian constraint for scheme IIa for model 8, for three radial grid spacings. We observe that although there is an initial growth of the Hamiltonian constraint violation, similarly to what happens with scheme I and also around the time the black hole forms, this violation now reaches a lower maximum than that observed in scheme I. Moreover, as in scheme I, the violations are significantly dissipated for $t \gtrsim 400$ and the evolution drives the values of the constraints to acceptable levels. Finally, the analysis with various grid spacings shows that the convergence order of the code is second order to reasonable accuracy, as expected.

4. Discussion

The endpoint of the superradiant instability of the Kerr BH, triggered by a confined bosonic scalar field, remains as an important open question in the theoretical understanding of BHs—see [35] for a review of superradiance. In particular, the discovery of new stationary BH solutions—Kerr BHs with scalar [11, 12] or Proca hair [13]—that exist at the threshold of superradiance, raises the question if these could be endpoints of the instability.

As a simpler model for this problem, with important technical advantages, recent studies of the fully non-linear evolution of the superradiant instability have considered the EMcKG system and focused on the case of a RN BH enclosed in a cavity [1, 2], which is also superradiantly unstable in the presence of a charged scalar field [4–8][8]. The dynamical evolution of

[8] See [36] for the non-linear evolution of a superradiantly unstable RN BH in asymptotically Anti-de-Sitter spacetime.

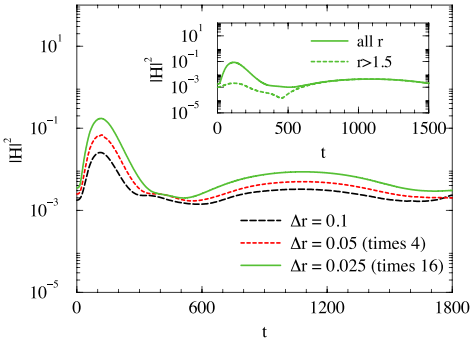

Figure 12. Time evolution of the L2 norm of the Hamiltonian constraint for model 8 using scheme IIa. The inset shows the evolution for the entire radial domain (solid line) and for $r > 1.5$ (dahsed line), thus removing the radial zones that eventually lie within the AH.

this unstable system has been shown to lead to the formation of hairy BHs at the threshold of superradiance. These BHs were found in [9] (see also [10]), and can be faced as the analogues, in this system, of Kerr BHs with scalar hair [11, 12].

The existence of charged scalar solitons in this same system, recently reported in [20, 21], some of which are unstable, raises the question about the endpoint of these unstable solitons. Understanding this question has been the main motivation of this paper. We have tackled the question by considering two different dynamical schemes, that impose the confinement rule for the scalar field in the cavity differently. Our main conclusion is that, albeit there are quantitative differences between these two schemes—most notably, the end state of some of our models is a hairy BH when using scheme I, and a bald RN BH when using scheme II –, the main message is similar. Indeed, we observe the same pattern for both schemes: there seems to be a critical value of a_0 for a given ϕ_0 below which the collapse of unstable solitons leads to a hairy BH rather than to a bald RN BH. Models 6–10 in particular provide a good example. The value of the critical a_0 differs, but we see the two possibles outcomes for both schemes; for scheme I the transition occurs from model 9 to 10, whereas for scheme II it occurs from model 8 to 9. In a nutshell, we believe our numerical results provide evidence that there is a second channel for the dynamical formation of a hairy BH at the threshold of superradiance: from the decay of certain unstable solitons. The first channel is, of course, the aforementioned growth of the superradiant instability.

There are a number of interesting physical questions in this system, which our study raises, for instance:

(1) is there a simple criterion/physical understanding separating the decay into a hairy BH versus a bald BH? We have observed that for a fixed value of ϕ_0 sufficiently small (large) values of a_0 produce a hairy (bald) BH. Can one get a deeper understanding?
(2) There are some stable hairy BHs that cannot form through the first channel, as they do not obey the $\mu < q$ superradiance requirement [5] or even a stronger lower bound [8]—see the discussion in [21]. Can these form from the evolution of an unstable soliton? More generically, what is the impact of the scalar field mass μ on our results?
(3) The hairy BHs that form through the 'old' channel (superradiant growth around a bald BH) are not very hairy, in the sense that the mass of the scalar configuration is not com-

parable to the mass of the BH. Could very hairy BHs, with almost all of the energy in the hair, form from the decay of unstable solitons?

Whereas all these questions are certainly worthwhile to address, our study has also exposed some frailties of this system that raise doubts on how much more one can pursue it, without introducing further complexity. The scalar-field-confining mirror did not impose important challenges when addressing *test* scalar field evolutions [4–8][9], or fully non-linear *stationary* solutions [9, 10, 20, 21]. When making fully non-linear dynamical evolutions, however, the 'virtual' mirror becames a source of constraint violations. In our previous simulations [1, 2], the scalar field was initialized with very small values and never became too large. In the case under study here, however, the scalar field is large from the outset, as it describes a self-gravitating scalar soliton, which makes the mirror a more important source of numerical error and, consequently, makes the evolutions more challenging. Moreover, in the horizonless case, the coordinate singularity (of spherical coordinates) at the origin also sources constraint violations. Fortunately, we have observed that the system evolves towards acceptable values of the constraint violations.

The presence of the coordinate singularity at $r = 0$ and of the mirror at a finite distance, both inevitably trigger the violation of the constraints. We believe there is no (easy) way around to avoid using this particular setup, ill-posed as it might. The major difficulty in our numerical setup is, actually, how to impose the mirror in a less restrictive way than the one we use. One possibility would be to consider the mirror as a shell of matter with a delta-function stress-energy tensor, having time-dependent stresses. The problem, however, is that the Klein–Gordon field would need to be coupled to the shell, and therefore a delta-function source would appear in the Klein–Gordon equation. While this is an appealing approach from a theoretical point of view, numerically it is not possible to handle a delta function in our computational grid. This is the reason why in our simplistic setup we instead impose that the field remains zero at one single point. At the continuum level this choice is equivalent to imposing an infinite barrier. We believe that forcing the field to vanish at one single radial point is the best one can do, numerics-wise.

To assess the impact of these numerical limitations on our results, we recall that in [20] it was shown that the solitons in a cavity are either stable or unstable against linear perturbations. If our simulations had no numerical error and the constraint equations were exactly satisfied, even unstable solitons would not collapse unless an extra perturbation were added. This is obviously not the case when solving the problem numerically. In our setup the numerical error from outside the cavity introduces the perturbation that causes the collapse of the solitons in the case of Scheme I. For Schemes IIa and b, we impose another type of perturbation only inside the cavity. As a result, for this perturbation we observe that the stable solitons do not form a BH. Therefore, even if the constraint violations were reduced, which is unrealistic in our setup, we believe we would obtain the same results because the perturbation is always of the same form.

As a final argument in favour of our results, we also note that the formation of a hairy BH means that the condition $\omega_c = \omega_\Phi$ is fulfilled, and that such particular equilibrium between the BH and the charged scalar field is reached. If the constraint violation was large enough to change the outcome, one would expect that a system satisfying the final 'fine-tuned' outcome between the frequencies would hardly be obtained from such an evolution. Therefore, if that were the case we would never get a hairy BH for any model. The hairy BH outcome can be

[9] For test fields, in fact, the confining mirror has been widely used in other studies of fields interacting with charged BHs, see e.g. [37–44].

seen as an 'attractor', even if there is some numerical error in the evolution (unavoidable in our approach, as mentioned before).

We close by returning to the parallelism with the asymptotically flat case. The 'cousin' solutions to the solitons studied herein are the well known *boson stars* [22], self-gravitating systems formed by massive scalar fields (eventually, but not necessarily, self-interacting). There are stable and unstable boson stars. Stable ones undergo oscillations when perturbed and show similar properties to other compact objects, such as neutron stars. Unstable boson stars, however, may collapse into BHs, radiate the energy excess or completely disperse away. These behaviours have been explicitly shown by numerical evolutions for spherically symmetric boson stars [45–49]. In that case, however, there are no hairy BHs [50], which require rotation and thus exist only in axisymmetry [27]. Thus, in a similar spirit to the results in this work, could unstable rotating boson (or Proca) stars form Kerr BHs with scalar (or Proca) hair? This is an interesting open question.

Acknowledgments

This work has been supported by the Spanish MINECO (AYA2013-40979-P, AYA2015-66899-C2-1-P), by the Generalitat Valenciana (PROMETEOII-2014-069, ACIF/2015/216), by the CONACyT-SNI-México, by the FCT (Portugal) IF programme, by the CIDMA (FCT) strategic project UID/MAT/04106/2013 and by the EU grants NRHEP–295189-FP7-PEOPLE-2011-IRSES and H2020-MSCA-RISE-2015 Grant No. StronGrHEP-690904. Computations have been performed at the Servei d'Informàtica de la Universitat de València and at the Blafis cluster at the University of Aveiro.

References

[1] Sanchis-Gual N, Degollado J C, Montero P J, Font J A and Herdeiro C 2016 Explosion and final state of an unstable Reissner–Nordstrm black hole *Phys. Rev. Lett.* **116** 141101
[2] Sanchis-Gual N, Degollado J C, Herdeiro C, Font J A and Montero P J 2016 Dynamical formation of a Reissner–Nordstrm black hole with scalar hair in a cavity *Phys. Rev.* D **94** 044061
[3] Hod S 2012 Stability of the extremal Reissner–Nordstroem black hole to charged scalar perturbations *Phys. Lett.* B **713** 505–8
[4] Hod S 2013 Analytic treatment of the charged black-hole-mirror bomb in the highly explosive regime *Phys. Rev.* D **88** 064055
[5] Herdeiro C A R, Degollado J C and Rnarsson H F 2013 Rapid growth of superradiant instabilities for charged black holes in a cavity *Phys. Rev.* D **88** 063003
[6] Degollado J C and Herdeiro C A R 2014 Time evolution of superradiant instabilities for charged black holes in a cavity *Phys. Rev.* D **89** 063005
[7] Hod S 2015 Universality in the relaxation dynamics of the composed black-hole-charged-massive-scalar-field system: the role of quantum Schwinger discharge *Phys. Lett.* B **747** 339–44
[8] Hod S 2016 The charged black-hole bomb: a lower bound on the charge-to-mass ratio of the explosive scalar field *Phys. Lett.* B **755** 177–82
[9] Dolan S R, Ponglertsakul S and Winstanley E 2015 Stability of black holes in Einstein-charged scalar field theory in a cavity *Phys. Rev.* D **92** 124047
[10] Basu P, Krishnan C and Subramanian P N B 2016 Hairy black holes in a box *J. High Energy Phys.* **2016** 41
[11] Herdeiro C A R and Radu E 2014 Kerr black holes with scalar hair *Phys. Rev. Lett.* **112** 221101
[12] Herdeiro C and Radu E 2015 Construction and physical properties of Kerr black holes with scalar hair *Class. Quantum Grav.* **32** 144001
[13] Herdeiro C, Radu E and Runarsson H 2016 Kerr black holes with Proca hair *Class. Quantum Grav.* **33** 154001

[14] Kleihaus B, Kunz J and Yazadjiev S 2015 Scalarized hairy black holes *Phys. Lett.* B **744** 406–12
[15] Herdeiro C A R, Radu E and Rnarsson H 2015 Kerr black holes with self-interacting scalar hair: hairier but not heavier *Phys. Rev.* D **92** 084059
[16] Delgado J F M, Herdeiro C A R, Radu E and Runarsson H 2016 Kerr–Newman black holes with scalar hair *Phys. Lett.* B **761** 234–41
[17] Dias O J C, Horowitz G T and Santos J E 2011 Black holes with only one Killing field *J. High Energy Phys.* JHEP07(2011)115
[18] Brihaye Y, Herdeiro C and Radu E 2014 MyersPerry black holes with scalar hair and a mass gap *Phys. Lett.* B **739** 1–7
[19] Herdeiro C, Kunz J, Radu E and Subagyo B 2015 MyersPerry black holes with scalar hair and a mass gap: Unequal spins *Phys. Lett.* B **748** 30–6
[20] Ponglertsakul S, Winstanley E and Dolan S R 2016 Stability of gravitating charged-scalar solitons in a cavity *Phys. Rev.* D **94** 024031
[21] Ponglertsakul S and Winstanley E 2016 Effect of scalar field mass on gravitating charged scalar solitons and black holes in a cavity *Phys. Lett.* B **764** 87–93
[22] Schunck F E and Mielke E W 2003 General relativistic Boson stars *Class. Quantum Grav.* **20** R301–56
[23] Brito R, Cardoso V, Herdeiro C A R and Radu E 2016 Proca stars: gravitating Bose–Einstein condensates of massive spin 1 particles *Phys. Lett.* B **752** 291–5
[24] Garca F and Landea I S 2016 Charged Proca stars *Phys. Rev.* D **94** 104006
[25] Duarte M and Brito R 2016 Asymptotically anti-de Sitter Proca Stars *Phys. Rev.* D **94** 064055
[26] Kastor D and Traschen J H 1992 Horizons inside classical lumps *Phys. Rev.* D **46** 5399–403
[27] Herdeiro C A R and Radu E 2014 A new spin on black hole hair *Int. J. Mod. Phys.* D **23** 1442014
[28] Montero P J and Cordero-Carrion I 2012 BSSN equations in spherical coordinates without regularization: vacuum and non-vacuum spherically symmetric spacetimes *Phys. Rev.* D **85** 124037
[29] Sanchis-Gual N, Degollado J C, Montero P J and Font J A 2015 Quasistationary solutions of self-gravitating scalar fields around black holes *Phys. Rev.* D **91** 043005
[30] Sanchis-Gual N, Degollado J C, Montero P J, Font J A and Mewes V 2015 Quasistationary solutions of self-gravitating scalar fields around collapsing stars *Phys. Rev.* D **92** 083001
[31] Cordero-Carrión I and Cerdá-Durán P 2012 Partially implicit Runge–Kutta methods for wave-like equations in spherical-type coordinates (arXiv:1211.5930 [math-ph])
[32] Cordero-Carrión I and Cerdá-Durán P 2014 *Advances in Differential Equations and Applications* (*SEMA SIMAI Springer Series* vol 4) (Switzerland: Springer) (https://doi.org/10.1007/978-3-319-06953-1_2)
[33] Alcubierre M 2008 *Introduction to* $3+1$ *Numerical Relativity* (New York: Oxford Univeristy Press)
[34] Torres J M and Alcubierre M 2014 Gravitational collapse of charged scalar fields *Gen. Relativ. Gravit.* **46** 1773
[35] Brito R, Cardoso V and Pani P 2015 Superradiance *Lect. Notes Phys.* **906** 1–237
[36] Bosch P, Green S R and Lehner L 2016 Nonlinear evolution and final fate of charged anti-de Sitter black hole superradiant instability *Phys. Rev. Lett.* **116** 141102
[37] Li R and Zhao J 2014 Superradiant instability of charged scalar field in stringy black hole mirror system *Eur. Phys. J.* C **74** 3051
[38] Li R, Zhao J-K and Zhang Y-M 2015 Superradiant instability of D-dimensional ReissnerNordstrm black hole mirror system *Commun. Theor. Phys.* **63** 569–74
[39] Li R and Zhao J 2015 Numerical study of superradiant instability for charged stringy black holemirror system *Phys. Lett.* B **740** 317–21
[40] Li R, Zhao J, Wu X and Zhang Y 2015 Scalar clouds in charged stringy black hole-mirror system *Eur. Phys. J.* C **75** 142
[41] Sakalli I and Tokgoz G 2015 Resonance spectra of caged stringy black hole and its spectroscopy *Adv. High Energy Phys.* **2015** 739153
[42] Li R, Tian Y, Zhang H-B and Zhao J 2015 Time domain analysis of superradiant instability for the charged stringy black holemirror system *Phys. Lett.* B **750** 520–7
[43] Huang Y, Liu D-J and Li X-Z 2017 Superradiant (in)stability of *D*-dimensional Reissner–Nordström-anti-de Sitter black hole mirror system *Int. J. Mod. Phys.* D (https://doi.org/10.1142/S0218271817501413)

[44] Hod S 2016 The spinning Kerr-black-hole-mirror bomb: a lower bound on the radius of the reflecting mirror *Phys. Lett.* B **761** 326–32
[45] Seidel E and Suen W-M 1990 Dynamical evolution of Boson stars. 1. Perturbing the ground state *Phys. Rev.* D **42** 384–403
[46] Alcubierre M, Guzman F S, Matos T, Nunez D, Urena-Lopez L A and Wiederhold P 2002 Galactic collapse of scalar field dark matter *Class. Quantum Grav.* **19** 5017
[47] Guzman F S 2004 Evolving spherical boson stars on a 3D Cartesian grid *Phys. Rev.* D **70** 044033
[48] Bernal A and Guzman F S 2006 Scalar field dark matter: non-spherical collapse and late time behavior *Phys. Rev.* D **74** 063504
[49] Bernal A, Barranco J, Alic D and Palenzuela C 2010 Multi-state Boson stars *Phys. Rev.* D **81** 044031
[50] Pena I and Sudarsky D 1997 Do collapsed boson stars result in new types of black holes? *Class. Quantum Grav.* **14** 3131–4

PHYSICAL REVIEW D **95,** 104028 (2017)

Numerical evolutions of spherical Proca stars

Nicolas Sanchis-Gual,[1] Carlos Herdeiro,[2] Eugen Radu,[2] Juan Carlos Degollado,[3] and José A. Font[1,4]

[1]*Departamento de Astronomía y Astrofísica, Universitat de València, Dr. Moliner 50, 46100 Burjassot (València), Spain*

[2]*Departamento de Física da Universidade de Aveiro and Centre for Research and Development in Mathematics and Applications (CIDMA), Campus de Santiago, 3810-183 Aveiro, Portugal*

[3]*Instituto de Ciencias Físicas, Universidad Nacional Autónoma de México, Apdo. Postal 48-3, 62251 Cuernavaca, Morelos, México*

[4]*Observatori Astronòmic, Universitat de València, C/ Catedrático José Beltrán 2, 46980 Paterna (València), Spain*

(Received 16 February 2017; published 22 May 2017)

Vector boson stars, or *Proca stars*, have been recently obtained as fully nonlinear numerical solutions of the Einstein-(complex)-Proca system [1]. These are self-gravitating, everywhere nonsingular, horizonless Bose-Einstein condensates of a massive vector field, which resemble in many ways, but not all, their scalar cousins, the well-known (scalar) boson stars. In this paper we report fully nonlinear numerical evolutions of Proca stars, focusing on the spherically symmetric case, with the goal of assessing their stability and the end point of the evolution of the unstable stars. Previous results from linear perturbation theory indicate that the separation between stable and unstable configurations occurs at the solution with maximal ADM mass. Our simulations confirm this result. Evolving numerically unstable solutions, we find, depending on the sign of the binding energy of the solution and on the perturbation, three different outcomes: (i) migration to the stable branch, (ii) total dispersion of the scalar field, or (iii) collapse to a Schwarzschild black hole. In the latter case, a long-lived Proca field remnant—a *Proca wig*—composed by quasibound states, may be seen outside the horizon after its formation, with a lifetime that scales inversely with the Proca mass. We comment on the similarities/differences with the scalar case as well as with neutron stars.

DOI: 10.1103/PhysRevD.95.104028

I. INTRODUCTION

In Minkowski spacetime, the linear, massive, Klein-Gordon equation has a general solution given in terms of Fourier modes, corresponding to different frequencies. The amplitudes of these modes can be chosen as to yield, at some given time, a *lumplike* solution, wherein all (or almost all) energy is localized in a compact spatial region. The different phase velocity of the different modes, however, implies this lump will be dispersed by the time evolution.

Solitonlike solutions of the Klein-Gordon field, corresponding to energy lumps that are preserved by the time evolution, require nonlinearities that compensate the field's natural tendency to disperse. These nonlinearities may be due to the field self-interactions [2], or due to gravity. Examples within the latter context were first discovered in [3,4], as static, spherically symmetric solutions of the Einstein–(massive, complex)Klein-Gordon system, and became known as (scalar) boson stars (SBSs)—see [5] for a review.

Unlike the (short-lived) flat space lumps described in the first paragraph, SBSs correspond to a *single* frequency mode with a very large occupation number. They are sometimes described as relativistic, self-gravitating, Bose-Einstein condensates. This single frequency appears as a harmonic time dependence for the scalar field. Thus, compatibility with a static geometry requires the field to be complex, containing two scalar degrees of freedom, both oscillating but with a phase difference of $\pi/2$. Physically, these oscillations prevent the collapse of the scalar field into a black hole and simultaneously evade no-soliton Derrick [6]/virial-type theorems. The opposite phases, on the other hand, shut down scalar field dissipation towards infinity, which is observed for real fields, for which only quasistationary configurations exist, albeit extremely long lived [7], dubbed oscillatons [8]. For rotating SBSs [9,10] moreover, the two opposite phases also shut down gravitational wave emission. We remark that SBSs require a mass term but no self-interactions, even though the latter may also be included [11–15].

The existence of boson stars as stationary solutions of the Einstein equations raises questions about their dynamics (see [16] for a review). In particular, one may ask if SBSs are stable, and, even more fundamentally, if they may form dynamically. For spherically symmetric SBSs, the first question was answered at the level of mode stability in [17,18]. Roughly, fundamental solutions (i.e. without nodes in the scalar field radial profile) that become too compact are unstable against radial perturbations. More precisely, the turnover point, stability-wise, corresponds to the solution with the maximum ADM mass for a given scalar field mass. These perturbative results were confirmed by fully nonlinear numerical simulations in [19], where,

moreover, the fate of the unstable solutions was reported to be either the formation of a black hole, or the migration to the stable branch, regardless of the sign of the binding energy. A different possible fate of unstable SBSs with *excess* (i.e. negative binding) energy is that they disperse entirely, which was reported in [20] for excited states and [21] for fundamental states (see also [22]).

Concerning the second question above, the dynamical formation of SBSs was first examined using nonlinear numerical simulations, in [23], where it was found that stable SBSs can form starting with generic initial data describing an unbound scalar field, after releasing the excess energy via the mechanism of gravitational cooling. For a discussion of SBS formation in cosmological scenarios see [24].

It has long been thought that there could be vector analogues to SBSs, but the former have only recently been constructed and are known as Proca stars (PSs) [1]—see also [25–27] for generalizations. These configurations have been found in the Einstein-(complex)-Proca system and, in analogy to their scalar cousins, they correspond to a single frequency mode building up a (vector), macroscopic, self-gravitating Bose-Einstein condensate. This frequency appears as a harmonic time dependence for the Proca potential and the domain of existence of PSs is very similar to that of SBSs, when presented in an ADM mass vs Proca frequency diagram—Fig. 1—except that the latter have a lower mass and a wider frequency range.

The stability properties of the spherical PS solutions also parallel those of the spherical SBSs. Analyzing radial perturbations, it was shown in [1] that there is a stable branch of PS solutions, corresponding in Fig. 1 to the line connecting $w/\mu = 1$ to the maximal ADM mass, and an unstable branch, corresponding to the remaining part of the spiraling curve. The purpose of this paper is to (1) confirm this picture by performing fully nonlinear time evolutions, rather than a linear frequency domain analysis, and (2) determine the fate of unstable solutions, by evolving a sample of representative cases.

The evolutions described herein confirm the picture obtained from perturbation theory, regarding the existence of a stable branch (connecting the vacuum with the solution with maximal ADM mass) and an unstable branch. For the latter, all configurations we have evolved with no added perturbation (only the discretization error of our numerical code) collapse into a black hole. Introducing a perturbation, however, can change the fate of an unstable solution in a way that depends on the sign of its binding energy. We illustrate this by a particular type of perturbation which makes unstable solutions with positive binding energy migrate to the stable branch, whereas unstable solutions with a negative binding energy (excess energy) undergo fission; i.e. they disperse entirely.

For the cases in which a black hole results from the evolution, after apparent horizon formation, we observe the possibility of a long-lived remnant Proca field lingering outside the horizon. A Fourier analysis, together with a fit of the Proca remnant, suggests this slowly decaying remnant is composed of quasibound states of the Proca field outside a Schwarzschild black hole. This type of *wig* around a black hole has been observed for the scalar field case in [28], and its lifetime scales with the inverse of the scalar/Proca field mass.

This paper is organized as follows. In Sec. II we present the covariant Einstein-(complex)-Proca model and the equations that are used for the numerical evolutions. In Sec. III we describe the initial data and in particular a set of five representative PS solutions that is used in our

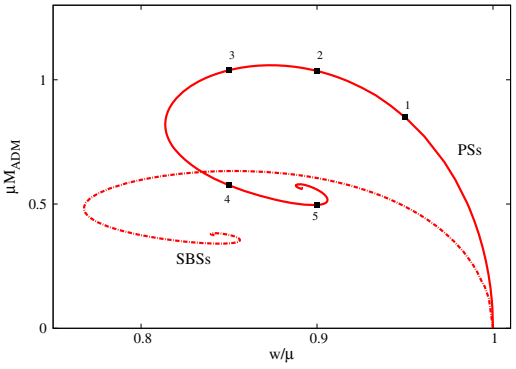

FIG. 1. Domain of existence of the spherical (fundamental) PSs (solid line) and spherical (fundamental) SBSs (dashed line) solutions in an ADM mass vs vector/scalar field frequency diagram. Both fields have been assumed to have mass μ. The five highlighted points correspond to the configurations to be evolved below.

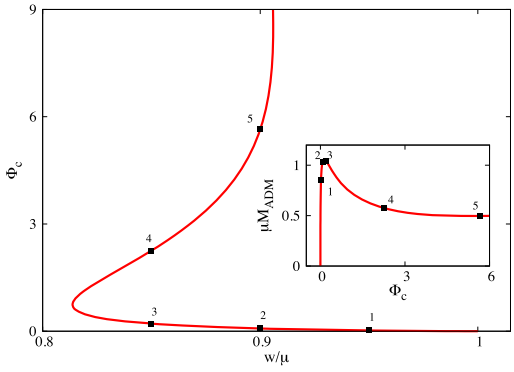

FIG. 2. Magnitude of the Proca electric potential at the origin, $\Phi_c(r=0)$, vs the frequency. The five highlighted points correspond to the same as in Fig. 1. The inset shows the ADM mass as a function of $\Phi_c(r=0)$.

numerical evolutions. A brief description of the numerical techniques is given in Sec. IV and our results are presented in Sec. V. Final remarks are presented in Sec. VI. A brief overview of technical details concerning the static Proca star solutions is given in Appendix A and a succinct assessment of our numerical code is given in Appendix B.

II. BASIC EQUATIONS

We investigate the dynamics of a complex Proca field by solving numerically the Proca equations coupled to the Einstein equations. The system is described by the action $\mathcal{S} = \int d^4x\sqrt{-g}\mathcal{L}$, where the Lagrangian density depends on the Proca potential $\mathcal{A}$, and field strength $\mathcal{F} = d\mathcal{A}$; it is given by

$$\mathcal{L} = \frac{R}{16\pi G_0} - \frac{1}{4}\mathcal{F}_{\alpha\beta}\bar{\mathcal{F}}^{\alpha\beta} - \frac{1}{2}\mu^2\mathcal{A}_\alpha\bar{\mathcal{A}}^\alpha, \tag{1}$$

where the bar denotes complex conjugation. In the following we briefly describe the main equations used for the numerical implementation, in order to perform time evolutions.

A. The BSSN equations

The evolution of the Einstein-Proca system is performed using the numerical code in spherical polar coordinates described in [29], which has been adapted to account for the Proca field (here we set $c = G_0 = 1$). We adopt Brown's covariant form [30,31] of the Baumgarte-Shapiro-Shibata-Nakamura (BSSN) formulation [32–34]. The conformally related spatial metric $\bar{\gamma}_{ij}$ is written as

$$\bar{\gamma}_{ij} = e^{-4\phi}\gamma_{ij}, \tag{2}$$

where γ_{ij} is the physical spatial metric, and e^ϕ a conformal factor. We note that

$$e^{4\phi} = (\bar{\gamma}/\gamma)^{1/3}, \tag{3}$$

with $\gamma = \det\gamma_{ij}$ and $\bar{\gamma} = \det\bar{\gamma}_{ij}$.

We introduce a background connection $\hat{\Gamma}^i_{jk}$ and define

$$\Delta\Gamma^i_{jk} = \bar{\Gamma}^i_{jk} - \hat{\Gamma}^i_{jk} \tag{4}$$

which, unlike the two connections themselves, transform as a tensor field. We also define the trace of these variables as

$$\Delta\Gamma^i \equiv \bar{\gamma}^{jk}\Delta\Gamma^i_{jk}. \tag{5}$$

It is not necessary for the background connection to be associated with any metric, but in practice we take it to be the Levi-Civita connection of flat spacetime in spherical coordinates.

We define the connection vector $\bar{\Lambda}^i$ as a new set of independent variables that are equal to the $\Delta\Gamma^i$ when the constraint

$$\mathcal{C}^i \equiv \bar{\Lambda}^i - \Delta\Gamma^i = 0 \tag{6}$$

holds. Defining $\partial_{\perp_n} \equiv \partial_t - \mathcal{L}_\beta$, where $\mathcal{L}_\beta$ denotes the Lie derivative along the shift vector β^i, we then obtain the following set of evolution equations:

$$\partial_{\perp_n}\bar{\gamma}_{ij} = -\frac{2}{3}\bar{\gamma}_{ij}\bar{D}_k\beta^k - 2\alpha\bar{A}_{ij}, \tag{7a}$$

$$\begin{aligned}\partial_{\perp_n}\bar{A}_{ij} = &-\frac{2}{3}\bar{A}_{ij}\bar{D}_k\beta^k - 2\alpha\bar{A}_{ik}\bar{A}^k{}_j + \alpha\bar{A}_{ij}K \\ &+ e^{-4\phi}[-2\alpha\bar{D}_i\bar{D}_j\phi + 4\alpha\bar{D}_i\phi\bar{D}_j\phi \\ &+ 4\bar{D}_{(i}\alpha\bar{D}_{j)}\phi - \bar{D}_i\bar{D}_j\alpha \\ &+ \alpha(\bar{R}_{ij} - 8\pi S_{ij})]^{\mathrm{TF}},\end{aligned} \tag{7b}$$

$$\partial_{\perp_n}\phi = \frac{1}{6}\bar{D}_k\beta^i - \frac{1}{6}\alpha K, \tag{7c}$$

$$\begin{aligned}\partial_{\perp_n}K = &\frac{\alpha}{3}K^2 + \alpha\bar{A}_{ij}\bar{A}^{ij} - e^{-4\phi}(\bar{D}^2\alpha + 2\bar{D}^i\alpha\bar{D}_i\phi) \\ &+ 4\pi\alpha(\rho + S),\end{aligned} \tag{7d}$$

$$\begin{aligned}\partial_{\perp_n}\bar{\Lambda}^i = &\bar{\gamma}^{jk}\hat{D}_j\hat{D}_k\beta^i + \frac{2}{3}\Delta\Gamma^i\bar{D}_j\beta^j + \frac{1}{3}\bar{D}^i\bar{D}_j\beta^j \\ &- 2\bar{A}^{jk}(\delta^i{}_j\partial_k\alpha - 6\alpha\delta^i{}_j\partial_k\phi - \alpha\Delta\Gamma^i_{jk}) \\ &- \frac{4}{3}\alpha\bar{\gamma}^{ij}\partial_j K - 16\pi\alpha\bar{\gamma}^{ij}S_j,\end{aligned} \tag{7e}$$

where α is the lapse function, $\hat{D}_i$ denotes a covariant derivative that is built from the background connection $\hat{\Gamma}^i_{jk}$ and the superscript TF denotes the trace-free part. The matter sources ρ, S_i, S_{ij} and S denote the density, momentum density, stress, and the trace of the stress as observed by a normal observer, respectively, and are defined by

$$\rho \equiv n_a n_b T^{ab}, \tag{8a}$$

$$S_i \equiv -\gamma_{ia}n_b T^{ab}, \tag{8b}$$

$$S_{ij} \equiv \gamma_{ia}\gamma_{jb}T^{ab}, \tag{8c}$$

$$S \equiv \gamma^{ij}S_{ij}. \tag{8d}$$

Here

$$n_a = (-\alpha, 0, 0, 0) \tag{9}$$

is the normal one-form on a spatial slice, and T^{ab} is the stress-energy tensor.

We compute the Ricci tensor $\bar{R}_{ij}$ associated with $\bar{\gamma}_{ij}$ from

$$\begin{aligned}\bar{R}_{ij} = &-\frac{1}{2}\bar{\gamma}^{kl}\hat{D}_k\hat{D}_l\bar{\gamma}_{ij} + \bar{\gamma}_{k(i}\hat{D}_{j)}\bar{\Lambda}^k + \Delta\Gamma^k\Delta\Gamma_{(ij)k} \\ &+ \bar{\gamma}^{kl}(2\Delta\Gamma^m_{k(i}\Delta\Gamma_{j)ml} + \Delta\Gamma^m_{ik}\Delta\Gamma_{mjl}).\end{aligned} \tag{10}$$

The Hamiltonian constraint takes the form

$$\mathcal{H} \equiv \frac{2}{3}K^2 - \bar{A}_{ij}\bar{A}^{ij} + e^{-4\phi}(\bar{R} - 8\bar{D}^i\phi\bar{D}_i\phi - 8\bar{D}^2\phi) - 16\pi\rho = 0, \tag{11}$$

and the momentum constraints can be written as

$$\mathcal{M}^i \equiv e^{-4\phi}\left(\frac{1}{\sqrt{\bar{\gamma}}}\hat{\mathcal{D}}_j(\sqrt{\bar{\gamma}}\bar{A}^{ij}) + 6\bar{A}^{ij}\partial_j\phi - \frac{2}{3}\bar{\gamma}^{ij}\partial_j K + \bar{A}^{jk}\Delta\Gamma^i_{jk}\right) - 8\pi S^i = 0. \tag{12}$$

B. The Proca equations

The Proca field is split into its scalar Φ, 3-vector a_i potential and a three-dimensional "electric" $\mathbf{E}$ and "magnetic" $\mathbf{B}$ fields. The evolution equations for the complex Proca field take the form [35]

$$\partial_t a_i = -\alpha(E_i + D_i\Phi) - \Phi D_i\alpha + \mathcal{L}_\beta a_i, \tag{13}$$

$$\partial_t E^i = \alpha(KE^i + \mu^2 a^i + \epsilon^{ijk}D_j B_k) - \epsilon^{ijk}B_j D_k\alpha + \mathcal{L}_\beta E^i, \tag{14}$$

$$\partial_t B^i = \alpha(KB^i - \epsilon^{ijk}D_j E_k) + \epsilon^{ijk}E_j D_k\alpha + \mathcal{L}_\beta B^i, \tag{15}$$

$$\partial_t\Phi = -a^i D_i\alpha + \alpha(K\Phi - D_i a^i) + \mathcal{L}_\beta\Phi. \tag{16}$$

The stress-energy tensor of the Proca field reads [1]

$$T_{ab} = -\mathcal{F}_{c(a}\bar{\mathcal{F}}^c_{b)} - \frac{1}{4}g_{ab}\mathcal{F}_{cd}\bar{\mathcal{F}}^{cd} + \mu^2\left[\mathcal{A}_{(a}\bar{\mathcal{A}}_{b)} - \frac{1}{2}g_{ab}\mathcal{A}_c\bar{\mathcal{A}}^c\right], \tag{17}$$

from which we can compute the source terms of the Einstein equations. These are given by

$$8\pi\rho = \gamma_{ij}(E^iE^j + B^iB^j) + \mu^2(\Phi^2 + \gamma^{kl}a_i a_j), \tag{18}$$

$$4\pi(\rho + S) = \gamma_{ij}(E^iE^j + B^iB^j) + 2\mu^2\Phi^2, \tag{19}$$

$$4\pi\left(S_{ij} - \frac{S}{3}\gamma_{ij}\right) = -\gamma_{ik}\gamma_{jl}(E^kE^l + B^kB^l) + \frac{\gamma_{ij}}{3}(E^2 + B^2) + \mu^2 a_i a_j - \mu^2\frac{\gamma_{ij}}{3}\gamma^{kl}a_k a_l, \tag{20}$$

$$4\pi j^i = \gamma^{li}\epsilon_{ljk}E^j B^k + \mu^2\Phi\gamma^{ik}a_k. \tag{21}$$

We can define the "Gauss" constraint as

$$G = D_i E^i + \mu^2\Phi = 0. \tag{22}$$

Since for the evolutions reported in this paper we are assuming spherical symmetry, we only need to consider the radial component of the vectors and the magnetic field $\mathbf{B} = 0$.

III. PROCA STAR SOLUTION AND INITIAL DATA

Proca stars were obtained in [1] as stationary solutions to the model described by the action (1). Here we focus on spherically symmetric Proca stars that we now briefly review, and that are taken as the initial data for the time evolutions performed in the next section.

A. The stationary solutions

We consider a spherically symmetric line element

$$ds^2 = -e^{2F_0}dt^2 + e^{2F_1}[dr^2 + r^2(d\theta^2 + \sin^2\theta d\varphi^2)], \tag{23}$$

where F_0, F_1 are radial functions and r, θ, φ correspond to isotropic coordinates. The Proca field ansatz is given in terms of another two real functions (V, H_1) which depend also on r,

$$\mathcal{A} = e^{-iwt}\left(iVdt + \frac{H_1}{r}dr\right), \tag{24}$$

where $w > 0$ is the frequency of the field. The Einstein-Proca equations are solved with appropriate boundary conditions, which are compatible with an approximate construction of the solutions on the boundary of the domain of integration. This ansatz corresponds to the conventions in [1] for the axisymmetric case, specialized to spherical symmetry. Illustrative examples of the four radial functions above, for two spherical Proca star solutions, can be found in Fig. 2 of Ref. [1] (but in a different radial coordinate). Some details on the construction of static Proca star solutions are given in Appendix A.

The magnitude of the Proca electric potential at the origin vs Proca field frequency diagram of the solutions is shown in Fig. 2, where we highlight the sample of numerical solutions that is used in the evolutions reported in Sec. V. The corresponding frequency, ADM mass, Noether charge Q [cf. Eq. (25)], magnitude of the Proca electric potential at the origin [cf. Eq. (26)] and also the apparent horizon (AH) mass resulting from the unperturbed evolution (see the next section), are summarized in Table I. The difference between the ADM mass and the AH mass is due to the numerical error (less than 1%) that comes mostly from the logarithmic radial grid. Computing the Komar mass with our evolution code gives the same AH mass.

TABLE I. Spherically symmetric Proca star models.

Model	ω/μ	$\mu M_{\rm ADM}$	$\mu^2 Q$	$\Phi_c(r=0)$	$\mu M_{\rm AH}$
PS1	0.95	0.849	0.864	0.0214	-
PS2	0.90	1.036	1.063	0.0779	-
PS3	0.85	1.039	1.065	0.2121	1.045
PS4	0.85	0.576	0.504	2.2547	0.578
PS5	0.90	0.496	0.412	5.6473	0.489

Taking more radial grid points, both converge to the correct Proca mass.

Proca stars carry a conserved Noether charge, Q, which is a measure of the number of Proca particles in the Bose-Einstein condensate. It is given by integrating the temporal component of the conserved current associated to the global $U(1)$ symmetry on a spacelike surface,

$$Q = \frac{i}{2}\int_\Sigma d^3x\sqrt{-g}(\bar{\mathcal{F}}^{t\beta}\mathcal{A}_\beta - \mathcal{F}^{t\beta}\bar{\mathcal{A}}_\beta). \tag{25}$$

Multiplying this number by the mass of one individual Proca particle, μ, one obtains a measure of the total energy excluding binding energy. A comparison with the ADM mass of each solution then discriminates solutions with a positive binding energy, $M_{\rm ADM} < \mu Q$, from the ones with a negative binding energy, or excess energy, $M_{\rm ADM} > \mu Q$. The latter, naturally, only occur in the unstable branch. The separation point (zero binding energy) turns out to occur very close to (but not exactly at) the solution with the minimum frequency (see Fig. 1 in [1]). This means that the classification of our five illustrative solutions is, from perturbation theory plus binding energy considerations, as follows:

(i) Models 1 and 2: stable (which implies positive binding energy);
(ii) Model 3: unstable with positive binding energy;
(iii) Model 4 and 5: unstable with negative binding energy/excess energy.

The translation between the four radial functions above, F_0, F_1, V, H_1, and the initial value for the Proca field variables described in Eqs (13)–(16) is given as follows:

$$\Phi = -n^\mu \mathcal{A}_\mu, \tag{26}$$

$$a_i = \gamma_i^\mu \mathcal{A}_\mu, \tag{27}$$

$$E^i = -i\frac{\gamma^{ij}}{\alpha}(D_i(\alpha\Phi) + \partial_t a_j). \tag{28}$$

Then, from (24), we obtain

$$\Phi = -i\frac{V}{\alpha}, \tag{29}$$

$$a_r = \frac{H_1}{r}, \tag{30}$$

$$E^r = i\frac{\gamma^{rr}}{\alpha}\left(D_r V + \omega\frac{H_1}{r}\right). \tag{31}$$

In the evolutions to be discussed below, one of the observables of interest is the energy in the Proca field as well as the energy in the black hole, in case one forms. A natural way to assign well-defined such energies in a stationary, asymptotically flat spacetime is by using Komar integrals. The Komar mass at infinity coincides with the ADM mass, $M_{\rm ADM}$. By using Gauss's law, this mass can be computed as a spatial volume integral of the "Komar energy density" along a spacelike slice from a horizon, in case one exists, up to spatial infinity, plus the horizon contribution, $M_{\rm AH}$, which is, again, computed as a Komar integral, $M_{\rm ADM} = M_{\rm AH} + E_{\rm PF}$, where [25]

$$E_{\rm PF} = -\int_\Sigma dr d\theta d\varphi (2T^t_t - T^\alpha_\alpha)\alpha\sqrt{\gamma}. \tag{32}$$

In our evolutions we use $E_{\rm PF}$ with the volume integral computed from the AH (origin) to spatial infinity, in case an AH is present (absent). For the horizon mass we use the irreducible mass computed from the horizon area, since the black hole that forms has no electric charge or rotation.

IV. NUMERICS

As mentioned before, the numerical relativity code we use to perform the evolution of the Einstein-Proca system is based on the code originally presented in [29]. The most salient feature of this code, as compared to other numerical relativity codes, is the fact that the equations are implemented and solved using spherical polar coordinates. The time update of the different systems of evolution equations (Einstein and Proca) is therefore done using the same type of techniques we have extensively used in our previous work. The interested reader is addressed in particular to Refs. [36–38] for complete details.

As a summary, we indicate here that the evolution equations are integrated using the second-order partially implicit Runge-Kutta (PIRK) method developed by [39,40]. This method allows us to handle the singular terms that appear in the evolution equations due to our choice of curvilinear coordinates. For the simulations presented in this paper, the original code had to be upgraded to account for the Proca field. Therefore, the evolution scheme for this field is the only feature which is new with respect to previous versions of the code. Therefore, it is worth discussing in some more detail our specific implementation.

Following [39,40] we cast the Einstein-Proca system of partial differential equations as

$$\begin{cases} u_t = \mathcal{L}_1(u,v), \\ v_t = \mathcal{L}_2(u) + \mathcal{L}_3(u,v), \end{cases} \tag{33}$$

where $\mathcal{L}_1$, $\mathcal{L}_2$ and $\mathcal{L}_3$ represent general nonlinear differential operators. In the second-order PIRK method the time update from time t^n to t^{n+1} is done according to the following two-step algorithm:

$$\begin{cases} u^{(1)} = u^n + \Delta t L_1(u^n, v^n), \\ v^{(1)} = v^n + \Delta t[\frac{1}{2}L_2(u^n) + \frac{1}{2}L_2(u^{(1)}) + L_3(u^n, v^n)], \end{cases} \tag{34}$$

$$\begin{cases} u^{n+1} = \frac{1}{2}[u^n + u^{(1)} + \Delta t L_1(u^{(1)}, v^{(1)})], \\ v^{n+1} = v^n + \frac{\Delta t}{2}[L_2(u^n) + L_2(u^{n+1}) + L_3(u^n, v^n) + L_3(u^{(1)}, v^{(1)})], \end{cases} \tag{35}$$

where L_1, L_2 and L_3 are the corresponding discrete operators. The explicit form of these operators for the (BSSN) Einstein evolution equations is shown in [29]. Regarding the Proca field, each time step starts by evolving explicitly the vector potential a_i, i.e. all the source terms of the evolution equations of these variables are included in the L_1 operator.

We then evolve the scalar potential Φ. More precisely, the corresponding L_2 and L_3 operators associated with the evolution equations for a_i are

$$L_{2(\Phi)} = -a^i D_i \alpha - \alpha D_i a^i, \tag{36}$$

$$L_{3(\Phi)} = \alpha K \Phi + \mathcal{L}_\beta \Phi. \tag{37}$$

The components of the electric field E^i are evolved partially implicitly, using the updated values of Φ and a_i. The corresponding operators are

$$L_{2(E^i)} = \alpha(KE^i + \mu^2 a^i + \epsilon^{ijk} D_j B_k) - \epsilon^{ijk} B_j D_k \alpha, \tag{38}$$

$$L_{3(E^i)} = \mathcal{L}_\beta E^i. \tag{39}$$

Finally, we note that the spatial derivatives in the spacetime evolution are computed using a fourth-order, centered, finite-difference approximation on a logarithmic grid (see [38]). Moreover, as customary in grid-based numerical relativity codes, we use fourth-order Kreiss-Oliger dissipation to avoid high frequency noise appearing near the outer boundary. Details about the convergence properties and accuracy of the code are given in Appendix B.

In the numerical simulations we have used a logarithmic radial grid that extends from the origin to $r = 50$ and uses a minimum resolution close to the origin of $\Delta r = 0.0125$.

V. RESULTS

A. Unperturbed evolutions

We start by evolving the five spherically symmetric Proca star models described in Table I without any additional perturbation (apart from the unavoidable discretization error).

In Fig. 3 we plot the time evolution of the Proca field energy computed from Eq. (32) and the irreducible mass of the AH, when the latter is present. The figure shows that the energy remains constant for models 1 and 2, hence showing their stability, at least in the absence of larger perturbations. For the other three models, the discretization error is sufficient to trigger the collapse of the solutions. At some point in the evolution an AH forms. This is confirmed in Fig. 4, where the time evolution of the minimum of the lapse function is plotted, showing it tends to 0, a signature of AH formation. The precise instants those horizons are found in our code are indicated by the three vertical dashed lines in the figure. Subsequently, all Proca field energy evolves towards being absorbed by the black hole. The results in Figs. 3 and 4 also indicate that decay is progressively faster as we move away from the threshold of stability solution (maximal ADM mass) in Fig. 1. These results match precisely the expectation from perturbation theory in the frequency domain [1].

Let us now turn our attention to Fig. 5. This figure shows the time evolution of the amplitude of the scalar potential at some extraction radius and for three representative models. The top panel (model 1) shows constant amplitude oscillations, with a frequency matching that of the Proca stars, as expected for a solution that is not changing in time. The

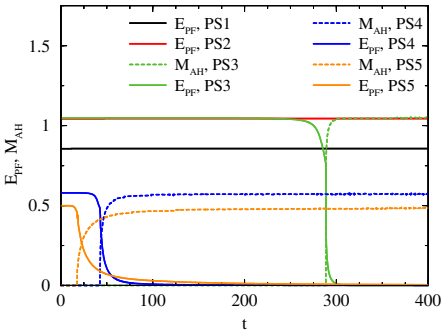

FIG. 3. Time evolution of the Proca field energy and the apparent horizon mass for the unperturbed models 1–5. In this and remaining time series, the time coordinate is given in units of μ.

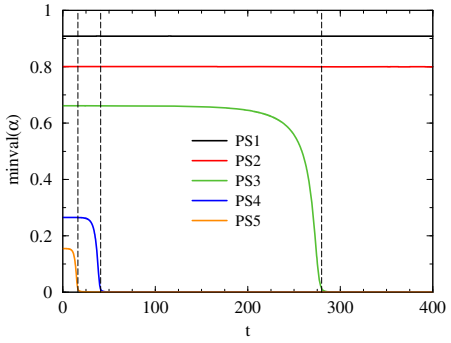

FIG. 4. Time evolution of the minimal value of the lapse for all unperturbed models. The vertical dashed lines indicate the time of formation of an AH for models 3–5.

Fourier transform of the time series reveals (inset) that the corresponding frequency is that of the Proca star. The middle panel (model 3) shows oscillations that remain constant up to $t \sim 150$, then grow and then decay to 0. At about $t \sim 300$ the AH is formed (Fig. 4) and shortly afterwards no noticeable Proca field remains outside the horizon. Again, the inset shows that the frequency in the time series is the one of the original Proca star. The bottom panel (model 5 and likewise for model 4) shows a different behavior from model 3 (middle panel), in spite of both leading to black hole formation. When the black hole is formed, a more significant part of the Proca field lingers for a longer period of time. This is already visible comparing the Proca field energy curves for models 4 or 5 and model 3, in Fig. 3. Moreover, the beating pattern observed in the bottom panel of Fig. 5 shows that more than one significant frequency is present. This is indeed confirmed by a Fourier analysis (inset). Such an analysis can be compared with the frequencies of the first few monopole quasibound states of a Proca field on a Schwarzschild BH [41]—Table II[1]—and yields the following conclusions:

(i) The initial part of the time series ($t = 0$–200, black solid line in the inset) contains the initial Proca star frequency $w/\mu = 0.9$; its frequency range is centered around $w/\mu = 0.96$–0.97, which matches the fundamental mode frequency, whose real part is $w \sim 0.966$–0.970, for $\mu M_{\rm ADM} = 0.5$ or 0.45 respectively (Table II). The peak frequency is slightly higher than the central one, suggesting that an overtone (rather than the fundamental mode) dominates the signal. This is consistent with the enveloping (dashed black) fit curve presented which has

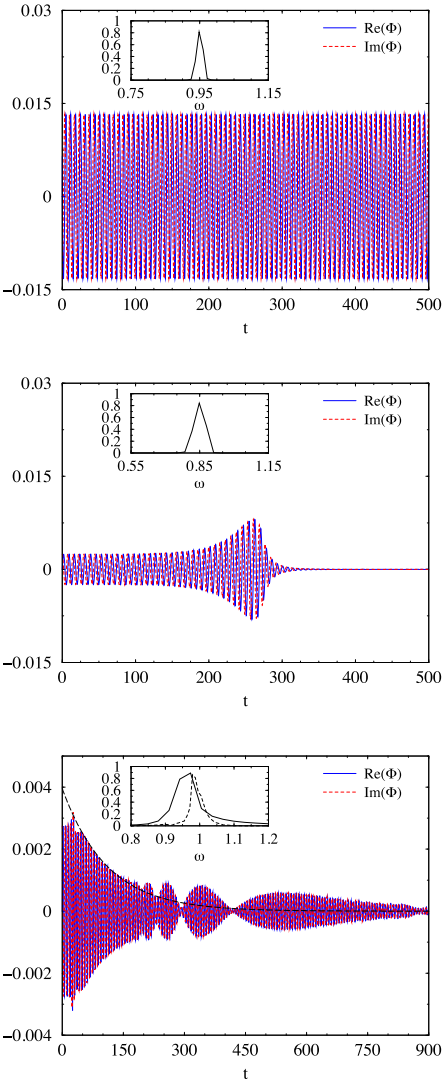

FIG. 5. Time evolutions of the amplitude of the scalar potential extracted at $r = 5$ for models 1 (top panel), 3 (middle panel), and 5 (bottom panel). The oscillation frequencies shown in the insets of the top and middle panel are in good agreement with the corresponding ω, in units of μ, of models 1–3 (see Table I). In the bottom panel, the initial decay of the wig is fitted by the enveloping function $e^{-\omega_I t}$, where for model 5, $\omega_I/\mu \sim 0.009$.

[1]We display the frequencies for both the fundamental mode ($n = 0$) and first overtones ($n = 1, 2, 3$), where n is the excitation quantum number [41] and for both $\mu M_{\rm ADM} = 0.5$ and $\mu M_{\rm ADM} = 0.45$. Since the original Proca star has mass $\mu M_{\rm ADM} = 0.496$, the mass of the Schwarzschild black hole resulting from the collapse of model 5, around which a small Proca field remnant lingers, is estimated to be in between these two values. We thank J. G. Rosa for providing us with these frequencies.

TABLE II. Frequencies for spherical (monopole) quasibound states of a Proca field (mass μ) around a Schwarzschild black hole (mass $M_{\rm ADM}$).

Mode	w/μ ($\mu M_{\rm ADM} = 0.45$)	w/μ ($\mu M_{\rm ADM} = 0.5$)
$n = 0$	$0.970 - 0.018i$	$0.966 - 0.025i$
$n = 1$	$0.986 - 0.005i$	$0.984 - 0.008i$
$n = 2$	$0.992 - 0.002i$	$0.991 - 0.003i$
$n = 3$	$0.995 - 0.001i$	$0.994 - 0.002i$

$\omega_I/\mu \sim 0.009$, a value closer to the imaginary part of the first overtone than that of the fundamental mode.

(ii) The later part of the time series ($t = 200$–900, dashed line in the inset) is narrower and centered around $w/\mu \sim 0.98$–0.99. The absence of the fundamental mode is expected as its lifetime is $\tau \sim 1/|\omega_I| \lesssim 100$. The signal is then composed essentially by the overtones which are longer lived than the fundamental mode, and have frequencies in the range $w/\mu \sim 0.98$–1: Table II. The beating pattern present shows the existence of more than one overtone.

These lingering Proca modes resemble the scalar quasibound states discussed in [28,37] and the beating pattern resembles that observed in superpositions of quasibound states of a scalar field around Schwarzschild black holes—see e.g. [42,43].

We recall that test field, frequency domain studies have shown that the Proca field exhibits quasibound states, i.e. solutions which are localized within the vicinity of a black hole [44]. These quasibound states, as in the scalar case, have complex frequencies and the imaginary part corresponds to the decay rate. In the low mass limit, the fundamental modes of these states are consistent with a hydrogenic spectrum. A thorough study of the quasibound states and the quasinormal modes of the Proca field in a Schwarzschild background can be found in [41]. The nonlinear dynamics of self-gravitating Proca quasibound states in both Schwarzschild and Kerr black holes has also been studied numerically in [35]. In particular, the study of Proca fields on the background of rotating black holes has been used to provide upper limits on the mass of the photon [45].

B. Perturbed evolutions

We turn now to the study of the dynamical behavior of Proca stars under perturbations. To illustrate this situation we add a perturbation (at the few % level) to the Proca field variables of the form $\tilde{A} \to \tilde{A}x$ where $\tilde{A}$ stands for Φ, a^r, E^r and x is a numerical factor. As a remark, we observe that this type of perturbation does not change the sign of the binding energy of the Proca star. Indeed, inspection of (25) and (32) shows that both these quantities scale as the square of the scaling factor. Thus, this scaling does not change the sign of their difference.

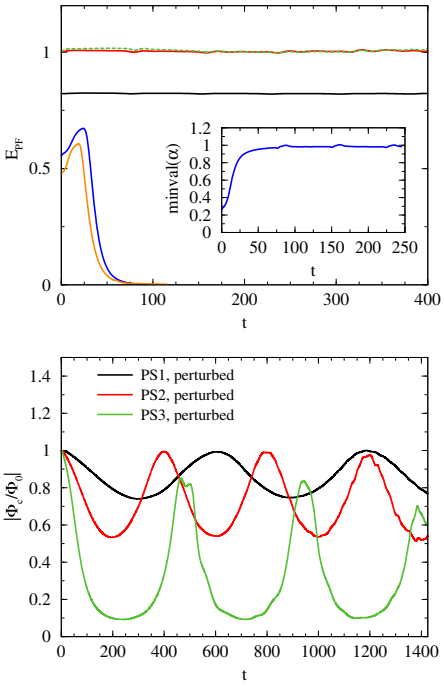

FIG. 6. (Top panel) Time evolution of the perturbed models. The inset shows the minimum value of the lapse of perturbed model 4. (Bottom panel) Time evolution of the magnitude of the Proca electric potential for models 1–3.

We first take $x = 1.02$. For this choice, the unstable Proca stars tend to collapse faster than the unperturbed solution with the same resolution. This is the expected result, since this perturbation increases, in particular, the central electric potential of the Proca star (cf. discussion on neutron stars in the conclusions).

Next, we choose $x = 0.98$. In this case, we are removing part of the Proca field and the outcome of the evolution is different for the unstable models, as exhibited in Fig. 6. In the top panel of Fig. 6, we plot the time evolution of the Proca field energy for the perturbed models (the color coding is the same as in Fig. 3). Models 1 (black solid line) appears stable. Models 2 (red solid line) and 3 (green dashed line), despite being fairly stable, exhibit some noticeable oscillations. We come back to these shortly. Models 4 and 5, on the other hand, show a total dispersive behavior: the energy of the Proca field goes to 0 *without* AH formation; moreover, the value of the lapse function tends to unity at the origin (inset), which is the behavior of flat spacetime. We remark that the slight increase in the Proca field energy clearly visible in the beginning of the evolution of models 4 and 5 is related to the evolution of the lapse function, as it adapts to the perturbation.

TABLE III. Final state of the five representative PS models considered in this paper.

Model	Perturbative analysis	Binding energy	Evolution (no perturbation)	Evolution (×0.98 perturbation)
PS1	Stable	> 0	Stable	Stable
PS2	Stable	> 0	Stable	Stable
PS3	Unstable	> 0	Collapse to BH	Migration
PS4	Unstable	< 0	Collapse to BH (+noticeable wig)	Dispersion
PS5	Unstable	< 0	Collapse to BH (+noticeable wig)	Dispersion

A more detailed investigation of what occurs for models 1–3 can be made by analyzing the behavior of the electric potential at the origin, which is displayed in the bottom panel of Fig. 6. All three models oscillate, but whereas the oscillations of models 1 and 2 are not damping the value of Φ_c, the ones of model 3 are clearly decreasing its value. We recall, from Fig. 2, that this scalar potential at the origin defines uniquely static Proca solutions. The decrease of its value for model 3 can be interpreted as a *migration* of the unstable star towards the stable branch. This conclusion is supported by computing the oscillation frequency of the perturbed models. For the perturbed model 3 it is ∼0.92, whereas for the perturbed model 2, it is ∼0.91. Thus, the perturbed model 3 is oscillating with a frequency which corresponds to a stable Proca star, very close to the one of model 2, which is in the stable branch. We recall that models 4 and 5 have negative binding energy (excess energy), unlike solution 3. It is therefore expectable that they could have a different evolution and disperse away. This is precisely what we observe in these perturbed evolutions.

To summarize, the perturbed evolutions indicate that, depending on the perturbation, but also on the sign of the binding energy, Proca stars can be subject to three different outcomes: collapse, dispersion/fission or migration.

VI. DISCUSSION

In this paper we have used numerical relativity techniques to study the stability and evolution of Proca stars. These are macroscopic, self-gravitating Bose-Einstein condensates composed by a massive, complex, vector field [1]. Considering the energy of these solutions, together with perturbative stability studies, leads to three different classes of solutions: (i) stable solutions (our models 1 and 2); (ii) unstable solutions with positive binding energy (our model 3); and (iii) unstable solutions with negative binding energy or excess energy (our models 4 and 5). Here, we have shown that the fate of the unstable solutions depends not only on the type of solutions but *also* on the type of perturbation. Our results are summarized in Table III and as follows.

When we evolve in time the configurations with no perturbations we observe the following behaviors: Models 1 and 2 evolve in time with almost no changes. The Proca field oscillates and the spacetime remains stationary. Configuration 3 collapses to form a black hole without a noticeable Proca field remnant, thus yielding a vacuum spacetime. For unstable configurations 4 and 5, however, even though a black hole is formed after the collapse a noticeable set of Proca quasibound states remains in its vicinity.

When we apply a perturbation, multiplying the fields by a constant of order unity, the stable configurations still display no evolution. Configuration 3 migrates towards stable states with lower mass, whereas configurations 4 and 5 are no more localized states and the Proca field disperses away.

The fates we have just described for Proca stars parallel quite closely those observed for scalar boson stars and discussed in detail in the introduction. But it is interesting to compare this dynamics with that of the well-known compact fermionic stars, namely neutron stars.

In an astrophysical context, the dynamical fate of neutron stars out of equilibrium has received enormous attention, as it plays a crucial role in significant scenarios of relativistic astrophysics such as supernovae, gamma-ray bursts, or binary neutron star mergers. Moreover, as a fundamental physics problem, critical phenomena in neutron stars at the threshold of black hole formation have also been examined for perfect fluid matter (see [46] and references therein). By triggering the collapse of initially stable models through suitable perturbations, it has been possible to elucidate the boundary between different types of critical behavior in neutron stars and its relationship with the boundary between dispersed and bound end states [46].

Radially unstable equilibrium models of neutron stars at very high densities can be built for any equation of state. Such models satisfy the condition $\partial M_{\rm ADM}/\partial \rho_{\rm c} < 0$, where $\rho_{\rm c}$ is the central rest-mass density. Therefore, any perturbation causes them to either collapse to a black hole or to expand to the stable branch of equilibrium models, at smaller central densities. The sign of the perturbation determines the path the unstable star follows. These observations parallel closely what we have described for bosonic stars (both scalar and vector).

While the two outcomes are mathematically viable, the migrating (i.e. expanding) path is ruled out from an astrophysical viewpoint. In a realistic scenario, stable neutron stars, as those formed following a supernova core collapse or an accretion-induced collapse of a white dwarf or those in x-ray binaries, can accrete matter and secularly

move towards larger central densities along the stable branch of equilibrium configurations. Beyond the maximum-mass limit collapse to a black hole ensues. There is, however, no secular mechanism that could evolve an unstable star to the stable branch. Similarly, if Proca stars form in nature, one may wonder if the migration dynamics we have observed is realized by any naturally occurring mechanism.

The nonlinear dynamics of a migrating relativistic spherical star was first investigated in [47], using a polytropic model with a central rest-mass density larger than that of the maximum-mass stable model. Under the radial perturbation induced by the truncation error of the numerical code, the star was found to expand and evolve towards a stable equilibrium configuration with a smaller central rest-mass density but with approximately the same rest-mass of the perturbed star. The stable configuration is reached asymptotically, as the star oscillates around a central density close to that of a stable star with the same rest mass. A similar behavior has been observed in numerical simulations of relativistic boson stars [19,22]. Contrary to the dispersive boson star case, for a neutron star with an ideal-fluid equation of state, the oscillations are gradually damped due to the dissipation of kinetic energy via shock heating.

We close with two remarks. Even though our results suggest that the dynamics and final states of PS is quite similar to SBS, the study of vector fields may yield extra value as compared to the scalar case. As a first example, consider the dynamics of Proca fields around black holes, which has already been considered in the literature, albeit less studied than the corresponding scalar dynamics. The existence of long-lived configurations around nonrotating black holes has been demonstrated in the test field limit [41,44] and in the full nonlinear regime solving the Einstein-Proca equations [35]. The inherent difficulty of adding rotation to the black hole is also present and a full evolution of a rotating black hole with a Proca field is not yet available. Still, since the super-radiant instability of a Proca field has a shorter time scale than its scalar counterpart [48], this offers a promising model for analyzing the nonlinear development of the super-radiant instability around Kerr black holes. Secondly, it has been recently argued [49] that photons can behave near stellar mass black holes as Proca particles, in view of the effective mass induced by the galactic plasma. Thus, the study of *real* Proca field interacting with black holes may describe astrophysical processes without invoking new exotic particles.

ACKNOWLEDGMENTS

This work has been supported by the Spanish Ministerio de Economía, Industria y Competitividad (MINECO) (Grants No. AYA2013-40979-P and No. AYA2015-66899-C2-1-P), by the Generalitat Valenciana (Grants No. PROMETEOII-2014-069 and No. ACIF/2015/216), by the Consejo Nacional de Ciencia y Tecnología (CONACyT)-México, by the Fundação para a Ciência e a Tecnologia (FCT) (Portugal) IF program, by the Center for Research & Development in Mathematics and Applications (CIDMA) (FCT) strategic project Grant No. UID/MAT/04106/2013 and by the European Union's Horizon 2020 research and innovation program under the Marie Sklodowska-Curie Grant No. 690904 and by the CIDMA project Grant No. UID/MAT/04106/2013. Computations have been performed at the Servei d'Informàtica de la Universitat de València and at the Blafis cluster at the University of Aveiro.

APPENDIX A: SPHERICALLY SYMMETRIC PROCA STAR SOLUTIONS

Spherically symmetric Proca stars solutions were discussed in Ref. [1]. In a Schwarschild-like coordinate system the element of line is

$$ds^2 = -N(\bar{r})\sigma^2(\bar{r})dt^2 + \frac{d\bar{r}^2}{N(\bar{r})} + \bar{r}^2(d\theta^2 + \sin^2 d\varphi^2). \tag{A1}$$

Comparison of the above line element with the isotropic metric (23) yields for the transformation

$$\frac{dr}{r} = \frac{d\bar{r}}{\bar{r}\sqrt{N(\bar{r})}}, \quad \text{while } e^{F_0} = \sigma\sqrt{N}, \quad e^{F_1} = \frac{\bar{r}}{r}. \tag{A2}$$

For the isotropic coordinates used in this paper, the Einstein equations reduce to two second-order equations for the metric functions F_0, F_1 (reinserting G_0),

$$F_0'' + F_0'\left(\frac{2}{r} + F_0' + F_1'\right) - 4\pi G_0 e^{-2F_0}\left[\left(V' + \frac{wH_1}{r}\right)^2 + 2e^{2F_1}\mu^2 V^2\right] = 0, \tag{A3}$$

$$F_1'' - F_0'F_1' + \frac{1}{r}(F_1' - F_0') + 4\pi G_0\mu^2\left(\frac{H_1^2}{r^2} + e^{2(F_1-F_0)}V^2\right) = 0, \tag{A4}$$

together with the constraint equation

$$0 = F_1'^2 + 2F_0'F_1' + \frac{2}{r}(F_0' + F_1') + 4\pi G_0 \times \left[e^{-2F_0}\left(V' + \frac{wH_1}{r}\right)^2 - \mu^2\left(\frac{H_1^2}{r^2} + e^{2(F_1-F_0)}V^2\right)\right]. \tag{A5}$$

The Proca equations are

$$wV' + \frac{H_1}{r}(w^2 - e^{2F_0}\mu^2) = 0, \tag{A6}$$

$$V'' + \frac{2V'}{r} + \left(V' + \frac{wH_1}{r}\right)(F_1' - F_0') + \frac{w}{r^2}(H_1 + rH_1') - e^{2F_1}\mu^2 V = 0, \tag{A7}$$

the vector potential being subject to the gauge condition $\nabla_\alpha \mathcal{A}^\alpha = 0$, which is actually a requirement from the field equations for the Proca field

$$H_1' + \left(F_0' + F_1' + \frac{1}{r}\right)H_1 - e^{2(F_1 - F_0)} rwV = 0. \tag{A8}$$

For this ansatz, the Noether charge reads

$$Q = 4\pi \int_0^\infty dr e^{F_1 - F_0} H_1 (wH_1 + rV'), \tag{A9}$$

and the energy density measured by a static observer is

$$-T_t^t = \frac{1}{2} e^{-2(F_1+F_0)}\left(V' + \frac{wH_1}{r}\right)^2 + \frac{1}{2}\mu^2\left(\frac{e^{2F_1}H_1^2}{r^2} + e^{-2F_0}V^2\right), \tag{A10}$$

while the Komar energy density entering the integral (32) is

$$2T_t^t - T_\alpha^\alpha = -e^{2(F_1+F_0)}\left(V' + \frac{wH_1}{r}\right)^2 - 2e^{-2F_0}\mu^2 V^2. \tag{A11}$$

The PSs possess the following expansion at the origin $r \to 0$,

$$F_0(r) = f_0 + \frac{4\pi G_0}{3} e^{2(f_1 - f_0)}\mu^2 v_0^2 r^2 + \mathcal{O}(r^4), \tag{A12}$$

$$F_1(r) = f_1 - \frac{4\pi G_0}{12} e^{2(f_1 - f_0)}\mu^2 v_0^2 r^2 + \mathcal{O}(r^4), \tag{A13}$$

$$H_1(r) = \frac{1}{3} e^{2(f_1 - f_0)} v_0 w r^2 + \mathcal{O}(r^4), \tag{A14}$$

$$V(r) = v_0 + \frac{1}{6} e^{2(f_1 - f_0)} v_0 (e^{2f_0}\mu^2 - w^2) r^2 + \mathcal{O}(r^4), \tag{A15}$$

where f_1, f_0 and v_0 are constants fixed by the numerics. The first terms in the expression of the solution as $r \to \infty$ read

$$F_0(r) = -\frac{M_{\rm ADM}}{r} + \ldots, \tag{A16}$$

$$F_1(r) = \frac{M_{\rm ADM}}{r} + \ldots, \tag{A17}$$

$$H_1(r) = -c_0 \frac{w}{\sqrt{\mu^2 - w^2}} e^{-r\sqrt{\mu^2 - w^2}} + \ldots, \tag{A18}$$

$$V(r) = c_0 \frac{e^{-r\sqrt{\mu^2 - w^2}}}{r} + \ldots, \tag{A19}$$

where c_0 is a constant. Observe that the PSs should satisfy the bound state condition $w < \mu$.

The solutions that smoothly interpolate between the two above asymptotic behaviors are found numerically. In numerical treatment, we set $\mu = 1$, $4\pi G_0 = 1$, by using a scaled radial coordinate $r \to r\mu$ (together with $w \to w/\mu$) and scaled potentials $H_1 \to H_1\sqrt{4\pi G_0}$, $V \to V\sqrt{4\pi G_0}$. Restricting to the fundamental set of solutions, we obtain the (w, M)-diagram, exhibited in Fig. 1. This spiral starts from $M = 0$ for $w/\mu = 1$, in which limit the Proca field becomes very diluted and the solution trivializes. At some intermediate frequency $w_m/\mu \simeq 0.875$, a maximal ADM mass $M_{\rm max} \simeq 1.058$ is attained. There is also a minimal allowed frequency $w_{\rm min} \simeq 0.814$ where $M \sim 0.82$.

APPENDIX B: CODE ASSESSMENT

Our numerical code was originally developed by [29]. The evolution equations are solved using techniques we have extensively tested and employed in previous works before [36–38]. For the current work, we upgraded the code to account for the Proca field. This appendix hence reports a succinct assessment of the upgraded code. We discuss in particular its convergence properties and the violations of the constraint equations, both for the Einstein and the Proca fields.

Figure 7 shows the convergence properties of the code. This figure displays the time evolution of the rescaled L2 norm of the Hamiltonian constraint (top panel) and of the Gauss constraint (bottom panel) for the unstable model 5. The L2 norm of a constraint C is given by

$$|C|^2 = \sqrt{\frac{\sum_{i=1}^N C_i^2}{N}}, \tag{B1}$$

where N indicates the number of radial grid points. The results have been obtained at three different radial resolutions, as indicated in the figure caption, and the blue and red solid curves have been multiplied by the appropriate numerical factors, 2 and 4, respectively, corresponding to second-order convergence (thus the three curves should overlap). The constraints are computed in the entire computational domain; hence the black hole puncture of this unstable model is also included. Black hole formation coincides with the rapid initial growth of the constraints. The violation of the

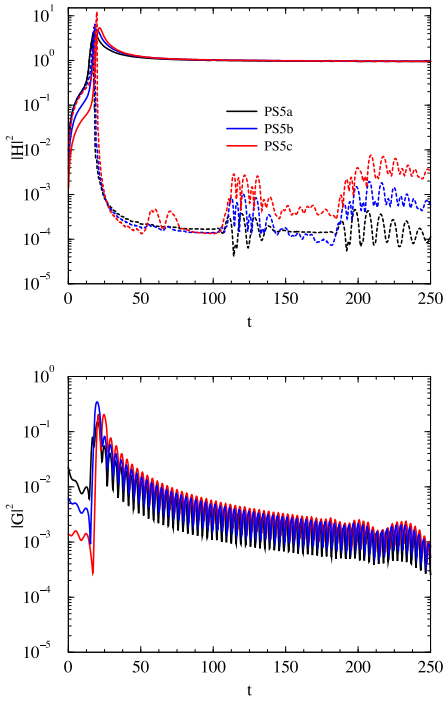

FIG. 7. Convergence analysis for model PS5 employing three different resolutions, $\Delta r = 0.0125$, black curves, $\Delta r = 0.0125/\sqrt{2}$, blue curves, and $\Delta r = 0.0125/2$, red curves. Top panel: L2 norm of the Hamiltonian constraint computed either at all radial points (solid lines) or outside of the AH (dashed lines). Bottom panel: L2 norm of the Gauss constraint computed at all radial points.

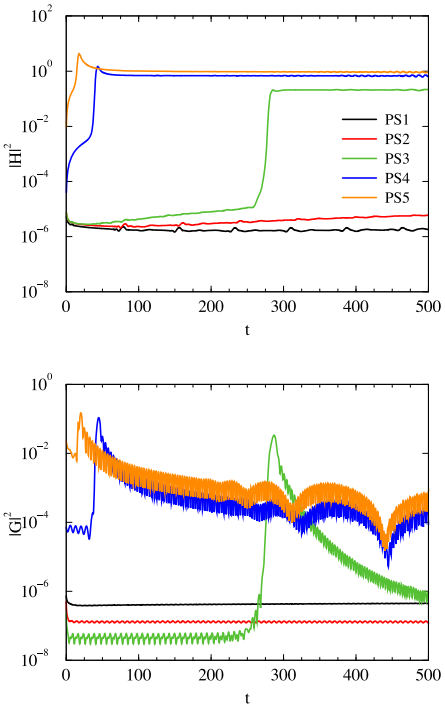

FIG. 8. Time evolution of the L2 norm of the constraints for all Proca star models, using our canonical radial resolution of $\Delta r = 0.0125$. Top panel: Hamiltonian constraint. Bottom panel: Gauss constraint.

Hamiltonian constraint levels off shortly thereafter and does not subsequently grow. Correspondingly, the violation of the Gauss constraint has decreased by about 2 orders of magnitude by the end of the simulation with respect to the value attained at the moment the black hole forms. In addition, the top panel of Fig. 7 also shows the Hamiltonian constraint when computed outside of the AH (as customary in numerical relativity studies, see e.g. [50,51]), which is indicated by the dashed lines. In this case, they show a fourth-order convergence, dominated by the spatial derivatives, and are multiplied by 4 and 16. Observe that the oscillations that appear after $t = 100$ are reflections on the outer boundary, which is at $r = 50$; we have checked, however, that these oscillations do not affect the results by putting the boundary further away. The overall effect of the reflection is to reduce the fourth order of convergence. As expected, when the causally disconnected AH interior is excluded in the L2 norm computation, the violations are reduced by several orders of magnitude. All in all, Fig. 7 shows that the PIRK time-evolution scheme of our numerical code has a global order of convergence close to 2.

Finally, Fig. 8 shows the time evolution of the L2 norm of the Hamiltonian constraint and of the Gauss constraint for all of our Proca star models. Both quantities are computed using all radial grid points, hence including the AH of the resulting black holes for models 3–5. The time evolution of the constraints for these models is characterized by the sudden growth at black hole formation, after which the Hamiltonian constraint attains a constant value and the Gauss constraint significantly drops. For the collapsing models, the higher the value of Φ_c the larger the violation of the constraints. On the other hand, for stable models 1 and 2, the violation of the constraints hardly grows in time and it stays at maximum values that are several orders of magnitude smaller than that of unstable models.

It should be noted, however, that the specific maximum violation the constraints attain is somewhat meaningless, as

this number may be arbitrarily reduced even at the same grid resolution. This can be achieved by taking a larger number of grid points and placing the outer boundary at the appropriate (further out) location, as follows from the definition of the L2 norm in Eq. (B1). Therefore, what is important when assessing the numerical code is to show that the constraints are bounded in time *and* that the numerical code is convergent.

[1] R. Brito, V. Cardoso, C. A. R. Herdeiro, and E. Radu, Phys. Lett. B **752**, 291 (2016).
[2] S. R. Coleman, Nucl. Phys. **B262**, 263 (1985); **B269**, 744 (E) (1986).
[3] D. J. Kaup, Phys. Rev. **172**, 1331 (1968).
[4] R. Ruffini and S. Bonazzola, Phys. Rev. **187**, 1767 (1969).
[5] F. E. Schunck and E. W. Mielke, Classical Quantum Gravity **20**, R301 (2003).
[6] G. H. Derrick, J. Math. Phys. (N.Y.) **5**, 1252 (1964).
[7] P. Grandclement, G. Fodor, and P. Forgacs, Phys. Rev. D **84**, 065037 (2011).
[8] E. Seidel and W. M. Suen, Phys. Rev. Lett. **66**, 1659 (1991).
[9] F. E. Schunck and E. W. Mielke, Phys. Lett. A **249**, 389 (1998).
[10] S. Yoshida and Y. Eriguchi, Phys. Rev. D **56**, 762 (1997).
[11] M. Colpi, S. L. Shapiro, and I. Wasserman, Phys. Rev. Lett. **57**, 2485 (1986).
[12] B. Kleihaus, J. Kunz, M. List, and I. Schaffer, Phys. Rev. D **77**, 064025 (2008).
[13] F. D. Ryan, Phys. Rev. D **55**, 6081 (1997).
[14] P. Grandclement, C. Som, and E. Gourgoulhon, Phys. Rev. D **90**, 024068 (2014).
[15] C. A. R. Herdeiro, E. Radu, and H. Rnarsson, Phys. Rev. D **92**, 084059 (2015).
[16] S. L. Liebling and C. Palenzuela, Living Rev. Relativ. **15**, 6 (2012).
[17] M. Gleiser and R. Watkins, Nucl. Phys. **B319**, 733 (1989).
[18] T. D. Lee and Y. Pang, Nucl. Phys. **B315**, 477 (1989).
[19] E. Seidel and W.-M. Suen, Phys. Rev. D **42**, 384 (1990).
[20] J. Balakrishna, E. Seidel, and W.-M. Suen, Phys. Rev. D **58**, 104004 (1998).
[21] F. S. Guzman, Phys. Rev. D **70**, 044033 (2004).
[22] S. H. Hawley and M. W. Choptuik, Phys. Rev. D **62**, 104024 (2000).
[23] E. Seidel and W.-M. Suen, Phys. Rev. Lett. **72**, 2516 (1994).
[24] A. R. Liddle and M. S. Madsen, Int. J. Mod. Phys. D **01**, 101 (1992).
[25] C. Herdeiro, E. Radu, and H. Runarsson, Classical Quantum Gravity **33**, 154001 (2016).
[26] F. Garca and I. S. Landea, Phys. Rev. D **94**, 104006 (2016).
[27] M. Duarte and R. Brito, Phys. Rev. D **94**, 064055 (2016).
[28] J. Barranco, A. Bernal, J. C. Degollado, A. Diez-Tejedor, M. Megevand, M. Alcubierre, D. Núñez, and O. Sarbach, Phys. Rev. Lett. **109**, 081102 (2012).
[29] T. W. Baumgarte, P. J. Montero, I. Cordero-Carrión, and E. Müller, Phys. Rev. D **87**, 044026 (2013).
[30] J. D. Brown, Phys. Rev. D **79**, 104029 (2009).
[31] M. Alcubierre and M. D. Mendez, Gen. Relativ. Gravit. **43**, 2769 (2011).
[32] T. Nakamura, K. Oohara, and Y. Kojima, Prog. Theor. Phys. Suppl. **90**, 1 (1987).
[33] M. Shibata and T. Nakamura, Phys. Rev. D **52**, 5428 (1995).
[34] T. W. Baumgarte and S. L. Shapiro, Phys. Rev. D **59**, 024007 (1998).
[35] M. Zilho, H. Witek, and V. Cardoso, Classical Quantum Gravity **32**, 234003 (2015).
[36] P. J. Montero and I. Cordero-Carrion, Phys. Rev. D **85**, 124037 (2012).
[37] N. Sanchis-Gual, J. C. Degollado, P. J. Montero, and J. A. Font, Phys. Rev. D **91**, 043005 (2015).
[38] N. Sanchis-Gual, J. C. Degollado, P. J. Montero, J. A. Font, and V. Mewes, Phys. Rev. D **92**, 083001 (2015).
[39] I. Cordero-Carrión and P. Cerdá-Durán, arXiv:1211.5930.
[40] I. Cordero-Carrión and P. Cerdá-Durán, *Advances in Differential Equations and Applications*, SEMA SIMAI Springer Series Vol. 4 (Springer International Publishing, Switzerland, 2014).
[41] J. G. Rosa and S. R. Dolan, Phys. Rev. D **85**, 044043 (2012).
[42] H. Okawa, H. Witek, and V. Cardoso, Phys. Rev. D **89**, 104032 (2014).
[43] J. Barranco, A. Bernal, J. C. Degollado, A. Diez-Tejedor, M. Megevand *et al.*, Phys. Rev. D **89**, 083006 (2014).
[44] D. V. Gal'tsov, G. V. Pomerantseva, and G. A. Chizhov, Izv. Vuz. Fiz. **27**, 81 (1984) [Sov. Phys. J. **27**, 697 (1984)].
[45] P. Pani, V. Cardoso, L. Gualtieri, E. Berti, and A. Ishibashi, Phys. Rev. Lett. **109**, 131102 (2012).
[46] S. C. Noble and M. W. Choptuik, Phys. Rev. D **93**, 024015 (2016).
[47] J. A. Font, T. Goodale, S. Iyer, M. Miller, L. Rezzolla, E. Seidel, N. Stergioulas, W.-M. Suen, and M. Tobias, Phys. Rev. D **65**, 084024 (2002).
[48] P. Pani, V. Cardoso, L. Gualtieri, E. Berti, and A. Ishibashi, Phys. Rev. D **86**, 104017 (2012).
[49] J. P. Conlon and C. A. R. Herdeiro, arXiv:1701.02034.
[50] D. Alic, W. Kastaun, and L. Rezzolla, Phys. Rev. D **88**, 064049 (2013).
[51] C. Reisswig, C. D. Ott, E. Abdikamalov, R. Haas, P. Mösta, and E. Schnetter, Phys. Rev. Lett. **111**, 151101 (2013).

PHYSICAL REVIEW D **96,** 024015 (2017)

Quasistationary solutions of scalar fields around collapsing self-interacting boson stars

Alejandro Escorihuela-Tomàs,[1] Nicolas Sanchis-Gual,[1] Juan Carlos Degollado,[2] and José A. Font[1,3]

[1]*Departamento de Astronomía y Astrofísica, Universitat de València, Dr. Moliner 50, 46100 Burjassot, València, Spain*

[2]*Instituto de Ciencias Físicas, Universidad Nacional Autónoma de México, Apartado Postal 48-3, 62251 Cuernavaca, Morelos, México*

[3]*Observatori Astronòmic, Universitat de València, Calle Catedrático José Beltrán 2, 46980 Paterna, València, Spain*

(Received 27 April 2017; published 13 July 2017)

There is increasing numerical evidence that scalar fields can form long-lived quasibound states around black holes. Recent perturbative and numerical relativity calculations have provided further confirmation in a variety of physical systems, including both static and accreting black holes, and collapsing fermionic stars. In this work, we investigate this issue yet again in the context of gravitationally unstable boson stars leading to black-hole formation. We build a large sample of spherically symmetric initial models, both stable and unstable, incorporating a self-interaction potential with a quartic term. The three different outcomes of unstable models, namely, migration to the stable branch, total dispersion, and collapse to a black hole, are also present for self-interacting boson stars. Our simulations show that for black hole-forming models, a scalar-field remnant is found outside the black-hole horizon, oscillating at a different frequency than that of the original boson star. This result is in good agreement with recent spherically symmetric simulations of unstable Proca stars collapsing to black holes [N. Sanchis-Gual, C. Herdeiro, E. Radu, J. C. Degollado, and J. A. Font, Phys. Rev. D **95**, 104028 (2017).].

DOI: 10.1103/PhysRevD.96.024015

I. INTRODUCTION

The development of stable numerical relativity codes based on hyperbolic formulations of Einstein's equations, accompanied with suitable gauge conditions, has been critical for recent advances in our understanding of astrophysical systems involving strong gravity. In particular, those technical developments have allowed accurate numerical evolutions of highly dynamical spacetimes up to, and well beyond, the formation of black holes. Further steps have also been taken with the incorporation of matter content in black-hole spacetimes, specifically in the form of scalar fields, a type of matter that has found recurrent use in numerical relativity. Within such a framework, recent studies of the Einstein-Klein-Gordon (EKG) system, both in the linear and nonlinear regimes, have shown that massive scalar fields surrounding black holes can accommodate a type of oscillatory mode which only decays at infinity [1–7]. These quasibound states may thus linger around the black hole in the form of a long-lived remnant (a *wig*) of scalar field. For both scalar fields around supermassive black holes and axionlike scalar fields around primordial black holes, it has been found that the fields can indeed survive for cosmological time scales [3]. Moreover, for spinning black holes, quasibound states can yield exponentially growing modes [8,9] and hairy black-hole solutions [10].

On the other hand, scalar fields are also known to allow for solitonlike solutions, i.e., static, spherically symmetric solutions of the EKG system for a massive and complex field [11,12], which are commonly known as boson stars (see Ref. [13] for a review). The dynamical fate of boson stars has been thoroughly investigated numerically, both using perturbation theory [14,15] and fully nonlinear numerical simulations [16–19]. Reference [16], in particular, first showed that the fate of unstable boson-star solutions was either the formation of a black hole or the migration of the star to the stable branch, regardless of the sign of the binding energy. A third outcome for unstable boson stars is their total dispersion [17,19,20], a situation that only happens for boson stars with negative binding energy.

In this work, we build a comprehensive sample of initial models of boson stars, incorporating a self-interaction potential with a quartic term. The inclusion of such self-interaction provides extra pressure support against gravitational collapse and increases the range of possible maximum masses of boson stars, allowing us to encompass models with astrophysical significance. Here, we revisit the stability of the solutions for different values of the self-interaction coupling constant λ, incorporating values as large as $\Lambda \equiv \lambda/4\pi G\mu^2 = 100$, not previously accounted for (here, μ is the bare mass of the scalar field). Our findings are consistent with the three different outcomes for unstable models, namely, migration to the stable branch, total dispersion, and collapse to a black hole, reported previously

for both the $\lambda = 0$ (mini)boson-star case and for self-interacting boson stars (see Refs. [16,17,19]).

We, however, focus on a particular subset of collapsing models. Making use of the specific techniques developed by Ref. [21] to evolve black-hole spacetimes in spherical symmetry using spherical-polar coordinates, we are able to follow the dynamics of the system for very long periods of time, well beyond black-hole formation and in an entirely stable manner. Using these techniques, we showed recently that quasibound states can form in the vicinity of a black hole born dynamically from the collapse of a neutron star surrounded by a scalar field [22]. Here, we show that long-lived quasibound states can also form after the collapse of a self-interacting boson star. Similar results have also recently been obtained in spherical simulations of unstable Proca stars collapsing to black holes [23] as well as for axion stars [24].

This paper is organized as follows. Section II briefly describes the mathematical formulation of the EKG system. Section III discusses the construction of the initial data, while Sec. IV gives a brief account of numerical aspects of the simulations. Our main findings and results are discussed in Sec. V. Finally, Sec. VI summarizes our conclusions. Greek indices run over spacetime indices, while latin indices run over spatial indices only. We use geometrized units, $c = G = 1$.

II. BASIC EQUATIONS

We investigate the dynamics of a self-interacting scalar-field configuration around a black hole by solving numerically the coupled EKG system

$$R_{\alpha\beta} - \frac{1}{2} g_{\alpha\beta} R = 8\pi T_{\alpha\beta}, \tag{1}$$

with the scalar-field matter content given by the stress-energy tensor

$$\begin{aligned} T_{\alpha\beta} = & \frac{1}{2}(D_\alpha \Phi)^*(D_\beta \Phi) + \frac{1}{2}(D_\alpha \Phi)(D_\beta \Phi)^* \\ & - \frac{1}{2} g_{\alpha\beta}(D^\sigma \Phi)^*(D_\sigma \Phi) - \frac{\mu^2}{2} g_{\alpha\beta}|\Phi\Phi^*| \\ & - \frac{1}{4}\lambda g_{\alpha\beta}|\Phi\Phi^*|^2. \end{aligned} \tag{2}$$

We consider the following potential for the scalar field $V(\Phi^2) = \mu^2|\Phi|^2 + \frac{\lambda}{2}|\Phi|^4$, where $V_{\rm int} \coloneqq \frac{1}{4}\lambda|\Phi|^4$ is a quartic self-interaction potential with coupling λ. We also introduce the dimensionless quantity $\Lambda \equiv \lambda/4\pi\mu^2$. The scalar field obeys the Klein-Gordon equation

$$\left(\Box - \frac{dV}{d|\Phi|^2}\right)\Phi = 0, \tag{3}$$

where the D'Alambertian operator is defined by $\Box \coloneqq (1/\sqrt{-g})\partial_\alpha(\sqrt{-g}g^{\alpha\beta}\partial_\beta)$. Φ is dimensionless, and μ has dimensions of $(\text{length})^{-1}$.

In spherical symmetry, the spatial line element can be written as

$$dl^2 = e^{4\chi}(a(t,r)dr^2 + r^2 b(t,r)d\Omega^2), \tag{4}$$

where $d\Omega^2 = d\theta^2 + \sin^2\theta d\varphi^2$ is the solid angle element and $a(t,r)$ and $b(t,r)$ are two nonvanishing metric functions. Moreover, χ is related to the conformal factor ψ as $\psi = e^\chi = (\gamma/\hat{\gamma})^{1/12}$, with γ and $\hat{\gamma}$ being the determinants of the physical and conformal 3-metrics, respectively. They are conformally related by $\gamma_{ij} = e^{4\chi}\hat{\gamma}_{ij}$.

In this work, we employ the Baumgarte-Shapiro-Shibata-Nakamura (BSSN) formalism of Einstein's equations [25,26] in which the evolved fields are the conformally related three-dimensional metric, the conformal exponent χ, the trace of the extrinsic curvature K, the independent component of the traceless part of the conformal extrinsic curvature, $A_a \equiv A^r{}_r, A_b \equiv A^\theta{}_\theta = A^\varphi{}_\varphi$, and the radial component of the conformal connection functions. The interested reader is pointed to Refs. [5,27,28] for further details. In particular, the explicit forms of the evolution equations for the gravitational field that we use in this work are given by Eqs. (9)–(11) and (13)–(15) in Ref. [5].

As in our previous work [29], in order to solve the Klein-Gordon equation, we use two first-order variables defined as

$$\Pi \coloneqq n^\alpha \partial_\alpha \Phi = \frac{1}{\alpha}(\partial_t \Phi - \beta^r \partial_r \Phi), \tag{5}$$

$$\Psi \coloneqq \partial_r \Phi. \tag{6}$$

Therefore, from Eq. (3), we obtain the following system of first-order equations:

$$\partial_t \Phi = \beta^r \partial_r \Phi + \alpha\Pi, \tag{7}$$

$$\partial_t \Psi = \beta^r \partial_r \Psi + \Psi \partial_r \beta^r + \partial_r(\alpha\Pi), \tag{8}$$

$$\begin{aligned} \partial_t \Pi = & \beta^r \partial_r \Pi + \frac{\alpha}{a e^{4\chi}}\left[\partial_r \Psi \right. \\ & \left. + \Psi\left(\frac{2}{r} - \frac{\partial_r a}{2a} + \frac{\partial r b}{b} + 2\partial_r \chi\right)\right] \\ & + \frac{\Psi}{a e^{4\chi}}\partial_r \alpha + \alpha K \Pi - \alpha(\mu^2 + \lambda\Phi^2)\Phi. \end{aligned} \tag{9}$$

The right-hand sides of the gravitational field evolution equations contain matter source terms (see Eqs. (9)–(11) and (13)–(15) in Ref. [5]), denoted by $\mathcal{E}$, S_a, S_b, and j_r. These terms are components of the energy-momentum

tensor, Eq. (2), or suitable projections thereof, and are given by

$$\mathcal{E} \coloneqq n^\alpha n^\beta T_{\alpha\beta} = \frac{1}{2}\left(|\Pi|^2 + \frac{|\Psi|^2}{a e^{4\chi}}\right) + \frac{1}{2}\mu^2|\Phi|^2 + \frac{1}{4}\lambda|\Phi|^4, \tag{10}$$

$$j_r \coloneqq -\gamma^\alpha_r n^\beta T_{\alpha\beta} = -\frac{1}{2}(\Pi^*\Psi + \Psi^*\Pi), \tag{11}$$

$$S_a \coloneqq T^r_r = \frac{1}{2}\left(|\Pi|^2 + \frac{|\Psi|^2}{a e^{4\chi}}\right) - \frac{1}{2}\mu^2|\Phi|^2 - \frac{1}{4}\lambda|\Phi|^4, \tag{12}$$

$$S_b \coloneqq T^\theta_\theta = \frac{1}{2}\left(|\Pi|^2 - \frac{|\Psi|^2}{a e^{4\chi}}\right) - \frac{1}{2}\mu^2|\Phi|^2 - \frac{1}{4}\lambda|\Phi|^4. \tag{13}$$

The Hamiltonian and momentum constraints are given by the following two equations:

$$\mathcal{H} \equiv R - (A_a^2 + 2A_b^2) + \frac{2}{3}K^2 - 16\pi\mathcal{E} = 0, \tag{14}$$

$$\mathcal{M}_r \equiv \partial_r A_a - \frac{2}{3}\partial_r K + 6A_a\partial_r\chi + (A_a - A_b)\left(\frac{2}{r} + \frac{\partial_r b}{b}\right) - 8\pi j_r = 0. \tag{15}$$

The latter two equations are only computed in our code to monitor the accuracy of the numerical evolutions.

III. INITIAL DATA

Spherical boson stars are described by the radial function $\Phi(r,t) = \Phi_0(r)e^{i\omega t}$, where ω is the oscillation frequency of the field. Following Ref. [30], we obtain the initial data for a boson star in polar-areal coordinates, for which the line element is given by

$$ds^2 = -\alpha^2(r')dt^2 + a^2(r')dr^2 + r'^2 d\Omega^2 \tag{16}$$

and r' is the radial coordinate. The EKG system for a boson star reads

$$\frac{\partial_{r'}a}{a} = \frac{1-a^2}{2r'} + 2\pi r'\left[\omega^2\Phi_0^2\frac{a^2}{\alpha^2} + \Psi_0^2 + a^2\Phi_0^2\left(\mu^2 + \frac{1}{2}\lambda\Phi_0^2\right)\right], \tag{17}$$

$$\frac{\partial_{r'}\alpha}{\alpha} = \frac{a^2-1}{r'} + \frac{\partial_{r'}a}{a} - 4\pi r' a^2\Phi_0^2\left(\mu^2 + \frac{1}{2}\lambda\Phi_0^2\right), \tag{18}$$

$$\partial_{r'}\Phi_0 = \Psi_0, \tag{19}$$

$$\partial_{r'}\Psi_0 = -\Psi_0\left(\frac{2}{r'} + \frac{\partial_{r'}\alpha}{\alpha} - \frac{\partial_{r'}a}{a}\right) - \omega^2\Phi_0^2\frac{a^2}{\alpha^2} + a^2(\mu^2 + \lambda\Phi_0^2)\Phi_0. \tag{20}$$

By solving these equations, we obtain the spacetime metric potentials, $g_{tt} = -\alpha^2$, $g_{rr} = a^2$, and the radial distribution of the scalar field, Φ_0. The mass of a boson star is computed using the definition of the Misner-Sharp mass function,

$$M_{\rm MS} = \frac{r'_{\rm max}}{2}\left(1 - \frac{1}{a^2(r'_{\rm max})}\right), \tag{21}$$

where $r'_{\rm max}$ is the radial coordinate at the outer boundary of our computational grid. The total mass of a boson star can also be computed using the Komar integral [31],

$$M_{\rm BS} = \int_\Sigma (2T^t_t - T^\alpha_\alpha)\alpha\sqrt{\gamma}drd\theta d\varphi, \tag{22}$$

where Σ is a spacelike slice extending from a horizon, in case one exists, up to spatial infinity. To study the stability properties of the constructed equilibrium models, we need to compute the Noether charge associated with the total bosonic number N, which is defined as

$$N = \int g^{0\nu} j_\nu \alpha\sqrt{\gamma}drd\theta d\varphi, \tag{23}$$

where $j_\nu = \frac{i}{2}(\Phi^*\partial_\nu\Phi - \Phi\partial_\nu\Phi^*)$ is the conserved current associated with the transformation of the U(1) group. Finally, the sign of the binding energy

$$E_{\rm b} = M_{\rm MS} - N\mu \tag{24}$$

will determine the outcome of unstable models.

Representative sequences of equilibrium models of boson stars are plotted in Fig. 1. This figure shows four different mass profiles as a function of the central scalar-field value for four different values of the self-interaction coupling constant, namely, $\Lambda = \{0, 10, 40, 100\}$. For any given Λ, two important points are explicitly indicated in each curve, the maximum mass, marked with a purple square, and the point at which $E_{\rm b} = 0$, marked with a cyan inverted triangle. For each sequence, the location of the maximum mass indicates the critical point separating the stable and the unstable branches. Boson stars situated at the left of the point of maximum mass are stable, while

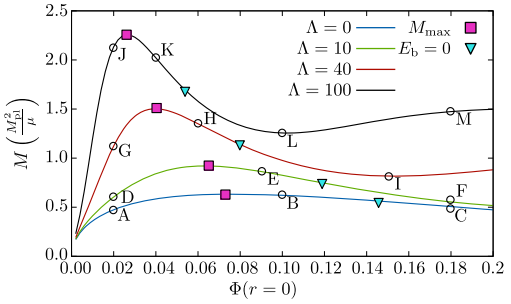

FIG. 1. Boson-star mass as a function of the central value of the scalar field for a few sequences of equilibrium models with $\Lambda = \{0, 10, 40, 100\}$. For each value of Λ, the purple squares indicate the maximum mass of the sequence, separating the stable and unstable branches, and the inverted cyan triangles indicate the point at which the binding energy is zero. The empty circles (and letters) indicate the specific models we evolve in this work.

those on the right are unstable. The maximum mass increases monotically with $\Lambda^{1/2}$ [13]. For sufficiently large values of Λ, the self-interaction term allows for significantly larger masses than for non-self-interacting (mini) boson stars.

We study the stability of these equilibrium models through numerical time evolutions. These are triggered by adding suitable small-amplitude perturbations to the initial data profiles. We consider two types of perturbations, either those associated with the intrinsic truncation error of the finite-difference representation of the Partial Differential Equations we solve or those associated with a functional modification of the actual radial distributions. While the evolutions of the boson stars may seem *a priori* easily predictable, telling from their location with respect to the maximum in the $M_{\rm BS}$ vs $\Phi(r=0)$ diagram, there are other aspects that may affect the actual evolutions to consider. In fact, depending on the sign of the binding energy, the point at which $E_{\rm b} = 0$, and on the perturbation, the stars will undergo different fates. On the one hand, as we show below, an unstable boson star with positive binding energy which is perturbed only with the discretization numerical error migrates to the model with the same mass in the corresponding stable branch. However, if it is perturbed by slightly increasing its mass, it can collapse gravitationally and form a black hole. On the other hand, a boson star with an excess energy, i.e., placed at the right of the zero binding energy point, is no longer bounded, and it will disperse away with time.

The specific boson-star models that we generate and evolve numerically are indicated by the empty circles in Fig. 1. Quantitative details of the main model parameters are reported in Table I. The boson-star initial configurations are built in polar-areal coordinates, but the time evolutions are performed in our code using isotropic coordinates, Eq. (4). To solve this problem, we have to take two steps; see Refs. [13,32]. First, we perform a change of coordinates from polar-areal to isotropic coordinates with

$$r_{\max} = \left[\left(\frac{1+\sqrt{a(r'_{\max})}}{2}\right)^2 \frac{r'_{\max}}{a(r'_{\max})}\right], \tag{25}$$

$$\frac{dr}{dr'} = a\frac{r}{r'}, \tag{26}$$

where Eq. (25) is used as the initial value to integrate Eq. (26) backward. Then, we obtain the conformal factor using

TABLE I. Initial parameters for the bosons stars with $\mu = 1$. Λ is the self-interaction coupling constant, $\Phi(r=0)$ is the central value of the scalar field, R is the radius, $M_{\rm MS}$ is the Misner-Sharp mass, $M_{\rm BS}$ is the scalar-field total mass, N is the bosonic number, E_b is the binding energy, and ω is the frequency. Models A, D, G, and J are stable; models B, E, H, and K can collapse to a black hole or migrate depending on the perturbation; and models C, F, I, L, and M disperse away.

Model	Λ	$\Phi(r=0)$	R	$M_{\rm MS}$	$M_{\rm BS}$	N	$E_{\rm b} = M_{\rm MS} - N\mu$	ω
A	0	0.02	68.79	0.47514	0.47517	0.48197	−0.00683	0.95394
B	0	0.10	32.00	0.62180	0.62029	0.63736	−0.01556	0.82269
C	0	0.18	28.18	0.50671	0.49702	0.47201	0.03470	0.76883
D	10	0.02	64.55	0.60425	0.60429	0.61585	−0.01160	0.94580
E	10	0.09	30.76	0.86314	0.86103	0.89092	−0.02778	0.79838
F	10	0.18	29.61	0.55419	0.53416	0.46712	0.08707	0.81866
G	40	0.02	57.72	1.12319	1.12327	1.16316	−0.03997	0.91481
H	40	0.06	30.39	1.35099	1.35036	1.40322	−0.05223	0.79616
I	40	0.15	33.13	0.81671	0.79145	0.70741	0.10930	0.86111
J	100	0.02	45.77	2.13376	2.13398	2.25789	−0.12413	0.86267
K	100	0.04	29.53	2.02134	2.02138	2.10953	−0.08819	0.79656
L	100	0.10	30.50	1.26039	1.23670	1.14872	0.11167	0.85837
M	100	0.18	30.70	1.47383	1.45448	1.38584	0.08799	0.85576

$$\psi = \sqrt{\frac{r'}{r}}. \tag{27}$$

With this procedure, our initial solution is described in isotropic coordinates, and we can write the initial values of the other scalar-field quantities as

$$\Phi(r, t = 0) = \Phi_0, \tag{28}$$

$$\Psi(r, t = 0) = \Psi_0, \tag{29}$$

$$\Pi(r, t = 0) = i\frac{\omega}{\alpha}\Phi_0. \tag{30}$$

Finally, we interpolate the solution in an isotropic grid employing a cubic-spline interpolation [33] that guarantees the continuity of the second derivative to minimize high-frequency noise associated with the interpolation.

IV. NUMERICAL FRAMEWORK

As in our previous papers, the BSSN evolution equations for the geometry and the evolution equations for the scalar field are solved numerically using a second-order Partially Implicit Runge-Kutta scheme [34]. This scheme can handle in a satisfactory way the singular terms that appear in the evolution equations due to our choice of curvilinear coordinates. Explicit details about our numerical implementation have been reported, e.g., in Ref. [29]. We also note that the convergence properties of our numerical code have been extensively tested before in various physical systems, including the EKG equations with self-interaction; see, e.g., Refs. [5,6,29,35].

In the simulations reported in this work, we consider two computational grids, namely, a grid to obtain the equilibrium models of boson stars in polar-areal coordinates and another one to evolve those models in isotropic coordinates. Our polar-areal grid is an equidistant grid with spatial resolution $\Delta r' = 0.001$ spanning the interval $r' \in [0.0, 150.0]$. On the other hand, our isotropic grid is composed of two patches, a geometrical progression in the interior part up to a given radius and a hyperbolic cosine outside. Using the inner grid alone would require too many grid points to place the outer boundary sufficiently far from the origin (and hence prevent the effects of possible spurious reflections), while using only the hyperbolic cosine patch would produce very small grid spacings in the inner region of the domain, leading to prohibitively small time steps due to the Courant-Friedrichs-Lewy condition. Details about the computational grid can be found in Ref. [6]. In our work, the minimum resolution Δr we choose for the isotropic logarithmic grid is $\Delta r = 0.025$. With this choice, the inner boundary is then set to $r_{\min} = 0.0125$, and the outer boundary is placed at $r_{\max} = 6000$ at the nearest (in some models, it is placed even further away, at $r_{\max} = 10000$). The time step is given by $\Delta t = 0.3\Delta r$ in order to obtain long-term stable simulations.

V. RESULTS

A. Stable models

Models A, D, G, and J in Fig. 1 are all stable models. Therefore, the time evolution of the physical quantities that characterize them, as, e.g., the central value of the scalar field, should remain constant. However, due to the grid discretization error, any of those quantities will instead oscillate around the equilibrium value. This is shown in Fig. 2, where we plot the central value of the scalar field for model A for two different resolutions of the polar-areal grid employed to build the initial data. In this figure, we can also observe how when the resolution of the initial data is reduced from $\Delta r' = 0.01$ to $\Delta r' = 0.001$ the amplitude of the oscillation is significantly reduced. All of our stable initial models are indeed seen to oscillate around the central equilibrium values. For an example of their stability, we plot in Fig. 3 the time evolution of the central scalar field for models A ($\Lambda = 0$) and J ($\Lambda = 100$). Note that the (purely numerical) secular drift of the initial central value of the scalar field of model A apparent in Fig. 3 and hardly visible in Fig. 2 (compare the two blue curves, both corresponding to the model with $\Lambda = 0$) is simply a consequence of the change of scale in the vertical axes of both figures. By Fourier transforming the time evolution of the central value of the scalar field, we obtain the corresponding frequency of oscillation ω of the models. Those values are reported in the last column of Table I. The stable models oscillate with a single fundamental frequency of which the value decreases with increasing Λ.

B. Unstable models

Another possible outcome of the evolution of our initial data is the total dispersion of the boson star or its gravitational collapse. Let us start considering the first possibility. Such an unstable situation will happen when the

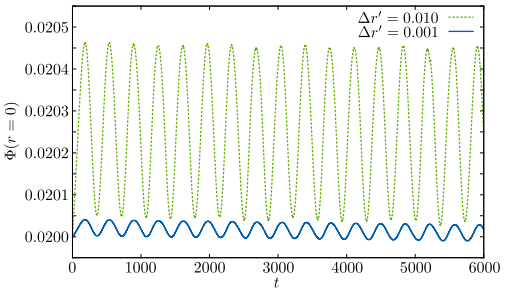

FIG. 2. Time evolution of the central value of the scalar field for boson-star model A [$\Phi(r = 0, t = 0) = 0.02$ and $\Lambda = 0$] for two different resolutions of the initial data grid ($\Delta r'$).

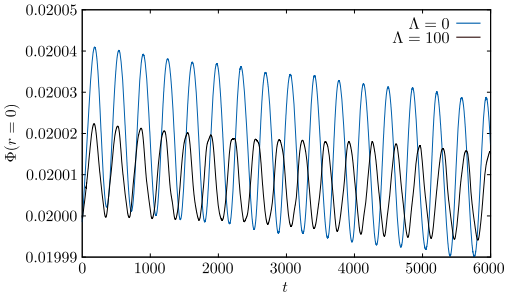

FIG. 3. Time evolution of the central value of the scalar field for a boson star with $\Phi(r=0,t=0)=0.02$ and two different values of the self-interaction coupling constant $\Lambda=\{0,100\}$, corresponding to models A and J, respectively. The evolutions were done with the grid resolution of the initial data $\Delta r'=0.001$.

binding energy is positive since, due to the energy excess, the star will no longer remain bounded. The subset of initial models that can follow this trend are boson stars C, F, I, L, and M in Fig. 1. For an example, we plot in Fig. 4 the radial profiles of the scalar field at selected times of the evolution corresponding to model C (indicated in the legend). In this case, the central value of the scalar field rapidly decreases with time, and the boson star suffers a drastic radial expansion and disperses away. All other unstable models (F, I, L, and M) with a positive binding energy display the same fate.

Let us now consider the evolution of initial models that are located in the unstable branch, i.e., between the critical point (maximum mass of the configuration) and the $E_b=0$ point. These are models B, E, H, and K in Fig. 1. Previous numerical work [20] has shown that the fate of these models is to collapse gravitationally to form a black hole. However, we find that these models can also *migrate* to the stable branch of equilibrium configurations, depending on the perturbation (see also earlier work by Ref. [16]). If the only perturbation of the initial data is the one due to the discretization error, the outcome is a migration to the stable branch. However, if we include a slightly larger perturbation in the initial data, the models collapse to form black holes. The first type of evolution, while mathematically plausible but unlikely on physical grounds, has been previously observed in the case of neutron stars (see Ref. [36] for details and arguments against this evolution), boson stars [16], and, recently, also in the case of unstable Proca stars [23]. A migrating boson star will result in a different boson star. It will have the same mass, but it will be located in the stable branch of the equilibrium configurations (and hence the central scalar field will have a smaller value). As an example, Fig. 5 shows the migration of boson-star models E and K. For model E, the star moves from a central value of the scalar field $\Phi(r=0,t=0)=0.09$ toward a final value of $\Phi(r=0)\sim 0.04$. This is precisely the value for which we obtain a stable boson star with the same mass (cf. Fig. 1). In the bottom panel of Fig. 5, one can also observe that, besides the overall migration, the evolution of model K excites more frequencies of oscillation than that of model E. This behavior is consistent with the fact that model K is "farther away" from its stable partner than model E and hence more perturbed. It also becomes more apparent the larger the value of the

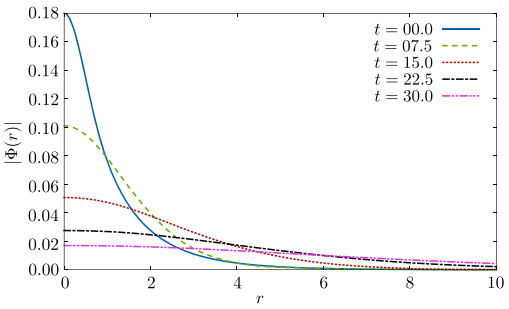

FIG. 4. Radial profile of the scalar-field amplitude for different times, $t=\{0.0,7.5,15.0,22.5,30.0\}$, with $\Phi(r=0,t=0)=0.18$ and $\Lambda=0.0$ corresponding with the C case.

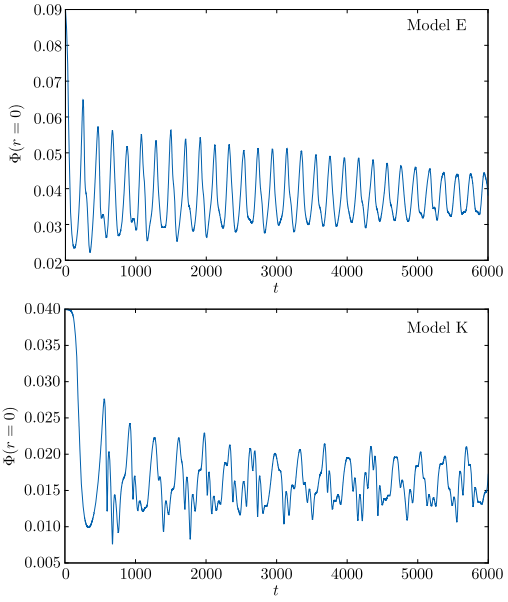

FIG. 5. Time evolution of the central value of the scalar field for the nonperturbed unstable boson-star models E ($\Lambda=10$; top panel) and K ($\Lambda=100$; bottom panel). The stars migrate to the stable branch and oscillate around the value corresponding to models with the same mass.

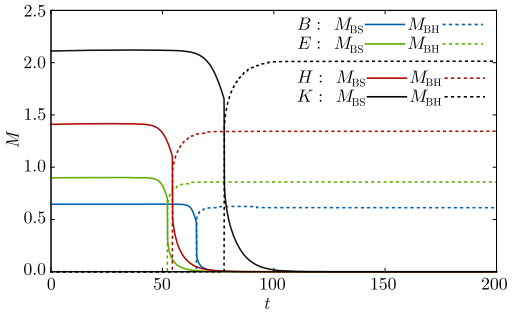

FIG. 6. Time evolution of the scalar-field mass/energy (continuous lines) and the black-hole mass (dashed lines) for the four different unstable models B, E, H, and K after the introduction of a 2% perturbation in the initial data.

self-interaction coupling constant is. We note that a similar coupling between modes was observed in dynamical studies of miniboson stars by Hawley and Choptuik [18]. In such a study, it was noticed that modes with different frequencies appear during the evolution of the boson star due to the nonlinear coupling through the gravitational field.

Let us now consider the evolution of truly perturbed unstable models. To perturb these models, we add an extra 2% value to the initial scalar field by multiplying Φ by 1.02 after solving Eqs. (17)–(20). We have checked by computing the binding energy that the perturbation does not change the sign. We then compute the auxiliary variables given by Eqs. (28)–(30) using the perturbed scalar field. For simplicity, after adding the perturbation, we do not recompute the spacetime variables a and α. This produces a slight violation of the constraints and leads to a small difference between the masses computed with Eqs. (22) and (21) in polar-areal coordinates. However, since the perturbation is fairly small (yet still larger than that associated with the discretization error), it does not substantially alter our original solution.

To diagnose the appearance of a black hole in the evolution, we compute the mass of the black hole through the apparent horizon (AH) area $\mathcal{A}$, using $M_{BH} = \sqrt{\mathcal{A}/16\pi}$. The time evolution of both the scalar-field energy (mass) and the black-hole mass for all unstable models is shown in Fig. 6. The mass of the boson star is computed using the Komar integral, Eq. (22). Contrary to the migrating case, adding a 2% perturbation on the initial data triggers the collapse of the solutions, and at some point in the evolution, an AH forms. This time is indicated in Fig. 6 by the sudden change that is observed in the evolution of the energy of the scalar field, which is associated with the sudden increase of the black-hole mass from a zero value.

Figure 6 shows that, as expected, there is a small difference between the boson-star masses computed with Eq. (22) and the black-hole masses computed through the apparent horizon. This is because some part of the scalar field is released after the collapse. For all models, the black-hole mass is consistently, and slightly, smaller (see Table II). This means that during the collapse to a black hole a remnant of the initial scalar field is not swallowed by the hole but instead lingers around in the form of a spherical shell or cloud. Figures 7 and 8 show the time evolution of the amplitude of the central value of the scalar potential for the four unstable models. This time series is extracted at an

TABLE II. Masses of unperturbed boson stars, M_{BS}; masses of the black holes formed following boson-star collapse, M_{BH}; and frequencies of the scalar-field quasibound states, either computed after black-hole formation, $\omega_{qb}^{(1)}$, or computed from the scattering of a Gaussian pulse, $\omega_{qb}^{(2)}$.

Model	Λ	$\Phi(r=0)$	M_{BS}	M_{BH}	$\omega_{qb}^{(1)}$	$\omega_{qb}^{(2)}$
B	0	0.10	0.62029	0.61271	0.99573	0.99574
E	10	0.09	0.86103	0.85875	0.99274	0.99274
H	40	0.06	1.35036	1.34378	0.98960	0.98960
K	100	0.04	2.02138	2.01382	0.98541	0.98541

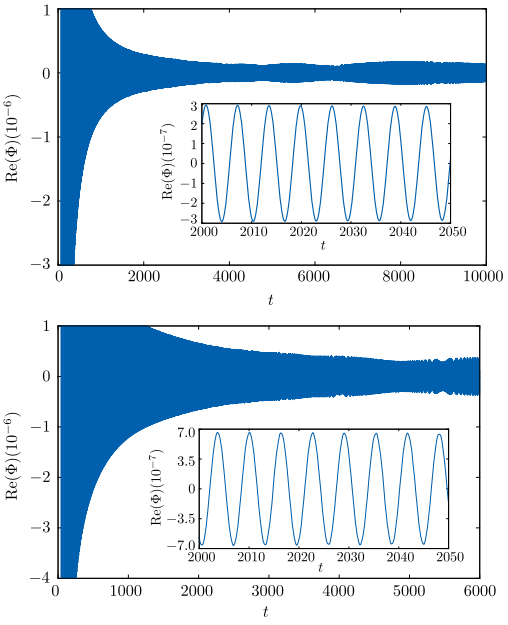

FIG. 7. Time evolution of the real part of the central value of the scalar field for the perturbed boson-star models B (top panel) and E (bottom panel). The insets show a magnified view of $t \in [2000, 2050]$ in the evolution to highlight the oscillatory behavior of the scalar field that lingers outside of the black hole.

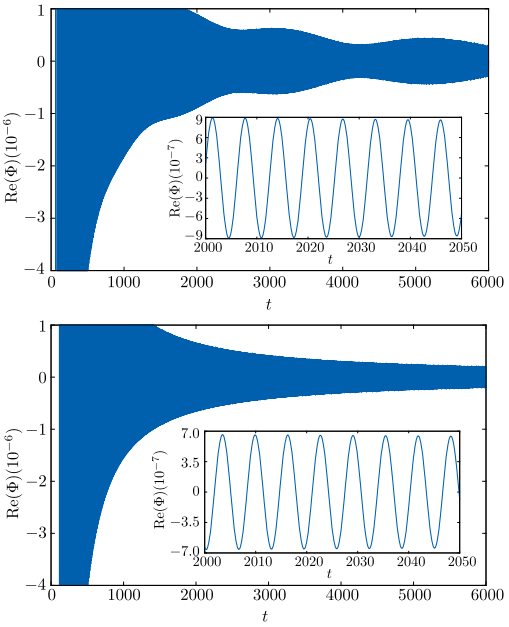

FIG. 8. Same as Fig. 7 but for models H (top panel) and K (bottom panel).

observation point with a fixed radius $r_{\rm obs} = 10$. The scalar field does not disappear after the formation of the AH [which takes place for all models (well) before $t = 100$; cf. Fig. 6], forming instead long-lived quasibound states. For all of the models, the field is seen to be clearly oscillating, as it is best visualized in the insets of the two figures. To identify the frequencies at which the field oscillates, we perform a Fourier transform of the time series and obtain the power spectrum. This power spectrum shows a set of distinct frequencies, as indicated in Table II. Moreover, models B, E, and H, show a distinctive beating pattern due to the presence of overtones of the fundamental frequency.

To compare the frequencies of the scalar clouds resulting from the collapse of boson stars with the known frequencies of quasibound states around Schwarzschild black holes, we consider next a scenario in which initially the black hole is already formed and has the same mass as that formed after the collapse of a boson star. This initial Schwarzschild black hole is surrounded by a Gaussian spherical shell of scalar field which is evolved maintaining the background metric fixed. In this setup, we find that after a short initial transient the field settles down into a long-lived mode akin to the ones shown in Figs. 7 and 8. To characterize this field, we Fourier transform its amplitude to obtain the oscillation frequencies $\omega_{\rm qb}^{(2)}$. The results are shown in the last column of Table II. The excellent

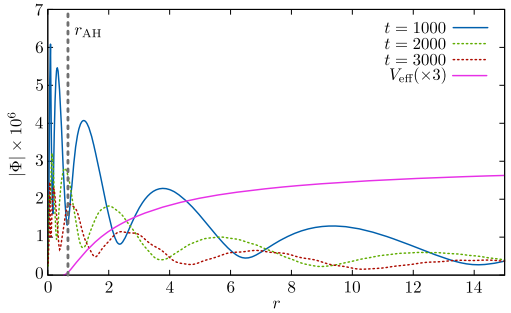

FIG. 9. Scalar-field profile for model E ($\Phi(r = 0) = 0.09$ and $\Lambda = 10.$). The vertical dashed line indicates the position of the AH. The plot also shows the (rescaled) effective potential for a scalar field in the test-field limit in the vicinity of a Schwarzschild black hole. Most of the scalar field remains bounded in a region close to the black hole.

agreement between the frequencies $\omega_{\rm qb}^{(1)}$ computed after black-hole formation and the frequencies $\omega_{\rm qb}^{(2)}$ computed from the Gaussian pulse is a clear indication that the configurations formed after the collapse of boson stars are indeed nonlinear quasibound states.

In Fig. 9, we show the radial profile of model E at various times after the black hole has formed. The plot also shows the effective potential for an equivalent Schwarzschild black hole, assuming the test-field approximation for the scalar cloud,

$$V_{\rm eff} = \left(1 - \frac{2M}{r}\right)\left(\frac{2M}{r^3} + \mu^2 + \lambda|\Phi|^2\Phi\right). \qquad (31)$$

This approximation is consistent with the fact that most of the scalar field is confined between the horizon and the potential barrier.

Finally, to study the effect of Λ on the frequencies and on the time decay of the quasibound states, we perform the same scattering experiment but keep the mass $M_{\rm BH}$ fixed. We find that for sufficiently long times $t \sim 10^5 M_{\rm BH}$ the effect of Λ on the scalar field becomes negligible. This result is expected because the field decays exponentially and the dominating term is the scalar-field mass. Therefore, despite the presence of nonlinear terms in the potential, the frequencies of all quasibound states will eventually tend to that of the quasibound state with $\Lambda = 0$ (for the same black-hole mass). The time scale to reach that situation depends on the value of Λ because the frequency is different for each value of the coupling constant (both the real and imaginary parts). Note that if we rescale the frequencies reported in Table II with the BH mass they do not coincide.

VI. CONCLUSIONS

We have presented a new numerical study of the Einstein-Klein-Gordon system in spherical symmetry. In particular, we have discussed numerical relativity simulations of a large number of initial models of boson stars, both stable and unstable, which incorporate a self-interaction potential with a quartic term. Self-interaction provides extra pressure support against gravitational collapse, increasing the range of possible maximum masses of boson stars, allowing us to encompass models with possibly larger astrophysical significance. We have revisited the stability of the initial solutions for different values of the self-interaction coupling constant Λ, as large as $\Lambda = 100$, not previously considered in the literature (to the best of our knowledge). Our simulations have shown that the three different outcomes for unstable models, namely, migration to the stable branch, total dispersion, and collapse to a black hole, reported before for the $\Lambda = 0$ (mini)boson-star case [16,17,19], are also present for self-interacting boson stars. We have focused our investigation on a subset of collapsing models, studying the effects the self-interaction potential may have in the presence of quasibound states. The existence of such long-lived quasibound states around black holes is supported by increasing numerical evidence, both based on perturbative calculations as on fully numerical relativity [1–7]. Moreover, they have been confirmed in a variety of physical systems, including both static and accreting black holes, and collapsing fermionic stars.

We note that several properties of scalar quasibound states with a mass term around black holes can be obtained studying the system in the frequency domain. The characteristic frequencies of oscillation and half-lives can be calculated using the continued fraction method first used by Leaver [37], the Wentzel-Kramers-Brillouin approximation [38], or the matching of asymptotic solutions [39]. The results obtained with these methods are consistent with the ones obtained in the time domain, as described in Ref. [5]. Furthermore, a comparison with quasibound states with self-interaction can be performed in the test-field approximation when the black hole has settled down, as we showed in Sec. V B.

In summary, in this work, we have revisited the existence of quasibound states in the context of gravitationally unstable boson stars leading to black-hole formation. We have found that for black hole-forming models a scalar-field remnant can indeed be found outside the black-hole horizon, oscillating at a different frequency than that of the original boson star. This result is in good agreement with recent spherically symmetric simulations of unstable Proca stars collapsing to black holes [23].

ACKNOWLEDGMENTS

We thank Carlos Herdeiro and João G. Rosa for useful discussions and comments on the manuscript. We also thank the anonymous referee for his/her helpful comments and suggestions. Work was supported by the Spanish MINECO (Grant No. AYA2015-66899-C2-1-P), by the Generalitat Valenciana (Grants No. PROMETEOII-2014-069 and No. ACIF/2015/216), by the CONACYT Network Project No. 280908 "Agujeros Negros y Ondas Gravitatorias," and by DGAPA-UNAM through Grant No. IA103616. The computations have been performed at the Servei d'Informàtica de la Universitat de València.

[1] H. Witek, V. Cardoso, A. Ishibashi, and U. Sperhake, Phys. Rev. D **87**, 043513 (2013).
[2] J. Barranco, A. Bernal, J. C. Degollado, A. Diez-Tejedor, M. Megevand, M. Alcubierre, D. Núñez, and O. Sarbach, Phys. Rev. D **84**, 083008 (2011).
[3] J. Barranco, A. Bernal, J. C. Degollado, A. Diez-Tejedor, M. Megevand, M. Alcubierre, D. Núñez, and O. Sarbach, Phys. Rev. Lett. **109**, 081102 (2012).
[4] J. Barranco, A. Bernal, J. C. Degollado, A. Diez-Tejedor, M. Megevand, M. Alcubierre, D. Núñez, and O. Sarbach, Phys. Rev. D **89**, 083006 (2014).
[5] N. Sanchis-Gual, J. C. Degollado, P. J. Montero, and J. A. Font, Phys. Rev. D **91**, 043005 (2015).
[6] N. Sanchis-Gual, J. C. Degollado, P. J. Montero, J. A. Font, and V. Mewes, Phys. Rev. D **92**, 083001 (2015).
[7] N. Sanchis-Gual, J. C. Degollado, P. Izquierdo, J. A. Font, and P. J. Montero, Phys. Rev. D **94**, 043004 (2016).
[8] S. L. Detweiler, Phys. Rev. D **22**, 2323 (1980).
[9] S. R. Dolan, Phys. Rev. D **76**, 084001 (2007).
[10] C. A. R. Herdeiro and E. Radu, Phys. Rev. Lett. **112**, 221101 (2014).
[11] D. J. Kaup, Phys. Rev. **172**, 1331 (1968).
[12] R. Ruffini and S. Bonazzola, Phys. Rev. **187**, 1767 (1969).
[13] S. L. Liebling and C. Palenzuela, Living Rev. Relativ. **15**, 6 (2012).
[14] M. Gleiser and R. Watkins, Nucl. Phys. **B319**, 733 (1989).
[15] T. D. Lee and Y. Pang, Nucl. Phys. **B315**, 477 (1989).
[16] E. Seidel and W.-M. Suen, Phys. Rev. D **42**, 384 (1990).
[17] J. Balakrishna, E. Seidel, and W.-M. Suen, Phys. Rev. D **58**, 104004 (1998).
[18] S. H. Hawley and M. W. Choptuik, Phys. Rev. D **62**, 104024 (2000).
[19] F. S. Guzman, Phys. Rev. D **70**, 044033 (2004).
[20] F. S. Guzmán, Revista Mex. Fís. **55**, 321 (2009).
[21] N. Sanchis-Gual, P. J. Montero, J. A. Font, E. Mller, and T. W. Baumgarte, Phys. Rev. D **89**, 104033 (2014).

[22] N. Sanchis-Gual, J. C. Degollado, P. J. Montero, J. A. Font, and V. Mewes, Phys. Rev. D **92**, 083001 (2015).
[23] N. Sanchis-Gual, C. Herdeiro, E. Radu, J. C. Degollado, and J. A. Font, Phys. Rev. D **95**, 104028 (2017).
[24] T. Helfer, D. J. E. Marsh, K. Clough, M. Fairbairn, E. A. Lim, and R. Becerril, J. Cosmol. Astropart. Phys. 03 (2017) 055.
[25] T. W. Baumgarte and S. L. Shapiro, Phys. Rev. D **59**, 024007 (1998).
[26] M. Shibata and T. Nakamura, Phys. Rev. D **52**, 5428 (1995).
[27] M. Alcubierre and M. D. Mendez, Gen. Relativ. Gravit. **43**, 2769 (2011).
[28] P. J. Montero and I. Cordero-Carrion, Phys. Rev. D **85**, 124037 (2012).
[29] N. Sanchis-Gual, J. C. Degollado, C. Herdeiro, J. A. Font, and P. J. Montero, Phys. Rev. D **94**, 044061 (2016).
[30] M. Colpi, S. L. Shapiro, and I. Wasserman, Phys. Rev. Lett. **57**, 2485 (1986).
[31] C. Herdeiro, E. Radu, and H. Rúnarsson, Classical Quantum Gravity **33**, 154001 (2016).
[32] C.-W. Lai, arXiv:gr-qc/0410040.
[33] W. H. Press, S. A. Teukolsky, W. T. Vetterling, and B. P. Flannery, *Numerical Recipes in Fortran* (Cambridge University Press, Cambridge, England, 1992).
[34] I. Cordero-Carrión and P. Cerdá-Durán, *Advances in Differential Equations and Applications*, SEMA SIMAI Springer Series Vol. 4, edited by F. Casas and V. Martínez (Springer, Switzerland, 2014).
[35] N. Sanchis-Gual, J. C. Degollado, P. J. Montero, J. A. Font, and C. Herdeiro, Phys. Rev. Lett. **116**, 141101 (2016).
[36] J. A. Font, T. Goodale, S. Iyer, M. Miller, L. Rezzolla, E. Seidel, N. Stergioulas, W.-M. Suen, and M. Tobias, Phys. Rev. D **65**, 084024 (2002).
[37] E. Leaver, Proc. R. Soc. A **402**, 285 (1985).
[38] R. Konoplya and A. Zhidenko, Rev. Mod. Phys. **83**, 793 (2011).
[39] J. G. Rosa and S. R. Dolan, Phys. Rev. D **85**, 044043 (2012).

PHYSICAL REVIEW D **96,** 104040 (2017)

Lensing and dynamics of ultracompact bosonic stars

Pedro V. P. Cunha,[1,2] José A. Font,[3,4] Carlos Herdeiro,[1] Eugen Radu,[1] Nicolas Sanchis-Gual,[3] and Miguel Zilhão[2,5]

[1]*Departamento de Física da Universidade de Aveiro and Centre for Research and Development in Mathematics and Applications (CIDMA), Campus de Santiago, 3810-183 Aveiro, Portugal*

[2]*CENTRA, Departamento de Física, Instituto Superior Técnico, Universidade de Lisboa, Avenida Rovisco Pais 1, 1049 Lisboa, Portugal*

[3]*Departamento de Astronomía y Astrofísica, Universitat de València, Dr. Moliner 50, 46100, Burjassot (València), Spain*

[4]*Observatori Astronòmic, Universitat de València, C/ Catedrático José Beltrán 2, 46980, Paterna (València), Spain*

[5]*Departament de Física Quàntica i Astrofísica & Institut de Ciències del Cosmos (ICC), Universitat de Barcelona, Martí i Franquès 1, 08028 Barcelona, Spain*

(Received 22 September 2017; published 22 November 2017)

Spherically symmetric bosonic stars are one of the few examples of gravitating solitons that are known to form dynamically, via a classical process of (incomplete) gravitational collapse. As stationary solutions of the Einstein–Klein-Gordon or the Einstein–Proca theory, bosonic stars may also become sufficiently compact to develop light rings and hence mimic, in principle, gravitational-wave observational signatures of black holes (BHs). In this paper, we discuss how these horizonless *ultracompact objects* (UCOs) are actually distinct from BHs, both phenomenologically and dynamically. In the electromagnetic channel, the light ring associated phenomenology reveals remarkable lensing patterns, quite distinct from a standard BH shadow, with an infinite number of Einstein rings accumulating in the vicinity of the light ring, *both inside and outside* the latter. The strong lensing region, moreover, can be considerably smaller than the shadow of a BH with a comparable mass. Dynamically, we investigate the fate of such UCOs under perturbations, via fully nonlinear numerical simulations and observe that, in all cases, they decay into a Schwarzschild BH within a time scale of $\mathcal{O}(M)$, where M is the mass of the bosonic star. Both these studies reinforce how difficult it is for horizonless UCOs to mimic BH phenomenology and dynamics, in all its aspects.

DOI: 10.1103/PhysRevD.96.104040

I. INTRODUCTION

The true nature of astrophysical black hole (BH) candidates has been a central question in relativistic astrophysics for decades. The observational elusiveness of their defining property—the existence of an event horizon—allows the possibility that they may, in reality, be some sort of exotic *horizonless* compact objects, whose phenomenology is sufficiently similar to that of BHs, so that current observations are unable to distinguish these two types of objects.

In this context, the recently opened gravitational-wave window to the Cosmos [1–3], offers a particularly well-suited channel to probe the nature of compact objects. Yet, it has been recently emphasized that observational degeneracy may still remain in this channel [4]. The correspondence between a BH's natural oscillation frequencies (so called quasinormal modes [5]) and light ring (LR) vibrations [6–8], implies that compact objects with a LR—henceforth *ultracompact objects* (UCOs)—but with no event horizon can mimic the initial part of the ringdown gravitational-wave signal of perturbed BHs. Later parts of the ringdown signal may have signatures of the true nature of the object (through the so called *echos* [9,10]), but the corresponding lower signal to noise ratio challenges clean detections of this part of the signal, at least in the near future—see [11–16] for recent discussions.

Is there, consequently, a real risk of observationally mistaking UCOs by BHs and vice-versa, with current and near future gravitational-wave measurements? To address this important question, one should start by revisiting the theoretical foundations of concrete UCOs models. Even though many variants of horizonless UCOs have been proposed in the literature, either as stationary solutions of well-defined models or as more speculative possibilities (see, e.g., [17–22]), they generically suffer from the absence of a plausible formation scenario. An exception, in this respect, are (scalar) boson stars, which, in spherical symmetry, have been shown to form from a process of gravitational collapse, due to an efficient cooling mechanism [23]. Moreover, boson stars are known to become UCOs, in parts of their domain of existence [24].

In this paper, we shall take spherically symmetric scalar boson stars, as well as their vector cousins, dubbed *Proca stars* [22], collectively referred to as *bosonic stars*, as a reference example of horizonless UCOs, and simultaneously as a proof of concept that BH mimickers are

dynamically possible through known physics. We then aim at assessing their quality as BH mimickers by performing the following two inquires: (1) when in the UCO regime, does *all their LR associated phenomenology* mimic that of a Schwarzschild BH? (2) if perturbed, do they really oscillate as a Schwarzschild BH?

Our study reveals that bosonic stars, both the scalar and the vector ones, fail to pass either of these tests. First, the same LR that allows them to, in principle, vibrate as BHs do, gives rise to a quite distinct pattern of light lensing from standard BH shadows. In a sense, the LR associated electromagnetic channel phenomenology raises the degeneracy of the gravitational channel phenomenology. Second, and more importantly, bosonic stars only become UCOs in a regime wherein they are also perturbatively unstable. Thus, the same perturbations that could make them vibrate as a BH will actually induce their gravitational collapse into one. By performing fully nonlinear simulations we show that this is a fast process, and a horizon forms within a few light-crossing times. All together, these results emphasize the difficulty, at least in spherical symmetry, in constructing a reasonable dynamical model of horizonless UCOs whose phenomenology can mimic that of a BH, in all its aspects.

This paper is organized as follows. In Sec. II we review the main physical properties of the ultracompact bosonic stars we shall be analyzing. In Sec. III we shall analyze their lensing, and compare it with that of a Schwarzschild BH. In Sec. IV we consider their behavior under perturbations, following, fully nonlinearly, their evolution and collapse into a BH. In Sec. V we present our final remarks. One Appendix addresses the $3+1$ formalism used in Sec. IV B.

II. ULTRACOMPACT BOSONIC STARS

The ultracompact bosonic stars we shall be considering in this paper are solutions of Einstein's gravity minimally coupled with a spin-s field, with $s=0$, 1. The scalar case was first discussed in [25,26] and it is reviewed in [18]. The vector case was first discussed in [22]. The models are summarized by the action (we use units with $c=1=\hbar$ and $4\pi G=1$)

$$\mathcal{S}=\int d^4x\sqrt{-g}\left[\frac{R}{4}+\mathcal{L}_{(s)}\right], \tag{1}$$

where the two corresponding matter Lagrangians are

$$\mathcal{L}_{(0)}=-g^{\alpha\beta}\bar{\Phi}_{,\alpha}\Phi_{,\beta}-\mu^2\bar{\Phi}\Phi, \tag{2}$$

$$\mathcal{L}_{(1)}=-\frac{1}{4}\bar{\mathcal{F}}_{\alpha\beta}\mathcal{F}^{\alpha\beta}-\frac{1}{2}\mu^2\bar{\mathcal{A}}_{\alpha}\mathcal{A}^{\alpha}. \tag{3}$$

Here, Φ is a complex scalar field and $\mathcal{A}$ is a complex 4-potential, with field strength $\mathcal{F}=d\mathcal{A}$. The overbar denotes complex conjugate and μ is the field's mass. In this paper, the conventions for scalars and vectors are those in [27] (see also [22,28,29]).

We shall be interested in spherically symmetric solutions. They are obtained using the line element

$$ds^2=-N(r)\sigma^2(r)dt^2+\frac{dr^2}{N(r)}+r^2(d\theta^2+\sin^2\theta d\varphi^2), \tag{4}$$

where $N(r)\equiv 1-2m(r)/r$, $m(r)$, $\sigma(r)$ are radial functions and r,θ,φ correspond to Schwarzschild-type coordinates. In particular the radial coordinate r is the geometrically meaningful *areal radius*, meaning that the proper area of a 2-sphere ($rt=$ constant) is $4\pi r^2$. The matter fields ansatz is given in terms of another real function $\phi(r)$ [two real functions $(V(r),H_1(r))$], for the scalar [vector] case:

$$\Phi=\phi(r)e^{-iwt},\qquad \mathcal{A}=\left[iV(r)dt+\frac{H_1(r)}{r}dr\right]e^{-iwt}, \tag{5}$$

where $w>0$ is the frequency of the field. The Einstein-matter equations are solved, numerically, with appropriate boundary conditions. The explicit form of these equations and boundary conditions, together with some examples of profiles of the matter and metric functions can be found in [27] (see also [22] for the Proca case).

In Fig. 1 we exhibit various properties of the scalar (left columns) and vector (right columns) bosonic stars which are relevant for our study. The top panels show the domain of existence of the solutions in an ADM mass, M, *vs*. a bosonic field frequency, w, diagram. Regardless of the spin, the solutions form a characteristic spiralling curve, starting from the Newtonian regime (as $w\to\mu$) wherein the bosonic stars tend to become dilute and weakly relativistic. Following the spiral from this Newtonian limit, the ADM mass reaches a maximum at some frequency. These maximal mass and corresponding frequency are, in units with $\mu=1$, $(M_{\rm max},w[M_{\rm max}])=(0.633,0.853)$ for the scalar case and $(M_{\rm max},w[M_{\rm max}])=(1.058,0.875)$ for the vector case. Perturbation theory computations for both the scalar [30,31] and vector cases [22] have shown that at this point in the spiral an unstable mode develops. More relativistic solutions become perturbatively unstable with different possible fates [32,33]. Further following the spiral, one finds several backbendings, each defining the end of a *branch*. As it can be seen in the inset of the top panels, the solution at which a LR is first seen (marked by a green square—see [24,34,35] for quantitative details) occurs in the third (fourth) branch for the scalar (vector) case, corresponding to $(M_{\rm LR},w[M_{\rm LR}])=(0.8424,0.383)$ for the scalar case and $(M_{\rm LR},w[M_{\rm LR}])=(0.8880,0.573)$ for the vector case. These are highly relativistic solutions, with redshift factors approaching those of an event horizon toward the center of the solutions. In each case, we have highlighted three solutions, denoted 1-3, in the insets of the top panels of Fig. 1, corresponding to the solutions we shall

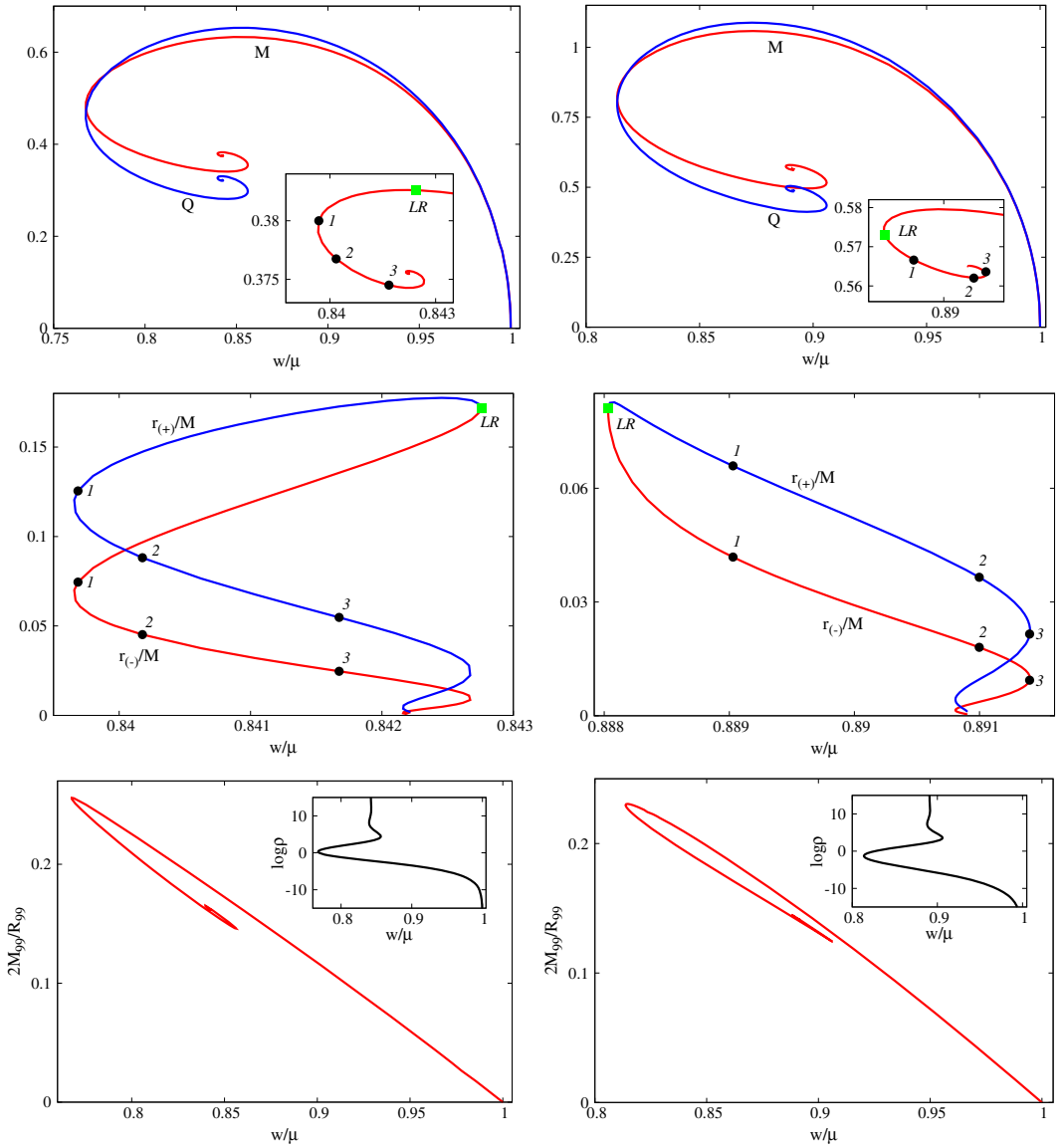

FIG. 1. (Top panels) Domain of existence of scalar boson stars (left) and Proca stars (right) in an ADM mass (M)/Noether charge (Q) *vs*. field frequency, w/μ, diagram. The green square marks the first solution with a LR. The three highlighted points correspond to the configurations we have analyzed in detail, in each case. (Middle panels) Areal radius of the inner r_- and outer r_+ LRs, normalized to the ADM mass, as a function of w, in the region where LRs appear. (Bottom panels) Compactness of the scalar boson stars (left) and Proca stars (right), as measured by $M_{99}/2R_{99}$ (see main text). The inset shows the (log of the) central density. Observe that ρ can get extremely large in the central region, although the solutions will not get more compact, as measured by $M_{99}/2R_{99}$.

TABLE I. Ultracompact bosonic star models.

Model	w/μ	$\mu M_{\rm ADM}$	$\mu^2 Q$	$r_{(-)}/M$	$r_{(+)}/M$
BS1	0.8397	0.3800	0.3274	0.074	0.126
BS2	0.8402	0.3767	0.3235	0.045	0.088
BS3	0.8417	0.3745	0.3209	0.024	0.053
PS1	0.8890	0.5666	0.4899	0.042	0.065
PS2	0.8911	0.5621	0.4849	0.016	0.034
PS3	0.8914	0.5636	0.4866	0.007	0.018

analyze below in more detail. These are ultracompact solutions and their physical properties are summarized in Table I. The top panels of Fig. 1 also show the Noether charge of the solutions, Q (see, e.g., [27] for quantitative expressions), corresponding to a locally conserved charge associated with the global $U(1)$ symmetry of each family of solutions. The ratio Q/M, in units with $\mu = 1$, provides a criterion for stability: $Q/M < 1$ implies excess energy and hence instability against fission into unbound bosonic particles. The point at which, in both cases, solutions have excess (rather than binding) energy occurs close to the minimum frequency, and thus already in the region of perturbative instability.

The middle panels in Fig. 1 exhibit the value of the areal radius of each LR, in units of the ADM mass, and its variation along the ultracompact bosonic star solutions. When the LR first appears in the spiral representing the family of bosonic star solutions it is actually *degenerate*. This solution marks the beginning of the ultracompact bosonic stars. Deeper into the center of the spiral, the bosonic stars have two LRs; in fact, generically, smooth ultracompact objects have an even number of LRs [36]. The outermost one (with radial coordinate $r_{(+)}$, blue line) always corresponds to an unstable photon orbit; the innermost (with radial coordinate $r_{(-)}$, red line) always corresponds to a stable orbit [36]. As the figure shows, the two radial coordinates start to bifurcate from the first ultracompact solution, but then converge again, towards the center of the spiral. Interestingly, the areal radius of the LRs is much smaller than that of a Schwarzschild BH, for which $r/M = 3$. This is associated with the fact these solutions are not constant-density stars, having a much denser central region (inset of bottom panels of Fig. 1). The three chosen solutions are also highlighted in these plots, and the corresponding LRs areal radii are given in Table I.

The bottom panel in Fig. 1 show a measure of the compactness of the bosonic stars. Since these stars have no hard surface, several measures of compactness are possible. In view of their exponential fall-off of the matter density, following, e.g., [28,37], we have defined compactness as the ratio of the Schwarzschild radius for 99% of the mass, denoted $2M_{99}$, to the areal radius that contains such mass, R_{99}. This quantity would be unity for a Schwarzschild BH. Here we see that the compactness increases from the Newtonian limit until the first back bending, but it decreases along the second branch. Then it increases along the third branch. Such compactness is not a monotonic function along the spiral and indeed the ultracompact solutions—in the sense of possessing a LR—are not the most compact ones, according to this definition. On the other hand, the central value of the energy density (see, e.g., [27] for quantitative expressions) is indeed a monotonically increasing function along the spiral, as shown in the inset of these plots. This behavior, together with the location of the LRs, show that for nonconstant density stars, like these bosonic stars, a global measure of compactness, such as $2M_{99}/R_{99}$, may be misleading, as the star may have a considerably denser central region, which is ultracompact, whereas the star as a whole is not.

III. LENSING

LRs are bound planar photon orbits (see [35] for a general discussion of bound photon orbits). Their existence around a compact object implies strong lensing effects. For the Schwarzschild BH, the LR occurs at an areal radius $r = 3M$ and it is an *unstable* photon orbit. Thus, scattering photons with an impact parameter ($\eta = L/E$, where E, L are the photon's energy and angular momentum, respectively) larger than (in modulus) that of the LR, η_{LR}, return to spatial infinity; but, when η is close to η_{LR}, $|\eta| \gtrsim |\eta_{LR}|$, the scattering angle can be arbitrarily large, in the sense that the photon may circumnavigate the BH an arbitrary number of times before bouncing back to infinity. If $|\eta| < |\eta_{LR}|$, on the other hand, the photon will end up falling into the BH. Thus the LR, defines an absorption cross section for light, the *BH shadow* [38,39]. This is a timely observable, due to ongoing attempts to measure the BH shadow of two supermassive BHs, by the Event Horizon Telescope [40,41].

In Fig. 2 (left panel) the BH shadow and lensing due to a Schwarzschild BH is shown. The setup is the one introduced in [42] and used by some of us in [24,34,35], wherein the numerical ray-tracing method is also described. In a nutshell, light emanates from a far away celestial sphere that is divided into four quadrants, each painted with one color (yellow, blue, green red). Black constant latitude and longitude lines are also drawn in the light-emitting celestial sphere. The observer is placed off-center, within the celestial sphere at some areal radius $r_{\rm obs}$. Directly in front of the observer, there is a point in the celestial sphere where the four quadrants meet, which is painted in white and blurred. The Schwarzschild BH is placed at the center of the celestial sphere.

The left panel of Fig. 2 has a few distinctive features. The white circle is the lensing, due to the BH, of the celestial sphere's white dot, which would be right in front of the observer if the BH would not be in the line of sight. It is an *Einstein ring* [43]—see [44] for an historical account of the prediction of multiple images of a source due to gravitational lensing. The black central disk is the BH shadow, whose edge corresponds to photons that skim the LR.

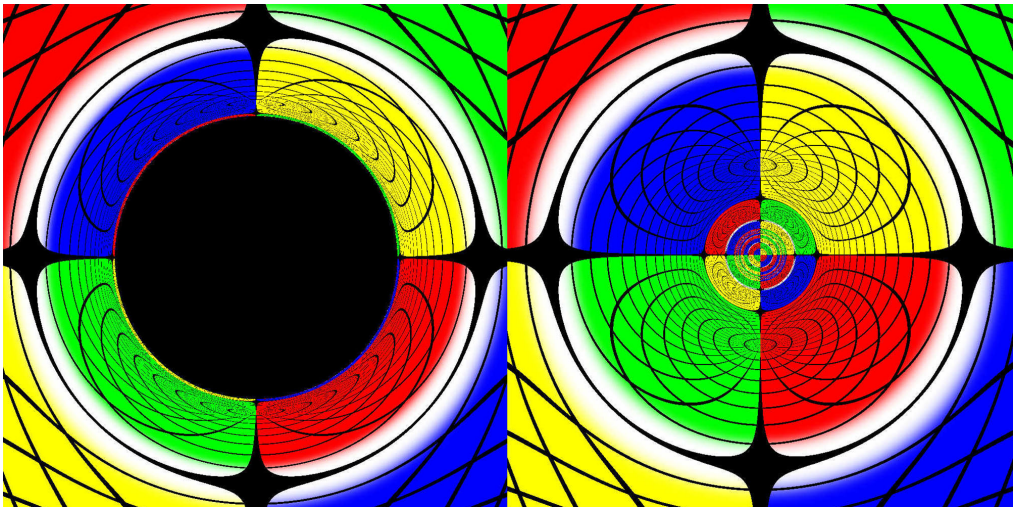

FIG. 2. Lensing and shadow of a Schwarzschild BH (left panel) and a comparable bosonic star (right panel, model PS2), in similar observation conditions, for which the observer is set at $r_{\rm obs} = 15M$. The Einstein ring has a similar dimension (white lensed region), but the strongly lensed region—shadow and near its edge for the BH vs. central rings for the star—is much smaller for the star.

In between this edge and the Einstein ring there are infinitely many copies of the celestial sphere, that accumulate in the neighbourhood of the shadow's edge, in a self-similar structure [42]. In the image only two of these copies are clearly visible.

The right panel of Fig. 2 shows the lensing pattern due to a bosonic star, model PS2, under similar observation conditions, i.e., and observer placed at the same $r_{\rm obs}$ and the BH replaced by the star at the center of the celestial sphere. Since the g_{tt} component of the metric is very close to zero within the star region, the numerical integration of the null geodesics is quite demanding. This issue is tamed by performing a conformal transformation to a spacetime with less extreme redshift factor, since such transformation leaves invariant null geodesic paths. This is an efficient procedure. We have checked different conformal transformations lead to the same image, validating the method.

Comparing the left and right panels of Fig. 2, leads to two main conclusions. First, the Einstein ring has a similar dimension. Since there is only one scale for either solution —the total mass—similar observation conditions imply the lensing is due to objects with the same total mass. This explains the same overall (weak) light bending that originates the Einstein ring. Second, the strong lensing region, which is due to photons with $\eta \sim \eta_{LR}$, is smaller for the star. This is a consequence of the smaller LRs, cf. the previous section: for ultracompact bosonic stars they occur at an areal radius $\ll 3M$.

The lensing for the six selected models of ultracompact bosonic stars (cf. Table I) is qualitatively similar. In Fig. 3 (left panel), we exhibit the one for model BS1, under similar observation conditions $r_{\rm obs} = 15M$ as the one for PS2 shown in the right panel of Fig. 2. As expected the Einstein ring has a similar scale, but the strong lensing region is smaller for the Proca star, which is, qualitatively, in agreement with its smaller (outer) LR. It is important to emphasize, however, that the angular size in the image is determined by the LR's impact parameter, and not by its areal radius [45].

The right panel of Fig. 3 shows a zoom of the left panel, around its central region. Circles, which are Einstein rings, are the lensing images of either the celestial sphere point in front of the observer (white circles) or the one behind the observer (black circles). These two types of circles alternate and appear to accumulate at a given angular radius. This can be confirmed in Fig. 4 (main panel), which displays the initial angle (which one can regard as the radial coordinate in the lensing images) vs. the scattering angle, i.e., the final angle in the celestial sphere. The scattering angle is here taken to be zero at the white dot of the celestial sphere (directly on the observer's line of sight, if the geometry were flat). Hence, multiples of 2π signal the formation of a white circle in the image, which can be seen by the horizontal dashed lines in Fig. 4. The peak on the plot is the finger print of the unstable LR. Had this been a BH, instead of a bosonic star, the left part of the peak would not exist, as it would correspond to the shadow. The region in between each consecutive black and a white circles in Fig. 3, contains a copy-image of the full celestial sphere. As familiar from particle physics/quantum mechanics, the

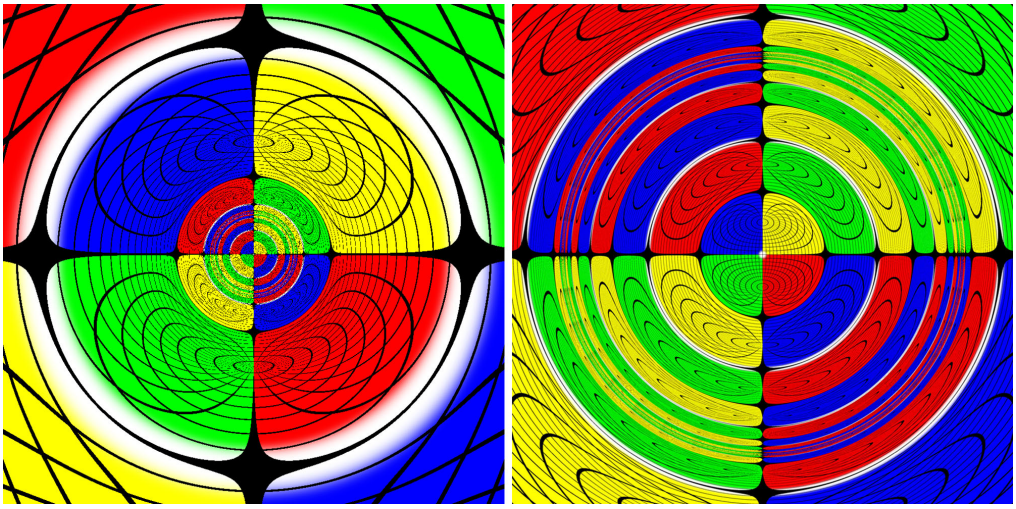

FIG. 3. Lensing by the boson star model BS1 (left panel) and a zoom around the strong lensing region (right panel).

outermost (unstable) LR, which is a bound state, appears as a pole in the scattering amplitude—Fig. 4.

The scattering angle divergence near the LR is logarithmic. This allows us to write the impact parameter of the Einstein ring of order k, corresponding to a scattering angle of $2\pi k$ as

$$\eta_{\rm ER}^{(k)} = \eta_{\rm LR} + be^{-2\pi k/a}, \tag{6}$$

where a, b are constants, the value of which depends on the LR being approached with values of η above or below $\eta_{\rm LR}$. Fig. 4 (inset) shows this relation is a good approximation to the numerical values, even for the lowest order Einstein rings.

Whereas the LR is not emphasized in the plots in Figs. 2 and 3, it stands out if instead we plot the *time delay function*. This function is defined as the variation of the coordinate time t, in units of M, required for the photon geodesic emanating from a particular pixel to reach a corresponding point on the celestial sphere [34]. This is a good diagnosis of the LR since photon trajectories that

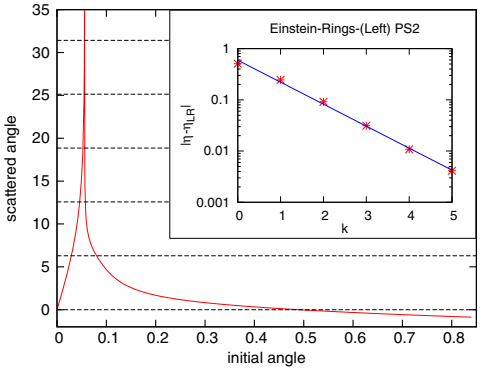

FIG. 4. (Main panel) Scattering angle vs. initial angle for the scattered photons in model PS2. (Inset) Value of $|\eta_{\rm ER}^{(k)} - \eta_{\rm LR}|$ given by Eq. (6) (blue solid line) vs. numerical values (star-like points) for the first five Einstein rings in model PS2.

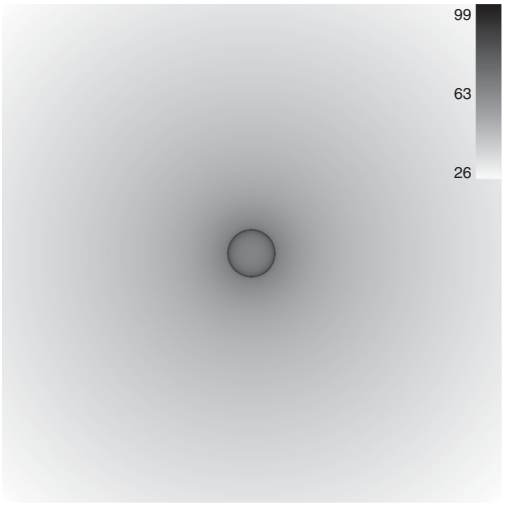

FIG. 5. Time delay heat map for model PS2.

skim the LR take much longer to return to spatial infinity. In Fig. 5 the time delay for model PS2 is portrayed as a heat map with the corresponding scale on the right of the image indicating the variation of the coordinate time (in units of M) for each photon to travel from the camera to the celestial sphere. The LR clearly stands out (compare with Fig. 2, right panel).

Figure 5 shows that UCOs like bosonic stars—made of dark matter that only affect light through the spacetime geometry—have a ring-like darker region, rather than a disklike shadow. Of course, it is possible that in a more realistic astrophysical environment, with an accretion disk light source, the whole central region becomes an effective shadow, cf. [46]. Likely, this depends on the accretion modeling and, in any case, this effective shadow will be considerably smaller than that of a comparable Schwarzschild BH.

Let us close this section by remarking that the innermost (stable) LR plays no significant role in the photon scattering problem we have just analyzed, but it potentially impacts in the spacetime stability [36,47,48].

IV. NONLINEAR EVOLUTIONS

We now turn to the dynamical evolution of ultracompact bosonic stars. As already mentioned, ultracompactness only occurs in the region of perturbative instability, for the model of bosonic stars we are analyzing. Thus, it is not surprising that these models evolve into different configurations when perturbed. As we shall see in the evolutions presented here, ultracompact bosonic stars decay into BHs, which is one of the possible fates already seen for unstable, but not ultracompact, bosonic stars [32,33]. The simulations herein, moreover, allow us to: (1) establish this is a more generic fate in the ultracompact case; (2) observe the timescale for the collapse, which turns out to be a short one. A different interesting question, which we shall not address herein since it is not the case for the solutions we are studying, is if there are any bosonic stars models, say, including rotation or self-interactions, for which ultracompact bosonic stars are perturbatively stable.

In the following we shall first consider the vector case and then, more briefly, the scalar case. Our numerical evolutions employ a Cauchy approach. We introduce the $3+1$ decomposition of all dynamical quantities in the standard fashion (see, e.g., [49–51] for details). Concretely, we introduce the 3-metric

$$\gamma_{\mu\nu} = g_{\mu\nu} + n_\mu n_\nu, \tag{7}$$

where n^μ denotes a timelike unit vector with normalization $n^\mu n_\mu = -1$. The full spacetime metric $g_{\mu\nu}$ can then be expressed as

$$\begin{aligned} ds^2 &= g_{\mu\nu}dx^\mu dx^\nu \\ &= -(\alpha^2 - \beta^i\beta_i)dt^2 + 2\beta_i dt dx^i + \gamma_{ij}dx^i dx^j, \end{aligned} \tag{8}$$

where the lapse function α and shift vector β^i describe the coordinate degrees of freedom.

A. Proca stars

In the Proca case, the evolutions have been performed using the same code and setup employed in [33], where we have also addressed spherical Proca star evolutions, albeit non-ultracompact. The Einstein-Proca equations are formulated in the BBSN approach [52,53] and the usual choice of $1+\log$ slicing condition and Gamma-driver shift conditions is made for the gauge equations. The code solves the evolution equations in spherical symmetry using spherical polar coordinates and a second-order partially implicit Runge-Kutta (PIRK) method [54,55].

Following [33,56], the Proca field is split into its $3+1$ variables, namely its scalar potential Φ, 3-vector potentials a_i and three-dimensional "electric" $\mathbf{E}$ field. From the ansatz (5), the initial value for the Proca field variables is given as follows:

$$\Phi = -n^\mu \mathcal{A}_\mu = -i\frac{V}{\alpha}, \tag{9}$$

$$a_i = \gamma_i^\mu \mathcal{A}_\mu = \frac{H_1}{r}, \tag{10}$$

$$\begin{aligned} E^i &= -i\frac{\gamma^{ij}}{\alpha}\left(D_i(\alpha\Phi) + \partial_t a_j\right) \\ &= i\frac{\gamma^{rr}}{\alpha}\left(D_r V + w\frac{H_1}{r}\right). \end{aligned} \tag{11}$$

Further details on the Einstein-Proca system can be found in [33,56].

For all evolutions presented herein, we have used the same logarithmic radial grid that extends from the origin to $r = 50$. We choose a time step of $\Delta t = C\Delta r$, where C is the Courant factor. For the ultracompact models, the minimum resolution close to the origin is $\Delta r = 0.0004$ and a Courant factor of $C = 0.4$ for models PS1 and PS2, and $\Delta r = 0.0002$ and $C = 0.8$ for PS3. It is worth pointing out the difficulty in performing long-term stable evolutions of these ultra-compact models as compared to the previous ones of [33], due to the extreme accuracy requirements close to the origin. The minimum radial step and time step are two orders of magnitude smaller than in [33], which involves a significant amount of computational time, even in spherical symmetry.

Figure 6 shows some of the main results concerning the evolutions of the models PS1-PS3. In the top panel of Fig. 6 we exhibit the time evolution of the Proca field energy $E_{\rm PF}$ (see Eq. (32) in [33]) and the irreducible mass of the

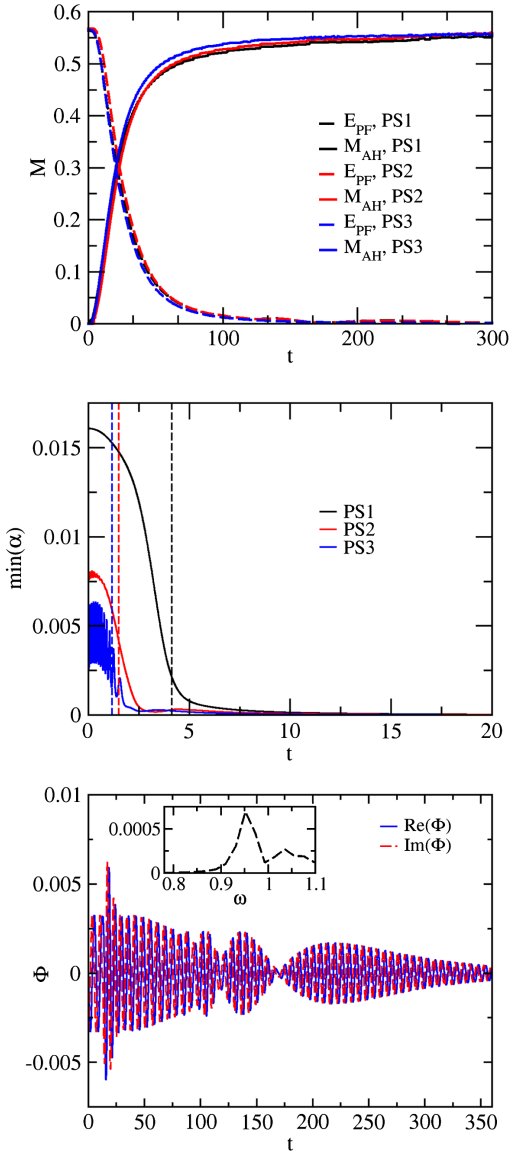

FIG. 6. (Top panel) Time evolution of the Proca field energy and AH mass for models 1, 2 and 3. (Middle panel) Time evolution of the minimal value of the lapse for all models. (Bottom panel, main) Time evolution of the amplitude of the scalar potential extracted at some point outside the horizon for model PS2. The inset shows the oscillation frequencies.

apparent horizon (AH), once the latter forms in the evolutions. The figure shows that for all three models, the discretization error of the numerical solution is sufficient to perturb the initial configurations and trigger the collapse of the ultra-compact Proca stars into BHs. At an early time in the evolution an AH forms. This is confirmed in the middle panel, where the commencing time evolution of the minimum of the lapse function is shown. This so-called "collapse-of-the-lapse" is a distinctive feature of AH formation. The time coordinates for which those three AHs are found, computed using the AH finder implemented in the code of [33], are indicated by the three vertical dashed lines in the middle panel of the figure. The corresponding times are ($t_{\rm PS1} = 4.122$, $t_{\rm PS2} = 1.502$, $t_{\rm PS3} = 1.178$) in units of $1/\mu$. As expected, the time scales of AH formation are smaller than those obtained for the much less compact models in [33]. The same trend we found in our previous work is also present in the ultracompact case—the more compact the model, the faster the AH appears.

Following AH formation, the Proca field energy evolves toward being absorbed by the Schwarzschild BH, but within the timescale of our simulations some matter field energy remains outside the horizon. This is confirmed in the bottom (main) panel of Fig. 6, wherein we exhibit the time evolution of the amplitude of the scalar potential at some extraction radius outside the horizon and for model PS1. The main plot shows that, when the BH forms, a part of the Proca field remains outside the horizon, with the real and imaginary parts oscillating with opposite phase. These are quasi-bound states of the Proca field around a Schwarzschild BH [33,56,57]. Moreover, a beating pattern can be observed, a hint that more than one quasibound state of the Proca field is present outside the Schwarzschild BH. The corresponding frequencies of oscillation, obtained by Fourier-transforming the time evolution in the main panel, are displayed in the inset.

In order to assess the accuracy of our nonlinear evolutions we have also performed a convergence test analysis for the Gauss constraint and the Hamiltonian constraint. The results are shown in Fig. 7 for model PS1. For both constraints we obtain the theoretical second-order convergence of the code.

To end this section, we comment that we have also evolved the ultracompact Proca stars with an added perturbation, instead of relying solely on the discretization numerical error to trigger the nonlinear dynamics. In [33] we observed this could change the fate of the star. For instance, by multiplying the Proca field by a number slightly smaller than one (namely 0.98), therefore introducing a constraint-violating perturbation, we noticed that the fate of the star could change from collapsing into a BH to either migrating or dispersing (see Table III in [33]).

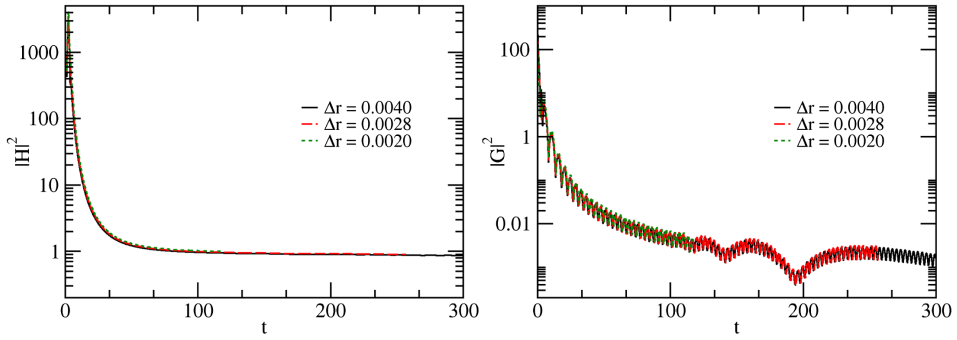

FIG. 7. Convergence analysis for model PS1 employing three different resolutions: $\Delta r = 0.0004$, black curves, $\Delta r = 0.0004/\sqrt{2}$, red curves, and $\Delta r = 0.0004/2$, green curves. Left panel: L2 norm of the Hamiltonian constraint. Right panel: L2 norm of the Gauss constraint. The curves have been conveniently rescaled for second-order convergence, hence the overlapping.

In the present case of ultra-compact stars, however, even when multiplying the initial Proca field by 0.9, the final fate of the nonlinear dynamics is still gravitational collapse. This shows that ultra-compact bosonic configurations are much more prone to rapidly decay into a Schwarzschild BH, confirming our naive intuition.

B. Boson (scalar) stars

In the scalar case we use a completely independent numerical code and computational infrastructure. The code employed for the numerical evolutions makes use of the EinsteinToolkit infrastructure [58–60], which uses the Cactus Computational Toolkit [61], a software framework for high-performance computing. Mesh-refinement capabilities are handled by the Carpet package [62,63] and AHs are tracked with AHFinderDirect [64,65]. The evolution of the spacetime metric is handled by Lean, originally presented in [66] for vacuum spacetimes. Matter terms are here coupled straightforwardly using a separate thorn within the Cactus framework.

As in the code of [33] employed in the Proca case, Lean also uses the BSSN formulation of the Einstein equations [52,53] with the moving puncture method [67,68] and the usual $1+\log$ slicing condition and Gamma-driver shift conditions for the gauge equations. We employ the method-of-lines, where spatial derivatives are approximated by fourth-order finite difference stencils, and we use the fourth-order Runge-Kutta scheme for the time integration. Kreiss-Oliger dissipation is applied to evolved quantities in order to damp high-frequency noise.

Some details about the $3+1$ decomposition of the Einstein-Klein-Gordon equations are presented in Appendix A. Note that, whereas the code used for the evolutions of Sec. IV A is a $1+1$ spherically-symmetric code, the one presented here evolves a three-dimensional grid. This makes the numerical evolutions much more time-consuming. For these evolutions we have used an octant Cartesian grid extending from the origin to $x^i = 20$ ($x^i = x$, y, z, and we use units where we fix $\mu = 1$) with 12 refinement levels. Resolution at the innermost refinement level was chosen to be $\Delta x^i = \frac{0.25}{2^{11}} \simeq 0.000122$ and time step $\Delta t = 0.4\Delta x^i$. Such high resolution is needed to properly resolve the very steep gradients close to the origin due to the high compactness of the star. The spatial discretization is therefore two orders of magnitude smaller than the typical one used for instance in [56], making these evolutions extremely time-consuming.

The results in the scalar case mimic closely the ones in the Proca case, despite the different spin of the fundamental field that constitutes the star and the different code/computational infrastructure used in the solutions, showing the robustness of the conclusions. In Fig. 8 we exhibit analogous plots, in the scalar case, to those shown in Fig. 6 for the Proca case. In the top panel of Fig. 8 we show the time evolution of the scalar field energy E_Φ, computed as

$$E_\Phi \equiv \int_{r>r_{\rm AH}} dxdydz\alpha\sqrt{\gamma}(T^i_i - T^t_t), \tag{12}$$

and the irreducible mass of the AH, once the latter forms in the evolution for model BS2. Again, the discretization error of the numerical solution is sufficient to trigger the collapse of the ultracompact scalar star into a BH. At an early time in the evolution an AH forms ($t_{\rm BS2} \approx 7.5$), which is marked by the red vertical dashed line in the plot. The formation of the horizon is again confirmed in the middle panel, where the time evolution of the minimum of the lapse function is shown. As for the Proca models, the minimum of the lapse function in the scalar case also tends to zero, signalling AH formation. Likewise, following AH formation, the scalar-field energy is increasingly absorbed by the Schwarzschild BH, but, as in the Proca case, some of the energy remains outside the horizon within the timescale of our simulations. This is confirmed in the bottom panel of Fig. 8, wherein we

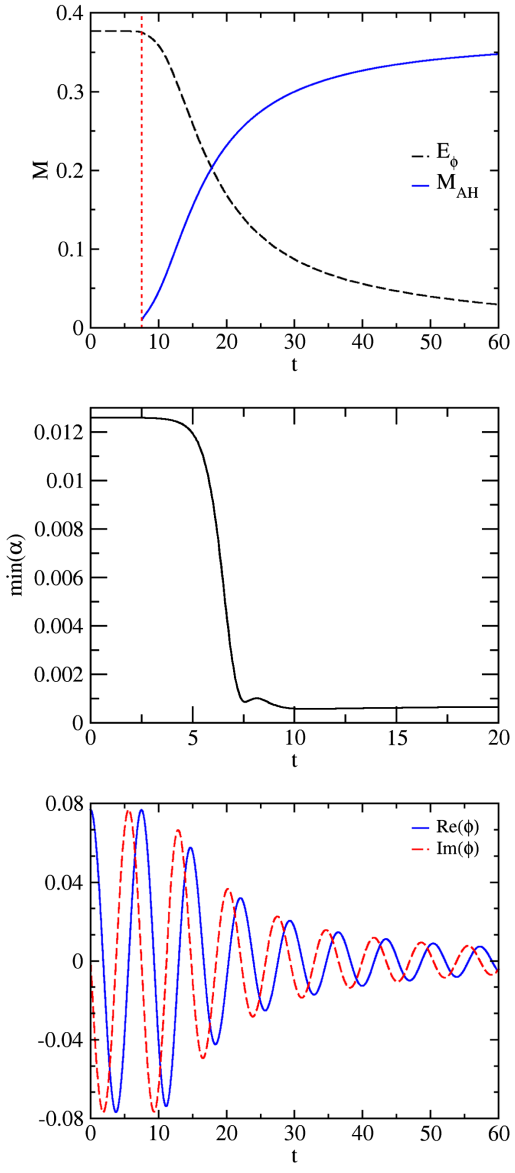

FIG. 8. (Top panel) Time evolution of the scalar-field energy and AH mass for model BS2. (Middle panel) Time evolution of the minimal value of the lapse for the same model. (Bottom panel) Time evolution of the real and imaginary part of the scalar field at a point outside the horizon.

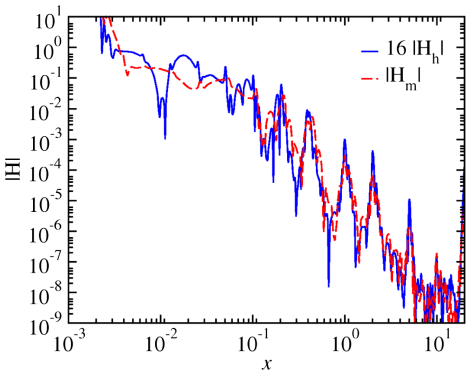

FIG. 9. Hamiltonian constraint violation at $t = 10$ along the x-axis. The resolution at the innermost refinement level for the red curve is $\Delta x^i = 0.000244$, whereas for the blue curve $\Delta x^i = 0.000122$ was used. The blue curve has been multiplied by 16, the expected factor for fourth-order convergence.

display the time evolution of the scalar field at some extraction radius outside the horizon. The real and imaginary parts oscillate with opposite phase corresponding to a quasi-bound start of the scalar field.

As we did in Sec. IV A for the Proca case, we also assess the code employed in the 3D simulations of spherical (scalar) boson stars presented in this section. To this aim we show in Fig. 9 the results of a convergence analysis on the Hamiltonian constraint violation at $t = 10$ along the x-axis. As expected, we observe the theoretical fourth-order convergence of our code.

Let us conclude this section by remarking that, since these simulations are computationally very demanding, and take a very long time, we have only evolved models BS1 and BS3 up to horizon formation. We anticipate their dynamics is identical to that of model BS2.

V. CONCLUSIONS AND FINAL REMARKS

The dawn of the era of gravitational-wave astronomy [1–3] promises to deliver detailed information about the nature of very compact objects in the Universe. The standard paradigm is that these are either BHs or neutron stars, but one cannot exclude, *a priori*, the possibility that other compact objects, of an even more exotic nature, may hide in the Cosmos.

Intriguingly, it has been recently pointed out that the gravitational-wave ringdown of a horizonless UCO could be identical, at least in its initial stages, to that of a BH, since such ringdown stage is a signature of a LR, rather than of a horizon [4]. Is therefore a risk of observationally

mistaking UCOs by BHs and vice-versa, with current and near-future gravitational-wave measurements?

In this paper we have tackled this question by considering a concrete UCO model. We have analyzed some of the LR associated phenomenology of a class of exotic compact objects: scalar and vector boson stars. On the one hand, such compact objects are known to form from an incomplete gravitational collapse, and, at least in spherical symmetry, this formation is quite generic [23]. This contrasts with other UCO models proposed in the literature, for which no detailed formation scenario is known. On the other hand, within the family of solutions of these objects, some are ultra-compact, i.e., they develop a LR. Since the spacetime geometry and matter field distribution for these bosonic stars are explicitly known they yield a privileged model to study the phenomenology of an UCO.

We have first analyzed the lensing of light by the ultracompact bosonic stars. Here, we have assumed that the scalar or vector matter (they are made of) interact very weakly with light, and thus the propagation of light is simply determined as the geodesic flow of the spacetime geometry. In other words, these bosonic stars are made of dark matter and thus they are permissive to electromagnetic radiation. Our analysis leads to two main conclusions, which are transversal to all explicit examples we have analyzed. First, the UCO produces no shadow, in contrast to a BH. Rather, it produces an annulus of darkness, associated to photon trajectories that come close to the LR and therefore take an arbitrarily long time to escape. This annular-like shadow, however, may be blurred into an apparent disk-like shadow, in an astrophysical context. Thus, this property, albeit a clear theoretical distinction from what happens for a BH, may not be a robust observable signature. Second, for comparable objects, the weak lensing region of the bosonic star and the BH is similar (measured, say, by the outermost Einstein ring), but the strong lensing region of the star is considerably smaller than that of a BH, under similar observational conditions. Thus, an ultracompact bosonic star and a Schwarzschild BH with the same mass, observed at a similar distance, will be distinguishable. That is, even if the lensing of the bosonic star produces an effective disklike shadow, due to the blurring of the annulus-like strong lensing region, this disk is considerably smaller than that of the shadow of the comparable Schwarzschild BH (e.g., ~ 6 times smaller for model PS2). Thus, it seems that even if the existence of a LR for a horizonless object can mimic a part of its gravitational wave relaxation signal, it does not mimic (simultaneously), its electromagnetic phenomenology.

After analyzing the lensing of light we have considered the dynamics of a perturbed ultracompact bosonic star. It was clear from the outset that, when in the ultracompact regime, the bosonic stars of the model we are considering (sometimes called mini-boson stars in the scalar case [18]) are unstable. Our fully nonlinear numerical simulations have allowed us to establish two conclusions about their fate. First, they collapse into a BH and this is a quite robust fate. That is, even varying the perturbation, which for less compact stars could change their fate into a migration or dispersion [33], ultracompact stars still collapse into a BH. Second, the collapse is fast, occurring within a few light crossing times.

Overall, the two aspects analyzed in this paper (lensing and dynamics) of this model of UCOs, emphasizes that it is quite challenging for a UCO model to mimic all the phenomenology and dynamics of a BH, at least in spherical symmetry, even if it can mimic some of it (like its ringdown). It would be quite interesting to see if by changing the model of bosonic stars, e.g., by introducing self-interactions or rotation, the conclusions we have obtained herein for the spherically symmetric mini-bosonic stars change.

Finally, we would like to emphasize that the UCOs we have considered actually possess two LRs. The phenomenology described herein is associated with the outermost unstable one. But the existence of an innermost stable one also may have important dynamical consequences, in particular with respect to the spacetime stability [47,48]. It has been recently proven [36] that for generic horizonless UCOs forming smoothly from incomplete gravitational collapse, within physically reasonable models, this stable LR is always present, and therefore the instability it may trigger, again challenging the possibility of physically realistic horizonless UCOs in the Universe.

ACKNOWLEDGMENTS

P. C. is supported by Grant No. PD/BD/114071/2015 under the FCT-IDPASC Portugal Ph.D. program. M. Z. acknowledges support by the ERC Starting Grant No. HoloLHC-306605 and FCT (Portugal) IF programme IF/00729/2015. This work has been supported by the Spanish MINECO (Grant No. AYA2015-66899-C2-1-P), by the Generalitat Valenciana (PROMETEOII-2014-069, ACIF/2015/216), by the FCT (Portugal) IF programme, by the CIDMA (FCT) Strategic Project No. UID/MAT/04106/2013 and by the European Union's Horizon 2020 research and innovation programme under the Marie Sklodowska-Curie Grant Agreement No. 690904 and by the CIDMA Project No. UID/MAT/04106/2013. Computations have been performed at the Servei d'Informàtica de la Universitat de València, at the Blafis cluster at the University of Aveiro and at the Baltasar cluster at IST. We would like to acknowledge networking support by the COST Action GWverse CA16104.

APPENDIX: 3+1 DECOMPOSITION FOR THE EINSTEIN-KLEIN-GORDON SYSTEM

Let us briefly present the $3+1$ decomposed equations of motion in the Einstein-Klein-Gordon case. To complete the

characterization of the full spacetime we define the extrinsic curvature

$$K_{ij} = -\frac{1}{2\alpha}(\partial_t - \mathcal{L}_\beta)\gamma_{ij}, \tag{A1}$$

and analogously introduce the "canonical momentum" of the complex scalar field Φ

$$K_\Phi = -\frac{1}{2\alpha}(\partial_t - \mathcal{L}_\beta)\Phi, \tag{A2}$$

where $\mathcal{L}$ denotes the Lie derivative. Our evolution system can then be written in the form

$$\partial_t \gamma_{ij} = -2\alpha K_{ij} + \mathcal{L}_\beta \gamma_{ij}, \tag{A3a}$$

$$\partial_t K_{ij} = -D_i\partial_j\alpha + \alpha(R_{ij} - 2K_{ik}K^k{}_j + KK_{ij}) + \mathcal{L}_\beta K_{ij} + 4\pi\alpha[(S-\rho)\gamma_{ij} - 2S_{ij}], \tag{A3b}$$

$$\partial_t \Phi = -2\alpha K_\Phi + \mathcal{L}_\beta \Phi, \tag{A3c}$$

$$\partial_t K_\Phi = \alpha\left(KK_\Phi - \frac{1}{2}\gamma^{ij}D_i\partial_j\Phi + \frac{1}{2}\mu^2\Phi\right) - \frac{1}{2}\gamma^{ij}\partial_i\alpha\partial_j\Phi + \mathcal{L}_\beta K_\Phi, \tag{A3d}$$

where D_i is the covariant derivative with respect to the 3-metric.

For the numerical simulations we rewrite the evolution equations above in the BSSN scheme [52,53], which renders the system well-posed. The full system of evolution equations is then

$$\partial_t\tilde{\gamma}_{ij} = \beta^k\partial_k\tilde{\gamma}_{ij} + 2\tilde{\gamma}_{k(i}\partial_{j)}\beta^k - \frac{2}{3}\tilde{\gamma}_{ij}\partial_k\beta^k - 2\alpha\tilde{A}_{ij}, \tag{A4a}$$

$$\partial_t\chi = \beta^k\partial_k\chi + \frac{2}{3}\chi(\alpha K - \partial_k\beta^k), \tag{A4b}$$

$$\partial_t\tilde{A}_{ij} = \beta^k\partial_k\tilde{A}_{ij} + 2\tilde{A}_{k(i}\partial_{j)}\beta^k - \frac{2}{3}\tilde{A}_{ij}\partial_k\beta^k + \chi(\alpha R_{ij} - D_iD_j\alpha)^{\mathrm{TF}} + \alpha(K\tilde{A}_{ij} - 2\tilde{A}_i{}^k\tilde{A}_{kj}) - 8\pi\alpha\left(\chi S_{ij} - \frac{S}{3}\tilde{\gamma}_{ij}\right), \tag{A4c}$$

$$\partial_t K = \beta^k\partial_k K - D^k\partial_k\alpha + \alpha\left(\tilde{A}^{ij}\tilde{A}_{ij} + \frac{1}{3}K^2\right) + 4\pi\alpha(\rho + S), \tag{A4d}$$

$$\partial_t\tilde{\Gamma}^i = \beta^k\partial_k\tilde{\Gamma}^i - \tilde{\Gamma}^k\partial_k\beta^i + \frac{2}{3}\tilde{\Gamma}^i\partial_k\beta^k + 2\alpha\tilde{\Gamma}^i_{jk}\tilde{A}^{jk} + \frac{1}{3}\tilde{\gamma}^{ij}\partial_j\partial_k\beta^k + \tilde{\gamma}^{jk}\partial_j\partial_k\beta^i - \frac{4}{3}\alpha\tilde{\gamma}^{ij}\partial_j K - \tilde{A}^{ij}(3\alpha\chi^{-1}\partial_j\chi + 2\partial_j\alpha) - 16\pi\alpha\chi^{-1}j^i, \tag{A4e}$$

$$\partial_t\Phi = -2\alpha K_\Phi + \mathcal{L}_\beta\Phi, \tag{A4f}$$

$$\partial_t K_\Phi = \alpha\left(KK_\Phi - \frac{1}{2}\gamma^{ij}D_i\partial_j\Phi + \frac{1}{2}\mu^2\Phi\right) - \frac{1}{2}\gamma^{ij}\partial_i\alpha\partial_j\Phi + \mathcal{L}_\beta K_\Phi, \tag{A4g}$$

with the source terms given by

$$\rho \equiv T^{\mu\nu}n_\mu n_\nu, \quad j_i \equiv -\gamma_{i\mu}T^{\mu\nu}n_\nu, \quad S_{ij} \equiv \gamma^\mu{}_i\gamma^\nu{}_j T_{\mu\nu}, \quad S \equiv \gamma^{ij}S_{ij}. \tag{A5}$$

For reasons of convenience, we evolve the real and imaginary part of the scalar field Φ as separate, independent, variables. Finally, the evolution is subject to a set of constraints given by

$$\mathcal{H} \equiv R - K_{ij}K^{ij} + K^2 - 16\pi\rho = 0, \tag{A6}$$

$$\mathcal{M}_i \equiv D^jK_{ij} - D_iK - 8\pi j_i = 0. \tag{A7}$$

[1] B. P. Abbott *et al.* (Virgo, LIGO Scientific Collaborations), Phys. Rev. Lett. **116**, 061102 (2016).
[2] B. P. Abbott *et al.* (Virgo, LIGO Scientific Collaborations), Phys. Rev. Lett. **116**, 241103 (2016).
[3] B. P. Abbott *et al.* (VIRGO, LIGO Scientific Collaborations), Phys. Rev. Lett. **118**, 221101 (2017).
[4] V. Cardoso, E. Franzin, and P. Pani, Phys. Rev. Lett. **116**, 171101 (2016); **117**, 089902(E) (2016).

[5] E. Berti, V. Cardoso, and A. O. Starinets, Classical Quantum Gravity **26**, 163001 (2009).
[6] C. J. Goebel, Astrophys. J. **172**, L95 (1972).
[7] V. Cardoso, A. S. Miranda, E. Berti, H. Witek, and V. T. Zanchin, Phys. Rev. D **79**, 064016 (2009).
[8] G. Khanna and R. H. Price, Phys. Rev. D **95**, 081501 (2017).
[9] V. Cardoso, S. Hopper, C. F. B. Macedo, C. Palenzuela, and P. Pani, Phys. Rev. D **94**, 084031 (2016).
[10] V. Cardoso and P. Pani, Nat. Astron. **1**, 586 (2017).
[11] J. Abedi, H. Dykaar, and N. Afshordi, Phys. Rev. D **96**, 082004 (2017).
[12] G. Ashton, O. Birnholtz, M. Cabero, C. Capano, T. Dent, B. Krishnan, G. D. Meadors, A. B. Nielsen, A. Nitz, and J. Westerweck, arXiv:1612.05625.
[13] R. H. Price and G. Khanna, Classical Quantum Gravity **34**, 225005 (2017).
[14] H. Nakano, N. Sago, H. Tagoshi, and T. Tanaka, Prog. Theor. Exp. Phys. **2017**, 071E01 (2017).
[15] Z. Mark, A. Zimmerman, S. M. Du, and Y. Chen, Phys. Rev. D **96**, 084002 (2017).
[16] C. Chirenti and L. Rezzolla, Phys. Rev. D **94**, 084016 (2016).
[17] M. Visser, *Lorentzian Wormholes: From Einstein to Hawking*, (American Institute of Physics, New York, 1995).
[18] F. E. Schunck and E. W. Mielke, Classical Quantum Gravity **20**, R301 (2003).
[19] S. D. Mathur, Fortsch. Phys. **53**, 793 (2005).
[20] P. O. Mazur and E. Mottola, Proc. Nat. Acad. Sci. **101**, 9545 (2004).
[21] E. G. Gimon and P. Horava, Phys. Lett. B **672**, 299 (2009).
[22] R. Brito, V. Cardoso, C. A. R. Herdeiro, and E. Radu, Phys. Lett. B **752**, 291 (2016).
[23] E. Seidel and W.-M. Suen, Phys. Rev. Lett. **72**, 2516 (1994).
[24] P. V. P. Cunha, C. A. R. Herdeiro, E. Radu, and H. F. Runarsson, Phys. Rev. Lett. **115**, 211102 (2015).
[25] D. J. Kaup, Phys. Rev. **172**, 1331 (1968).
[26] R. Ruffini and S. Bonazzola, Phys. Rev. **187**, 1767 (1969).
[27] C. A. R. Herdeiro, A. M. Pombo, and E. Radu, Phys. Lett. B **773**, 654 (2017).
[28] C. Herdeiro and E. Radu, Classical Quantum Gravity **32**, 144001 (2015).
[29] C. Herdeiro, E. Radu, and H. Runarsson, Classical Quantum Gravity **33**, 154001 (2016).
[30] M. Gleiser and R. Watkins, Nucl. Phys. **B319**, 733 (1989).
[31] T. D. Lee and Y. Pang, Nucl. Phys. **B315**, 477 (1989); **B315**, 129 (1988).
[32] E. Seidel and W.-M. Suen, Phys. Rev. D **42**, 384 (1990).
[33] N. Sanchis-Gual, C. Herdeiro, E. Radu, J. C. Degollado, and J. A. Font, Phys. Rev. D **95**, 104028 (2017).
[34] P. V. P. Cunha, J. Grover, C. Herdeiro, E. Radu, H. Runarsson, and A. Wittig, Phys. Rev. D **94**, 104023 (2016).
[35] P. V. P. Cunha, C. A. R. Herdeiro, and E. Radu, Phys. Rev. D **96**, 024039 (2017).
[36] P. V. P. Cunha, E. Berti, and C. A. R. Herdeiro, arXiv: 1708.04211.
[37] P. Amaro-Seoane, J. Barranco, A. Bernal, and L. Rezzolla, J. Cosmol. Astropart. Phys. 11 (2010) 002.
[38] J. M. Bardeen, in *Black Holes (Les Astres Occlus)*, edited by C. Dewitt and B. S. Dewitt (Gordon and Breach, New York, 1973), p. 215.
[39] H. Falcke, F. Melia, and E. Agol, Astrophys. J. **528**, L13 (2000).
[40] S. Doeleman, E. Agol, D. Backer, F. Baganoff, G. C. Bower, A. Broderick, A. Fabian, V. Fish, C. Gammie, P. Ho, M. Honman, T. Krichbaum, A. Loeb, D. Marrone, M. Reid, A. Rogers, I. Shapiro, P. Strittmatter, R. Tilanus, J. Weintroub, A. Whitney, M. Wright, and L. Ziurys, arXiv:0906.3899.
[41] R.-S. Lu, A. E. Broderick, F. Baron, J. D. Monnier, V. L. Fish, S. S. Doeleman, and V. Pankratius, Astrophys. J. **788**, 120 (2014).
[42] A. Bohn, W. Throwe, F. Hébert, K. Henriksson, D. Bunandar, M. A. Scheel, and N. W. Taylor, Classical Quantum Gravity **32**, 065002 (2015).
[43] A. Einstein, Science **84**, 506 (1936).
[44] J. Renn, T. Sauer, and J. Stachel, Science **275**, 184 (1997).
[45] P. V. P. Cunha, C. A. R. Herdeiro, B. Kleihaus, J. Kunz, and E. Radu, Phys. Lett. B **768**, 373 (2017).
[46] F. H. Vincent, Z. Meliani, P. Grandclement, E. Gourgoulhon, and O. Straub, Classical Quantum Gravity **33**, 105015 (2016).
[47] J. Keir, Classical Quantum Gravity **33**, 135009 (2016).
[48] V. Cardoso, L. C. B. Crispino, C. F. B. Macedo, H. Okawa, and P. Pani, Phys. Rev. **D90**, 044069 (2014).
[49] E. Gourgoulhon, arXiv:gr-qc/0703035.
[50] M. Alcubierre, *Introduction to 3+1 Numerical Relativity*, International Series of Monographs on Physics (Oxford University Press, New York, 2008).
[51] V. Cardoso, L. Gualtieri, C. Herdeiro, and U. Sperhake, Living Rev. Relativity **18**, 1 (2015).
[52] M. Shibata and T. Nakamura, Phys. Rev. D **52**, 5428 (1995).
[53] T. W. Baumgarte and S. L. Shapiro, Phys. Rev. D **59**, 024007 (1998).
[54] I. Cordero-Carrión and P. Cerdá-Durán, arXiv:1211.5930.
[55] I. Cordero-Carrión and P. Cerdá-Durán, *Advances in Differential Equations and Applications*, SEMA SIMAI Springer Series Vol. 4 (Springer International Publishing, Switzerland, 2014).
[56] M. Zilhão, H. Witek, and V. Cardoso, Classical Quantum Gravity **32**, 234003 (2015).
[57] J. G. Rosa and S. R. Dolan, Phys. Rev. D **85**, 044043 (2012).
[58] F. Löffler, J. Faber, E. Bentivegna, T. Bode, P. Diener, R. Haas, I. Hinder, B. C. Mundim, C. D. Ott, E. Schnetter, G. Allen, M. Campanelli, and P. Laguna, Classical Quantum Gravity **29**, 115001 (2012).
[59] EinsteinToolkit, "Einstein Toolkit: Open software for relativistic astrophysics."
[60] M. Zilhão and F. Löffler, Int. J. Mod. Phys. A **28**, 1340014 (2013).
[61] Cactus developers, "Cactus Computational Toolkit."
[62] E. Schnetter, S. H. Hawley, and I. Hawke, Classical Quantum Gravity **21**, 1465 (2004).
[63] Carpet, Carpet: Adaptive Mesh Refinement for the Cactus Framework.
[64] J. Thornburg, Classical Quantum Gravity **21**, 743 (2004).
[65] J. Thornburg, Phys. Rev. D **D54**, 4899 (1996).
[66] U. Sperhake, Phys. Rev. D **76**, 104015 (2007).
[67] M. Campanelli, C. O. Lousto, P. Marronetti, and Y. Zlochower, Phys. Rev. Lett. **96**, 111101 (2006).
[68] J. G. Baker, J. Centrella, D.-I. Choi, M. Koppitz, and J. van Meter, Phys. Rev. Lett. **96**, 111102 (2006).

Monthly Notices of the ROYAL ASTRONOMICAL SOCIETY

MNRAS **470,** L54–L58 (2017) doi:10.1093/mnrasl/slx078
Advance Access publication 2017 May 17

Completion of the universal *I*–Love–*Q* relations in compact stars including the mass

Borja Reina,[1,2]★ Nicolas Sanchis-Gual,[3] Raül Vera[1] and José A. Font[3,4]

[1]*Departamento de Física Teórica e Historia de la Ciencia, University of the Basque Country UPV/EHU, Apartado 644, E-48080 Bilbao, Spain*
[2]*School of Mathematical Sciences, Dublin City University, Glasnevin, Dublin 9, Ireland*
[3]*Departamento de Astronomía y Astrofísica, Universitat de València, Dr. Moliner 50, E-46100 Burjassot, València, Spain*
[4]*Observatori Astronòmic, Universitat de València, C/ Catedrático José Beltrán 2, E-46980 Paterna ,València, Spain*

Accepted 2017 May 12. Received 2017 May 12; in original form 2017 February 16

ABSTRACT

In a recent paper, we applied a rigorous perturbed matching framework to show the amendment of the mass of rotating stars in Hartle's model. Here, we apply this framework to the tidal problem in binary systems. Our approach fully accounts for the correction to the Love numbers needed to obtain the universal *I*–Love–*Q* relations. We compute the corrected mass versus radius configurations of rotating quark stars, revisiting a classical paper on the subject. These corrections allow us to find a universal relation involving the second-order contribution to the mass δM. We thus complete the set of universal relations for the tidal problem in binary systems, involving four perturbation parameters, namely *I*, Love, *Q* and δM. These relations can be used to obtain the perturbation parameters directly from observational data.

Key words: gravitational waves – binaries: general – stars: neutron – stars: rotation.

1 INTRODUCTION

The construction of analytic models of astrophysical compact bodies in general relativity (GR) relies on the matching of space–time theory. The idea is to consider two different bounded regions, namely an interior fluid and a vacuum exterior, and to impose appropriate matching conditions on a time-like hypersurface Σ separating them. Therefore, a global model is constructed by joining the common boundary data on Σ. While the search for an exact global model for a rotating compact body is a major challenge, the situation becomes tractable when one resorts to approximate methods such as perturbation theory. In this context, models that describe rotating stars (Hartle 1967), tidal effects (Damour & Nagar 2009) or collapsing stars (Brizuela et al. 2010) have been developed.

Although the matching of space–time in the exact case has been well understood for decades, the matching in a perturbative scheme has needed a much longer concoction. The first fully general and consistent perturbation theory of hypersurfaces to second order is due to Mars (2005). On top of a background space–time where two regions are matched on some Σ_0, first and second-order problems for the corresponding regions are developed. The theory provides the common boundary data on Σ_0 for such problems and the *gauge-independent* equations for the quantities that describe the deformation of the surface. Perturbed matching is commonly treated in the literature by prescribing some extension of the exact matching conditions to the perturbative scheme, or assuming the continuity of the functions driving the perturbations across Σ_0 (see Mars, Mena & Vera 2007). However, this is not ensured a priori, and assuming explicit choices of coordinates (and gauges) in which the perturbations satisfy certain continuity and differentiability conditions may subtract generality to the model. Even worse, it may lead to wrong outcomes. We discuss two relevant examples next.

The first example has to do with slowly rotating relativistic stars. In their pioneering work, Hartle and Thorne presented the general relativistic treatment of isolated rotating compact stars in equilibrium (Hartle 1967; Hartle & Thorne 1968), known as 'Hartle's model' in short. This stands as the basis to construct analytical models in axial symmetry (see Stergioulas 2003, and references therein). A perturbative scheme is built upon a spherical non-rotating configuration, on top of which stationary (rotating) and axial perturbations are taken to second order. Models are built assuming a perfect fluid interior with barotropic equation of state (EOS) that rotates rigidly and with no convective motions. Under these assumptions, the perturbations are described by four functions, whose values at the surface of the star determine the dragging of inertial frames, the deformation and the total mass of the star in terms of the central density. At each order, those values are computed as follows: (i) integrating from the regular centre, given an EOS; (ii) solving the asymptotically flat vacuum exterior; and (iii) assuming the continuity of the functions across the surface choosing an explicit coordinate system.

Assumption (iii) has significant implications on the properties of the stellar models. As shown by Reina & Vera (2015), using the framework of Mars (2005), a relevant perturbative function presents a discontinuity proportional to the (background) energy density in

★ E-mail: borja.reina@dcu.ie

the stellar surface. This function enters the computation of the mass of the star at second-order δM and, therefore, the original expression for the total mass of the rotating star given in Hartle (1967) has to be amended. Idealized, constant-density stars, originally studied by Chandrasekhar & Miller (1974), were subsequently analysed in Reina (2016), showing that the deviations in the mass–radius diagrams are far from negligible.

The second example has to do with the so-called *I*–Love–*Q* relations (Yagi & Yunes 2013b), where '*I*' and '*Q*' refer to the moment of inertia and the quadrupole moment of the star, respectively, and the Love numbers 'k_l' are associated with the tidal field due to the presence of a companion star. The most basic treatment of this problem fits in Hartle's scheme and can be solved in the regime of stationary and axial perturbations (see Damour & Nagar 2009, and references therein). Although I, k_l and Q depend individually strongly on the EOS, they are related in an EOS-independent way. Yagi & Yunes (2013b) found that these relations split into two different categories: ordinary EOS stars and quark stars. However, using a correction identified in Damour & Nagar (2009) as a pathological behaviour of one of the field equations across the surface of homogeneous stars, Yagi & Yunes (2014) obtained an amended expression for the Love numbers, which leads to universal *I*–Love–*Q* relations. As hinted by the correction to the original Hartle's model, it is straightforward to show that the solution to the tidal problem is indeed related: The result of Yagi & Yunes (2013b) was incorrect due to the assumption of continuity of the perturbations across Σ_0 because a function connected to the Love numbers exhibits a discontinuity proportional to the energy density at the stellar surface, which does not vanish in quark stars. Let us note that the jumps in the tidal problem were already addressed by Price & Thorne (1969) and Campolattaro & Thorne (1970). Although exact only for $l \geq 2$, these discontinuities had somehow been forgotten.

The aim of this Letter is to recall the perturbed matching conditions from Reina & Vera (2015) to then (i) apply the corrections in the context of Hartle's model to quark stars with linear EOS, revisiting the work of Colpi & Miller (1992); (ii) set forth the discontinuities involved in the $l \geq 2$ sector of the first-order tidal-field problem and show how those conditions, which indeed coincide with those in Price & Thorne (1969), lead to the corrections recognized in Damour & Nagar (2009) and used in Hinderer et al. (2010) and Yagi & Yunes (2014); and (iii) complete the *I*–Love–*Q* relations incorporating δM, now correctly computed, that indicate universal relations for all perturbative quantities.

2 SETTING AND FIELD EQUATIONS

We start with the construction of the global background configuration. Consider two static spherically symmetric space–time $(\mathcal{V}^+, g^+, \Sigma_0^+)$ and $(\mathcal{V}^-, g^-, \Sigma_0^-)$, with $g^\pm = -\mathrm{e}^{\nu^\pm}\mathrm{d}t_\pm^2 + \mathrm{e}^{\lambda^\pm}\mathrm{d}r_\pm^2 + r_\pm^2(\mathrm{d}\theta_\pm^2 + \sin^2\theta_\pm \mathrm{d}\varphi_\pm^2)$, that are matched across the boundaries, $\Sigma_0 := \Sigma_0^\pm = \{r^\pm = a^\pm\}$ with constants $a^\pm > 0$. The interior region (+) radial coordinate ranges in $r^+ \in (0, a^+)$ and the exterior (−) radial coordinate ranges in $r^- \in (a^-, \infty)$. The matching conditions for this setting are $a := a^+ = a^-$, $[\lambda] = [\nu] = [\nu'] = 0$, where $' := \mathrm{d}/\mathrm{d}r$ and $[f]$ is the difference of the function f evaluated on Σ_0 from the (+) and (−) sides, i.e. $[f] := f^+|_{\Sigma_0} - f^-|_{\Sigma_0}$.

The perfect fluid interior is described by its unit fluid flow $\boldsymbol{u}$, whose energy density $E \geq 0$ and pressure $P \geq 0$ are related by a barotropic EOS $E(P)$. The mass function is defined by $\mathrm{e}^{-\lambda^+(r_+)} = 1 - 2M^+(r_+)/r_+$. The Tolman–Oppenheimer–Volkoff (TOV) equations hold (Hartle 1967) and determine the interior configuration, given the central value of the energy density $E(0) := E_\mathrm{c}$. Function ν is determined up to an additive constant. The asymptotically flat vacuum exterior is Schwarzschild, determined by the total mass M, explicitly $\mathrm{e}^{\nu^-(r_-)} = \mathrm{e}^{-\lambda^-(r_-)} = 1 - \frac{2M}{r_-}$.

Given this matter content, the matching conditions are interpreted as follows: $[\lambda] = 0$ fixes the constant M to be the mass of the fluid, $M = M^+(a)$, $[\nu] = 0$ fixes the value of ν^+ at the origin, and $[\nu'] = 0$ is just $P(a) = 0$, which determines a.

2.1 Perturbative scheme for rotating stars

Hartle's model is based upon the following forms for the perturbation tensors in each region (let us drop $\pm$ for clarity) to first and second order, respectively,[1]

$$K_1^\mathrm{H} = -2r^2\,\omega(r)\sin^2\theta \mathrm{d}t\mathrm{d}\varphi, \tag{1}$$

$$\begin{aligned} K_2^\mathrm{H} = {} & (-4\mathrm{e}^{\nu(r)}h(r,\theta) + 2r^2\sin^2\theta\omega^2(r))\mathrm{d}t^2 \\ & + 4\mathrm{e}^{2\lambda(r)}r^{-1}m(r,\theta)\mathrm{d}r^2 + 4r^2k(r,\theta)(\mathrm{d}\theta^2 + \sin^2\theta\mathrm{d}\varphi^2), \end{aligned} \tag{2}$$

where $h(r,\theta) = h_0(r) + h_2(r)P_2(\cos\theta)$, $m(r,\theta) = m_0(r) + m_2(r)P_2(\cos\theta)$ and $k(r,\theta) = k_0(r) + k_2(r)P_2(\cos\theta)$. The perturbed (unit) fluid flow with rigid rotation, and no convection reads $\boldsymbol{u}^{(1)} = \Omega\partial_\varphi$ and $\boldsymbol{u}^{(2)} = \mathrm{e}^{-3\nu/2}(\Omega^2 g_{\varphi\varphi} + 2\Omega K_{1r\varphi}^\mathrm{H} + K_{2rt}^\mathrm{H}/2)\partial_t$, for a constant Ω. Hence, the energy density and pressure perturbations enter only the second order as $E^{(2)}(r,\theta) = E_0^{(2)}(r) + E_2^{(2)}(r)P_2(\cos\theta)$, $P^{(2)}(r,\theta) = P_0^{(2)}(r) + P_2^{(2)}(r)P_2(\cos\theta)$. It is convenient to introduce a rescaled pressure defined by $\tilde{P}_{0/2}^{(2)} := P_{0/2}^{(2)}/2(E+P)$. The first- and second-order quantities rescale under a perturbation parameter ε, so that any functions $A^{(1)}$ and $A^{(2)}$ at first and second order, respectively, enter the model through the scale invariants $\varepsilon A^{(1)}$ and $\varepsilon^2 A^{(2)}$.

A convenient substitution to the function ω in (1) is $\tilde{\omega}(r) := \Omega - \omega(r)$, that satisfies the single ODE (43) in Hartle (1967). It is integrated from the origin $\tilde{\omega}^+(0) := \tilde{\omega}_c$ outwards. Given that the relevant quantity is $\varepsilon\tilde{\omega}_c$, one is free to fix either $\tilde{\omega}_c = 1$ or $\varepsilon = 1$ (as in Hartle 1967). For convenience, we choose the former. In the exterior, $\tilde{\omega}^-(r_-) = \Omega - 2Jr_-^{-3}$ for some constant J.

The $l = 0$, 2 sectors of the second-order perturbations can be studied independently. In the $l = 0$ sector, a gauge fixing allows us to set $k_0 = 0$ (see Reina & Vera 2015), so that the only functions involved are $\{m_0, h_0\}$. In the interior, a first integral (see equation 64 in Reina & Vera 2015, or equation 90 in Hartle 1967) is used to substitute h_0^+ by $\tilde{P}_0^{(2)}$ and the rest of the field equations provide a inhomogeneous system of first-order ODEs for the set $\{m_0^+, \tilde{P}_0^{(2)}\}$ (see equations 61 and 62 in Reina & Vera 2015, or equations 97 and 100 in Hartle 1967). The equations are integrated from a regular origin taking $\tilde{E}_0^{(2)}(0) = 0$ to obtain the perturbed configuration quantities in terms of E_c. For the exterior, we have

$$m_0^-(r_-) = \delta M - \frac{J^2}{r_-{}^3}, \quad h_0^-(r_-) = \frac{1}{r_- - 2M}\left(-\delta M + \frac{J^2}{r_-{}^3}\right), \tag{3}$$

for some arbitrary constant δM (Hartle 1967).

The $l = 2$ sector involves the functions h_2, k_2 and m_2. The field equations provide a quadrature for m_2, a first integral that relates h_2 and $\tilde{P}_2^{(2)}$, and a system of coupled first-order ODEs (see equations 67 and 68 in Reina & Vera 2015, or equations 125 and 126 in Hartle

[1] The function $m(r,\theta)$ in equation (2) corresponds to the m used in Hartle (1967), whereas m in Reina & Vera (2015) is $re^{-\lambda}m$ here.

1967) for the pair $\{h_2, \upsilon := h_2 + k_2\}$. For a regular origin, the set $\{h_2^+, \upsilon^+\}$ is determined up to one arbitrary constant. The exterior is found in terms of an arbitrary constant K and the Legendre functions of the second kind ($Q^m_{l=2}$) (Hartle & Thorne 1968):

$$h_2^-(r_-) = K\,Q_2^2\left(\frac{r}{M}-1\right) + J^2\left(\frac{1}{Mr_-^3}+\frac{1}{r_-^4}\right), \tag{4}$$

$$\upsilon^+(r_-) = K\frac{2M}{\sqrt{r_-(r_--2M)}}Q_2^1\left(\frac{r_-}{M}-1\right) - \frac{J^2}{r_-^4}. \tag{5}$$

2.2 Tidal problem

We summarize next the even sector of the linearized perturbations of a spherically symmetric perfect fluid body due to a quadrupolar tidal field. This problem was analysed in Hinderer (2008) using the methods developed in Thorne & Campolattaro (1967) to study non-radial modes of pulsation. For simplicity, we restrict the discussion to the static limit of the perturbations. The (even) tensor perturbation reads in the Regge–Wheeler gauge (Hinderer 2008)

$$K_1^T = \sum_{l,m}\left\{\mathrm{e}^{\nu(r)}H_0(r)_{lm}\mathrm{d}t^2 + \mathrm{e}^{\lambda(r)}H_2(r)_{lm}\mathrm{d}r^2 + r^2K(r)_{lm}(\mathrm{d}\theta^2+\sin^2\theta\,\mathrm{d}\varphi^2)\right\}Y_{lm}(\theta,\varphi). \tag{6}$$

The equations for the different modes $\{l, m\}$ decouple, and those for the $\{l \geq 2, m = 0\}$ modes yield $H_2^+(r_+)_l = H_0^+(r_+)_l$ plus the coupled ODEs (dropping the $m = 0$ label):

$$r_+^2\upsilon^{+\prime}H_{0\,l}^{+\prime} = \mathrm{e}^{\lambda^+}(l(l+1)-2)K_l^+ + (r_+(\lambda^{+\prime}+\upsilon^{+\prime}) - (r_+\upsilon^{+\prime})^2 - \mathrm{e}^{\lambda^+}l(l+1)+2)H_{0\,l}^+, \tag{7}$$

$$K_l^{+\prime} = H_{0\,l}^{+\prime} + \upsilon^{+\prime}H_{0\,l}^+. \tag{8}$$

The system is integrated from a regular origin, and is usually written as a single second-order ODE for the functions H_{0l} (see equations 27 and 29 in Damour & Nagar 2009).

In vacuum, equations (7) and (8) hold with $\mathrm{e}^{\upsilon^-} = \mathrm{e}^{-\lambda^-} = 1 - \frac{2M}{r_-}$, and the general solution for H_{0l} reads[2]

$$H_{0\,l}^-(r_-) = a_{lP}\hat{P}_l^2\left(\frac{r_-}{M}-1\right) + a_{lQ}\hat{Q}_l^2\left(\frac{r_-}{M}-1\right), \tag{9}$$

for arbitrary constants a_{lP} and a_{lQ} (Damour & Nagar 2009).

3 MATCHING TO SECOND ORDER OF ROTATING COMPACT STARS

The solutions discussed in the previous section depend on some integration constants left undetermined. These must be fixed by the relations that the interior and exterior problems satisfy on the common boundary Σ_0, and are, in turn, related to functions on Σ_0 that eventually describe the deformation of the surface. The full set of perturbed matching conditions in this second-order context (1 and 2), from a pure geometrical description, were consistently derived and discussed in Reina & Vera (2015), using the framework developed by Mars (2005). We briefly review the results concerned here before discussing quark stars.

[2] $\hat{P}_l^2 := \left(\frac{2^l}{\sqrt{\pi}}\frac{\Gamma(l+1/2)}{\Gamma(l-1)}\right)^{-1}P_l^2$ and $\hat{Q}_l^2 := \left(\frac{\sqrt{\pi}}{2^{l+1}}\frac{\Gamma(l+3)}{\Gamma(l+3/2)}\right)^{-1}Q_l^2$.

The matching conditions for the first-oder perturbation tensor (1) are $[\omega] = [\omega'] = 0$ (see Proposition 1 and the gauge discussion in Reina & Vera 2015), and therefore

$$J = \frac{1}{6}a^4\tilde{\omega}^{+\prime}(a) \quad \text{and} \quad \Omega = \tilde{\omega}^+(\mathrm{a}) + \frac{2\mathrm{J}}{\mathrm{a}^3}. \tag{10}$$

J and Ω are thus obtained, given $\tilde{\omega}_c$ (=1). The stellar angular momentum and velocity are $J^S = \varepsilon J$ and $\Omega^S = \varepsilon\Omega$. Given some angular velocity Ω^S as data, ε is determined by $\varepsilon = \Omega^S/\Omega$. The *moment of inertia* is defined as $I := J^S/\Omega^S = J/\Omega$.

For the second order, in the $l = 0$ sector, we need for our purposes here only (Theorem 1 in Reina & Vera 2015)

$$[m_0] = -4\pi\frac{a^3}{M}(a-2M)E(a)\tilde{P}_0^{(2)}(a), \tag{11}$$

$$E(a)\left(2\tilde{P}_0^{(2)}(a) + \frac{M}{a^2}\mathrm{e}^{\lambda(a)/2}\Xi_0\right) = 0. \tag{12}$$

Given that the set $\{m_0^+(r_+), \tilde{P}_0^{(2)}(r_+)\}$ has been determined in the interior, (11) fixes δM in (3) as

$$\delta M = m_0^+(a) + \frac{J^2}{a^3} + 4\pi\frac{a^3}{M}(a-2M)E(a)\tilde{P}_0^{(2)}(a). \tag{13}$$

The total mass, in terms of a fixed E_c, reads

$$M_T(E_c) = M(E_c) + \varepsilon^2\delta M(E_c). \tag{14}$$

The second- order correction to the mass $\delta M^S := \varepsilon^2\delta M$ is usually called the change in mass. The correction to the original Hartle's model comes from the discontinuity (11), yielding the last term in (13). Equation (12) provides Ξ_0 if $E(a) \neq 0$ (see below), which describes the star $l = 0$ deformation (in the gauge used) through the average radius of the rotating star $R_T = a - \varepsilon^2\mathrm{e}^{-\lambda(a)/2}\Xi_0/2$ (Reina & Vera 2015), producing the usual $R_T = a + \varepsilon^2 a(a-2M)\tilde{P}_0^{(2)}(a)/M$ (Hartle 1967).

The matching conditions for the $l = 2$ sector can be split into two sets. The first one contains two purely geometrical (independent of Einstein's equations) relations

$$[h_2] = 0, \quad [k_2] = 0. \tag{15}$$

The second set is obtained by combining the rest of the geometrical matching conditions with the field equations. That results in the following four matching conditions:

$$\left[h_2'\right] = 4\pi E(a)\frac{a^2}{M}\left\{h_2(a) + \frac{1}{3}\mathrm{e}^{2\lambda(a)}\left((a-M)^2+M^2\right)\tilde{\omega}^{+2}(a)\right\}, \tag{16}$$

$$\left[k_2'\right] = 4\pi E(a)\frac{a^2}{M}\left\{h_2(a) + \frac{1}{3}a(a+2M)\mathrm{e}^{\lambda(a)}\tilde{\omega}^{+2}(a)\right\}, \tag{17}$$

$$[m_2] = \frac{8}{3}\pi a^4E(a)\mathrm{e}^{\lambda(a)}\tilde{\omega}^{+2}(a), \tag{18}$$

$$E(a)\left\{h_2(a) - \frac{1}{4}\nu'(a)\mathrm{e}^{-\lambda(a)/2}\Xi_2 + \frac{1}{3}a^2\mathrm{e}^{\lambda(a)}\tilde{\omega}^{+2}(a)\right\} = 0. \tag{19}$$

Again, the last equation provides Ξ_2, accounting for the star deformation (eccentricity), if $E(a) \neq 0$ (see below).

The two conditions (15) fix both the constant from the homogeneous part in $\{h_2^+, \upsilon^+\}$ and K from the exterior solutions (4) and (5). K provides the *quadrupolar moment* Q^S by

$$Q^S = \varepsilon^2 Q = \varepsilon^2\left(\frac{8}{5}KM^3 + \frac{J^2}{M}\right). \tag{20}$$

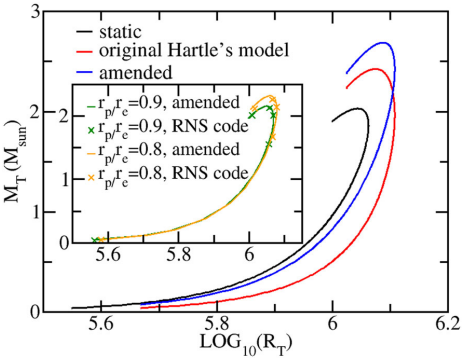

Figure 1. Total mass versus radius diagram for strange stars. For the rotating models (red and blue curves), significant differences appear when the total mass is correctly computed. Inset (polar-to-equatorial axis ratio): $r_{\rm p}/r_{\rm e}$=0.9: L_2-norm{amended, Hartle}={0.037, 0.075}; $r_{\rm p}/r_{\rm e}$ = 0.8: {0.10, 0.17}.

Table 1. Strange star models. $R_{\rm S} = 2M$ stands for the Schwarzschild radii, where M is the static mass. $\varepsilon^2\delta M^O/M$ is the fractional change in mass computed in the original Hartle's model, while $\varepsilon^2\delta M/M$ is the corrected version.

E_c (10^{14} g cm^{-3})	a ($R_{\rm S}$)	M ($M_\odot$)	$\frac{\varepsilon^2\delta M^O}{M}$	$\frac{\varepsilon^2\delta M}{M}$	R_T (km)	λ_2
4.10	31.6	0.038	0.016	0.958	4.67	457×10^6
5.66	3.42	1.000	0.134	0.624	12.0	2540
6.84	2.67	1.400	0.164	0.524	12.7	497
19.18	1.85	2.030	0.194	0.310	11.8	23

A relevant dimensionless quantity independent of ε (the rotation) is $\overline{Q} := Q^S M/J^{S2} = QM/J^2$ (Yagi & Yunes 2013a).

To illustrate the relevance of the corrections to previous work implied by the above discontinuities, we build numerically equilibrium models of strange stars and compare with Hartle's original approach taken by Colpi & Miller (1992). We use the MIT bag model with a linear EOS of the type $P = \frac{1}{3}(E - 4B)$, $E \geq 4B$, where B is the *bag constant*. As in Colpi & Miller (1992), we use $B = 56.25$ MeV fm^{-3}. We consider a range of E_c from 4.1×10^{14} to 4.4×10^{15} g cm^{-3}. Within this range, the smallest value of E_c generates a non-rotating model of $\sim$0.04 $M_\odot$, while the largest mass achieved is $\sim$2 $M_\odot$, corresponding to $E_c = 1.9 \times 10^{15}$ g cm^{-3}.

Fig. 1 shows the mass of the configurations against the mean radius for both the static case and the rotating case, assuming a fixed rotational velocity $\Omega^S = \sqrt{M/a^3}$ (the mass-shedding limit). The inset shows the comparison with the *exact* results, computed with the RNS code without the slow-rotation approximation (Stergioulas, Bulik & Kluzniak 1999), for two values of the polar-to-equatorial axis ratio. For a given central energy density, the mass increases due to rotation. The correction to the computation of the total mass of the rotating stars leads to significantly higher values than those in Colpi & Miller (1992, compare red and blue curves). In particular, the maximum mass is 2.69 $M_\odot$, $\sim$11 per cent larger than that attained in Hartle's approach. In addition, Table 1 reports the numerical values of relevant model parameters (compare with Table 1 of Colpi & Miller 1992). We find that the maximum mass difference is $\sim$0.5 $M_\odot$, achieved for a density $E_c = 6.34 \times 10^{14}$ g cm^{-3}.

4 TIDAL LINEARIZED MATCHING

A similar analysis can be carried out for the perturbations describing the full tidal problem (equation 6), generalizing the matching conditions from Reina & Vera (2015) to a non-axisymmetric set-up. Such study will be presented elsewhere. However, under the assumption of staticity made in Section 2.2, the matching for the axisymmetric $\{l \geq 2, m = 0\}$ sector of the tidal problem becomes a subcase of the matching given by equations (1) and (2) after (i) setting $\omega = 0$ and (ii) identifying $h(r, \theta) = -H_0(r, \theta)/4$, $m(r, \theta) = H_2(r, \theta)/4$ and $k(r, \theta) = K(r, \theta)/4$. Proposition 2 in Reina & Vera (2015) ensures then that the corresponding spherical-harmonic decomposition coefficients for all $l \geq 2$ satisfy equations equivalent to (15) and (16)–(18), leading to

$$[H_{0l}] = 0, \quad [K_l] = 0, \tag{21}$$

$$\left[H_{0l}'\right] = \left[K_l'\right] = \frac{4\pi a^2}{M} E(a) H_{0l}(a), \quad [H_{2l}] = 0, \tag{22}$$

while the analogous to (19) for all $l \geq 2$ leads to

$$E(a)\left(H_{0l}(a) + \nu'(a) e^{-\lambda(a)/2}\, \Xi_l^{(\rm tid)}\right) = 0. \tag{23}$$

Two remarks are in order. First, conditions (21) are independent of the field equations and therefore H_{0l} and K_l will be continuous irrespective of the theory used. However, the continuity of H_{2l} (as well as condition 23) is a consequence of both the geometrical matching plus Einstein's equations for a perfect fluid. For other matter content or theory of gravity, the geometric matching conditions from Proposition 2 in Reina & Vera (2015) must be conveniently combined with the corresponding field equations. Of course, if E presents a jump at $r = a$ (and $H_{0l}(a) \neq 0$), so will H_{0l}' and K_l'.

Secondly, the deformation of the star (in the gauge used) due to the tidal field is encoded in $\Xi_l^{(\rm tid)}$. It is remarkable that the perturbed matching procedure allows its determination only when $E(a) \neq 0$, through (23). This is equivalent to what happens to Ξ_0 and Ξ_2 in the rotating star setting (equations 12 and 19). However, as shown in Reina & Vera (2015), $\Xi_l^{(\rm tid)}$ satisfy the vanishing of the second factor in (23) even when $E(a) = 0$ whenever a solution of the problem for all orders of the perturbative expansion exists – this is, in fact, the argument implicitly used in the literature, for example, Hartle (1967).

It is convenient to define the function $y := rH_0'/H_0$ in order to compute the Love numbers. The boundary conditions are directly obtained from (21) and (22), and read

$$[y] = 4\pi a^3 E(a)/M. \tag{24}$$

This expression recovers the correction addressed in Damour & Nagar (2009) for homogeneous stars, which is used in Hinderer et al. (2010) for other EOS with non-vanishing energy density at the boundary. The constant ratio $a_l := a_{lQ}/a_{lP}$ of the exterior solution (9) is thus determined from the interior, using (24), by

$$\begin{aligned} a_l &= -\left.\frac{\partial_{r_-}\hat{P}_l^2 - (y_l^-/a)\hat{P}_l^2}{\partial_{r_-}\hat{Q}_l^2 - (y_l^-/a)\hat{Q}_l^2}\right|_{r_-=a} \\ &= -\left.\frac{\partial_{r_+}\hat{P}_l^2 - (y_l^+/a)\hat{P}_l^2 + (4\pi a^2 E(a)/M)\hat{P}_l^2}{\partial_{r_+}\hat{Q}_l^2 - (y_l^+/a)\hat{Q}_l^2 + (4\pi a^2 E(a)/M)\hat{Q}_l^2}\right|_{r_+=a}. \end{aligned} \tag{25}$$

We compare the exterior solution (9) with the internally and externally generated parts of the gravitational potential W defined in the DSX approach (see section IV.C in Damour & Nagar 2009) in order to relate the constant a_l (25) to the *tidal Love numbers*

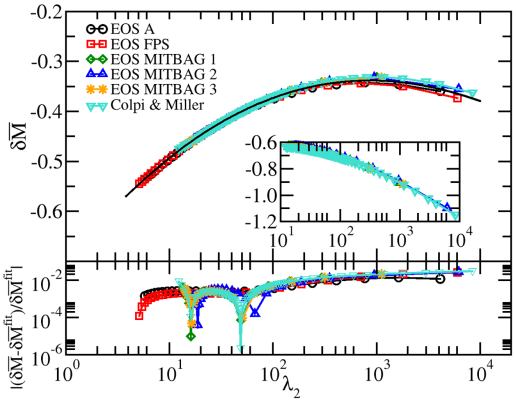

Figure 2. Universal relation between $\overline{\delta M}$ and λ_2 for six EOS. The black solid line fits the numerical data to $\log\overline{\delta M} = -0.703 + 0.255\log\lambda_2 - 0.045(\log\lambda_2)^2 - 5.707\times10^{-4}(\log\lambda_2)^3 + 2.207\times10^{-4}(\log\lambda_2)^4$. The relative error is shown in the bottom panel. The inset shows the incorrect version of $\overline{\delta M}$ for strange star EOS.

$k_l = \frac{1}{2}\left(\frac{M}{a}\right)^{2l+1} a_l$. In the numerical analysis, we concentrate on $l = 2$ and we shall use instead the quantity $\lambda_2 := a_2/3$ (see Yagi & Yunes 2013a).

5 UNIVERSALITY OF *I*–LOVE–*Q* RELATIONS

We turn next to discuss the implications our approach has in the universality of *I*–Love–*Q* relations. Let us first define the rotation-independent (and dimensionless) quantity $\overline{\delta M} := M^3\delta M^S/J^{S2} = M^3\delta M/J^2$. Using the correct (amended) expressions for $\overline{\delta M}$ and λ_2, we compute their relation for six different EOS configurations, including two neutron stars and four quark stars. We choose a range of λ_2 between $10^{0.7}$ and 10^4, which comprises a range of TOV configurations with mass $M_\odot \leq M \leq 2.3M_\odot$ (the actual range depends on the particular EOS). The numerical results are summarized in Fig. 2. We find a strong indication of a universal relation between $\overline{\delta M}$ and λ_2, as the fit of the numerical data shows (the relative error is displayed in the bottom panel). Such a universal relation is not found for strange stars when using the original (*incorrect*) version of $\overline{\delta M}$, as shown in the inset of the top panel.

Therefore, the right use of the perturbed matching yields the corrections used in Yagi & Yunes (2014) to find universal *I*–Love–*Q* relations. Our results show that the second-order $l = 0$ parameter $\overline{\delta M}$ completes the universal relations that involve the first-order parameter I, the second-order $l = 2$ parameter $\overline{Q}$ and the tidal number k_2. This can be used to fix the problems inherent, precisely, to the relations involving (only) the latter three parameters. As discussed in Yagi & Yunes (2013a), $\overline{Q}$ is defined from M, but the relevant observational quantity is the mass M_T (14). From observables, one would need to calculate the corresponding static configuration to find M, so as to make the universal *I*–Love–*Q* relations truly useful in observational astrophysics (at least for weak magnetic fields; Haskell et al. 2014). That procedure is model-dependent and, in this regard, the use of M_T instead of M in, for example, $\overline{Q}$ is claimed in Yagi & Yunes (2013a) to be of little numerical importance. In this work, we have shown that the inclusion of $\overline{\delta M}$ in the *I*–Love–*Q* relations provides, however, a complete set of relations between all perturbation quantities (to this order), which allows us to obtain any such quantity from observational input alone.

ACKNOWLEDGEMENTS

We thank Emanuele Berti for suggesting this investigation and Nikolaos Stergioulas for providing the exact data. This work is supported by the Spanish Ministerio de Economa, Industria y Competitividad (MINECO) and European Regional Development Fund (FEDER) (AYA2013-40979-P, AYA2015-66899-C2-1-P, FIS2014-57956-P), the Generalitat Valenciana (PROMETEOII-2014-069, ACIF/2015/216) and the Basque Government (IT-956-16, POS-2016-1-0075).

REFERENCES

Brizuela D., Martín-García J. M., Sperhake U., Kokkotas K. D., 2010, Phys. Rev. D, 82, 104039
Campolattaro A., Thorne K. S., 1970, ApJ, 159, 847
Chandrasekhar S., Miller J. C., 1974, MNRAS, 167, 63
Colpi M., Miller J. C., 1992, ApJ, 388, 513
Damour T., Nagar A., 2009, Phys. Rev. D, 80, 084035
Hartle J. B., 1967, ApJ, 150, 1005
Hartle J. B., Thorne K. S., 1968, ApJ, 153, 807
Haskell B., Ciolfi R., Pannarale F., Rezzolla L., 2014, MNRAS, 438, L71
Hinderer T., 2008, ApJ, 677, 1216
Hinderer T., Lackey B. D., Lang R. N., Read J. S., 2010, Phys. Rev. D, 81, 123016
Mars M., 2005, Class. Quantum Gravity, 22, 3325
Mars M., Mena F. C., Vera R., 2007, Class. Quantum Gravity, 24, 3673
Price R. H., Thorne K. S., 1969, ApJ, 155, 163
Reina B., 2016, MNRAS, 455, 4512
Reina B., Vera R., 2015, Class. Quantum Gravity, 32, 155008
Stergioulas N., 2003, Living Rev. Relativ., 6
Stergioulas N., Bulik T., Kluzniak W., 1999, A&A, 352, L116
Thorne K. S., Campolattaro A., 1967, ApJ, 149, 591
Yagi K., Yunes N., 2013a, Phys. Rev. D, 88, 023009
Yagi K., Yunes N., 2013b, Science, 341, 365
Yagi K., Yunes N., 2014, Science, 344, 1250349

This paper has been typeset from a TEX/LATEX file prepared by the author.

Bibliography

[1] B. P. Abbott et al. "GW151226: Observation of Gravitational Waves from a 22-Solar-Mass Binary Black Hole Coalescence." In: *Phys. Rev. Lett.* 116.24 (2016), p. 241103. DOI: 10.1103/PhysRevLett.116.241103. arXiv: 1606.04855 [gr-qc].

[2] B. P. Abbott et al. "GW170608: Observation of a 19-solar-mass Binary Black Hole Coalescence." In: *Astrophys. J.* 851.2 (2017), p. L35. DOI: 10.3847/2041-8213/aa9f0c. arXiv: 1711.05578 [astro-ph.HE].

[3] B. P. Abbott et al. "GW170814: A Three-Detector Observation of Gravitational Waves from a Binary Black Hole Coalescence." In: *Phys. Rev. Lett.* 119.14 (2017), p. 141101. DOI: 10.1103/PhysRevLett.119.141101. arXiv: 1709.09660 [gr-qc].

[4] B. P. Abbott et al. "Observation of Gravitational Waves from a Binary Black Hole Merger." In: *Physical Review Letters* 116.6, 061102 (Feb. 2016), p. 061102. arXiv: 1602.03837 [gr-qc].

[5] B. P. Abbott et al. "GW170104: Observation of a 50-Solar-Mass Binary Black Hole Coalescence at Redshift 0.2." In: *Phys. Rev. Lett.* 118.22 (2017), p. 221101. DOI: 10.1103/PhysRevLett.118.221101. arXiv: 1706.01812 [gr-qc].

[6] B. Abbott et al. "GW170817: Observation of Gravitational Waves from a Binary Neutron Star Inspiral." In: *Phys. Rev. Lett.* 119.16 (2017), p. 161101. DOI: 10.1103/PhysRevLett.119.161101. arXiv: 1710.05832 [gr-qc].

[7] M. Alcubierre et al. "Symmetry without symmetry: Numerical simulation of axisymmetric systems using Cartesian grids." In: *International Journal of Modern Physics D* 10.03 (2001), pp. 273–289.

[8] T. Alexander and P. Natarajan. "Rapid growth of seed black holes in the early universe by supra-exponential accretion." In: *Science* 345.6202 (2014), pp. 1330–1333.

[9] D. Alic, W. Kastaun, and L. Rezzolla. "Constraint damping of the conformal and covariant formulation of the Z4 system in simulations of binary neutron stars." In: *Physical Review D* 88.6 (2013), p. 064049.

[10] D. Alic et al. "Conformal and covariant formulation of the Z4 system with constraint-violation damping." In: *Physical Review D* 85.6 (2012), p. 064040.

[11] B. M. Argrow. "Computational analysis of dense gas shock tube flow." In: *Shock Waves* 6.4 (1996), pp. 241–248. ISSN: 1432-2153. DOI: 10.1007/BF02511381. URL: https://doi.org/10.1007/BF02511381.

[12] A. Arvanitaki and S. Dubovsky. "Exploring the String Axiverse with Precision Black Hole Physics." In: *Phys.Rev.* D83 (2011), p. 044026. DOI: 10.1103/PhysRevD.83.044026. arXiv: 1004.3558 [hep-th].

[13] A. Arvanitaki et al. "String Axiverse." In: *Phys.Rev.* D81 (2010), p. 123530. DOI: 10.1103/PhysRevD.81.123530. arXiv: 0905.4720 [hep-th].

[14] J. G. Baker et al. "Gravitational-wave extraction from an inspiraling configuration of merging black holes." In: *Physical Review Letters* 96.11 (2006), p. 111102.

[15] J. Balakrishna, E. Seidel, and W.-M. Suen. "Dynamical evolution of boson stars. 2. Excited states and selfinteracting fields." In: *Phys. Rev.* D58 (1998), p. 104004. DOI: 10.1103/PhysRevD.58.104004. arXiv: gr-qc/9712064 [gr-qc].

[16] J. M. Bardeen, W. H. Press, and S. A. Teukolsky. "Rotating black holes: Locally nonrotating frames, energy extraction, and scalar synchrotron radiation." In: *Astrophys.J.* 178 (1972), p. 347. DOI: 10.1086/151796.

[17] J. Barranco et al. "Are black holes a serious threat to scalar field dark matter models?" In: *Phys.Rev.* D84 (2011), p. 083008. DOI: 10.1103/PhysRevD.84.083008. arXiv: 1108.0931 [gr-qc].

[18] J. Barranco et al. "Schwarzschild black holes can wear scalar wigs." In: *Phys.Rev.Lett.* 109 (2012), p. 081102. DOI: 10.1103/PhysRevLett.109.081102. arXiv: 1207.2153 [gr-qc].

[19] J. Barranco et al. "Schwarzschild scalar wigs: spectral analysis and late time behavior." In: *Phys.Rev.* D89 (2014), p. 083006. DOI: 10.1103/PhysRevD.89.083006. arXiv: 1312.5808 [gr-qc].

[20] T. W. Baumgarte and S. L. Shapiro. "Numerical integration of Einstein's field equations." In: *Phys. Rev. D* 59.2, 024007 (Jan. 1999), p. 024007. eprint: gr-qc/9810065.

[21] T. W. Baumgarte and S. L. Shapiro. "Numerical relativity and compact binaries." In: *Phys. Rep.* 376 (Mar. 2003), pp. 41–131. eprint: gr-qc/0211028.

[22] T. W. Baumgarte et al. "Numerical relativity in spherical polar coordinates: Evolution calculations with the BSSN formulation." In: *Phys. Rev. D* 87.4, 044026 (Feb. 2013), p. 044026. arXiv: 1211.6632 [gr-qc].

[23] T. W. Baumgarte et al. "Numerical relativity in spherical polar coordinates: Evolution calculations with the BSSN formulation." In: *Physical Review D* 87.4 (2013), p. 044026.

[24] M. C. Begelman. "Evolution of supermassive stars as a pathway to black hole formation." In: *Mon.Not.Roy.Astron.Soc.* 402 (Feb. 2010), pp. 673–681. DOI: 10.1111/j.1365-2966.2009.15916.x. arXiv: 0910.4398.

[25] M. C. Begelman. "Can a spherically accreting black hole radiate very near the Eddington limit." In: *Monthly Notices of the Royal Astronomical Society* 187.2 (1979), pp. 237–251.

[26] M. C. Begelman. "Evolution of supermassive stars as a pathway to black hole formation." In: *Monthly Notices of the Royal Astronomical Society* 402.1 (2010), pp. 673–681.

[27] M. C. Begelman, M. Volonteri, and M. J. Rees. "Formation of supermassive black holes by direct collapse in pre-galactic haloes." In: *Monthly Notices of the Royal Astronomical Society* 370.1 (2006), pp. 289–298.

[28] M. C. Begelman, M. Volonteri, and M. J. Rees. "Formation of supermassive black holes by direct collapse in pregalactic halos." In: *Mon.Not.Roy.Astron.Soc.* 370 (2006), pp. 289–298. DOI: 10.1111/j.1365-2966.2006.10467.x. arXiv: astro-ph/0602363 [astro-ph].

[29] J. D. Bekenstein. "Black holes and entropy." In: *Phys.Rev.* D7 (1973), pp. 2333–2346. DOI: 10.1103/PhysRevD.7.2333.

[30] S. Bernuzzi and D. Hilditch. "Constraint violation in free evolution schemes: Comparing the BSSNOK formulation with a conformal decomposition of the Z4 formulation." In: *Physical Review D* 81.8 (2010), p. 084003.

[31] E. Berti, V. Cardoso, and A. O. Starinets. "Quasinormal modes of black holes and black branes." In: *Class.Quant.Grav.* 26 (2009), p. 163001. DOI: 10.1088/0264-9381/26/16/163001. arXiv: 0905.2975 [gr-qc].

[32] H. Bethe. *The theory of shock waves for an arbitrary equation of state.* Tech. Paper 545, Office of Scientific Research and Development. 1942.

[33] M. Bezares, C. Palenzuela, and C. Bona. "Final fate of compact boson star mergers." In: *Physical Review D* 95.12 (2017), p. 124005.

[34] C. Bona et al. "General-covariant evolution formalism for numerical relativity." In: *Phys. Rev. D* 67.10, 104005 (May 2003), p. 104005. eprint: gr-qc/0302083.

[35] C. Bona et al. "General-covariant evolution formalism for numerical relativity." In: *Physical Review D* 67.10 (2003), p. 104005.

[36] S Bonazzola. "S. Bonazzola, E. Gourgoulhon, P. Grandclément, and J. Novak, Phys. Rev. D 70, 104007 (2004)." In: *Phys. Rev. D* 70 (2004), p. 104007.

[37] P. Bosch, S. R. Green, and L. Lehner. "Nonlinear Evolution and Final Fate of Charged Anti–de Sitter Black Hole Superradiant Instability." In: *Phys. Rev. Lett.* 116.14 (2016), p. 141102. DOI: 10.1103/PhysRevLett.116.141102. arXiv: 1601.01384 [gr-qc].

[38] R. Brito, V. Cardoso, and P. Pani. "Black holes as particle detectors: evolution of superradiant instabilities." In: *Classical and Quantum Gravity* 32.13 (2015), p. 134001.

[39] R. Brito, V. Cardoso, and P. Pani. "Superradiance." In: *Lect. Notes Phys.* 906 (2015), pp.1–237. DOI: 10.1007/978-3-319-19000-6. arXiv: 1501.06570 [gr-qc].

[40] R. Brito et al. "Proca stars: Gravitating Bose–Einstein condensates of massive spin 1 particles." In: *Phys. Lett.* B752 (2016), pp. 291–295. DOI: 10.1016/j.physletb.2015.11.051. arXiv: 1508.05395 [gr-qc].

[41] D. Brizuela et al. “High-order perturbations of a spherical collapsing star.” In: *PRD* 82.10 (2010), p. 104039. DOI: 10.1103/PhysRevD.82.104039. URL: {http://link.aps.org/doi/10.1103/PhysRevD.82.104039}.

[42] V. Bromm and A. Loeb. “Formation of the first supermassive black holes.” In: *Astrophys. J.* 596 (2003), pp. 34–46. DOI: 10.1086/377529. arXiv: astro-ph/0212400 [astro-ph].

[43] V. Bromm and A. Loeb. “Formation of the first supermassive black holes.” In: *The Astrophysical Journal* 596.1 (2003), p. 34.

[44] J. D. Brown. “Covariant formulations of BSSN and the standard gauge.” In: *Phys. Rev. D* 79 (2009), p. 104029.

[45] M. Campanelli et al. “Accurate evolutions of orbiting black-hole binaries without excision.” In: *Physical Review Letters* 96.11 (2006), p. 111101.

[46] V. Cardoso and P. Pani. “The observational evidence for horizons: from echoes to precision gravitational-wave physics.” In: (2017). arXiv: 1707.03021 [gr-qc].

[47] V. Cardoso and S. Yoshida. “Superradiant instabilities of rotating black branes and strings.” In: *Journal of High Energy Physics* 2005.07 (2005), p. 009.

[48] V. Cardoso et al. “Geodesic stability, Lyapunov exponents and quasinormal modes.” In: *Phys. Rev.* D79 (2009), p. 064016. DOI: 10.1103/PhysRevD.79.064016. arXiv: 0812.1806 [hep-th].

[49] V. Cardoso et al. “Gravitational-wave signatures of exotic compact objects and of quantum corrections at the horizon scale.” In: *Phys. Rev.* D94.8 (2016), p. 084031. DOI: 10.1103/PhysRevD.94.084031. arXiv: 1608.08637 [gr-qc].

[50] V. Cardoso et al. “The Black hole bomb and superradiant instabilities.” In: *Phys.Rev.* D70 (2004), p. 044039. DOI: 10.1103/PhysRevD.70.049903, 10.1103/PhysRevD.70.044039. arXiv: hep-th/0404096 [hep-th].

[51] S. Chandrasekhar. “The highly collapsed configurations of a stellar mass (Second paper).” In: *Monthly Notices of the Royal Astronomical Society* 95 (1935), pp. 207–225.

[52] S. Chandrasekhar. “The highly collapsed configurations of a stellar mass.” In: *Monthly Notices of the Royal Astronomical Society* 91 (1931), pp. 456–466.

[53] S. Chatrchyan et al. “Observation of a new boson at a mass of 125 GeV with the CMS experiment at the LHC.” In: *Physics Letters B* 716.1 (2012), pp. 30–61.

[54] P. Cinnella and C. Corre. “Numerical investigation of three-dimensional transonic flows of Bethe-Zel’dovich-Thompson fluids.” In: *APS Division of Fluid Dynamics Meeting Abstracts*. Nov. 2006.

[55] A. Collaboration. “Search for the Standard Model Higgs boson in the diphoton decay channel with 4.9 fb-1 of pp collisions at sqrt (s)= 7 TeV with ATLAS.” In: *arXiv preprint arXiv:1202.1414* (2012).

[56] C. Collaboration et al. “A new boson with a mass of 125 GeV observed with the CMS experiment at the large hadron collider.” In: *Science* 338.6114 (2012), pp. 1569–1575.

[57] M. Colpi and J. C. Miller. "Rotational properties of strange stars." In: *ApJ* 388 (1992), pp. 513–520. DOI: 10.1086/171170.

[58] R. S. Conklin, B. Holdom, and J. Ren. "Gravitational wave echoes through new windows." In: *arXiv preprint arXiv:1712.06517* (2017).

[59] I. Cordero-Carrión, P. Cerdá-Durán, and J. M. Ibáñez. "Gravitational waves in dynamical spacetimes with matter content in the fully constrained formulation." In: *Physical Review D* 85.4 (2012), p. 044023.

[60] A. Cruz-Osorio, F. S. Guzman, and F. D. Lora-Clavijo. "Scalar Field Dark Matter: behavior around black holes." In: *JCAP* 1106 (2011), p. 029. DOI: 10.1088/1475-7516/2011/06/029. arXiv: 1008.0027 [astro-ph.CO].

[61] P. V. Cunha et al. "Lensing and dynamics of ultracompact bosonic stars." In: *Physical Review D* 96.10 (2017), p. 104040.

[62] T. Damour, N. Deruelle, and R. Ruffini. "On quantum resonances in stationary geometries." In: *Nuovo Cimento Lettere* 15 (1976), pp. 257–262.

[63] T. Damour and A. Nagar. "Relativistic tidal properties of neutron stars." In: *PRD* 80.8 (2009), p. 084035. DOI: 10.1103/PhysRevD.80.084035. URL: {http://link.aps.org/doi/10.1103/PhysRevD.80.084035}.

[64] J. C. Degollado and C. A. R. Herdeiro. "Time evolution of superradiant instabilities for charged black holes in a cavity." In: *Phys.Rev.* D89 (2014), p. 063005. DOI: 10.1103/PhysRevD.89.063005. arXiv: 1312.4579 [gr-qc].

[65] S. Detweiler. "Klein-Gordon equation and rotating black holes." In: *Physical Review D* 22.10 (1980), p. 2323.

[66] S. L. Detweiler. "KLEIN-GORDON EQUATION AND ROTATING BLACK HOLES." In: *Phys.Rev.* D22 (1980), pp. 2323–2326. DOI: 10.1103/PhysRevD.22.2323.

[67] F. Di Giovanni et al. "Dynamical formation of Proca stars and quasi-stationary solitonic objects." In: *arXiv preprint arXiv:1803.04802* (2018).

[68] S. R. Dolan. "Instability of the massive Klein-Gordon field on the Kerr spacetime." In: *Phys.Rev.* D76 (2007), p. 084001. DOI: 10.1103/PhysRevD.76.084001. arXiv: 0705.2880 [gr-qc].

[69] S. R. Dolan. "Superradiant instabilities of rotating black holes in the time domain." In: (2012). arXiv: 1212.1477 [gr-qc].

[70] W. E. East. "Superradiant instability of massive vector fields around spinning black holes in the relativistic regime." In: *Physical Review D* 96.2 (2017), p. 024004.

[71] W. E. East and F. Pretorius. "Superradiant instability and backreaction of massive vector fields around Kerr black holes." In: *Physical review letters* 119.4 (2017), p. 041101.

[72] W. E. East, F. M. Ramazanoğlu, and F. Pretorius. "Black hole superradiance in dynamical spacetime." In: *Physical Review D* 89.6 (2014), p. 061503.

[73] A. Escorihuela-Tomàs et al. "Quasistationary solutions of scalar fields around collapsing self-interacting boson stars." In: *Physical Review D* 96.2 (2017), p. 024015.

[74] J. A. Font et al. “Three-dimensional numerical general relativistic hydrodynamics. II. Long-term dynamics of single relativistic stars.” In: *Physical Review D* 65.8 (2002), p. 084024.

[75] H. Furuhashi and Y. Nambu. “Instability of massive scalar fields in Kerr-Newman spacetime.” In: *Progress of theoretical physics* 112.6 (2004), pp. 983–995.

[76] M. Gleiser and R. Watkins. “Gravitational Stability of Scalar Matter.” In: *Nucl. Phys.* B319 (1989), pp. 733–746. DOI: 10.1016/0550-3213(89)90627-5.

[77] N. K. Glendenning and C. Kettner. “Possible third family of compact stars more dense than neutron stars.” In: *Astron. Astrophys.* 353 (Jan. 2000), pp. L9–L12. eprint: astro-ph/9807155.

[78] C. J. Goebel. “Comments on the ”vibrations” of a Black Hole.” In: *Astrophys. J.* 172 (Mar. 1972), p. L95. DOI: 10.1086/180898.

[79] A. Guardone and L. Vigevano. “Roe Linearization for the van der Waals Gas.” In: *Journal of Computational Physics* 175 (Jan. 2002), pp. 50–78. DOI: 10.1006/jcph.2001.6915.

[80] C. Gundlach et al. “Constraint damping in the Z4 formulation and harmonic gauge.” In: *Classical and Quantum Gravity* 22.17 (2005), p. 3767.

[81] F. S. Guzman. “Evolving spherical boson stars on a 3-D Cartesian grid.” In: *Phys. Rev.* D70 (2004), p. 044033. DOI: 10.1103/PhysRevD.70.044033. arXiv: gr-qc/0407054 [gr-qc].

[82] F. S. Guzman. “Evolving spherical boson stars on a 3D Cartesian grid.” In: *Physical Review D* 70.4 (2004), p. 044033.

[83] F. Guzmán. “The three dynamical fates of Boson Stars.” In: *Revista mexicana de física* 55.4 (2009), pp. 321–326.

[84] Z. Haiman and A. Loeb. In: *Astrophys. J.* 552 (2001), p. 459.

[85] Z. Haiman and A. Loeb. “What is the highest plausible redshift of luminous quasars?” In: *The Astrophysical Journal* 552.2 (2001), p. 459.

[86] J. B. Hartle. “Slowly Rotating Relativistic Stars. I. Equations of Structure.” In: *ApJ* 150 (1967), pp. 1005–1029. DOI: 10.1086/149400.

[87] J. B. Hartle and K. S. Thorne. “Slowly Rotating Relativistic Stars. II. Models for Neutron Stars and Supermassive Stars.” In: *ApJ* 153 (1968), pp. 807–834. DOI: 10.1086/149707.

[88] S. H. Hawley and M. W. Choptuik. “Boson stars driven to the brink of black hole formation.” In: *Phys. Rev.* D62 (2000), p. 104024. DOI: 10.1103/PhysRevD.62.104024. arXiv: gr-qc/0007039 [gr-qc].

[89] C. Herdeiro and E. Radu. “Construction and physical properties of Kerr black holes with scalar hair.” In: *Class. Quant. Grav.* 32.14 (2015), p. 144001. DOI: 10.1088/0264-9381/32/14/144001. arXiv: 1501.04319 [gr-qc].

[90] C. A. R. Herdeiro, J. C. Degollado, and H. F. Rúnarsson. “Rapid growth of superradiant instabilities for charged black holes in a cavity.” In: *Phys.Rev.* D88 (2013), p. 063003. DOI: 10.1103/PhysRevD.88.063003. arXiv: 1305.5513 [gr-qc].

[91] C. A. Herdeiro and E. Radu. "Kerr black holes with scalar hair." In: *Physical review letters* 112.22 (2014), p. 221101.

[92] D. Hilditch et al. "Compact binary evolutions with the Z4c formulation." In: *Physical Review D* 88.8 (2013), p. 084057.

[93] T. Hinderer et al. "Tidal deformability of neutron stars with realistic equations of state and their gravitational wave signatures in binary inspiral." In: *PRD* 81.12 (2010), p. 123016. DOI: 10.1103/PhysRevD.81.123016. URL: {http://link.aps.org/doi/10.1103/PhysRevD.81.123016}.

[94] S. Hod. "Analytic treatment of the charged black-hole-mirror bomb in the highly explosive regime." In: *Physical Review D 88,* 064055 (2013). arXiv: 1310.6101 [gr-qc].

[95] S. Hod. "On the instability regime of the rotating Kerr spacetime to massive scalar perturbations." In: *Physics Letters B* 708.3-5 (2012), pp. 320–323.

[96] S. Hod. "Stability of the extremal Reissner-Nordstroem black hole to charged scalar perturbations." In: *Phys. Lett.* B713 (2012), pp. 505–508. DOI: 10.1016/j.physletb.2012.06.043. arXiv: 1304.6474 [gr-qc].

[97] W. Hu, R. Barkana, and A. Gruzinov. "Fuzzy Cold Dark Matter: The wave properties of ultralight particles." In: *Phys. Rev. Lett.* 85 (2000), pp. 1158–1161. DOI: 10.1103/PhysRevLett.85.1158. arXiv: astro-ph/0003365.

[98] J.-c. Hwang. "Roles of a coherent scalar field on the evolution of cosmic structures." In: *Phys. Lett.* B401 (1997), pp. 241–246. DOI: 10.1016/S0370-2693(97)00400-0. arXiv: astro-ph/9610042.

[99] J. M. Ibáñez et al. "Anomalous dynamics triggered by a non-convex equation of state in relativistic flows." In: *ArXiv e-prints* (Dec. 2017). arXiv: 1712.03248 [astro-ph.HE].

[100] J. M. Ibáñez et al. "On the convexity of relativistic hydrodynamics." In: *Classical and Quantum Gravity* 30.5, 057002 (Mar. 2013), p. 057002. DOI: 10.1088/0264-9381/30/5/057002.

[101] J. M. Ibañez et al. "Neutron-star collapse and gravitational waves with a non-convex equation of state." In: *in preparation* (2018).

[102] J. Ibáñez et al. "Anomalous dynamics triggered by a non-convex equation of state in relativistic flows." In: *Monthly Notices of the Royal Astronomical Society* 476.1 (2018), pp. 1100–1110.

[103] M. Kamionkowski, J. Pradler, and D. G. E. Walker. "Dark energy from the string axiverse." In: (2014). arXiv: 1409.0549 [hep-ph].

[104] G. Kauffmann and M. Haehnelt. "A unified model for the evolution of galaxies and quasars." In: *Monthly Not. R. Astron Soc.* 311 (Jan. 2000), pp. 576–588. DOI: 10.1046/j.1365-8711.2000.03077.x. eprint: astro-ph/9906493.

[105] G. Khanna and R. H. Price. "Black Hole Ringing, Quasinormal Modes, and Light Rings." In: *Phys. Rev.* D95.8 (2017), p. 081501. DOI: 10.1103/PhysRevD.95.081501. arXiv: 1609.00083 [gr-qc].

[106] J. Kormendy and K. Gebhardt. In: *AIP Conference Proceedings: 20th Texas Symposium* 586 (2001), pp. 363–381.

[107] T. D. Lee and Y. Pang. "Stability of Mini - Boson Stars." In: *Nucl. Phys.* B315 (1989). [,129(1988)], p. 477. DOI: 10.1016/0550-3213(89)90365-9.

[108] S. L. Liebling and C. Palenzuela. "Dynamical boson stars." In: *Living Reviews in Relativity* 15.1 (2012), p. 6.

[109] M. Mars. "First- and second-order perturbations of hypersurfaces." In: *CQG* 22.16 (2005), pp. 3325–3348. DOI: 10.1088/0264-9381/22/16/013.

[110] D. J. E. Marsh and P. G. Ferreira. "Ultra-Light Scalar Fields and the Growth of Structure in the Universe." In: *Phys. Rev.* D82 (2010), p. 103528. DOI: 10.1103/PhysRevD.82.103528. arXiv: 1009.3501 [hep-ph].

[111] T. Matos, F. S. Guzman, and L. A. Urena-Lopez. "Scalar field as dark matter in the universe." In: *Class. Quant. Grav.* 17 (2000), pp. 1707–1712. DOI: 10.1088/0264-9381/17/7/309. arXiv: astro-ph/9908152.

[112] T. Matos and L. A. Urena-Lopez. "A Further analysis of a cosmological model of quintessence and scalar dark matter." In: *Phys.Rev.* D63 (2001), p. 063506. DOI: 10.1103/PhysRevD.63.063506. arXiv: astro-ph/0006024 [astro-ph].

[113] T. Matos and L. A. Urena-Lopez. "Quintessence and scalar dark matter in the universe." In: *Class. Quant. Grav.* 17 (2000), pp. L75–L81. DOI: 10.1088/0264-9381/17/13/101. arXiv: astro-ph/0004332.

[114] L. Mayer et al. "Direct formation of supermassive black holes via multi-scale gas inflows in galaxy mergers." In: *Nature* 466 (Aug. 2010), pp. 1082–1084. DOI: 10.1038/nature09294. arXiv: 0912.4262.

[115] L. Mayer et al. "Direct formation of supermassive black holes via multi-scale gas inflows in galaxy mergers." In: *Nature* 466.7310 (2010), pp. 1082–1084.

[116] J. C. McKinney et al. "Three-dimensional general relativistic radiation magnetohydrodynamical simulation of super-Eddington accretion, using a new code HARMRAD with M1 closure." In: *Monthly Notices of the Royal Astronomical Society* 441.4 (2014), pp. 3177–3208.

[117] P. J. Montero, T. W. Baumgarte, and E. Müller. "General relativistic hydrodynamics in curvilinear coordinates." In: *Physical Review D* 89.8 (2014), p. 084043.

[118] P. J. Montero and I. Cordero-Carrión. "BSSN equations in spherical coordinates without regularization: Vacuum and nonvacuum spherically symmetric spacetimes." In: *Physical Review D* 85.12 (2012), p. 124037.

[119] P. J. Montero, J. A. Font, and M. Shibata. "Nada: A new code for studying self-gravitating tori around black holes." In: *Physical Review D* 78.6 (2008), p. 064037.

[120] P. J. Montero, H.-T. Janka, and E. Müller. "Relativistic collapse and explosion of rotating supermassive stars with thermonuclear effects." In: *The Astrophysical Journal* 749.1 (2012), p. 37.

[121] D. J. Mortlock et al. "A luminous quasar at a redshift of z= 7.085." In: *Nature* 474.7353 (2011), pp. 616–619.

[122] T. Nakamura, K. Oohara, and Y. Kojima. "General Relativistic Collapse to Black Holes and Gravitational Waves from Black Holes." In: *Prog. Theor. Phys. Suppl.* 3 (1987), pp. 1–218.

[123] H. Okawa, H. Witek, and V. Cardoso. "Black holes and fundamental fields in Numerical Relativity: initial data construction and evolution of bound states." In: *Phys.Rev.* D89 (2014), p. 104032. DOI: 10.1103/PhysRevD.89.104032. arXiv: 1401.1548 [gr-qc].

[124] D. N. Page. "Classical and quantum decay of oscillations: Oscillating self-gravitating real scalar field solitons." In: *Physical Review D* 70.2 (2004), p. 023002.

[125] C. Palenzuela et al. "Gravitational wave signatures of highly compact boson star binaries." In: *Physical Review D* 96.10 (2017), p. 104058.

[126] S. Ponglertsakul and E. Winstanley. "Effect of scalar field mass on gravitating charged scalar solitons and black holes in a cavity." In: *Physics Letters B* 764 (2017), pp. 87–93.

[127] S. Ponglertsakul, E. Winstanley, and S. R. Dolan. "Stability of gravitating charged-scalar solitons in a cavity." In: *Phys. Rev.* D94.2 (2016), p. 024031. DOI: 10.1103/PhysRevD.94.024031. arXiv: 1604.01132 [gr-qc].

[128] W. H. Press and S. A. Teukolsky. "Floating Orbits, Superradiant Scattering and the Black-hole Bomb." In: *Nature* 238 (1972), pp. 211–212. DOI: 10.1038/238211a0.

[129] F. Pretorius. "Evolution of binary black-hole spacetimes." In: *Physical review letters* 95.12 (2005), p. 121101.

[130] R. H. Price and K. S. Thorne. "Non-Radial Pulsation of General-Relativistic Stellar Models. II. Properties of the Gravitational Waves." In: *ApJ* 155 (1969), pp. 163–182. DOI: 10.1086/149857.

[131] B. Reina. "Slowly rotating homogeneous masses revisited." In: *mnras* 455.4 (2016), pp. 4512–4517. DOI: 10.1093/mnras/stv2599. eprint: {http://mnras.oxfordjournals.org/content/455/4/4512.full.pdf+html}. URL: {http://mnras.oxfordjournals.org/content/455/4/4512.abstract}.

[132] B. Reina and R. Vera. "Revisiting Hartle's model using perturbed matching theory to second order: amending the change in mass." In: *CQG* 32.15 (2015), p. 155008. URL: {http://stacks.iop.org/0264-9381/32/i=15/a=155008}.

[133] B. Reina et al. "Completion of the universal I–Love–Q relations in compact stars including the mass." In: *Monthly Notices of the Royal Astronomical Society: Letters* 470.1 (2017), pp. L54–L58.

[134] J. Rosa. "The Extremal black hole bomb." In: *JHEP* 1006 (2010), p. 015. DOI: 10.1007/JHEP06(2010)015. arXiv: 0912.1780 [hep-th].

[135] M. Ruiz, M. Alcubierre, and D. Nunez. "Regularization of spherical and axisymmetric evolution codes in numerical relativity." In: *General Relativity and Gravitation* 40.1 (2008), pp. 159–182.

[136] M. Ruiz, D. Hilditch, and S. Bernuzzi. "Constraint preserving boundary conditions for the Z4c formulation of general relativity." In: *Physical Review D* 83.2 (2011), p. 024025.

[137] V. Sahni and L.-M. Wang. "A New cosmological model of quintessence and dark matter." In: *Phys.Rev.* D62 (2000), p. 103517. DOI: 10.1103/PhysRevD.62.103517. arXiv: astro-ph/9910097 [astro-ph].

[138] N. Sanchis-Gual et al. "Fully covariant and conformal formulation of the Z4 system in a reference-metric approach: Comparison with the BSSN formulation in spherical symmetry." In: *Phys. Rev. D* 89.10, 104033 (May 2014), p. 104033. arXiv: 1403.3653 [gr-qc].

[139] N. Sanchis-Gual et al. "Quasistationary solutions of self-gravitating scalar fields around collapsing stars." In: *Phys. Rev. D* 92.8, 083001 (Oct. 2015), p. 083001. arXiv: 1507.08437 [gr-qc].

[140] N. Sanchis-Gual, V. Quilis, and J. A. Font. "An estimate of the gravitational-wave background from the observed cosmological distribution of quasars." In: *in preparation* (2018).

[141] N. Sanchis-Gual et al. "Dynamical formation of a hairy black hole in a cavity from the decay of unstable solitons." In: *Classical and Quantum Gravity* 34.16 (2017), p. 165001.

[142] N. Sanchis-Gual et al. "Dynamical formation of a Reissner-Nordström black hole with scalar hair in a cavity." In: *Physical Review D* 94.4 (2016), p. 044061.

[143] N. Sanchis-Gual et al. "Explosion and final state of an unstable Reissner-Nordström black hole." In: *Physical review letters* 116.14 (2016), p. 141101.

[144] N. Sanchis-Gual et al. "Numerical evolutions of spherical Proca stars." In: *Physical Review D* 95.10 (2017), p. 104028.

[145] N. Sanchis-Gual et al. "Quasistationary solutions of scalar fields around accreting black holes." In: *Physical Review D* 94.4 (2016), p. 043004.

[146] N. Sanchis-Gual et al. "Quasistationary solutions of self-gravitating scalar fields around black holes." In: *Physical Review D* 91.4 (2015), p. 043005.

[147] K. Schertler et al. "Quark phases in neutron stars and a third family of compact stars as signature for phase transitions[1]." In: *Nuclear Physics A* 677 (Sept. 2000), pp. 463–490. DOI: 10.1016/S0375-9474(00)00305-5. eprint: astro-ph/0001467.

[148] E. Seidel and W.-M. Suen. "Dynamical Evolution of Boson Stars. 1. Perturbing the Ground State." In: *Phys. Rev.* D42 (1990), pp. 384–403. DOI: 10.1103/PhysRevD.42.384.

[149] E. Seidel and W.-M. Suen. "Formation of solitonic stars through gravitational cooling." In: *Phys. Rev. Lett.* 72 (1994), pp. 2516–2519. DOI: 10.1103/PhysRevLett.72.2516. arXiv: gr-qc/9309015 [gr-qc].

[150] E. Seidel and W.-M. Suen. "Formation of solitonic stars through gravitational cooling." In: *Physical review letters* 72.16 (1994), p. 2516.

[151] S. Serna and A. Marquina. "Anomalous wave structure in magnetized materials described by non-convex equations of state." In: *Physics of Fluids* 26.1, 016101 (Jan. 2014), p. 016101. DOI: 10.1063/1.4851415.

[152] M. Shibata and T. Nakamura. "Evolution of three-dimensional gravitational waves: Harmonic slicing case." In: *Phys. Rev. D* 52 (Nov. 1995), pp. 5428–5444.

[153] M. Shibata and S. L. Shapiro. "Collapse of a rotating supermassive star to a supermassive black hole: Fully relativistic simulations." In: *The Astrophysical Journal Letters* 572.1 (2002), p. L39.

[154] A. A. Starobinsky. "Amplification of waves during reflection from a rotating black hole." In: *Zh. Eksp. Teor. Fiz.* 64 (1973), p. 48.

[155] N. Stergioulas. "Rotating Stars in Relativity." In: *Living Reviews in Relativity* 6.3 (2003). URL: {http://www.livingreviews.org/lrr-2003-3}.

[156] N. Stergioulas. *The structure and stability of rotating relativistic stars.* Tech. rep. University of Wisconsin, Milwaukee, 1996.

[157] N. Stergioulas and J. L. Friedman. "Comparing models of rapidly rotating relativistic stars constructed by two numerical methods." In: *arXiv preprint astro-ph/9411032* (1994).

[158] P. A. Thompson. "A Fundamental Derivative in Gasdynamics." In: *Physics of Fluids* 14 (Sept. 1971), pp. 1843–1849. DOI: 10.1063/1.1693693.

[159] M. Volonteri, F. Haardt, and P. Madau. "The Assembly and Merging History of Supermassive Black Holes in Hierarchical Models of Galaxy Formation." In: *Astrophys.J.* 582 (Jan. 2003), pp. 559–573. DOI: 10.1086/344675. eprint: astro-ph/0207276.

[160] A Voss. "Exact Riemann Solution for the Euler Equations with Nonconvex and Nonsmooth Equation of State." unpublished thesis. PhD thesis. University of Wuppertal, 2005.

[161] VVG. *Valencia Virgo Group.* URL: https://www.uv.es/virgogroup/.

[162] J. Westerweck et al. "Low significance of evidence for black hole echoes in gravitational wave data." In: *arXiv preprint arXiv:1712.09966* (2017).

[163] A. Weyhausen, S. Bernuzzi, and D. Hilditch. "Constraint damping for the Z4c formulation of general relativity." In: *Physical Review D* 85.2 (2012), p. 024038.

[164] H. Witek et al. "Superradiant instabilities in astrophysical systems." In: *Phys.Rev.* D87 (2013), p. 043513. DOI: 10.1103/PhysRevD.87.043513. arXiv: 1212.0551 [gr-qc].

[165] K. Yagi and N. Yunes. "Erratum for the Report: "I-Love-Q: Unexpected Universal Relations for Neutron Stars and Quark Stars" by K. Yagi and N. Yunes." In: *Science* 344.6186 (2014), pp. 1250349–1250349. ISSN: 0036-8075. DOI: 10.1126/science.1250349. eprint: {http://science.sciencemag.org/content}. URL: {http://science.sciencemag.org/content/344/6186/1250349}.

[166] K. Yagi and N. Yunes. "I-Love-Q: Unexpected Universal Relations for Neutron Stars and Quark Stars." In: *Science* 341.6144 (2013), pp. 365–368. ISSN: 0036-8075. DOI: 10.1126/science.1236462. eprint: {http://science.sciencemag.org/content/341/6144/365.full.pdf}. URL: {http://science.sciencemag.org/content/341/6144/365}.

[167] Y. Zel'dovich. "On the possibility of rarefaction shock waves." In: *Zh. Eksp. Teor. Fiz.* 4 (1946), pp. 363–364.

[168] T. J. Zouros and D. M. Eardley. "Instabilities of massive scalar perturbations of a rotating black hole." In: *Annals of physics* 118.1 (1979), pp. 139–155.

[169] T. Zouros and D. Eardley. "Instabilities of massive scalar perturbations of a rotating black hole." In: *Annals Phys.* 118 (1979), pp. 139–155. DOI: 10.1016/0003-4916(79)90237-9.